Preparation of F/Sb-doped SnO_2 nanoparticles for composite film used as IR-shielding layer of silicon solar cell

Russameeruk Noonuruk

A THESIS SUBMITTED IN PARTIAL FULFILLMENT OF THE REQUIREMENT FOR THE DEGREE OF DOCTOR OF PHILOSOPHY IN NANOSCIENCE AND NANOTECHNOLOGY

COLLEGE OF NANOTECHNOLOGY

KING MONGKUT'S INSTITUTE OF TECHNOLOGY LADKRABANG

2017

KMITL-2017-NT-D-001-001

Thesis Title	Preparation of F/Sb-doped SnO_2 nanoparticles for composite film used as IR-shielding layer of silicon solar cell
Student	Ms. Russameeruk Noonuruk
Student ID	55670151
Degree	Doctor of Philosophy
Program	Nanoscience and Nanotechnology
Year	2017
Thesis Advisor	Assoc. Prof. Dr. Wisanu Pecharapa
Thesis Co-advisor	Dr. Jaran Sritharathikhun

ABSTRACT

In this research, the conductive oxide nanoparticles of fluoride (F)-, antimony (Sb)-doped tin oxide (SnO_2) were synthesized by sonochemical-assisted precipitation process using metal chloride as starting precursor. After that, the conductive oxide nanoparticles was mixed with tetraethyl orthosilicate (TEOS) and (3-Glycidyloxypropyl)trimethoxysilane (GLYMO) used as starting material for silica film. Coating films composed of a continuous silica matrix homogenously dispersed with ATO and FATO nanoparticles were deposited by sol-gel spin-coating process. Effects of synthesis parameters including dopant concentration and ultrasonic radiation on crucial physical properties of conductive oxide nanoparticles were investigated. Structural properties of nanoparticles were characterized by XRD. The size, shape and crystal structure of the particles were observed by transmission electron microscope (TEM). Surface chemical state analysis was carried out by X-ray photoelectron spectroscopy (XPS). Chemical boding of nanoparticles was characterized by Raman spectroscopy. Moreover, optical and electrical properties were investigated by UV-Vis spectroscopy and Hall measurement, respectively. The results revealed that the as-synthesized powder in SnO_2 phase with less agglomeration can be obtained by sonochemical-assisted precipitation process. It is suggested that the sonochemical process generates localized high temperature area guiding to crystallite growth, nucleation and flocculation of particles. The resistance of SnO_2 nanoparticles was decreases after F and Sb doping, suggesting that the incorporation of

F- and Sb^{5+} ions can enhance the conductivity and IR shielding properties of SnO_2. The temperature measurement results indicate that nanoparticles were dispersed in SiO_2 matrix, the temperature of silicon solar cell was preserved, decreasing slower than the case of non IR-shielding layers. Moreover, the V_{oc} value of 5:5FATO composite film has a bit higher than that of other materials as additional exposure time, implying the feasibility of IR irradiation shielding of the composite film.

Keywords: Tin oxide, Conductive nanoparticles, Sonochemical-assisted precipitation process, Spin coating method

หัวข้อวิทยานิพนธ์	การเตรียมอนุภาคนาโน F/Sb-doped SnO_2 เพื่อใช้เป็นชั้นฟิล์มคอมโพสิต สำหรับป้องกันรังสีอินฟราเรดของเซลล์แสงอาทิตย์แบบซิลิคอน
นักศึกษา	นางสาวรัศมีรักษ์ หนูนุรักษ์
รหัสประจำตัว	๕๕๖๗๐๑๕๑
ปริญญา	ปรัชญาดุษฎีบัณฑิต
สาขาวิชา	นาโนวิทยาและนาโนเทคโนโลยี
พ.ศ.	๒๕๖๐
อาจารย์ที่ปรึกษาวิทยานิพนธ์	รองศาสตราจารย์ ดร.วิษณุ เพชรภา
อาจารย์ที่ปรึกษาวิทยานิพนธ์ร่วม	ดร. จรัญ ศรีธาราธิคุณ

บทคัดย่อ

งานวิจัยนี้ทำการสังเคราะห์ผงนาโนนำไฟฟ้าของสารประกอบทินออกไซด์ที่เจือด้วย ฟลูออรีน แอนติโมนี จากสารตั้งต้นชนิดโลหะคลอไรด์ด้วยกระบวนการตกตะกอนร่วมที่ใช้คลื่นอัลตราโซนิคในการสั่นช่วย หลังจากนั้นนำผงนาโนนำไฟฟ้าที่เตรียมได้ผสมกับสารละลาย tetraethyl orthosilicate (TEOS) และ (3-Glycidyloxypropyl)trimethoxysilane (GLYMO) ซึ่งเป็นสารตั้งต้นของซิลิกา ในการเตรียมฟิล์มนาโนคอมโพสิตของผงนาโนไฟฟ้าที่กระจายตัวบนซิลิกาด้วยกระบวนการโซลเจล แบบหมุนเคลือบ ในงานวิจัยนี้ได้ศึกษาผลกระทบของตัวแปรที่มีผลต่อการสังเคราะห์และลักษณะทางกายภาพของผงนาโนนำไฟฟ้าทินออกไซด์ ได้แก่ ปริมาณการเจือของสาร และผลกระทบของการนำคลื่นอัลตราโซนิคมาประยุกต์ใช้ในการสังเคราะห์ผงนาโนนำไฟฟ้า และทำการวิเคราะห์โครงสร้างของผงนาโนนำไฟฟ้าที่เตรียมได้ด้วยเทคนิคการเลี้ยวเบนของรังสีเอกซ์ (XRD) วิเคราะห์โครงสร้างระดับจุลภาคและสัณฐานวิทยาด้วยกล้องจุลทรรศน์อิเล็กตรอนแบบส่องผ่าน (TEM) วิเคราะห์ธาตุและองค์ประกอบของสารด้วยเทคนิคการปลดปล่อยอนุภาคของอิเล็กตรอนด้วยรังสีเอกซ์ (XPS) และวิเคราะห์เชิงพันธะด้วยเครื่องรามานสเปกโตรสโกปี รวมทั้งวิเคราะห์สมบัติทางแสงและทางไฟฟ้าด้วยเทคนิค ยูวี-วิส สเปกโตสโกปีและเทคนิคของฮอลล์ ตามลำดับ จากผลการวิเคราะห์ พบว่า การสังเคราะห์สารด้วยกระบวนการตกตะกอนร่วมที่ใช้คลื่นอัลตราโซนิคในการสั่นช่วยนั้น ส่งผลให้ผงนาโนที่เตรียมได้มีการกระจายตัวที่ดี และปรากฏเฟสทินออกไซด์โดยไม่ต้องผ่านกระบวนการเผาเปลี่ยนเฟส เนื่องจากคลื่นอัลตราโซนิคสามารถให้อุณหภูมิและพลังงานที่สูง และส่งผลต่อการก่อตัว การโตของผลึกอนุภาคทินออกไซด์ และป้องกันการเกาะกลุ่มกันของผงนาโน ส่วนสมบัติการนำไฟฟ้าและ

การป้องกันรังสีอินฟาเรดของทินออกไซด์นั้นมีค่าเพิ่มขึ้นหลังจากการเจือ F และ Sb ฟิล์มนาโนคอมโพสิต เพราะว่าการเจือ F และ Sb ส่งผลต่อการเพิ่มขึ้นของอิเล็กตรอนอิสระในทินออกไซด์ ทำให้ค่าความต้านทานของฟิล์มลดลง หลังจากนั้นได้นำฟิล์มคอมโพสิตที่มีผงนาโนกระจายตัวในซิลิกาเพื่อทดสอบสมบัติการป้องกันรังสีอินฟาเรด พบว่า เซลล์แสงอาทิตย์แบบซิลิคอนและมีชั้นฟิล์มคอมโพสิตอยู่ด้านบนนั้น สามารถลดอัตราการเพิ่มขึ้นของอุณหภูมิในเซลล์แสงอาทิตย์ได้ดีกว่า เมื่อเวลาในการฉายแสงเพิ่มมากขึ้น นอกจากนี้ พบว่า ค่า *Voc* ของเซลล์แสงอาทิตย์ที่ใช้ 5:5FATO ฟิล์มเป็นชั้นป้องกันรังสีอินฟาเรดมีค่าสูงกว่าฟิล์มคอมโพสิตตัวอื่นที่ได้ศึกษาในงานวิจัยนี้ จากผลการทดลองบ่งบอกว่า การนำฟิล์มคอมโพสิตนี้สามารถนำมาใช้ป้องกันรังสีอินฟาเรดได้

คำสำคัญ: ทินออกไซด์, ผงนาโนนำไฟฟ้า, ฟิล์มบาง, กระบวนการตกตะกอนร่วมที่ใช้คลื่นอัลตราโซนิคในการสั่นช่วย, การหมุนเคลือบ

ACKNOWLEDGMENT

This thesis was successfully completed by supporting of my best advisor, Assoc. Prof. Dr. Wisanu Pechara and co-advisor, Dr. Jaran Sritharathikhun. I would like to thank to him for his great supporting everything in my life and my thesis.

I would like to thank Thailand Graduate Institute of Science and Technology (TGIST, contract No. 0156009) for scholarship support.

This work was financially supported by KMITL research fund. This work has partially been supported by the National Nanotechnology Center (NANOTEC), NSTDA, Ministry of Science and Technology, Thailand, through its program of Center of Excellence Network.

Authors gratefully acknowledge the support College of Nanotechnology, King Mongkut's Institute of Technology Ladkrabang (KMITL), Faculty of Engineering, Rajamangala University of Technology Thanyaburi (RMUTT) for XRD measurement, Center of Excellence in Glass Technology and Material Science (CEGM), Nakhon Pathom Rajabhat University for diffuse reflectance measurement

CONTENTS

Page

CONTENTS (CONT.)

Page

CONTENTS (CONT.)

Page

LIST OF TABLES

Table **Page**

LIST OF FIGURES

Figure **Page**

LIST OF FIGURES (CONT.)

Figure **Page**

LIST OF FIGURES (CONT.)

Figure **Page**

LIST OF FIGURES (CONT.)

Figure **Page**

LIST OF FIGURES (CONT.)

Figure **Page**

LIST OF FIGURES (CONT.)

Figure **Page**

CHAPTER 1

INTRODUCTION

1.1 Motivation

In the recent times, global warming is a serious threat to our planet which will ultimately result in the demise of the planet. The use of fossil fuel for generation of electricity produces the excessively injurious pollutants that are a contributing factor to the cause of global warming. Solar energy is a promising renewable energy source because it can reduce the quantity of pollution and toxic waste [1,2]. Solar cells are an alternative energy technology which is direct conversion of incident light in to electricity [3]. In solar radiation, energy radiates from the sun in form of electromagnetic wave, including visible, ultraviolet light (UV) and infrared (IR) radiation. Most of the solar energy can be transmitted to ground level, and only parts of the UV ($\lambda < 0.4$ μm) and IR ($\lambda > 0.7$ μm) radiation are strongly damped. In a practical situation, the IR radiation generates the thermal energy resulting in the temperature inside in the solar cells. Fesharaki *et al.* [4] reported that the increase in temperature inside the device affects the efficiency losses in solar cell. Heat transmission and heat diffusion was reduced by IR-shielding through blocking the wavelength of 780-2500 nm. Transparent conducting oxides (TCOs) are promising candidates as IR-shielding materials because they allow a high level of transmission of visible light and possess the ability to shield IR radiation. TCOs generally can absorb light in the ultraviolet regime due to its large band gap as well as in the IR regime due to its free carrier absorption [5]. The carrier concentration is important for IR-shielding because it dominates the optical properties of materials in the visible and IR regime. The band gap of TCOs can be shifted towards shorter wavelengths with $\lambda < 300$ nm due to the higher carrier entering states at the bottom of the conduction band. The longer wavelength exhibits surface plasmon resonance (SPR) frequencies in the near-infrared (NIR) region due to lower charge carrier densities than noble metals.

In most case, IR-shield coatings can be prepared by several techniques including sputtering [6], electron beam evaporation [7] and chemical vapor deposition [8]. These techniques involve vacuum treatment and high-temperature, which increase the rate of consumption of energy and cost of equipment.

Low-cost and economical alternative fabrication techniques include wet chemical deposition like conventional dip-coating or spin-coating sol-gel method [9]. The fabrication of TCO nanoparticle dispersion in silica film matrix deposited by sol-gel method can retain high visible transparency and can reduce NIR transmittance. Moreover, the advantage of TCO/silica nanocomposite coatings does not require high temperature because the TCO particles formation can be separated from the deposition of the nanocomposite layer. The heat treatment of the layers can take place at temperatures which are below 150 °C that is undamaged the solar cell [10]. Therefore it is possible to produce layers on polymer-like polycarbonate or to use this layer as interfacial layer in organic bulk-heterojunction solar cells which are specially built in the standard architecture [11].

Tin oxide (SnO_2) has recently received considerable interest in TCO materials due to alternatively low-cost to rather expensive indium tin oxide, excellent thermal properties and stability in oxidizing environment [12]. However, low optical and electrical performance due to its stoichiometry, low intrinsic carrier density and mobility are still its major drawbacks. The charge carrier concentration in SnO_2 and electrical conductivity can be effectively heightened by the incorporation of extrinsic dopants. Doping is accomplished either by adding a higher-valent metal, by replacing some oxygen with fluorine, or by oxygen vacancies. The appropriate dopants typically utilized for increasing the conductivity and optical properties of SnO_2 are In, Sb, F and Mo that can provide oxygen vacancies generating free electrons to promote higher conductivity of the SnO_2 host [13]. Furthermore, the resistivity of SnO_2 particles can be reduced by controlling their sizes down to nanoscale regime, which have a high driving force of densification. The nanomaterials have fewer adjacent coordinate atoms as compared with the bulk atoms resulting to drastic increase of large specific surface areas. Recently, many processes such as precipitation process sol-gel method and hydrothermal method have been employed to synthesize tin-oxide-based materials in form of low dimensional nanostructure with the improvement in physical, optical, catalytic and electric properties. Among these techniques, the precipitation method has significant advantages over the others such as simplicity of solution concentration, simply synthesized process, ease of doping and low time and energy consumption. Nevertheless, agglomeration of ultra-fine nanoparticles is still critical for this synthesis process. This difficulty can be overcome by the assistance of sonochemical technique which

is one of effective method to synthesize ultra-fine nano-structured materials with less agglomeration and rapid crystal growth due to cavitation effect in chemical process during high ultrasonic irradiation [14].

In this work, an endeavor was taken on the synthesis of F- and Sb- doped SnO_2 nanoparticles employing sonochemical-assisted precipitation process. Effect of doping concentrations on physical structures, optical and electrical properties of Sb-doped SnO_2 nanoparticles was investigated. Effect of F/Sb-codoepd SnO_2 nanoparticles dispersed in silica film coating on solar cell was investigated.

1.2 Objective of the study

This thesis is conducted in order to

1.2.1 study the synthesis of F/Sb doped SnO_2 nanoparticles via the sonochemical process.

1.2.2 study the preparation of F/Sb-doped SnO_2 nanoparticles dispersed in silica films via spin-coating process.

1.2.3 study the IR-shielding properties of composite films on solar cell.

1.3 Scope of the study

The scope of this thesis is as follows;

1.3.1 Characterization of F/Sb doped SnO_2 nanoparticle synthesized via the sonochemical process and investigation on the effect of calcination temperature and dopant content on physical , electrical and optical and electrical properties.

1.3.2 Characterization of F/Sb-doped SnO_2 nanoparticles dispersed in silica films via spin-coating process and investigation on the effect of calcination temperature and dopant content on physical and optical properties.

1.3.3 Proving and analyzing IR shielding coating of composite film on solar cell.

1.4 Expected Results

1.4.1 The relevant parameters of the synthesis such as calcinations temperature, fluorine doping content, antimony doping content, co-doping content and nanoparticles concentration will be notified.

1.4.2 The meaning of transparent conducting oxide and IR-shielding properties will be clearly understood.

CHAPTER 2
THEORETICAL BACKGROUND

In overview, the objective of this chapter is to investigate the feature of IR shielding for solar cells, the properties of transparent conducting oxide material, the meaning of composite, the synthesis techniques and application of IR shielding feature. In this chapter, the relevant theories are explained.

2.1 IR shielding feature for solar cells

In general, solar cells exploit the photovoltaic effect that is the direct conversion of incident light in to electricity. Electron-hole pairs generated by solar photons are separated at an interface of two materials of different conduction polarities. Solar cells represent a very promising renewable energy which will reduce our dependence on fossil oil. In solar radiation, energy radiated from the sun in form of electromagnetic wave, including visible, ultraviolet light (UV) and infrared (IR) radiation. Most of the solar energy can be transmitted to ground level, and only parts of the UV ($\lambda < 0.4$ μm) and IR ($\lambda > 0.7$ μm) radiation are strongly damped. In a practical situation, the IR radiation generates the thermal energy resulting in the temperature inside in the solar cells. Fesharaki et al. [4] reported that the increase in temperature inside the devices could result in the efficiency losses in solar cells. In Figure 2.1, the total power loss due to the increase in temperature was from around 750 mW down to 458 mw [15]. Heat transmission and heat diffusion could be reduced by IR-shielding through blocking the wavelength of 780-2500 nm. Therefore, unwanted thermal gain can be blocked by selective absorption/reflection of ultraviolet and near-infrared (NIR). Near infrared cut off coatings can effectively reduce heat transmission and heat diffusion through blocking the near infrared rays of 780–2500 nm to attain the purpose of energy conservation.

When electromagnetic radiation impinges on a material, one fraction can be transmitted, a second fraction is reflected, and a third fraction is absorbed [16]. Energy conservation yields, at each wavelength, that

$$T(\lambda) + R(\lambda) + A(\lambda) = 1 \tag{2.1}$$

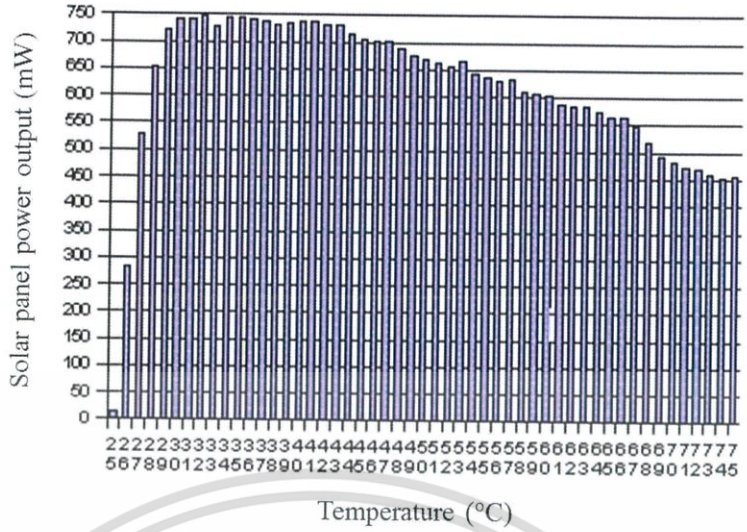

Figure 2.1 The relationship between temperature and solar panel power output measured. A 150 w halogen office lamp was used at a distance of 55 mm from the solar panel as a sun substitute [15].

where T, R, and A denote transmittance, reflectance, and absorbance, respectively. Another fundamental relationship, also founded on energy conservation and referred to as Kirchhoff's law that is

$$A(\lambda) = E(\lambda) \tag{2.2}$$

with E being emittance, i.e., the fraction of the black-body radiation that is given off at a particular wavelength. Equation is of practical relevance mainly for $\lambda > 3$ μm.

A basic reason why transparent conducting oxides are important is their ability to be transparent in a limited and well-defined range, normally encompassing visible light in the $0.4 < \lambda < 0.7$ μm wavelength interval, while they can reflect infrared (IR) and absorb the ultraviolet (UV). Figure2.2 (a) shows optical reflection, transmission and absorption spectra for a typical commercial ZnO on glass which collectively shows the key spectral features of a TCO material [16]. First, the material is quite transparent, ~80%, in the visible portion of spectrum, 400-700 nm. Across this spectral region where the sample in transparent, oscillations due to thin film interference effects can be seen in both the transmission and reflection spectra. The short wavelength cut off in the transmission at ~300 nm is due to the fundamental band gap excitation form the valence band to the conduction band as depicted in the Fig.2.2 (b). The gradual long wavelength decrease in the transmission starting at ~ 1,000 nm and the corresponding increase in the reflection starting

at 1,500 nm are due to collective oscillation of conduction band electrons known as plasma oscillation or plasmons for short. There can also be substantial absorption due to these plasma oscillations as-is the case for this particular sample with the maximum absorption occurring at the characteristic plasma wavelength, λ_p, as shown in Figure 2.2. As the number of electrons in the conduction band, N, is increased, such as by substitution doping, the plasma wavelength shifts to shorter wavelengths as $\lambda_p \propto \sqrt{N}$ which creates a fundamental tradeoff between conductivity and the long wavelength transparency limit. At very high electron concentrations, this can even decrease the visible wavelength transparency.

Figure 2.3 (a) shows how the infrared transparency increases for SnO_2 as the sheet resistance is increased from 5 to 100 Ω/□. Even though both of these SnO_2 samples have similar visible wavelength transparency, the 5 Ω/□ sample would be unusable as transparent conductor for telecom applications at 1,500 nm or for giving a high solar throughput. Figure 2.3 (b) shows how the plasma wavelength varies with the dopant level in Ti doped In_2O_3 and hence how TCO properties can be tuned. Collectively, the examples shown in Figure 2.2 and 2.3 should make it clear that there is no such thing as a single best TCO and those TCOs must be tailored to the constraints of the IR shielding application.

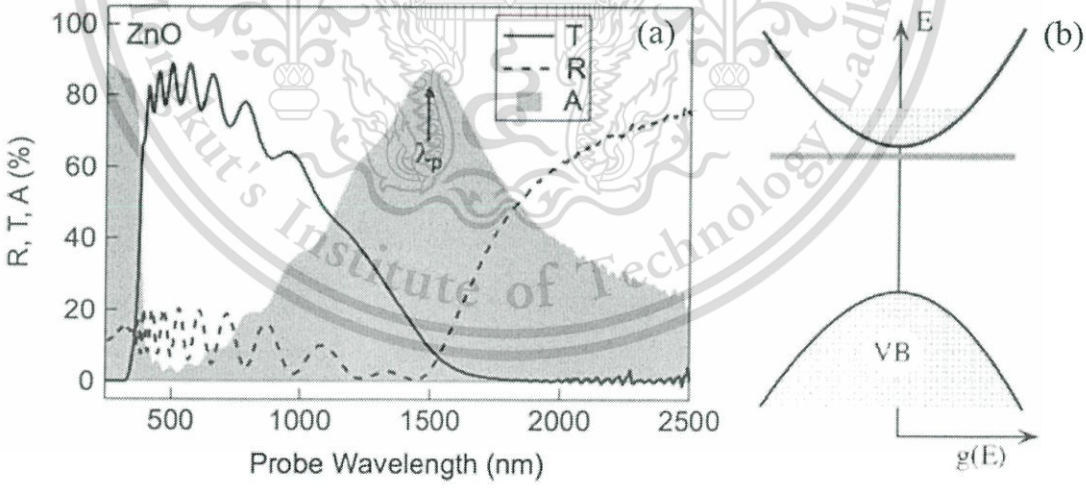

Figure 2.2 (a) Optical spectra of typical (ZnO) transparent conductor and (b) Schematic electronic structure of conventional TCO materials [16].

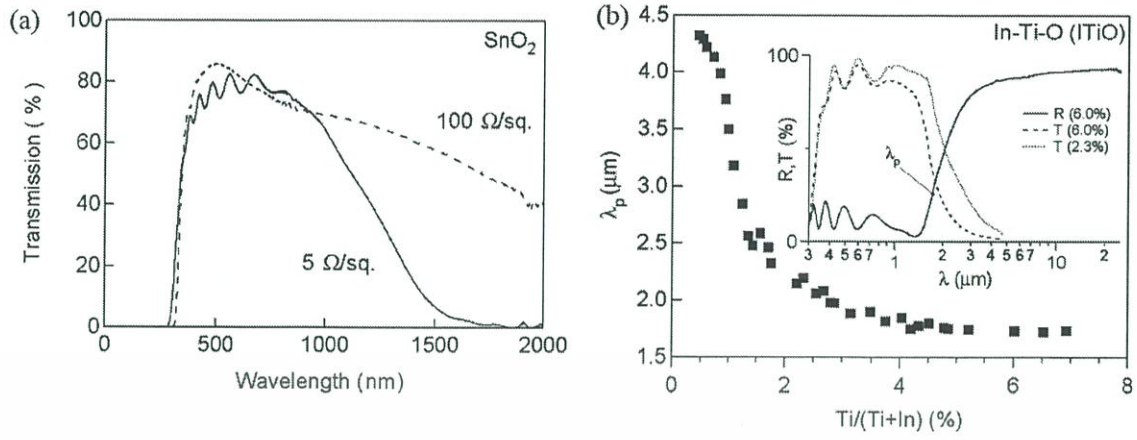

Figure 2.3 (a) Optical spectra of TCO materials: SnO_2 and (b) Ti-doped In_2O_3 from van Hest *et al.* [17].

2.2 Transparent conducting oxide (TCO) [18,19]

2.1.1 Theoretical background of TCO materials

Theoretical modeling and empirical analysis suggest that the special combination of high electrical conductivity and optical transparency can be realized by selecting a wide band-gap metal oxide which could be rendered degeneracy (metal-like electronic behavior) through suitable incorporation of native donors or substitutional dopants into the host lattice.

For the n-type doped metal oxides, native donor- or extrinsic dopant-induced charges (electrons) form a level just below the bottom of the conduction band which is empty in the intrinsic semiconductors. With the increase of doping density, these impurity levels eventually merge and form a continuous band, as is illustrated in Figure 2.4 (b). Beyond a certain critical concentration; n_c (called Mott carrier density), the donor band overlaps with the conduction band and electrons behave like free charge carriers. The oxides are degenerated in nature. For p-type doped metal oxides, impurity dopants result in the formation of acceptor levels located above the top of the valence band. As the doping density increases, a continuous acceptor band forms and overlaps with the valence band at a critical concentration; n_c, resulting in the degeneration of the oxides.

Figure 2.4 presents a simplified illustration of the doping process, without taking into account the possible change of the band-gap. Actually, above the critical concentration (n_c), the mutual exchange and Coulombic interactions between the added free electrons in the conduction band and the electron-impurity

scattering lead to an upward shift of valence band and downward shift of conduction band, hence, the band gap is reduced. However, the fundamental optical transition in degenerated oxides requires higher energies, since the highest occupied level becomes higher due to the added free electrons which will result in the larger optical band gap (so called Burstein-Moss effect). Figure 2.5 depicts the band gap change based on these two effects, where E_0 is the intrinsic band-gap, E_1 is the varied band-gap due to electron-impurity scattering, E_2 is the varied band-gap due to Burstein-Moss effect. The actual band-gap change consequently includes these above two effects.

Besides the degeneracy, a second feature of TCO materials is their free-electron-like conduction band minimum, formed from the *s* states of metal ions. This is a condition for small effective mass of the free charge carriers, and thus high charge mobility. This feature is shared practically by all the commonly used TCO systems such as indium oxide, tin oxide, zinc oxide, and it also gives the direction for the development of new TCO materials.

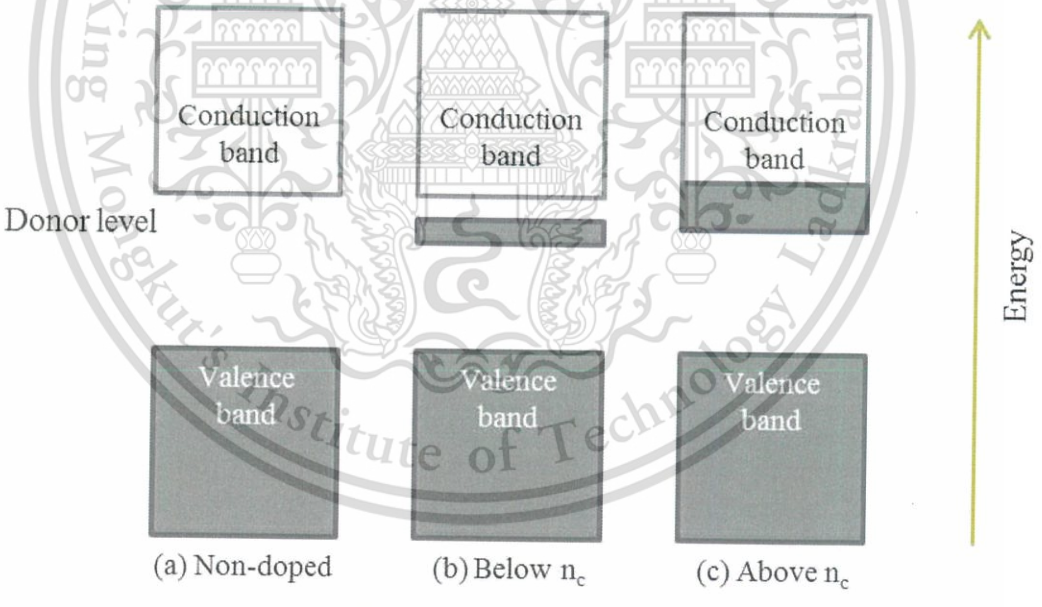

Figure 2.4 Schematic descriptions of the n-type doping: with the increase of doping density is the critical concentration called Mott carrier density.

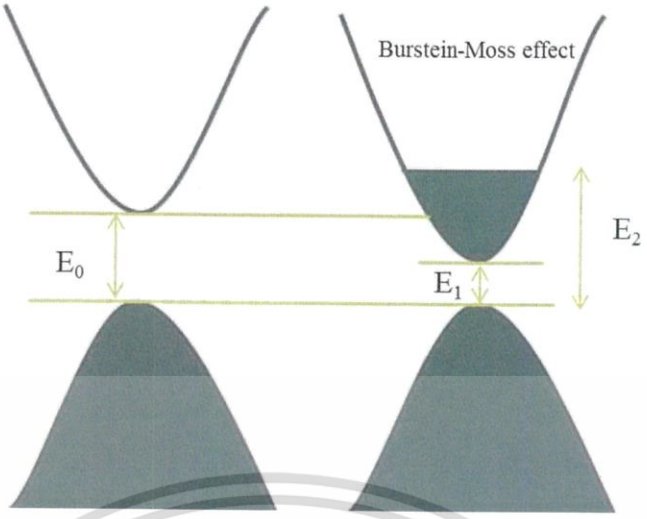

Figure 2.5 Band-gap changes based on electron-impurity scattering and Burstein-Moss effect. E_0 is the intrinsic band-gap, E_1 is the varied band-gap due to electron-impurity scattering, E_2 is the varied band-gap due to Burstein-Moss effect.

2.2.2 Crucial selections of conductive dopant materials

(1) Band-gap energy of the metal oxide: The fundamental requirement for the band-gap energy of a metal oxide concerns the photon absorption-induced transmittance loss in the visible spectrum. Generally, a small band gap is advantageous for the electron excitation from valence band to conduction band, resulting in high conductivity. However, this manner decreases the optical transparency, since photons with energy corresponding to the visible light spectrum (wavelength from 350 nm to 750 nm) can be absorbed. When the band gap energy is above 3 eV, the photons lying in the visible range are not absorbed and thus the optical transparency remains high.

(2) Properties of host metal oxide: Realization of high conductivity in wide band-gap metal oxide is largely dependent on the electron affinity or work function of the material. For the n-type doped metal oxides, high electron affinity of the host metal oxide is suggested to be beneficial to achieve high electron concentration and degeneracy. For the p-type metal oxides, this rule suggests that a low work function of the host metal oxide is required. However, low work function is not easy to be satisfied for most of the wide band-gap metal oxides, owing to the nature of the metal-oxygen bond. This might be one of the reasons that not so many p-type TCO materials have been reported so far (except the Cu+ containing oxides

$CuAlO_2$, $CuGaO_2$). Metal chalcogenides have somewhat lower work function than metal oxides, making them better candidates for the p-type TCO materials.

(3) Choice of the dopants: In order to accomplish efficient doping, the lattice stability of the host metal oxide should be considered. It is generally affected by the disparities between dopant atoms and the corresponding host atoms. According to the Hume-Rothery rule, the atomic radii differences between the dopant and host atoms/ions should be less than 15%. Otherwise, the distortion of the host metal oxide lattice will result in generating unfavorable "killer defects", which will compensate the extra electrons or holes induced by the dopants. For example, for the n-type doped metal oxides, cation vacancies will start to form when the lattice stability is decreased. For the p-type doped metal oxides, the presence of anion vacancies will act as a response towards the lattice distortion, both of which will pin the free charge carriers and thus weaken the doping effect. Besides, dopants should be able to form shallow donor levels as a result of the doping process.

2.2.3 TCO material Candidates

Commercially, thin films of indium-tin-oxide (ITO) have been the standard material used for transparent electrodes in optoelectronic devices. However, the high cost and scarcity of indium as well as difficulties of processing ITO has motivated a search for other materials that can potentially replace ITO as demand grows. Since this realization, many other TCO materials have been developed, namely n-type semiconductors with tin oxide, indium oxide, or zinc oxide as the main component, as listed in Table 2.1. Commonly investigated replacement materials include doped zinc oxide (ZnO), indium oxide (In_2O_3) and tin oxide (SnO_2). In recent years, great attention has been paid on the synthesis, characterization and applications of metal-doped SnO_2 or ZnO based transparent conducting oxides owing to alternatively low-cost to rather expensive indium tin oxide. However, Al- and Ga-doped zinc oxides (AZO and GZO, respectively) are also good alternatives to ITO, but they tend to degrade faster than ITO and FTO in hot, moist atmospheres. The appropriate material typically utilized for conductive oxide is metal doped SnO_2 due to excellent electronically stability in oxidizing environment and low-toxicity material with good thermal and chemical stabilities [20].

Table 2.1 Common transparent conductive oxide.

Main Component	Dopant
Tin oxide (SnO_2)	Fluorine (F) [21]
	Antimony (Sb) [22]
Indium oxide (In_2O_3)	Tin (Sn) [23]
	Zinc (Zn) [24]
Zinc oxide (ZnO)	Aluminum (Al) [25]
	Gallium (Ga) [26]

2.3 TCO based tin oxide (SnO_2) [16]

2.3.1 Crystal structure of SnO_2

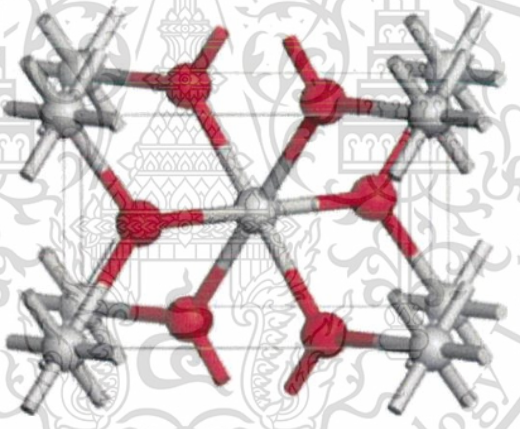

Figure 2.6 Crystal structure tetragonal SnO_2 [27].

Tin Oxide (SnO_2) occurs in nature as the mineral Cassiterite. It possesses the rutile crystal structure with a tetragonal unit cell and a = b = 4.738 Å and c = 3.188 Å. The crystal lattice of SnO_2 is shown in Figure 2.6, where the sixfold coordination of the Sn atoms to the oxygen nearest neighbors can be observed. Each oxygen octahedral in SnO_2 is connected to two adjacent octahedral through edge sharing along the c-axis, and connected to other octahedral through corner sharing.

The lower symmetry of the tetragonal crystal structure of SnO_2 leads to an anisotropy in the electronic and optical properties. For example, the smaller distance between Sn atoms along the c-axis, may

facilitate a higher atomic orbital overlap and thus a more conductive pathway for electron transport. This has been confirmed in conductivity measurements on single crystals of the isostructural rutile compound TiO_2 with conductivity five to ten times greater along the c-axis as compared to the <110>.

2.3.2 Electrical properties of SnO_2

Tin oxide is an n-type conductor, in which wide band-gap and high conductivity coexist. As in the case of other binary metal oxides (e.g. ZnO, In_2O_3), oxygen vacancies are responsible for conduction electron-carrier generation in SnO_2. The electron generation can be described by the following equation, using Kröger-Vink notation:

$$O_o^x \rightarrow V_o^{\bullet\bullet} + 2e' + \tfrac{1}{2}O_2(g) \qquad (2.3)$$

According to this equation, oxygen anions escaping the crystal structure ($\tfrac{1}{2}O_2$) from an occupied oxygen site creates a doubly ionized vacancy site ($V_{\ddot{O}}$) and two free electron carriers. Creation of multiple carriers from a single defect is highly desirable, due to minimization of carrier scattering on crystal impurities. The presence of oxygen vacancies in bulk SnO_2 is observed by X-ray diffraction and coulometric titration experiments. This oxygen non-stroichiometry in bulk SnO_{2-x} is in the x = 0.02-0.034 over the temperature range of 700-900 K. Such a vacancy concentration yields up to $5\times 10^{20}/cm^3$, assuming all vacancies are doubly ionized. In fact, the most relevant chemical diffusion process in undoped and cation-doped SnO_{2-x} single crystals is due to oxygen anions, indicating the low formation energy of oxygen vacancies. This donor level lies about 30 and 140 meV below the conduction band for the single and doubly ionized states, respectively. The oxygen deficiency can be easily controlled in thin films by adjusting the oxygen partial pressure during sputtering or other deposition. A decrease of the carrier concentration with higher oxygen partial pressure indicates a decreasing number of oxygen vacancies in SnO_{2-x} thin films.

Apart of oxygen deficiency, a variety of dopants have been employed to induce conductivity in SnO_2. In case of donor doping, the most common choices are Sb^{5+} substitution on the Sn^{4+} site and F^{1-} on the O^{2-} site. Some of the less traditional n-type dopants are Mo, Ta and Cl. In most of these doping scenarios a single electron is produced per substitution. Anion doping by F^{1-} on the threefold coordinated O^{2-} site is the least ambiguous method for electron generation. Moreover, the crystal lattice is affected the

least by this substitution, due to the similarity of the oxygen and fluorine ionic radii. Such a size-matched dopant minimizes the lattice distortion, thus preserving the transport properties of the undoped lattice. Doping by the larger Cl^- anion, which also prefers a sixfold coordinated environment results in lowering carrier mobility and carrier concentration. The incorporation of Ta produces free electrons, but only low doping levels of a few at.% of Ta and Mo can be accommodated in the SnO_2 lattice beyond which the conductivity of doped SnO_2 decreases due to a reduction in mobility.

Group II and III cation dopants, such as In, Ga, Al, Fe, Zn, etc., as well as substitution on the anion site by N^{3-} create acceptor-like states in SnO_2. Incorporation of Zn is reported to decrease the electron carrier concentration, whereas SnO_2:Fe gas sensors showed p-type response in an oxygen atmosphere. A few reports on p-type tin oxide use high doping levels (typically > 8at%) of In, Ga or Al to produce a low hole carrier concentration. It is typically difficult to induce hole carriers in wide band-gap oxide semiconductors. The reason for such behavior lies in the generation of compensating donor-states. Based on thermoluminescence measurement, modeling, and first-principle calculations, the number of oxygen vacancies and tin (or trivalent acceptor dopant) interstitials is predicted to increase with a higher acceptor doping level. Therefore only low hole carrier concentrations can be achieved and a changeover to n-type carriers with time may occur, due to slow diffusion processes at room temperature.

2.3.3 Optical properties of SnO_2

The interest in SnO_2 coatings is due to the coexistence of high conductivity and transparency in the visible range of the electromagnetic radiation spectrum. For TCO applications, a band-gap of at least 3.1 eV is required. Undoped conductive tin oxide films exhibit a larger band-gap, typically greater than 3.6 eV. The direct nature of the band edge transition is established from band structure calculations. In addition, a direct gap is indicated by the good linear fit of the $\alpha h\nu (h\nu - E_g)^{1/2}$ relationship shown in Figure 2.7, where α is the absorption coefficient, $h\nu$ is the incident photon energy, and E_g is the band-gap energy required to promote an electron from the top of the valence band to the first available unoccupied state in the conduction band. With addition of various donor dopants (Sb and F), Figure 2.8, the energy needed for the transition of an electron increases due to filling of the conduction band with free electron carriers. This effect is known as the Burstein-Moss shift, responsible for band-gap widening with an increase in carrier concentration.

Undoped and doped tin oxides are highly transparent in the visible-light wavelength range (400-800 nm) as shown in Figure 2.8. The high transparency can be explained by a low concentration of mid-gap states, typically responsible for absorption of photons with energies below the band-gap value. Refractive index values between 1.9 and 2 are commonly observed in SnO_2 thin films.

Optical transmission of the conductive SnO_2 films is limited in the near infra-red (IR) region. This plasma wavelength (or more commonly plasma frequency) depends on the carrier concentration and effective mass. Thus, the observation of the plasma frequency (ω_p) together with the measured carrier concentration (N) allows the determination of the carrier effective mass (m^*), which is expressed from the classical Drude theory as:

$$\omega_p = \frac{4\pi N e^2}{\varepsilon \varepsilon_0 m^*} \tag{2.4}$$

where e is the electron charge, ε is the high frequency dielectric constant, and ε_0 is the permittivity of free space. The electron effective mass of doped SnO_2 derived from these measurements is in the range of 0.15-0.4 m_0. This is close to the average value of 0.25 m_0 reported for the single crystal. The high reflectivity in the near IR region below the plasma wavelength allows the use of highly doped SnO_2 as low-emissivity window coatings.

The properties of SnO are in little studies, but band-gap values in the 2.7-2.9 eV range are reported. The band-gap value below 3.1 eV leads to absorption the visible range and thus coloration of SnO thin films.

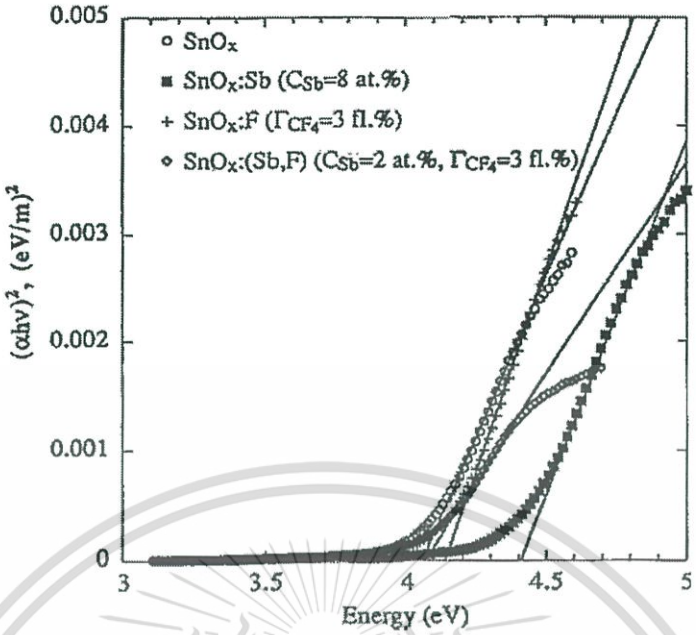

Figure 2.7 Direct band-gap evolution and Burstein-Moss shift to the band edge with Sb-, F- doping of tin oxide thin films [28].

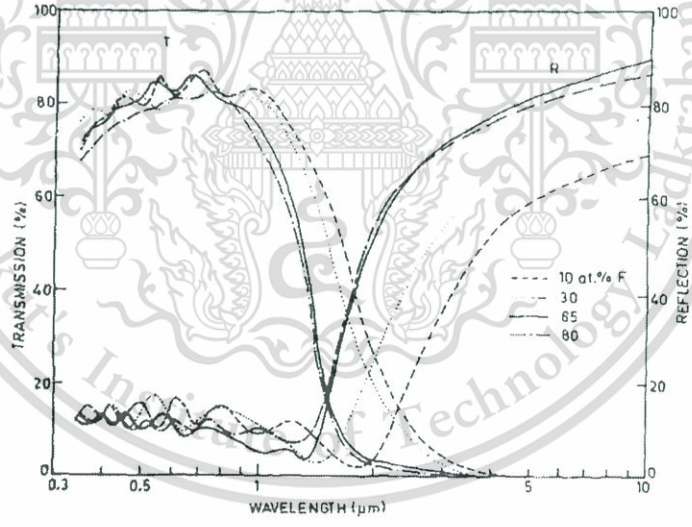

Figure 2.8 Transmission and reflection spectra of F-doped SnO_2. The crossover between the transmission and reflection curves in the IR-range shows the position of the plasma wavelength due to free carrier reflection [29].

2.4 Nanoparticle-based materials and their optical and electrical properties [30,31]

Nanoparticles are generally considered to be a number of atoms or molecules bonded together in a cluster with a radius less than 100 nm. A nanometer is 10^{-9} meters (m) or 10 angstroms (Å), so particles having a radius of ~1000 Å or less can be considered to be nanoparticles. For example, a cluster of 1 nm radius has approximately 25 atoms with most of the atoms on the surface of the cluster. This definition based on size is not totally satisfactory because it does not really distinguish between molecules and nanoparticles. Since an atom generally has ~1 Å size, a cluster of 1 nm radius would consist of ~ 25 atoms and most of the atoms would be on the surface. Compared to some large molecules with hundreds or thousands of atoms, such as many polymer molecules, a nanoparticle might be much smaller. The nanosize by itself does not warrant unique nanomaterial behaviors or exciting properties. What makes nanoparticles such an interesting and unique material category is that their size is smaller than the critical dimensions that characterize many physical phenomena, such as thermal diffusion length, light wavelength, and electron mean free path. When a dimension is less than these critical lengths, new physics or chemistry is likely to occur, such as catalytic properties or quantum effects.

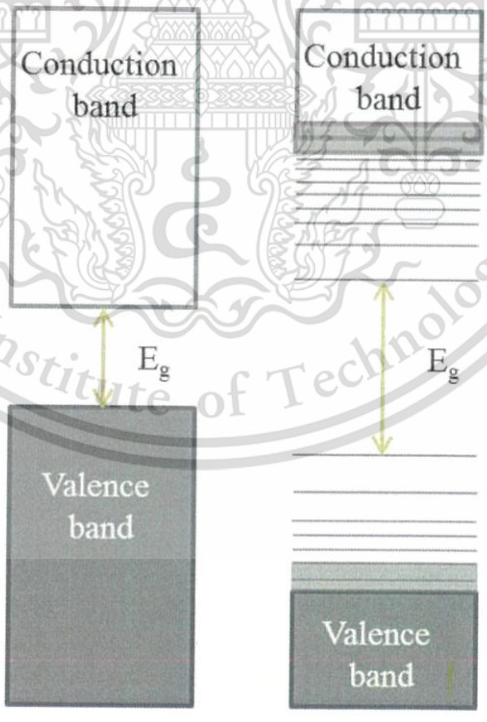

Figure 2.9 A comparison of the electronic energy states of different types of semiconductor materials: (a) bulk inorganic semiconductors and (b) inorganic semiconductor nanocrystals.

Semiconductor nanocrystals (NCs) are small crystalline particles which are typically synthesized with dimensions in the range of 1–100 nm. Since the discovery of nanocrystals embedded in glasses in the early 1980s, they have attracted considerable attention as an important component of materials. Semiconductor materials are characterized by their band structures (direct or indirect) and a band gap energy (E_g) that falls within a range of between $0 < E_g < 4$ eV, and can be thought of as the minimum energy required to excite an electron from the valence band (VB) to the conduction band (CB) (Figure 2.9 (a)). Furthermore, if one dimension of a semiconductor is smaller than the Bohr exciton radius of the material, the band structure will be modified and blue shifted to higher energy by the quantum confinement effect. In the limit of very small particle size, the so-called strong confinement regime, quantized levels appear which is distinct with the continuous band of bulk counterparts and shows characteristics of the discrete molecular semiconductors (Figure 2.9). The quantum size effect opens up possibilities for the fine-tuning of the band structures and thereby the optical and electrical properties of semiconductor NCs by simply controlling their sizes. Apart from the size-effect, the physical and chemical properties of semiconductor NCs are highly dependent on their compositions, shapes, structures, and surface chemistry, which have enabled semiconductor NCs to be utilized as active materials in various applications and fields. NCs has attracted considerable attention due to their tunable energy structures, high optical absorption coefficients, large dipole moments, and the potential multiple exciton generation properties.

The effects of refined microstructures on electrical conductivity of nanoparticles and nanoparticle-based materials are complex, since conductivity may originate from distinctly different mechanisms. Electrical conductivity in metals can be hindered by various electron scatterings, and the total resistivity of a metal is a combination of the contribution of individual and independent scattering, which includes thermal scattering, defect scattering, and surface scattering (including grain boundary scattering). Thermal scattering originates from electron collisions with vibrating atoms (phonons) displaced from their equilibrium lattice positions. Defect scattering can be divided into impurity scattering, lattice defect scattering, and grain boundary scattering. Increased perfection of nanoparticles and nanoparticle-based materials, such as reduced impurities, structural defect, and dislocations, would increase the electrical conductivity. However, the defect scattering makes a minor contribution to the total electrical resistivity at room temperature, and thus the reduction of defects has very small influence on the electrical resistivity,

mostly unnoticeable experimentally. Surface scattering, on the other hand, plays a very important role in determining the total electrical resistivity of nanostructured materials. With decreased nanoparticle or grain sizes, the electrical conductivity decreases.

2.5 Nanoparticle synthesis [32]

Nanoparticle synthesis involves the creation of nanoparticles form ions, atoms or molecules. Different from conventional micron-sized particle synthesis, nanoparticle synthesis often involves careful design of nanoparticle atomic structure, composition, size and even specific composition distribution. Synthesized nanoparticles generally range from <100 atoms to 100 nm in size. Nanoparticle synthesis is the first necessary and fundamental step for the entire nanoparticle-based material field and plays pivotal roles in the continuous advancement of nanomaterials.

2.5.1 Nanoparticle growth process

For nanoparticle synthesis, just as for micron-sized particle synthesis, there are two essential steps: nucleation and growth of nanoparticles. At the beginning of the nanoparticle formation process, this system is very important for nucleation. Sometimes this can involve very short time scales, such as sub-picoseconds. After nuclei are formed and remain stable, nanoparticle growth needs to be carefully controlled in order to obtain targeted particle size, shape, and distribution. An integrated understanding of nanoparticle growth across a variety of timescales, such as from femtoseconds to hours or even days, is needed.

(1) Nucleation: There are two types of nucleation: homogeneous and heterogeneous. In homogeneous nucleation, nuclei are formed in a completely uniform environment. In heterogeneous nucleation, nuclei are preferentially formed on some media such as existing particles or the walls of the container. Reactant addition mode, stirring rate, container surface condition, temperature uniformity, and many other factors can all affect the nucleation process. For example, fast nucleation results in a high particle concentration and ultimately yields small particles, while a slow nucleation results in a low concentration of embryonic seeds that consume the same amount of precursor and therefore results in a population of proportionally larger particles as depicted in Figure. 2.10 [33].

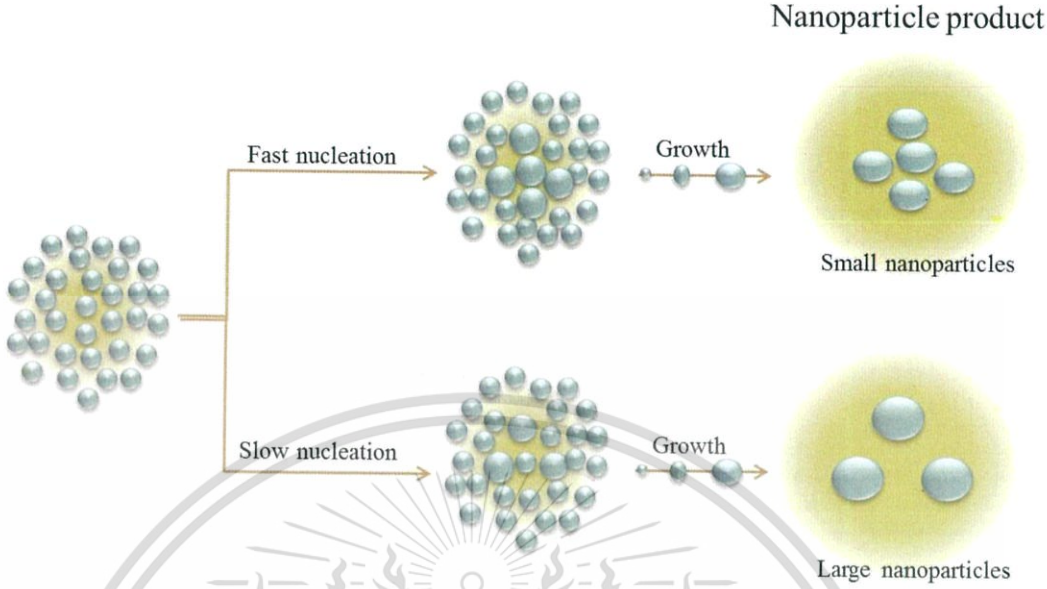

Figure 2.10 Comparable between fast nucleation and slow nucleation.

Homogeneous Nucleation: The local fluctuation of solution concentration generates the possibility of forming small nuclei, a new phase in the liquid that is composed of the intended new species. Whether the new phase remains stable or not depending on the chemical potentials of the old and new phases. When the initial bulk phase forms phase, the new phase will become stable and grow after some critical size is exceeded. For nucleation to occur, supersaturation of the solution is necessary. To achieve the desired supersaturation state, the solution can be oversaturated either by dissolving the solute at higher temperature or by adding reactants to produce a supersaturated solution. In other words, the work of nucleus formation must be overcome for the process to proceed. If a system is free from other preferential nucleation sites, such as container walls or other surfaces, homogeneous nucleation occurs when the precursor concentration increases to above the nucleation threshold.

Heterogeneous Nucleation: When nuclei originate on the surface of foreign species, such as impurities, dispersed particles, or container walls heterogeneous formation of nuclei occurs. Heterogeneous nucleation on a foreign surface has a lower surface energy and a diminished thermodynamic barrier, which leads to a lower critical supersaturation as shown in Figure 2.11. Although traditionally not quite desirable, heterogeneous nucleation has found new applications such as coating one type of particles with a layer of

the second type of species. With the increasing interest in forming unique composition nanoparticles and templating, heterogeneous nucleation is being utilized in increasingly creative manners for novel materials and properties.

(2) Growth: After stable nuclei are formed, nanoparticles can grow in three ways: homogeneous growth, Ostwald ripening, and aggregation. The ability to control the growth of nuclei determines if the obtained particles will be nano-sized or micron-sized and how wide the particles size distribution will be. During homogeneous nanoparticle growth, nucleus size increases by molecular addition. Along with nucleus growth, solution supersaturation decreases as shown in Figure 2.12 [34]. There are three discrete steps for nanoparticle growth: diffusion of the growing species from the solution to the nucleus surface, adsorption of the growing species onto the nucleus, and the incorporation of the growing species into the nucleus. Nanoparticle growth process can be diffusively-controlled or particle surface reaction controlled. If the growth is controlled by diffusion, concentration gradient and temperature distribution in the given system are important factors in determining the growth rate.

For homogeneous nanoparticle growth, diffusively-controlled growth is often encountered. No new nuclei form as long as the consumption of precursor by the growing nanoparticles is not exceeded by the rate of precursor addition. At this stage, smaller particles grow more quickly than larger ones because the free energy driving force is larger for smaller particles. As a result, the particle size distribution becomes smaller. This is called focusing in size. Nearly nonodispersed size distribution can be obtained at this stage.

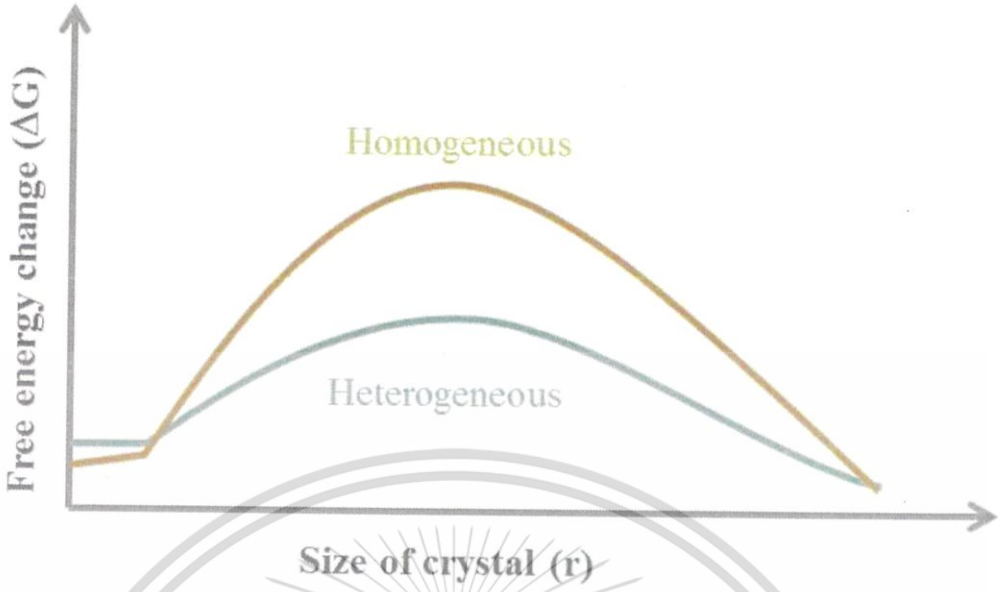

Figure 2.11 Supersaturation state of homogeneous and heterogeneous nucleation.

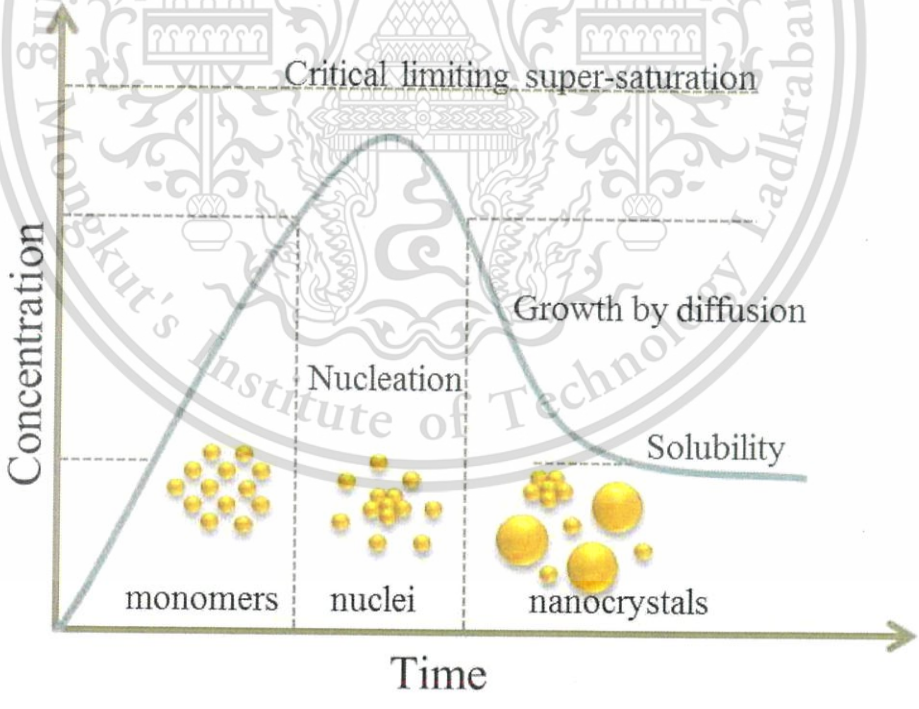

Figure 2.12 Schematic illustration of the nucleation and growth process of nanocrystals in solution.

Because of the large surface area and high surface energy available, nanoparticles can also grow through aggregation of small particles or unstable nuclei. Aggregation occurs by engulfing smaller particles onto the surfaces of large particle clusters; the growth rate is higher than that through molecular addition, but the process is not controllable. More problematically, smaller nanoparticles or nuclei tend to aggregate with large particles more often than with the same size counterparts. This is because when the surface charge density is the same, the aggregation rate decreases exponentially. In addition, the barrier for aggregation increases with the particle size. This means that aggregation is a more dominant phenomenon for nanoparticles compared with their micron-size counterparts. To prevent aggregation of nanoparticles, stabilizing agents can be used. When stabilizing agent molecules attach to nanoparticle surfaces, they satirically stabilize nanoparticles in the solution, mediate nanoparticle growth/aggregation, and passivate the electronic states of nanoparticle surfaces.

Particle size growth is a relatively well-discussed topic, under the assumption that particles are spherical and grow isotropically. This concept works well for amorphous particles. Many nanoparticles, however, are crystalline and the surface energies are different at different crystallographic orientations, which need to be considered during growth. Anisotropic particles growth is thermodynamically favored. This is also the basis for synthesizing nanobelts, nanoribbons, nanotubes, nanoprisms, nanorods, etc. When the surface energies of different crystal planes are not drastically different, the isotropic assumption is acceptable and equiaxed particles can be made.

2.5.2 Precipitation method

Aqueous precipitation is one of the earliest techniques in nanoparticle synthesis. The technique is simple, inexpensive and can be used to synthesize single or multicomponent nanoparticles. The process generally starts with a solution of metal salts, such as alkoxides, nitrates, or chlorides. The experiment procedure of precipitation method is shown in Figure 2.13. Upon the addition of a proper reagent, precipitate forms: $M^{n+}+nX^{-}\rightarrow MX_n$

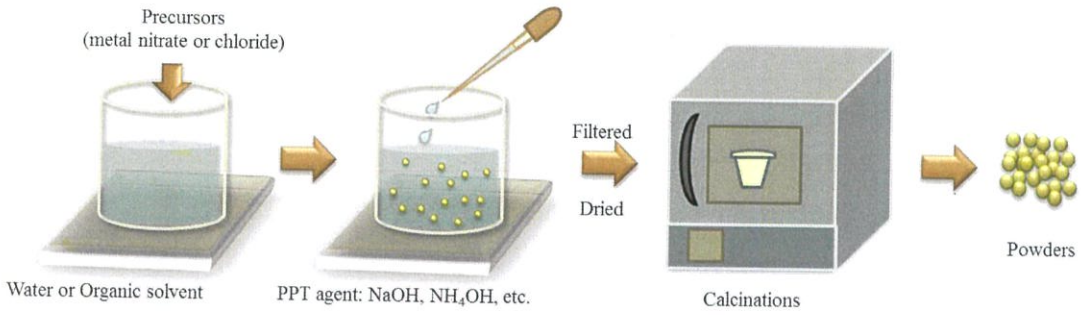

Figure 2.13 Schematic illustration of precipitation method.

Under supersaturation, the precipitate nucleates and grows which can stay as-synthesized or be dehydrated to form simple or complex nanoparticles. In a strict sense, precipitation is mainly suited for the synthesis of oxides. A prerequisite for aqueous precipitation is that the formed precipitates must have a very low solubility in water. During precipitation, the kinetics of nucleation and particle growth in a solution reaches a critical supersaturation for the participating species to control the precipitation factor such as the pH, temperature, and concentration of the reactants. Organic molecules can be used to control the release of the reactants in the solution during the precipitation process. However, nanoparticles can also undesirably adsorb or react with species in the environment. If nothing else, nanoparticles have a high tendency for agglomeration at a dry state.

2.5.3 Sonication-assisted Synthesis

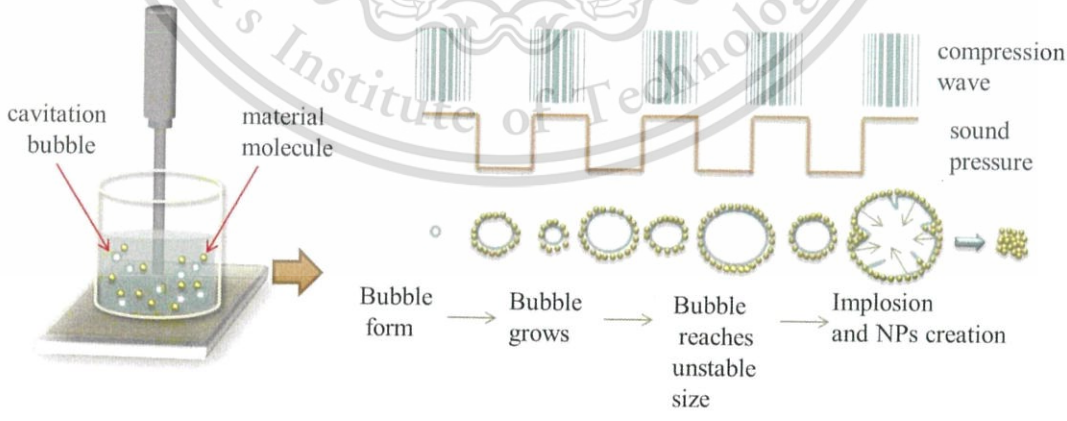

Figure 2.14 Schematic illustration of during the sonication.

Recently, ultrasound has been introduced for nanoparticle synthesis. Rapid heating is realized from sonication of a liquid, similar to microwave-induced heating. Ultrasound provides strong mechanical force that can disperse reactants easily and thoroughly. During the sonication of a liquid, cavitation forms the implosive collapse of bubbles, resulting in localized hot spots with effective temperature as high as 5000 K and lifetimes of a few nanoseconds or less as illustrated in Figure 2.14. Thus, chemical reactions mostly take place inside the bubbles. However, the extremely rapid cooling rate accompanying the process greatly favors the synthesis of amorphous nanoparticles. The shape and size of the nanoparticles can be controlled by adjusting the power of the ultrasonic irradiation.

N. Ghows and M.H. Entezari [35] reported that CdS/TiO_2 core/shell nanoparticles were made by microemulsion under ultrasound. TiO_2 and CdS in the resulting particles were anatase and hexagonal, respectively. The TiO_2 coating thickness on CdS nanoparticles can be controlled. After 30 minutes of sonication, the particles are mostly amorphous. By increasing the time of sonication to 90 minutes and 120 minutes, the X-ray diffraction peaks become sharper and indicate increased crystallinity as shown in Figure 2.13. Compared to conventional synthesis, which requires thermal treatment at 673-723 K to induce and improve the crystallinity of the deposited layer, sonochemical synthesis is more effective as it take advantage of the ultrasonic power for the crystallization of TiO_2 and CdS. Crystalline TiO_2 can be formed in the dispersion and inherently bind to CdS particles without any post thermal treatment. The average particle size is about 8 nm from the half-width of the X-ray diffraction peak of the (101) plane.

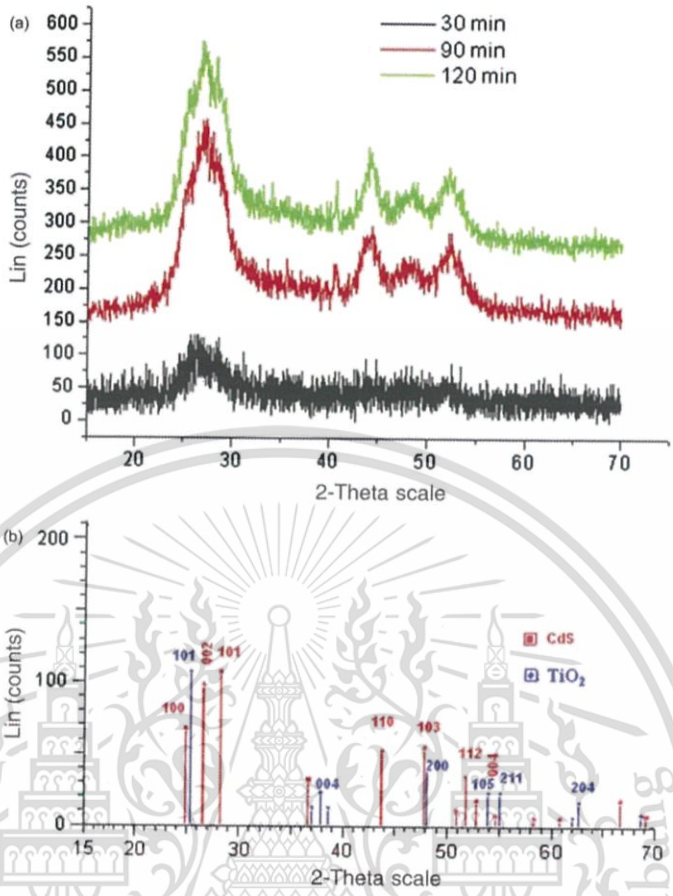

Figure 2.15 X-ray diffraction patterns of the prepared CdS/TiO_2 composite at different sonication times (mole ratio = 2.5).

The enhancement of the crystal phase of the product in the presence of ultrasound can be explained according to the cavitation process. The chemical and physical effects of ultrasound arise from acoustic cavitation. When a bubble is formed in the microemulsion system, there is a possibility for small droplets of oil to accumulate at the interface of the bubble produce by ultrasound. This behavior arises from the higher tendency of the oil droplets to interact with the bubble interface than with the water phase. The implosion of a bubble generates many local hot spots in the solution and promotes the reactions. The formation, growth, and crystallization of composite nuclei are accelerated under these conditions. The high temperature produced during the cavitation facilitates the crystallization of the product. The hot spots produced during the sonication play the same role as the calcination process. The advantages of the

ultrasound-assisted technique include chemical homogeneity and reactivity through mixing at the atomic level, better dispersion even without a surfactant or a dispersant and high crystallinity of nanoparticles.

2.6 Nanocomposite thin films preparation [36]

Nanocomposite materials are a new form of nanocrystalline materials and have been investigated tremendously because these may have superior properties due to the size effect and especially due to the mixing of different nano-phases with different properties. This material represents a new class of film, powder, or bulk materials that are, in the simplest case, composed of two phases with a grain size below 100 nm, typically about 10 nm or smaller. This is illustrated in Figure 2.14. As mentioned, increased activity on the synthesis of nanocomposite films in recent years is due to the combining advantages of thin films and nanocomposite structures. So far, a number of techniques have been used to synthesize nanocomposite films in which the starting material can be either in the solid, the liquid, or the gaseous state (Table 2.2). In principle, any method capable of producing films can be used to produce nanocomposite films. If a phase transformation is involved, e.g., liquid to solid or vapor to solid, then certain steps have to be taken to control the nucleation and growth rates in order to control the composite's structure and properties. The particle's second-phase size, morphology, and texture can be varied by suitably modifying or controlling the process variables in each of these methods.

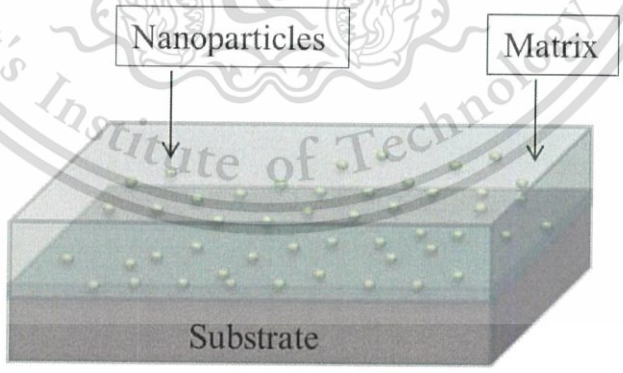

Figure 2.16 Schematic diagram of nanocomposite material.

In sol-gel methods, organometallic salts, such as metal alkoxides, are deposited on porous electrode substrates and hydrolyzed under controlled condition, forming a colloidal sol and a condensation step with organic monomers to form a gel. The deposition by methods such as by spin coating or dip coating is followed by a drying and firing process, leading to the formation of a dense film. The key feature in this sequence is sol-gel polymerization, which can be described by a two-step reaction: initiation via the hydrolysis of alkoxy ligands and polycondensation via an oxolation reaction. The particle concentration, viscosity, concentration, and stability of the sol-gel influence the deposition parameters and film quality and have to be controlled carefully.

Table 2.2 Methods to synthesize nanocomposite films

Starting phase	Techniques
Vapor	Co-sputtering (PLD)
	Co-evaporation (CVD)
	Pulse laser deposition (PLD)
Liquid	Electrodeposition
	Sol-gel process
	Casting
Solid	Mechanical alloying/milling
	Spark erosion
	Powder processing

2.7 Literature reviews

Wu *et al.* [37] had synthesized F-doped SnO_2 nanocrystals using sol–gel process followed by a hydrothermal treatment. The diameter of the F-doped SnO_2 nanocrystal in rutile-type structure was approximately 10 nm calculated from XRD. TEM images showed small particles and good dispersion as illustrated in Figure 2.17. The electrical resistivity properties of F-doped SnO_2 nanocrystals were measured by a four-point probe measurement as shown in Figure 2.18. The results showed that sheet resistances (R_s) of F-doped SnO_2 decreased with the increasing NH_4F/Sn molar ratio in the range from 0 to 2. However, further increase of NH_4F/Sn molar ratio from 2 to 5 resulted to higher sheet resistance. The sheet resistance of fluorine doped SnO_2 powder was 110 Ω/□ when NH_4F/Sn molar ratio equaled to 2.

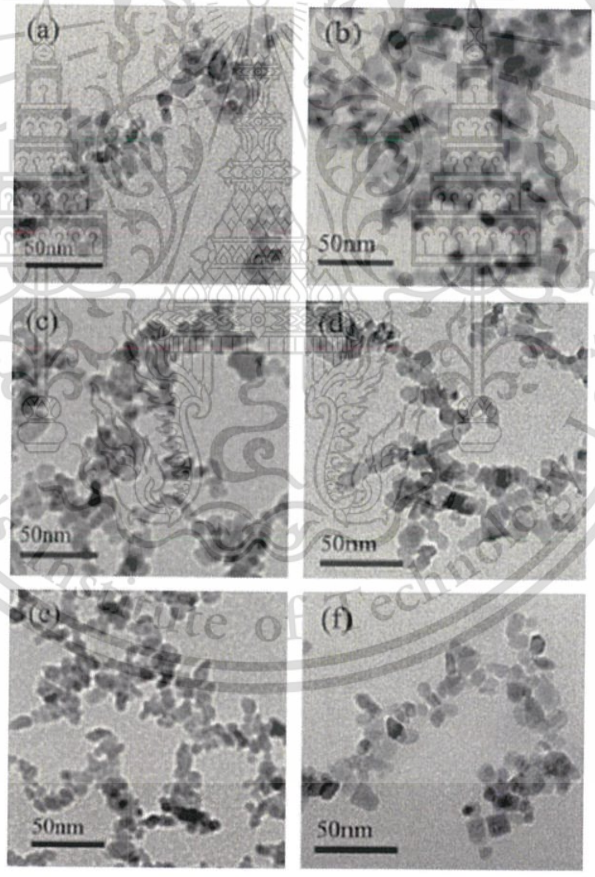

Figure 2.17 TEM images of SnO_2 nanocrystals with doping ratio of (a) undoped SnO_2, (b) NH_4F/Sn=0.5, (c) NH_4F/Sn=1.5, (d) NH_4F/Sn=0.5, (e) NH_4F/Sn=2 and NH_4F/Sn=5 [37].

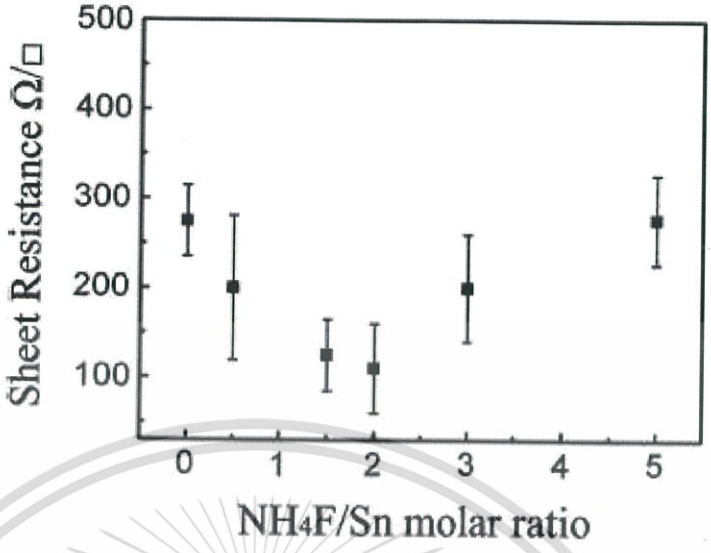

Figure 2.18 Sheet resistance of SnO_2 powder doped with different NH_4F/Sn molar ratio [37].

Krishnakumar *et al.* [38] reported that Sb-doped SnO_2 nanostructures were prepared using chemical precipitation technique. The $SnCl_2$, $SbCl_3$ were used as starting precursor of antinomy and tin, respectively. The antimony composition was varied from 5 to 20wt%. The lower resistance was observed at composition of Sn:95 and Sb:05, when compared with SnO_2 and higher doping concentration of antimony. The average crystalline size of Sb-doped SnO_2 was decreased from 30 to 11 nm after Sb concentration increased calculated from XRD pattern and it was further confirmed by TEM observation in Figure 2.19.

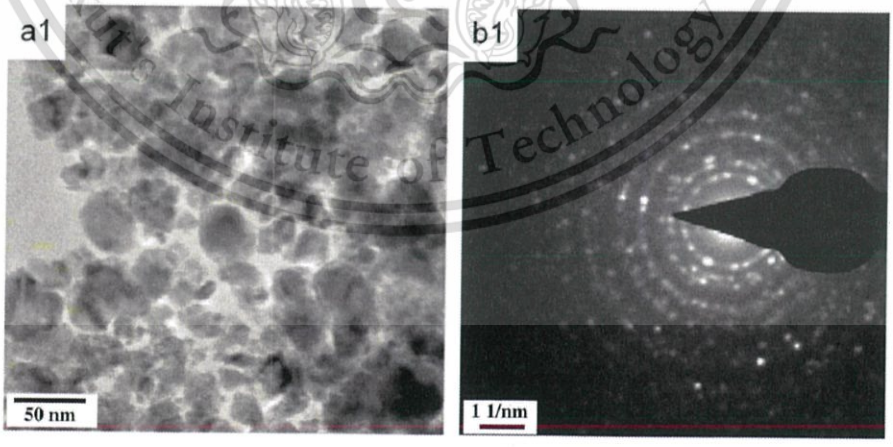

Figure 2.19 TEM micrograph (a) 5wt% Sb-doped SnO_2 and (b) its SAED pattern [38].

Li *et al.* [39] reported that indium tin oxide powders were synthesized by a co-precipitation process. The process of ITO nanoparticles synthesized by co-precipitation is shown in Figure 2.20. A mixture of $In(OH)_3$, InOOH and $Sn_3O_2(OH)_2$ preferred the path of pure $In(OH)_3 \rightarrow In_2O_3$ during calcinations in Ar gas and the powders with rhombohedral and cubic structured crystalline ITO were obtained at 600°C as illustrated in Figure 2.21. If this powder was thermally calcined under Ar gas, the color turned into slight blue due to removal of oxygen from ITO particles. So a decrease in the conductivity at about 400°C was matching the exothermic peak during thermal analysis process and the mass of powder did not lose from TC curve as demonstrated in Figure 2.22. These results showed that the ITO particles possessed oxygen vacancies after calcination at 400°C.

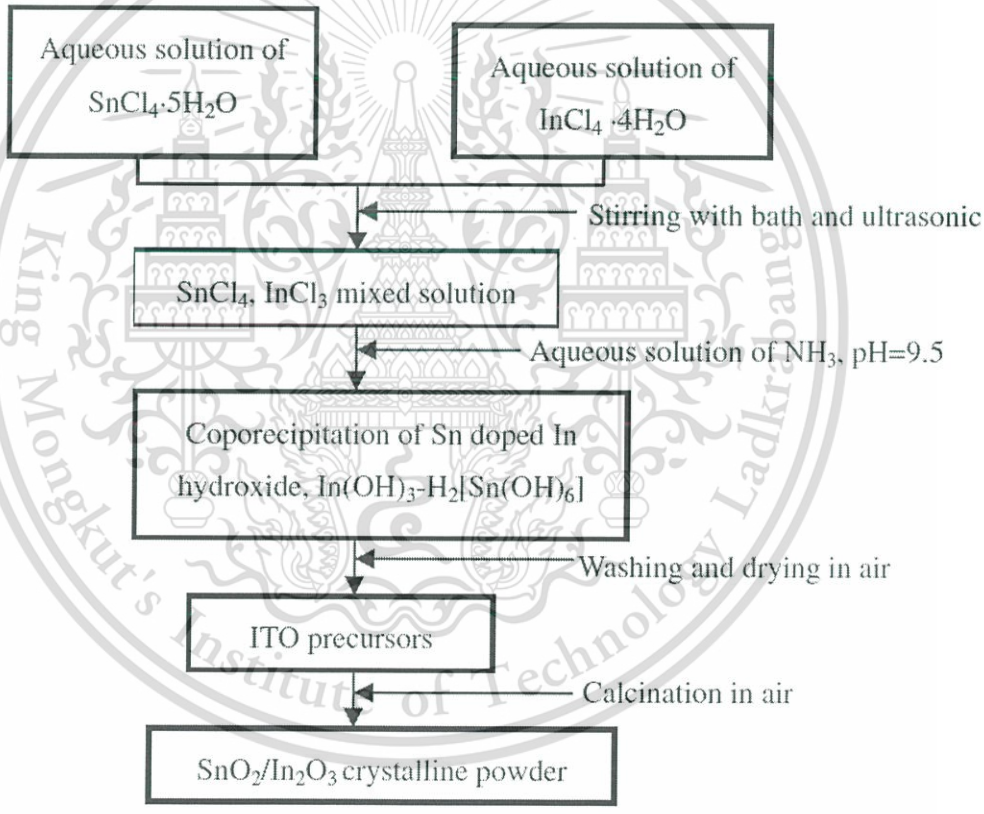

Figure 2.20 Process of ITO nanoparticles synthesized by co-precipitation [39].

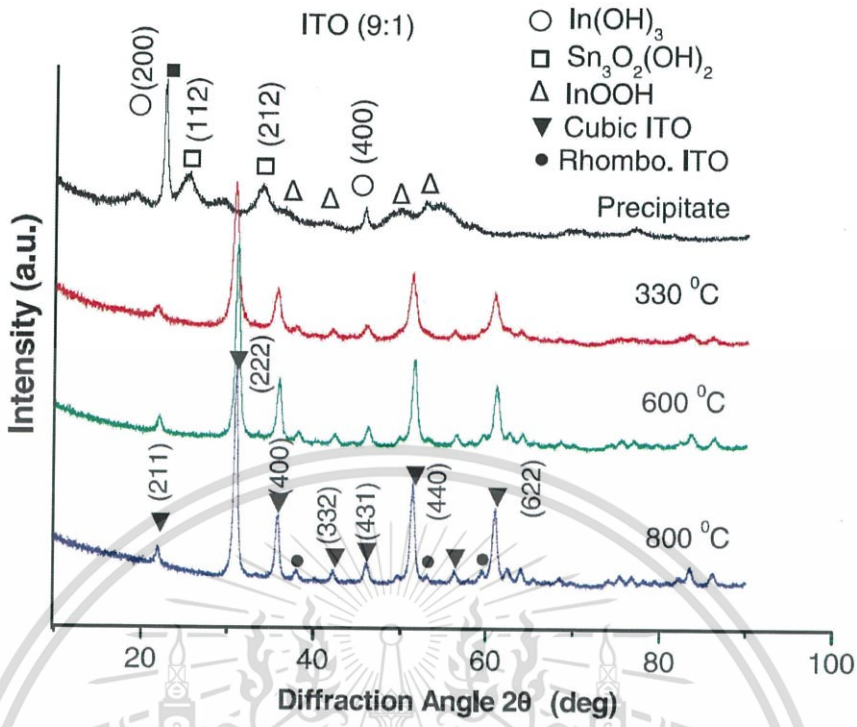

Figure 2.21 The variations of XRD patterns of ITO particles at the various calcination temperatures [39].

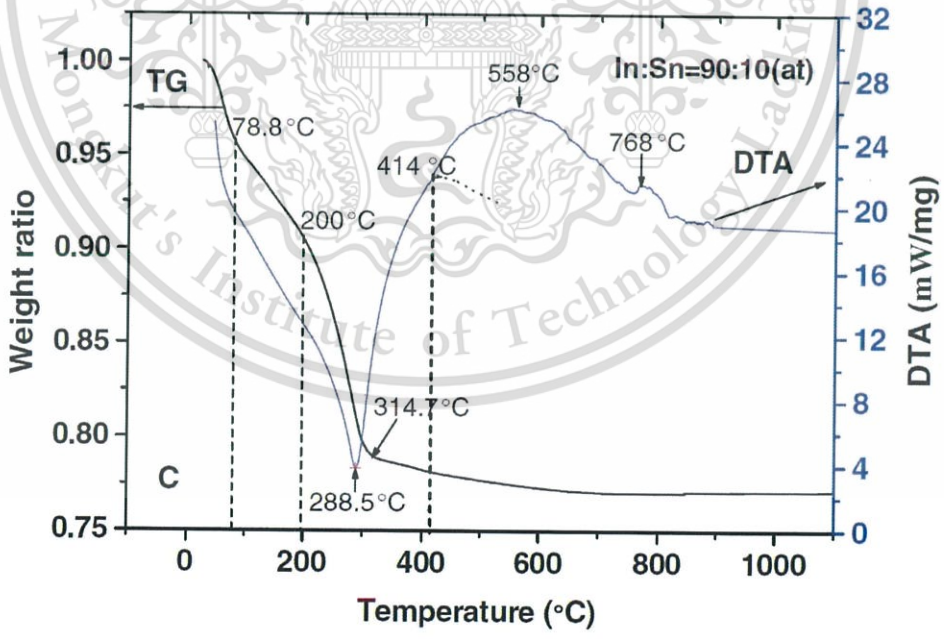

Figure 2.22 Thermal analysis of the ITO precursor sample with thermal temperature [39].

Silva *et al.* [40] reported that indium tin oxide nanoparticles were synthesized by a nonhydrolytic sol-gel method. The XRD patterns in the Figure 2.23 indicated the preferential formation of metastable hexagonal phase ITO in corundum type as opposed to cubic phase ITO when the reflux time was less than 3 h and the heat treatment temperature was below 600°C. Figure 2.24 shows morphology of ITO particle with 4h reflux time at treatment temperature of 600°C.

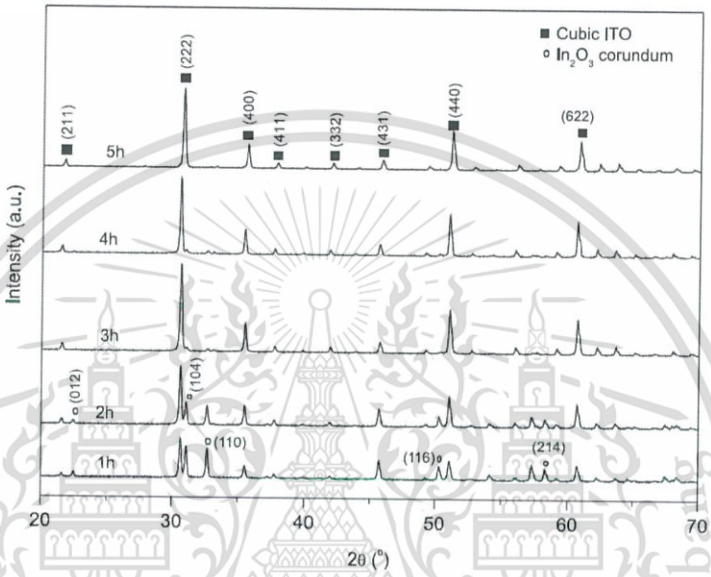

Figure 2.23 XRD patterns of ITO powders with different reflux times treated at 600°C [40].

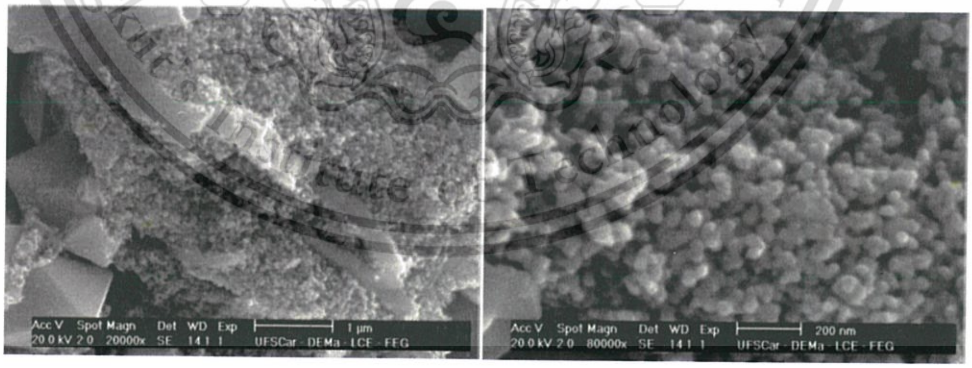

Figure 2.24 SEM images of ITO powders after 4h reflux time at treatment temperature of 600°C in different magnitude [40].

Zhang *et al.* [41] reported that Sb-doped SnO_2 nanoparticles (at ratio of Sb/Sn, 5:100) were synthesized by mild hydrothermal method free from the widely used metal chlorides. The result indicated that all Sb ions came into the SnO_2 lattice to substitute Sn ions, though the hydrothermal temperature was as low as 120°C. In Table 2.3, the electrical conductivity and crystalline size were changed after increasing the heat treatment temperature accelerates the growth of the nanoparticles. The highest electrical conductivity (8×10^2 S cm^{-1}) is obtained at a hydrothermal temperature 140°C and the TEM image of this particle was shown in Figure. 2.25.

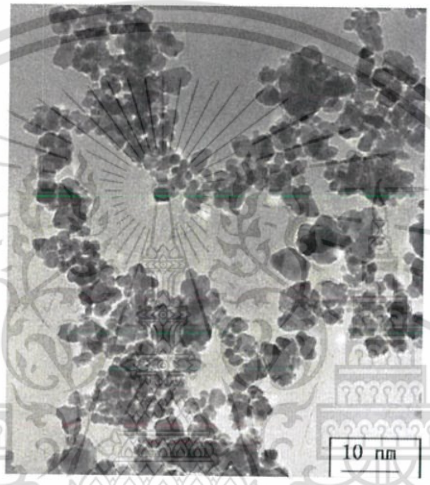

Figure 2.25 TEM images of ATO nanoparticle at hydrothermal treatment of 140°C [41].

Table 2.3 Characterizations of the hydrothermally synthesized ATO nanoparticle [41].

Hydrothermal Temperature (°C)	D_{XRD} (nm)	Conductivity (10^2 S cm^{-1})
120	2.7	2
140	3.2	8
170	4.0	6

Jung *et al.* [42] reported that nano-sized antimony-doped tin oxide particles were synthesized using DC arc plasma jet. As shown in Figure 2.26, the precursors $SnCl_4$ and $SbCl_5$ was injected into the plasma flame in the vapor phase. ATO powder could conveniently be synthesized without any other post-treatment in this study. SEM image indicated that the size of particles synthesized using the Ar carrier gas was smaller than the particles prepared using the O_2 carrier gas as illustrated in Figure 2.27.

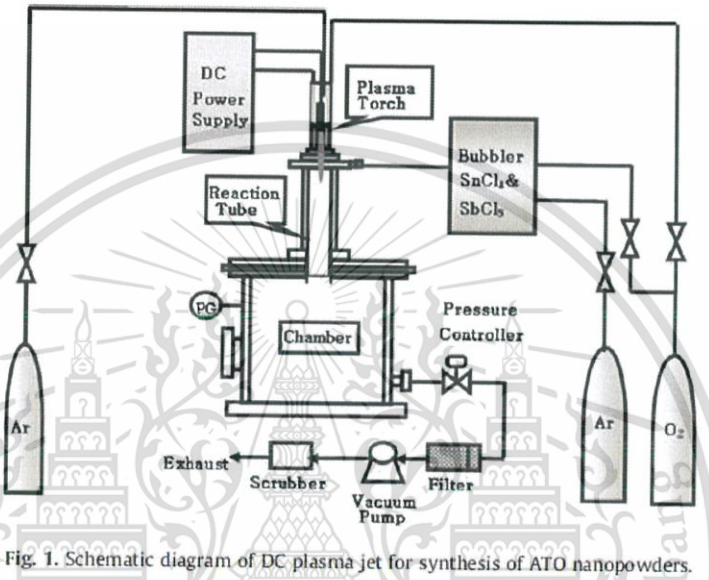

Figure 2.26 Schematic diagram of DC plasma jet for synthesis of ATO nanopowders [42].

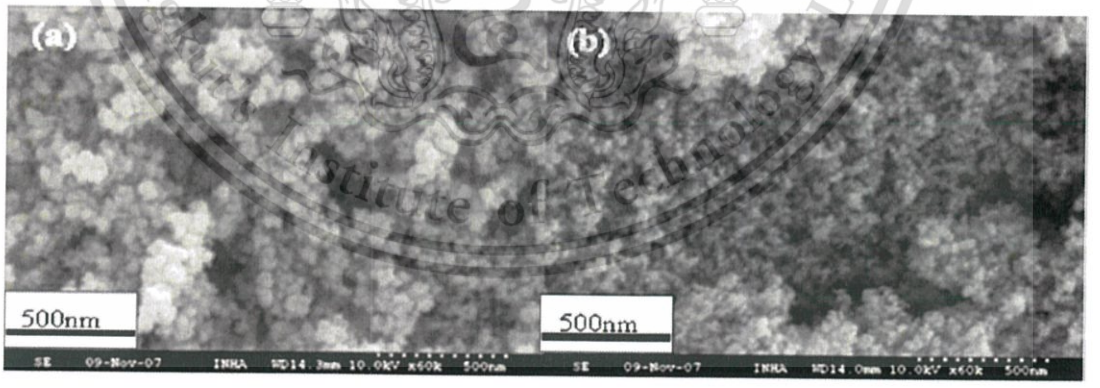

Figure 2.27 SEM images of ATO synthesized under different carrier gas (a) O_2 andn (b) Ar [42].

Sadegh *et al.* [43] reported that they had successfully synthesized nanocrystalline $In(OH)_3$ and In_2O_3 nanoparticles through a sonochemical reaction. This report studied the effect of concentration of

$In(CH_3COO)_3$ and NaOH with different aging times and different sonicated power. The schematic of the experimental setup is depicted in Figure 2.28. The reactions proceeded under ultrasonic conditions resulting in approximately spherical and uniform $In(OH)_3$ and In_2O_3 nanoparticles as shown by SEM obervations in Figure 2.29. It appeared that higher ultrasound power and frequency resulted in better separation and size distribution in the product. The In_2O_3 nanoparticle was obtained by calcination at 400 °C and its morphology was shown in Figure 2.29(f).

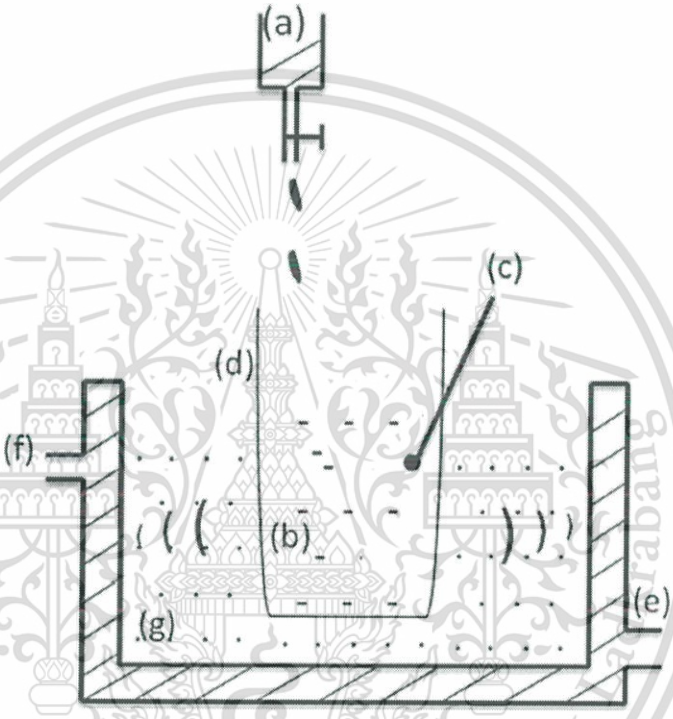

Figure 2.28 Schematic of the experimental setup used for the sonochemical reactions: (a) NaOH vessel, (b) In(OAc) solution, (c) thermometer, (d) reaction cell, (e) double jacketed vessel, (f) water circulation and (g0 ultrasound bath [43].

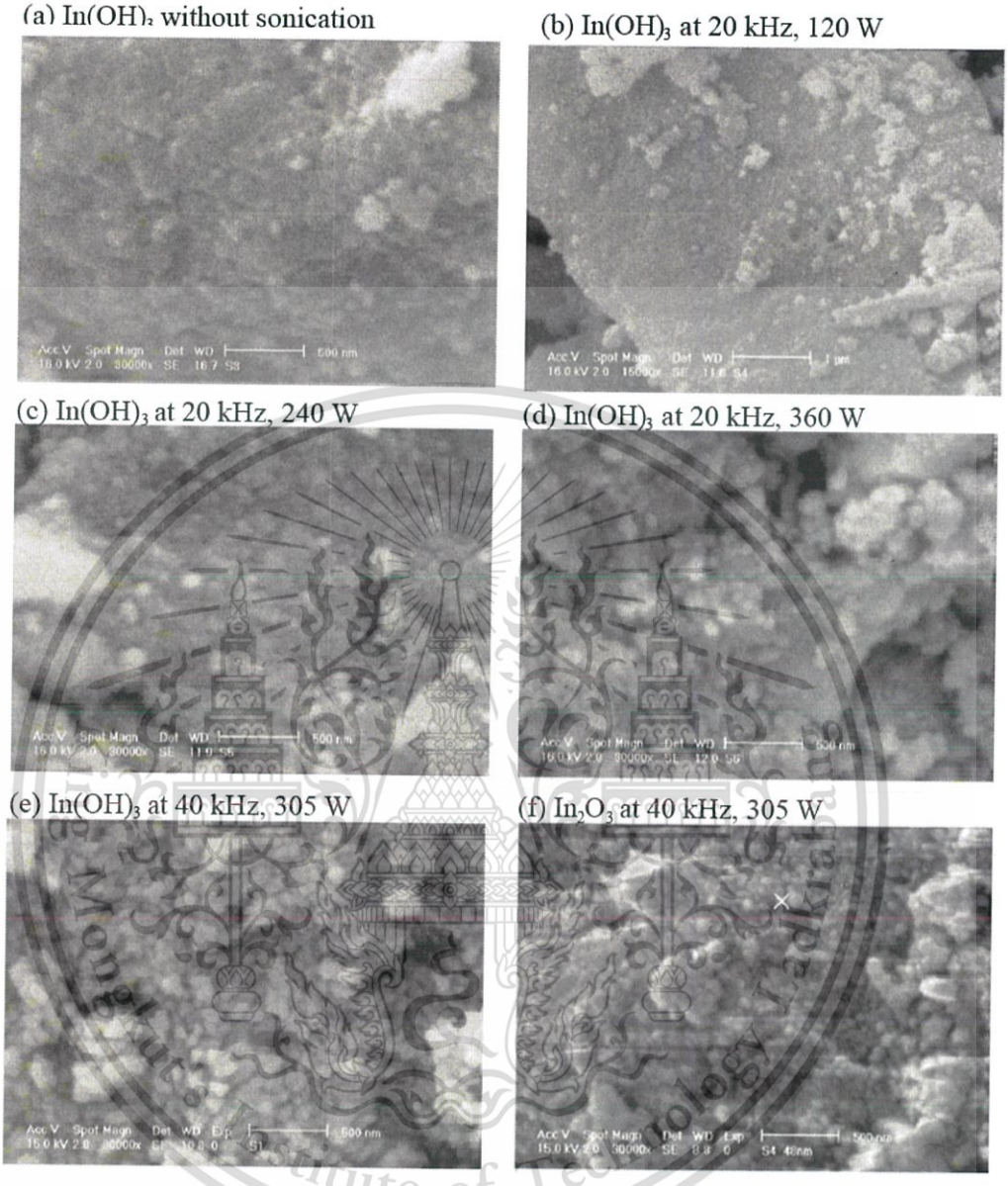

Figure 2.29 SEM images of synthesized powders with different ultrasonic power and frequency [43].

Qmidi *et al.* [44] reported that Sb-doped ZnO nanostructures were prepared by ultrasonic irradiation method without using any organic compound and additional post treatment. Nanostructures of ZnO doped with Sb^{3+} ions with dopant content ranging from x = 0.00 to 0.15 were prepared in water using 60 min ultrasonic irradiation. The SEM images in Figure 2.30 indicated that the doping greatly changed morphology and size of the pure ZnO. It is evident that ZnO nanostructures are mainly plates with different sizes. The morphology and size of Sb-doped ZnO nanostructures changed with increasing mole fraction of Sb^{3+} ions.

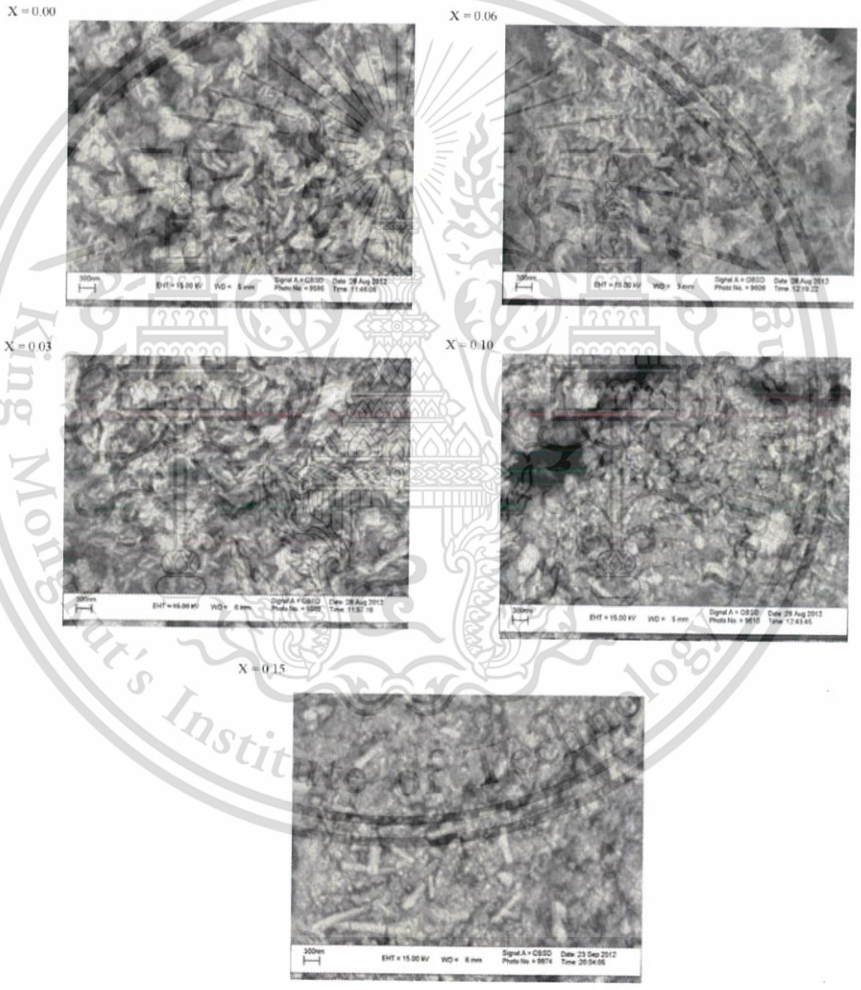

Figure 2.30 SEM images of Sb-doped ZnO nanostructures with various mole fraction of Sb^{3+} ions [44].

Tran *et al.* [45] investigated of the effects of the growth of SnO_2 nanoparticles on the structural properties of glass–ceramic planar waveguides. (100-x) SiO_2–x SnO_2 (x from 12 to 60 mol%) glass–ceramic thin films were prepared by the sol–gel processing method, obtaining high SnO_2 concentrations (up to 60 mol%) for the first time. Figure 2.31 shows the SnO_2 nanocrystals dispersed in the amorphous silica matrix. Using an appropriate thermal process, SnO_2 nanocrystals were nucleated in the glassy silica matrix, providing optical waveguides for $x \leq 30$ mol%. FTIR results provided information on the structural evolutions of the matrix which resulted from the formation and the growth of the SnO_2 nanocrystals as illustrated in Figure 2.32.

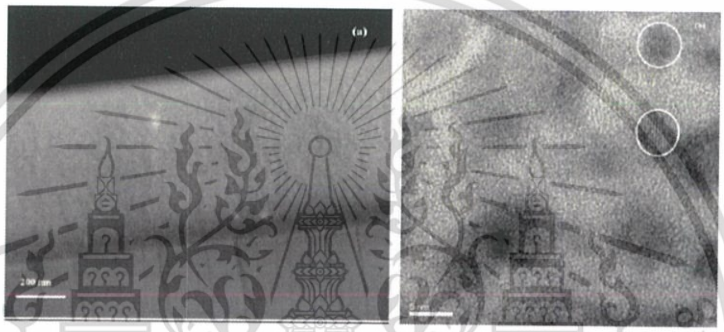

Figure 2.31 SEM and TEM images of a 75 SiO_2–25 SnO_2 glass–ceramic sample heat-treated for 1 h at (a) 600 °C and at (b) 1100 °C, respectively. The circles highlight SnO_2 nanocrystals dispersed in the amorphous silica matrix [45].

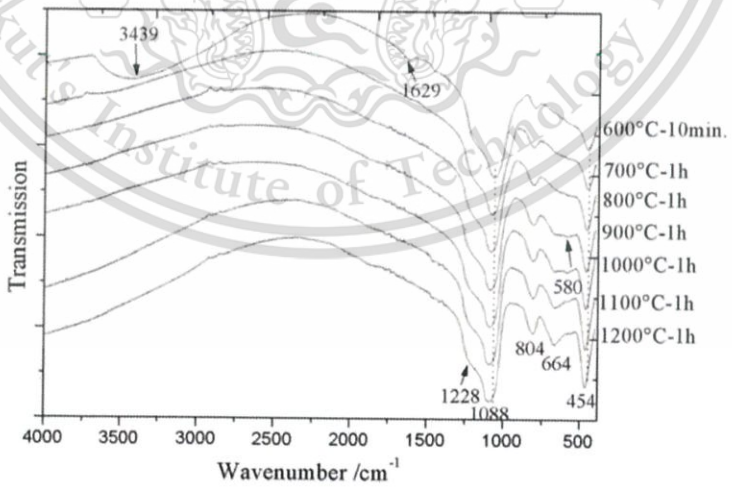

Figure 2.32 Evolution of the FTIR spectra of a 70 SiO_2-30 SnO_2 glass-ceramic sample with increasing annealing temperatures [45].

Li *et al.* [46] reported that nano-antimony-doped oxide was synthesized by sol-gel method as illustrated in Figure 2.13. A colloidal dispersion of ATO nanoparticles in distilled water was achieved using a milling process. This study showed that the pH value, dispersant type and dosage, and grinding time had a considerable impact on the stability of the ATO suspensions. An ATO suspension with pH =6–10 has a higher zeta potential and better stability. Among the several dispersants studied in this paper, polyacrylamide and sodium polyphosphate could improve the stability of the ATO suspension significantly as shown in Figure. 2.34. An ATO suspension with 8 wt% sodium polyphosphate, pH = 9, and a grinding time of 36 h can be stored for more than one year at room temperature. This work developed a robust and reliable method for the preparation of stable suspensions of ATO nanoparticles for thermal insulation glass paint. The stable dispersion of ATO nanoparticles was used to prepare nano-thermal insulation glass paint to block near-infrared ray of sunlight.

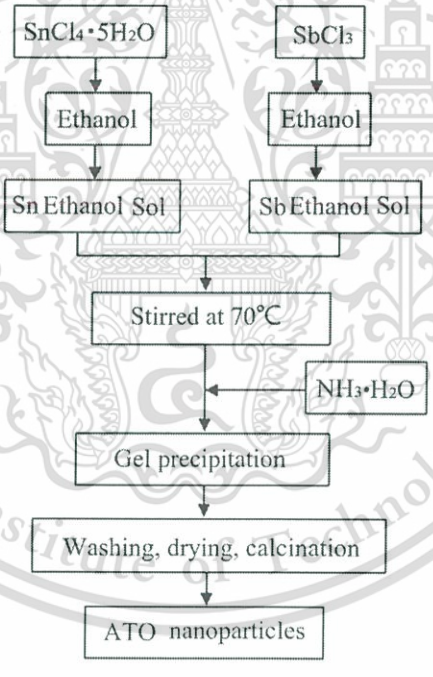

Figure 2.33 The preparation of nano-sized antimony tin oxide using the sol-gel [46].

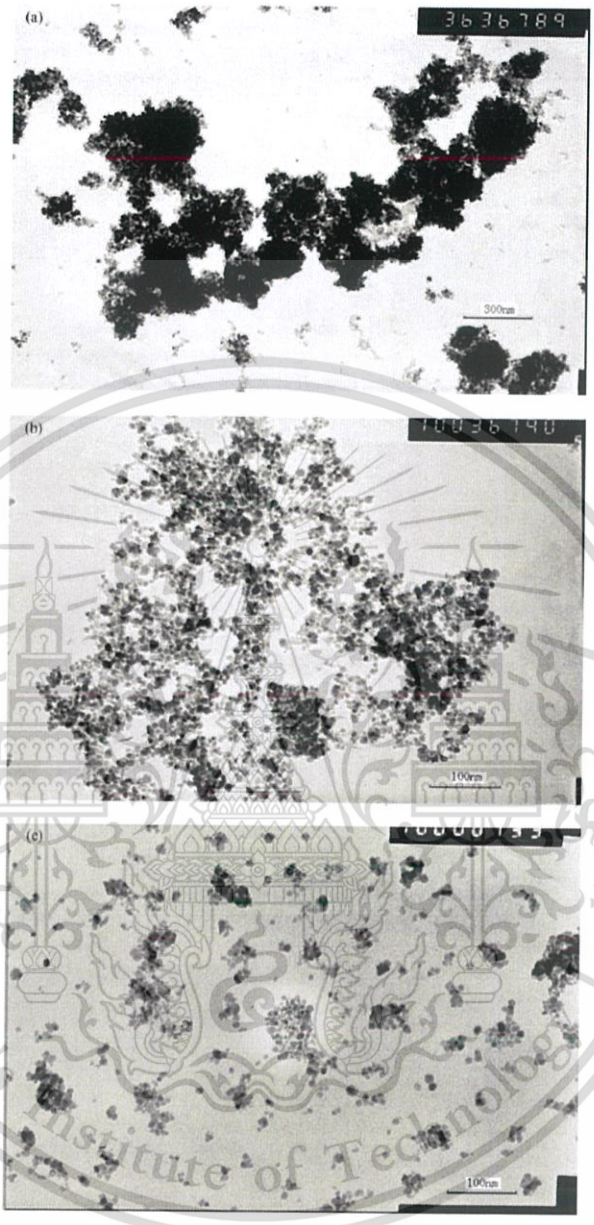

Figure 2.34 TEM image of ATO suspension (a) without dispersant, (b) with Polyethylene glycol 4000 dispersant and (c) Sodium polyphosphate [46].

Cho *et al.* [47] reported that nanosized colloidal indium tin oxide (ITO) dispersion was prepared by milling ITO powder together with isopropyl tri(N-ethylenediamino)ethyl titanate as disperstant. Experimental procedure in this method is depicted in Figure 2.35. The nanosized colloidal ITO dispersion was prepared for electrically conductive and transparent coating materials. ITO sol was deposited on a cathode ray tupe (CRT) panel for antistatic or electromagnetic shielding purposes and alkyl silicate was used for the formation of an antireflective over-coat layer as illustrated in Figure 2.36. The double-layered coating film showed a low minimum reflectance of about 1% as shown in Figure 2.37 and a sheet resistance of the order of 10^4 Ω/□ which was enough to satisfy antireflective and antistatic properties. The electrical resistance and visible light reflectance of the coating film were affected by the secondary particles.

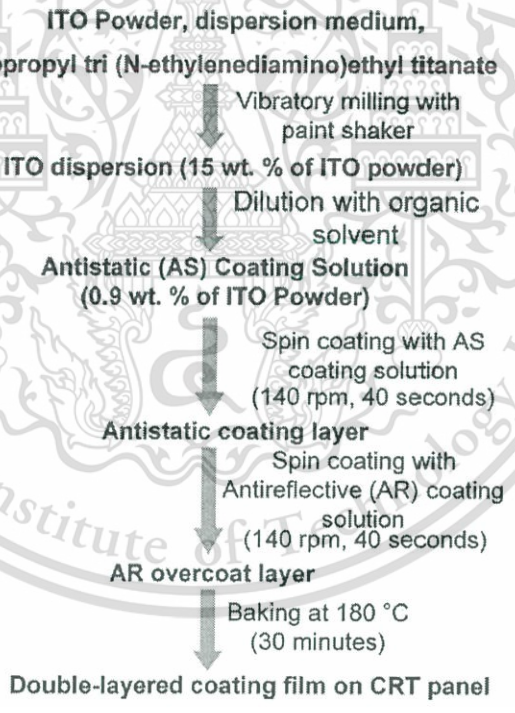

Figure 2.35 Experiment procedure of colloidal indium tin oxide nanoparticles coating [47].

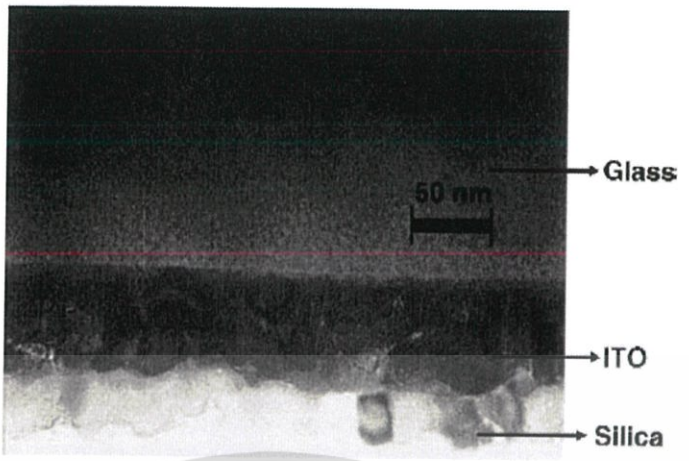

Figure 2.36 SEM image of double-layerd indium tin oxide/silica coating layer [47].

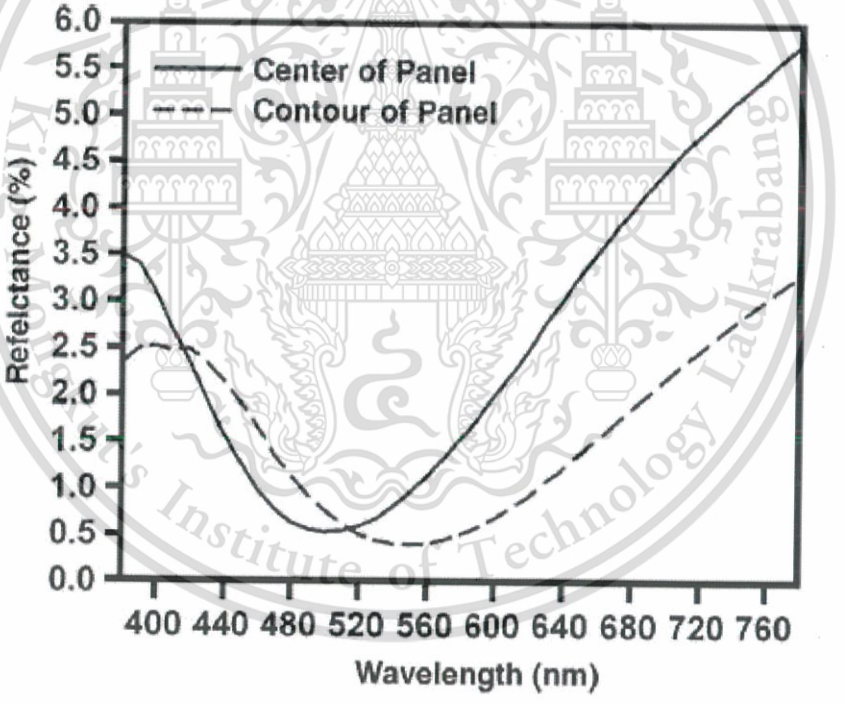

Figure 2.37 Visible light reflectance of cathode ray tube panel as a function of the wavelength of incident light. The secondary particle size and dispersant concentration of colloidal ITO dispersion are 101 nm and 0.67 wt%, respectively [47].

Goebbert *et al.* [48] reported that crystalline SnO_2, SnO_2:Sb and In_2O_3:Sn nanoparticles, fully redispersable in water or ethanol had been prepared. The growth of the particles was controlled in an aqueous ammonia solution by chemical modification of the particle surface. The obtained suspension was stable at pH > 8 for ATO and pH < 6 for ITO. Transparent conducting coatings with thickness up to 500 nm/layer had been obtained by spin coating. The transmission in the visible range measure against air was about 90% as shown in Figure 2.38. This reflects the beneficial effect of using particles in the nonometer range for coating production as these particles practically do not scatter the visible light. The annealed ITO and ATO coatings showed a similar increase of the annealed ITO and ATO coating showed a similar increase of the reflectance in the IR range due to the conducting properties of the materials. However, the deposited ITO film had a lower reflectance due to the lower density of the electrons.

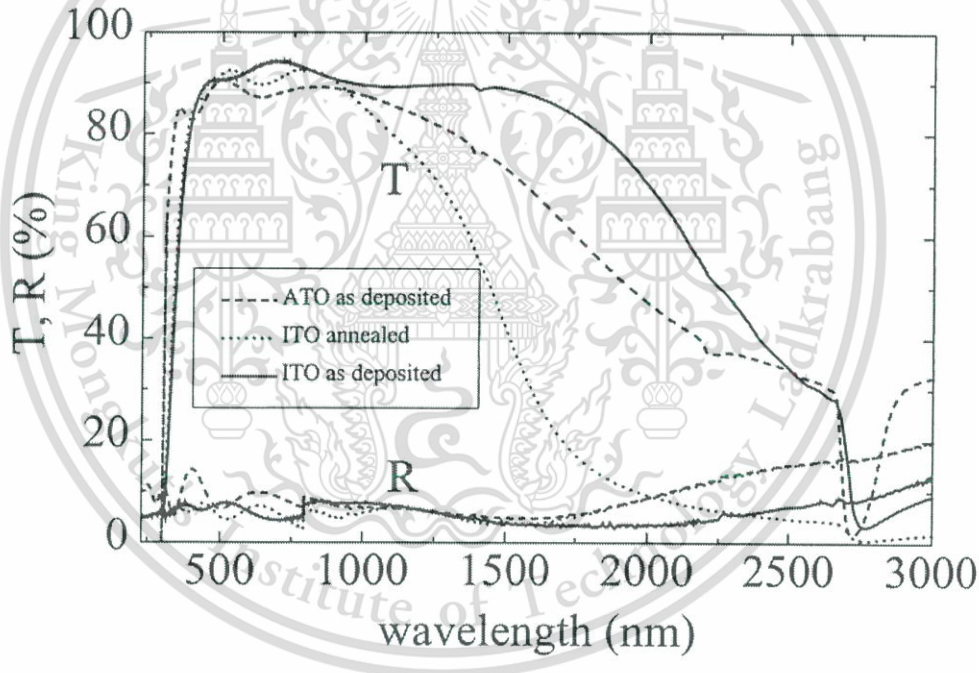

Figure 2.38 Reflectance and transmission spectrum of ATO and ITO coating annealed at 550 °C for 30 min (Sheet resistance: ATO = 430 Ω/□ , ITO = 1 kΩ/□, ITO (annealed) = 250 Ω/□) [48].

Katagiri *et al.* [49] reported that infrared-shielding coating films were prepared by dispersing indium tin oxide nanoparticles in a silica matrix as illustrated in Figure 2.39. Hydrophobized ITO nanoparticles were synthesized via a liquid phase process. Coating films composed of a continuous silica matrix dispersed with ITO nanoparticles was obtained using perhydropolysilazane (PHPS) as a precursor. PHPS was completely converted to silica by exposure to the vapor from aqueous ammonia at 50 °C. In Figure 2.40, the surface plasmon resonance (SPR) absorption of the ITO nanoparticles could be tuned by varying the concentration of Sn doping from 3 to 30 mol%. The shortest SPR wavelength and strongest SPR absorption were obtained for the ITO nanoparticles doped with 10% Sn because they possessed the highest electron carrier density. The prepared coating films could efficiently shield IR radiation even though they were more than 80% transparent in the visible range as shown in Figure2.41. The coating film with the greatest IR-shielding ability completely blocked IR light at wavelengths longer than 1400 nm.

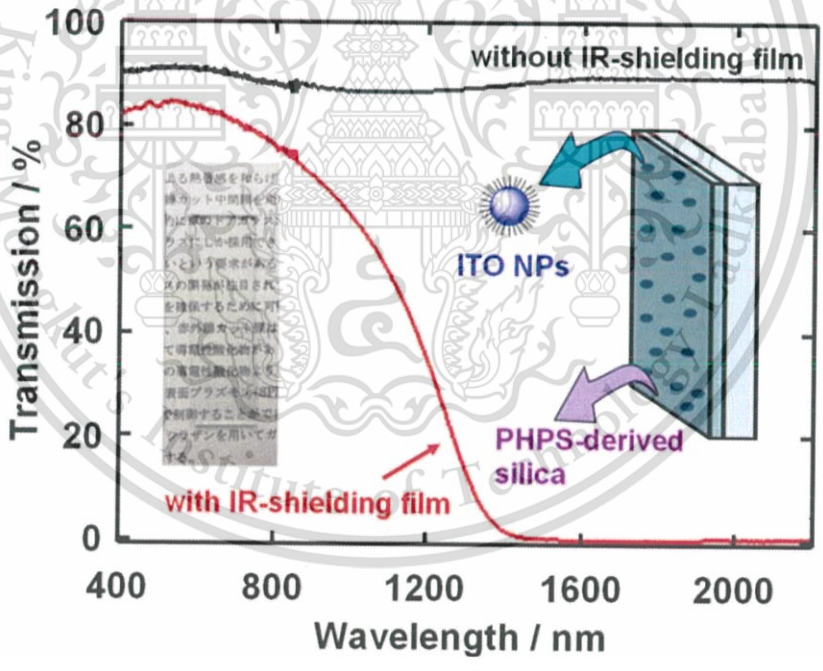

Figure 2.39 Schematics of ITO nanoparticles dispersed in a silica matrix for IR-shielding application [49].

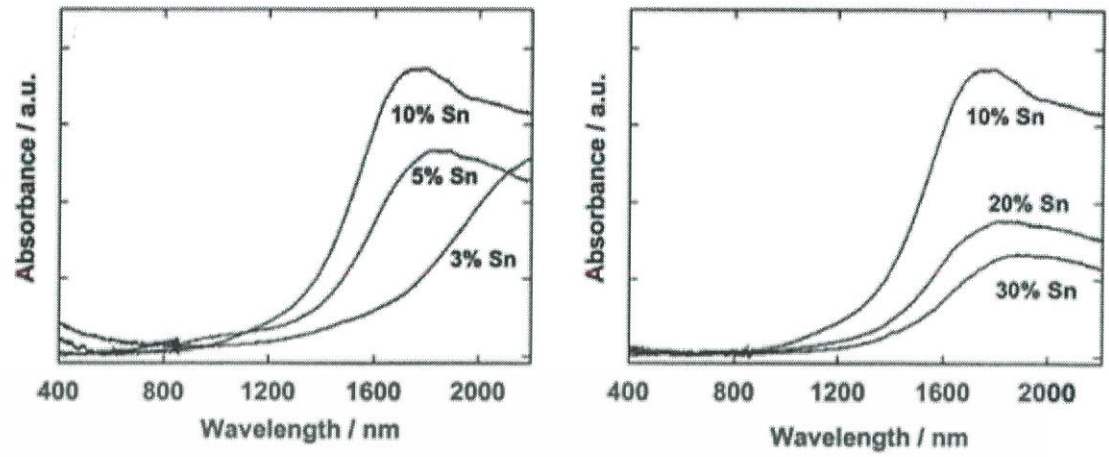

Figure 2.40 UV-vis-NIR spectra of ITO nanoparticle with different Sn concentration [49].

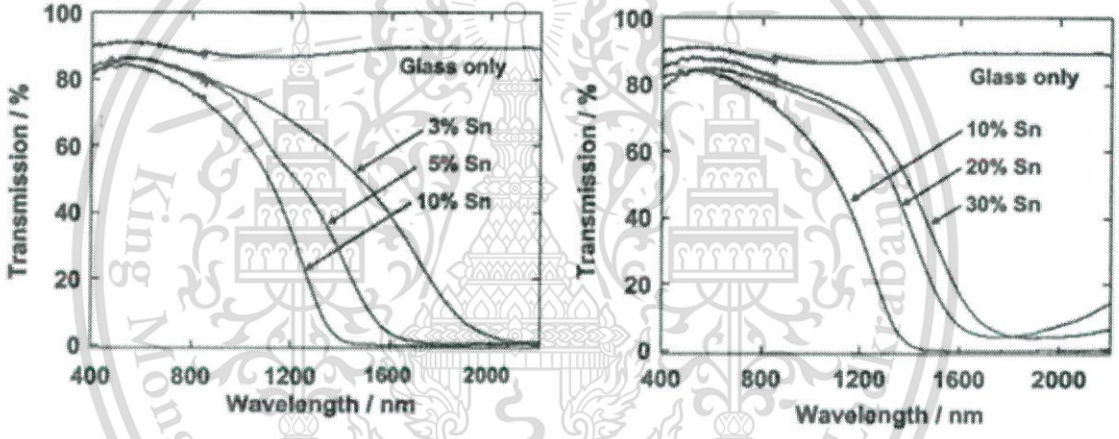

Figure 2.41 UV-vis-NIR spectra of ITO nanoparticle dispersed in silica matrix with different Sn concentration [49].

CHAPTER 3

EXPERIMENTS

This chapter explains the preparation of SnO_2 and F-doped SnO_2 nanoparticle systhesized by ultrasonic-assisted precipitation process. Sb- and F/Sb-doped SnO_2 were synthesized by sonochemical-assisted precipitation. Then, the synthesized nanoparticles were used for fabrication of nanocomposite film. Finally, the films were applied on IR-shielding coating in solar cells.

3.1 Preparation of SnO_2 nanoparticles via ultrasonic-assisted precipitation process

SnO_2 nanoparticles were synthesized by ultrasonic-assisted precipitation process using 0.2 M stannic chloride pentahydrate as exhibited in Figure 3.1. The sonication was operated at 120 W with frequency of 40 kHz using ultrasonic bath.

3.1.1 Materials and equipment

1) Stannic chloride pentahydrate ($SnCl_4 \cdot 5H_2O$)
2) Deionized water and ethanol
4) Beaker, magnetic bar and magnetic stirrer
6) Ultrasonic bath
7) Calcination oven
8) Centrifuge machine

3.1.2 Experimental details

All equipment are illustrated in Figure 3.2. Firstly, 14.024 g $SnCl_4 \cdot 5H_2O$ was dissolved in 200 ml deionized water and kept under sonication in ultrasonic bath at 60°C for 20 min until homogeneous solution was reached. Then, the aqueous ammonia was added dropwise into solution under ultrasonic bath for 1 h. The precipitate of tin hydroxide was obtained and then aged for 24 h at room temperature. The precipitate was washed several times with deionized water and ethanol via centrifugation to remove chlorine ions and other residues. The

conventional precipitation method was prepared by magnetic stirrer under similar condition. Finally, the as-synthesized precipitates were dried in oven at 80 °C and then calcined at 400 °C for 2 h.

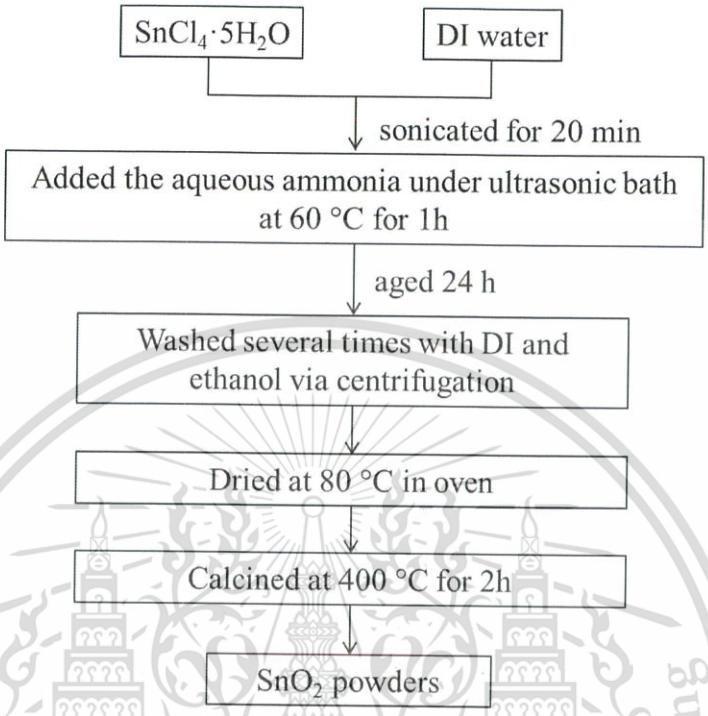

Figure 3.1 Experiment procedure of tin oxide nanoparticles.

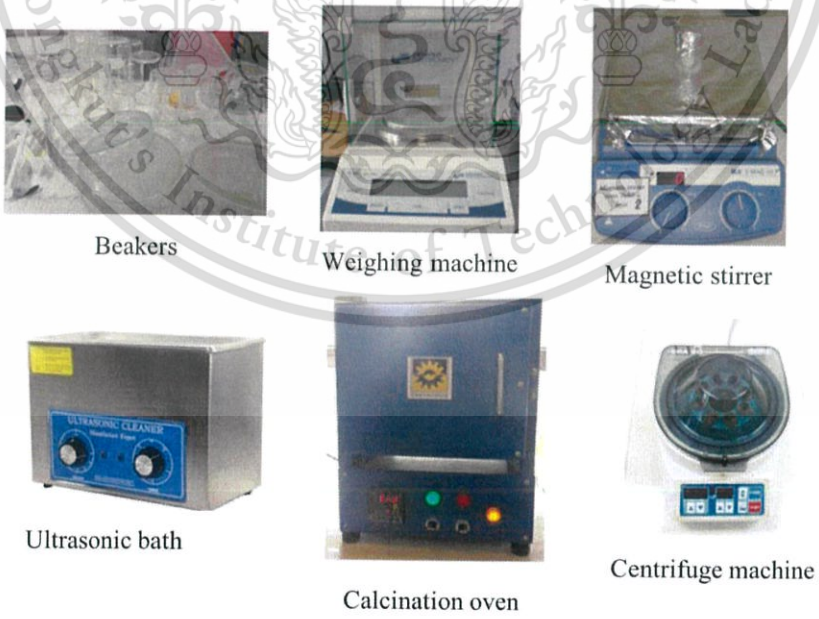

Figure 3.2 Equipment used in nanoparticles synthesis.

3.2 Preparation of F-doped SnO_2 (FTO) nanoparticles via ultrasonic-assisted precipitation

In this synthesis, all equipment were used as SnO_2 nanoparticle synthesis but precursor sort of fluorine was added. The starting precursor of fluorine dopant is ammonium fluoride (NH_4F) and the experiment procedure is shown in Figure 3.3.

The composition of fluoride was varied from 0 to 20 mol%. 0.2 M of $SnCl_4$ and NH_4F was dissolved in deionized water under sonication in ultrasonic bath operated at 120 W with frequency of 40 kHz. The suspension was sonicated at 60°C for 20 min until homogeneous solution was obtained. Then, aqueous ammonia was dropped into solution within operating time of 2 h. The gelatinous precipitated product was washed several times with deionized water and ethanol via centrifugation to remove chlorine ions. Finally, the as-synthesized products were dried in oven at 80 °C and then calcined at 400°C for 2 h.

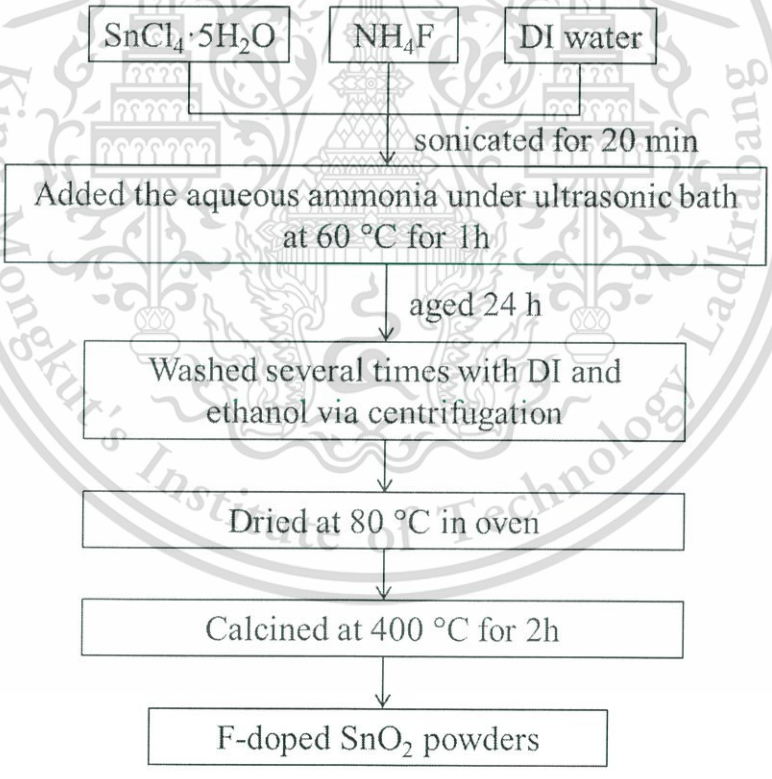

Figure 3.3 Experiment procedure of F-doped SnO_2 nanoparticles.

3.3 Preparation of Sb-doped SnO_2 (ATO) nanoparticles via sonochemical assisted precipitation

3.2.1 Materials and equipment

In this synthesis, the source of ultrasonic radiation was changed from the ultrasonic bath to direct-immersion ultrasonic which has higher energy radiation. The ultrasonic horn using Sonic model VCX 750 (750W, 20kHz) are shown in Figure 3.4. The starting precursor of antimony dopant is antimony chloride ($SbCl_3$) and the experiment procedure is illustrated in Figure 3.5.

3.1.2 Experimental details

0.2 M of $SnCl_4$ and $SbCl_3$ powders with Sb concentration at 0, 5, 10, 15 and 20 mol% were dissolved in absolute ethanol and then acetylacetone was added. The precursor was stirred for 20 min at room temperature until homogeneous solution was reached. The solution was sonicated for 30 min by a direct-immersion ultrasonic. The aqueous ammonia was added drop wise to the stock solution during sonication until the pH value of the solution was reached to the range of 9-10. After sonication for 30 min, the completely precipitates product was obtained and allowed to cool down to room temperature. The precipitates were washed several times with deionized water via centrifugation at 4500 rpm for 4 min. Finally, the as-precipitated powders were dried slowly at 80 °C and calcined at temperature of 400°C for 2 h.

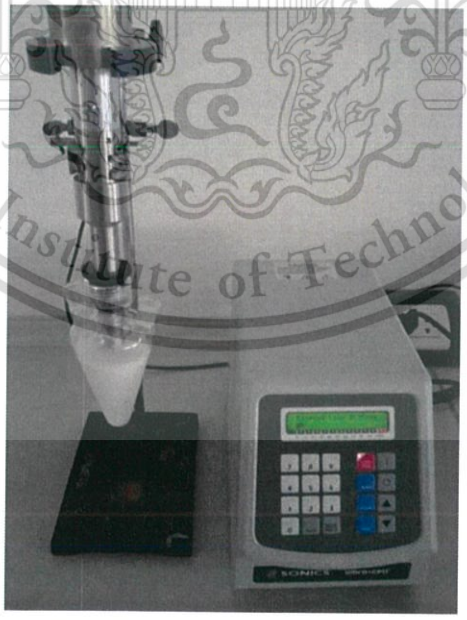

Figure 3.4 Ultrasonic horn (Sonic model VCX 750)

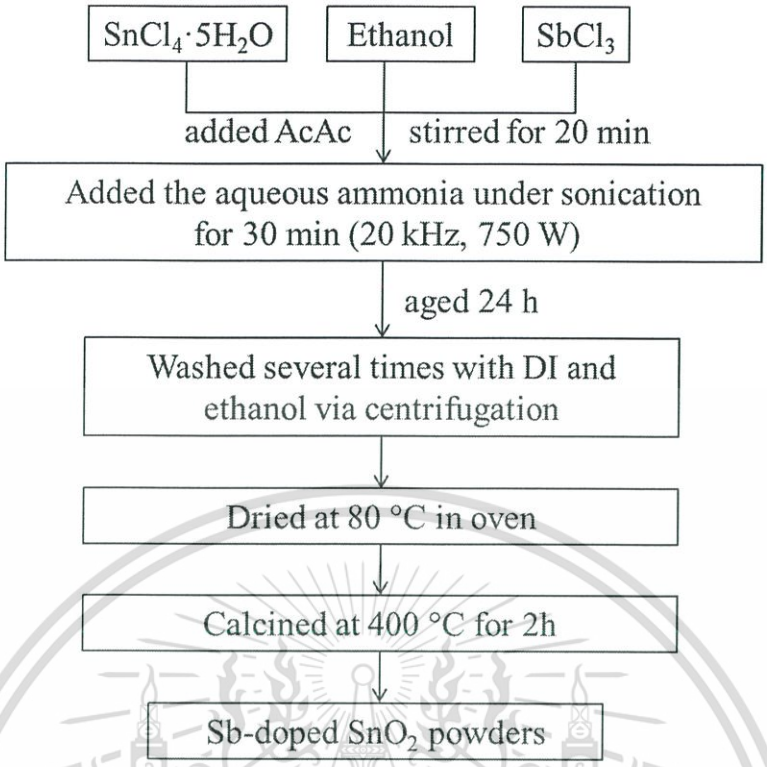

Figure 3.5 Experiment procedure of Sb-doped SnO_2 nanoparticles.

3.4 Preparation of F/Sb-doped SnO_2 (FATO) nanoparticles via sonochemical assisted precipitation process

In this synthesis, all equipment were used as ATO nanoparticle synthesis but precursor sort of fluorine was added. The starting precursor of fluorine dopant is ammonium fluoride (NH_4F).

F-doped SnO_2, Sb-doped SnO_2 and F/Sb-codoped SnO_2 (FATO) nanopowders were synthesized by sonochemical process as illustrated in Figure 3.6 Stannic chloride pentahydrate ($SnCl_4 \cdot 5H_2O$) was used as a host precursor while antimony(III) chloride ($SbCl_3$) and ammonia fluoride (NH_4F) were chosen as Sb and F dopant precursor, respectively. The composition of antimony was fixed at 5 mol% and 10 mol% while the fluoride composition was varied from 1-10 mol%. The F/Sb-codoped SnO_2 nanopowders were named F:Sb mol% FATO following the mol% ratio such as 1:5FATO. The starting precursors were dissolved in absolute ethanol and acetylacetone was slowly added. The precursor was vigorously stirred for 20 min at room temperature until homogeneous solution was reached. Ammonia solution was added drop wise to the stock solution during sonication until the pH value of the solution was reached to the range of 9-10. The solution was

sonicated for 30 min by a direct-immersion ultrasonic horn. The gelatinous precipitated products were obtained and allowed to cool down to room temperature then the product was washed several times with deionized water via centrifugation to remove both ammonia and chlorine ions and dried slowly at 80 °C overnight in an oven. Finally, the samples were calcined at 400 °C for 2 h to ensure the complete decomposition of the organic polymer and improve crystallinity of the particles.

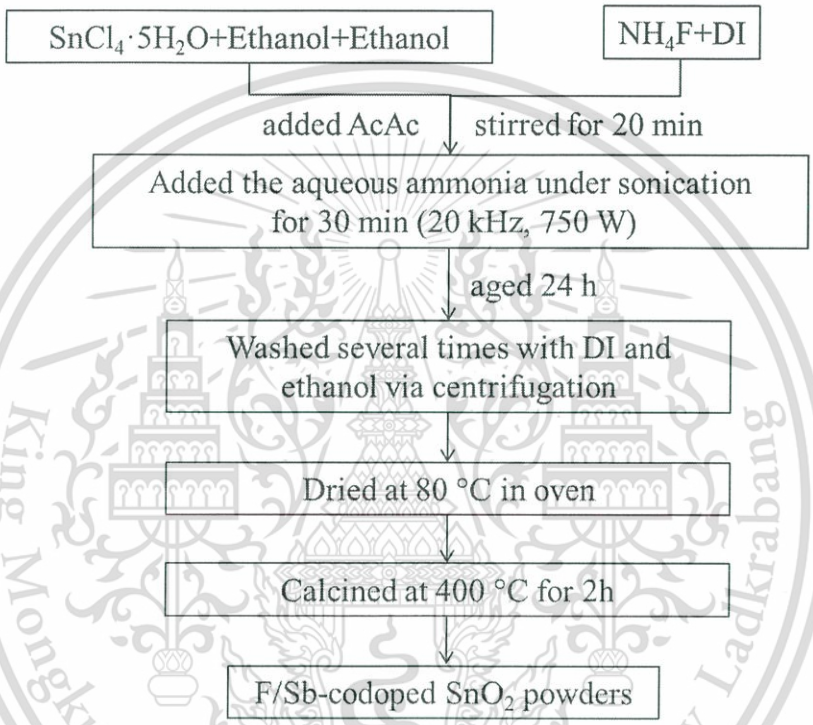

Figure 3.6 Experiment procedure of F/Sb-codoped SnO_2 nanoparticles.

3.5 Preparation of nanocomposite films deposited by sol-gel spin-coating process

3.5.1 Materials and equipment

1) (3-Glycidyloxypropyl) trimethoxysilane

2) Tetraethyl orthosilicate

2) Absolute ethanol

3) Deionized water and ethanol

4) Beaker, magnetic bar and magnetic stirrer

6) Ultrasonic bath

7) Spin coater

3.5.2 Experimental details

The nanoparticles dispersed in silica thin film were prepared by sol-gel spin coating process as exhibited in Figure 3.7. The model of spin coater is VTC-100 compact spin coater as shown in Figure 3.8. A stock solution of (3-Glycidyloxypropyl) trimethoxysilane (GYMO) with tetraethyl orthosilicate (TEOS) sol-gel precursor was prepared by hydrolyzing GLYMO and TEOS separately in ethanol (Absolute, ≥99.8%, Sigma-Aldrich) and distilled water under acidic condition before mixing together and stirred for 24 h prior to usage. The molar ration of GYMO:TEOS:EtOH:H_2O:HCl were 1:1.63:2.19:5:0.26. Coating procure with various nanoparticle types were prepared. Before deposition, both substrates were cleaned ultrasonically in deionized water, acetone and isopropanol for 10 min, respectively. The solution was coated on the substrates by spinner at speed of 2000 rpm for 40 s followed by heating on a hot plate at 100 °C for 10 min. The precursor was coated on glass substrate by spin coating technique. The films were treated at 150 °C for 1 h on hotplate.

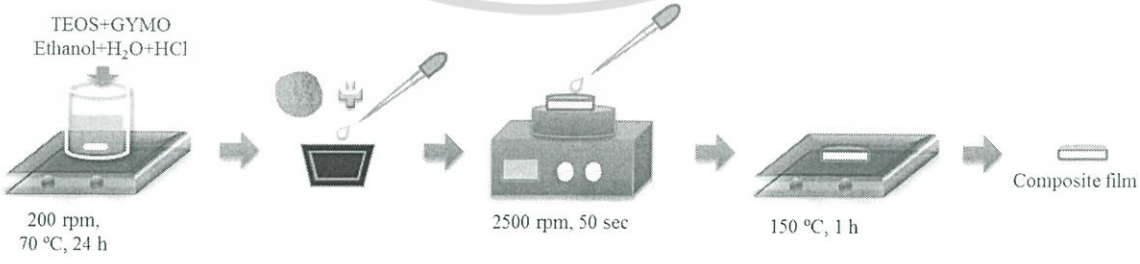

Figure 3.7 Preparation of composite film using sol-gel spin-coating method.

Figure 3.8 Image of VTC-100 compact spin coater.

3.6 Characterization

1) The structural properties of powders were characterized by XRD (PANalytical X'Pert Pro) operated at 40 kV and 30 mA using Cu-K_α radiation over a 2θ from 20° to 80° with step of 0.02°/sec.

2) The size, shape and crystal structure of the particles were observed by TEM (FEI, TECNAI $G^2$20) operated at 200 kV. Chemical bonding of powders was characterized by Raman spectroscopy carried out in the range of 300-800 cm^{-1}.

3) The chemical state analyses of the samples were carried out by X-ray photoelectron spectroscopy (Kratos analytical, AXIS $ULTRA^{DLD}$) using Al-K_α with radiation at 1.4 keV.

4) The resistivity (ρ) and carrier concentration (n) of the films were measured at room temperature using Hall measurement system in Van der Pauw configuration. Before Hall measurement, the 0.6 g of nanopowder was pressed into circular pellet of 1.5 mm diameter under 2.5 ton pressures for 2 min by hydraulic pelletizer as illustrated in Figure 3.9. Then the pellets were sintered at 1000 °C for 30 min giving the pellet with thickness of 1 mm.

5) Reflectance spectra were recorded in a wavelength of 200-1500 nm using UV-Vis spectrophotometer on model Shimadzu UV-3600.

6) The normalized V_{oc} of reference solar cell using composite film for IR-shielding layer were measured under continued exposure of halogen lamp as illustrated in Figure 3.10

7) The temperature of silicon solar cell was measured using thermocouple with multimeter under solar simulator exposure. The schematic of this measurement is shown in Figure 3.11.

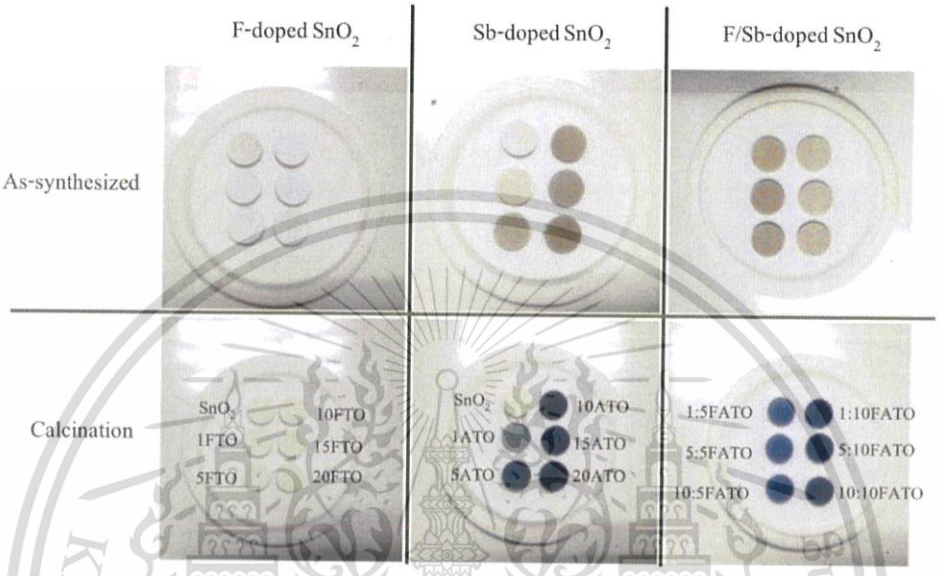

Figure 3.9 Image of all nanopartilces in the pellet form.

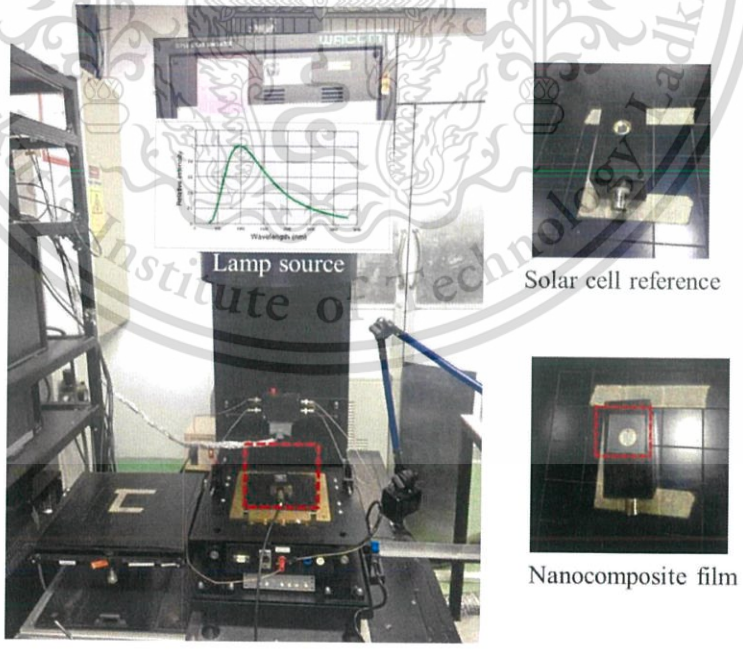

Figure 3.10 Schematic of normalized V_{oc} measurement under halogen lamp exposure.

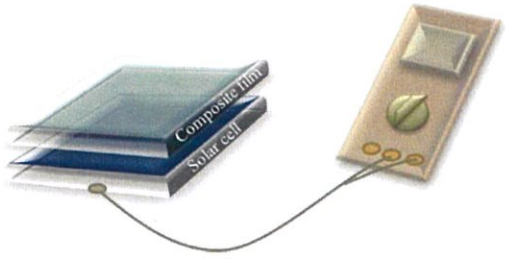

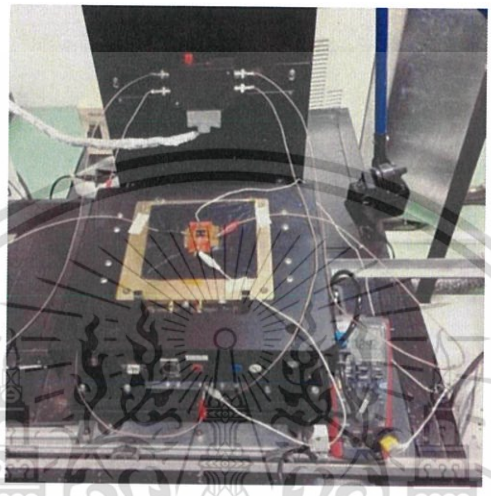

Figure 3.11 Schematic of temperature measurement using thermocouple under solar simulator.

CHAPTER 4

RESULTS AND DISCUSSION

4.1 SnO_2 nanoparticles via ultrasonic-assisted precipitation process

The thermal behaviors of as-synthesized precipitates SnO_2 powders prepared with and without sonication are shown in Figure 4.1 (a) and (b), respectively. The TG/DTA curves of as-synthesized precipitates detected at around 70°C and 230°C are assigned to the removal of absorbed water and alcohol and the decomposition of NH_4^+ in the powder according to the Eq.4.1 [50],

$$SnCl_4 + 4NH_4OH_4 \longrightarrow SnOH_4 + 4NH_4Cl. \quad (4.1)$$

The noticeable peak position about 485°C of sample prepared without sonication is attributed to the dehydroxylation and phase transformation of the as-precipitated product according to the Eq. 4.2,

$$Sn(OH)_4 \longrightarrow SnO_2 + 4H_2O. \quad (4.2)$$

Interestingly, the phase transformation peak of sample synthesized by ultrasonic-assisted method clearly shifts to lower temperature at around 375°C. The shift could be due to increase of the surface area possibly resulting from the size decrease of material. During ultrasonic radiation through a liquid, ultrasound can efficiently generates expansion and compression cycles leading to the cavitation in an aqueous medium. The cavitation effect in chemical process by restrains aggregation of particles can consequently decrease the particle size and reduce temperature of phase transformation [51].

Figure 4.2 shows the XRD patterns of as-synthesized and SnO_2 nanoparticles synthesized with and without sonication assistance. After calcinations at 400 °C, the sharpness and intensity of diffraction peaks increases remarkably, indicating the transformation of amorphous phase to well-defined crystallization of SnO_2 after calcination at this temperature range. All diffraction peaks of SnO_2 nanoparticles prepared with/without sonication evidently reveal polycrystalline phase of tetragonal SnO_2 crystal structure [52]. In addition, average crystallite sizes of the SnO_2 nanoparticles were calculated by well-known Scherrer's equation as follows [53]:

$$D = \frac{0.9\lambda}{\beta \cos\theta}, \tag{4.3}$$

where λ is the X-ray's wavelength (0.154 nm), β is the peak width at half-maximum (FWHM), θ is the diffracted angle of the corresponding peak. From Scherrer's equation, the broader intensity peaks of as-precipitated powders indicate that their average size is about 13-15 nm. It is noticed that the diffraction peaks of SnO_2 powders prepared by an assistance of ultrasonic possess higher sharpness than one prepared by conventional process due to the lower temperature phase transformation of $Sn(OH)_4$ to SnO_2.

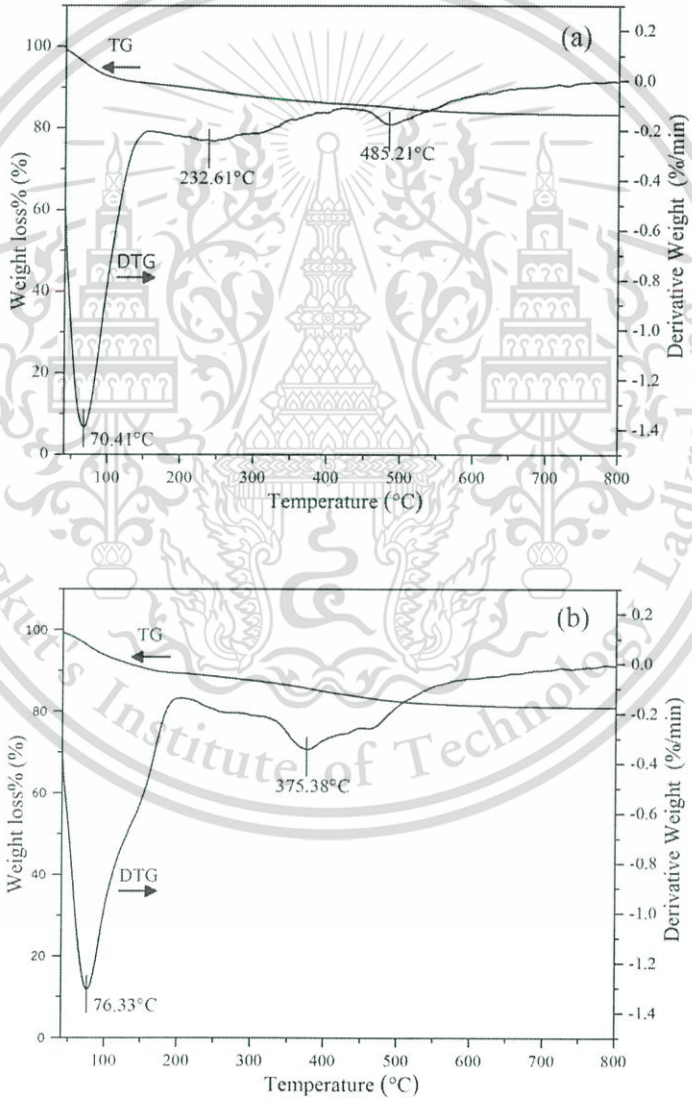

Figure 4.1 TG/DTA curves of as-synthesized SnO_2 powders (a) without and (b) with sonication.

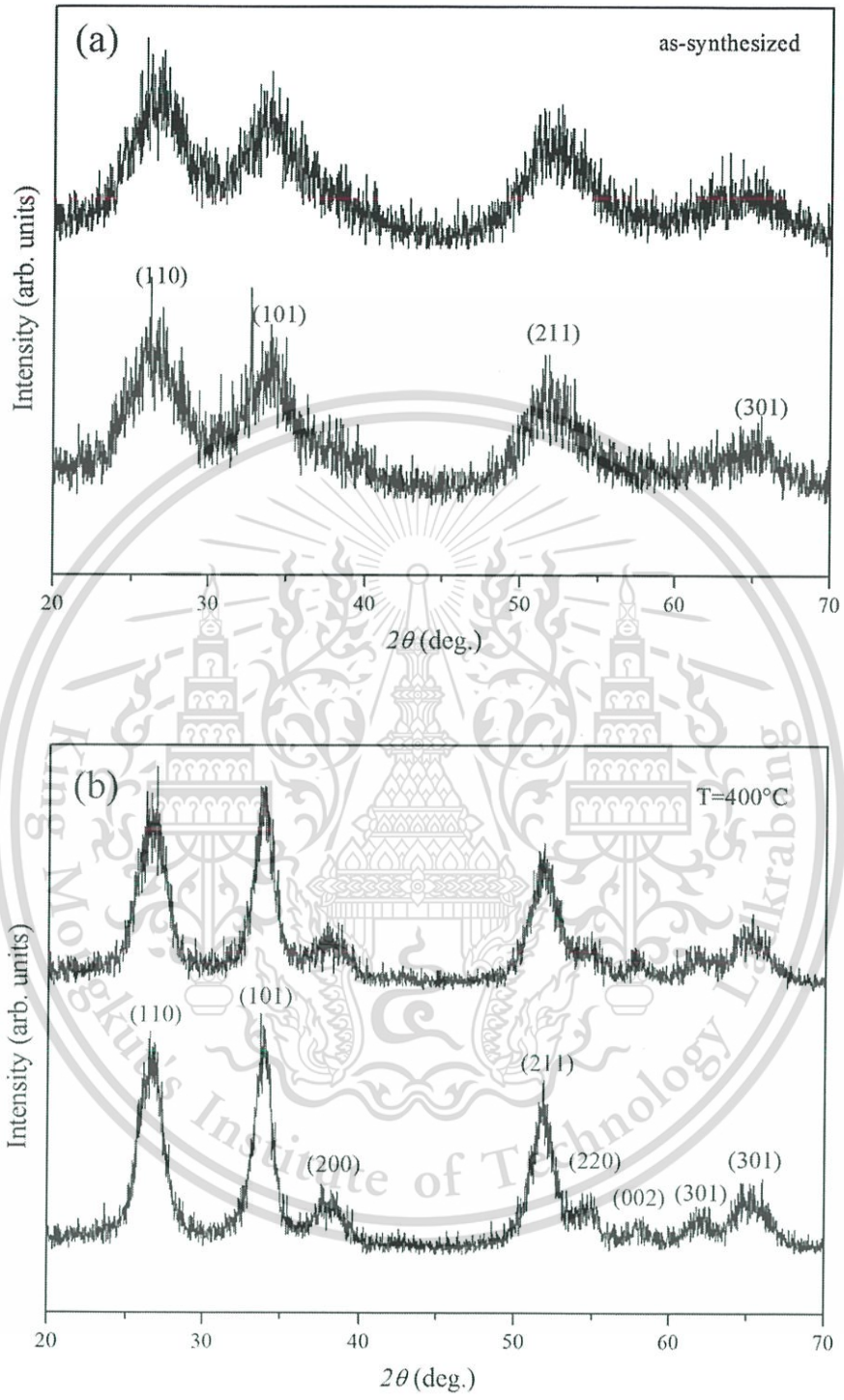

Figure 4.2 XRD patterns of (a) as-precipitated powders and (b) after-calcinedSnO_2 nanoparticles with/without sonication.

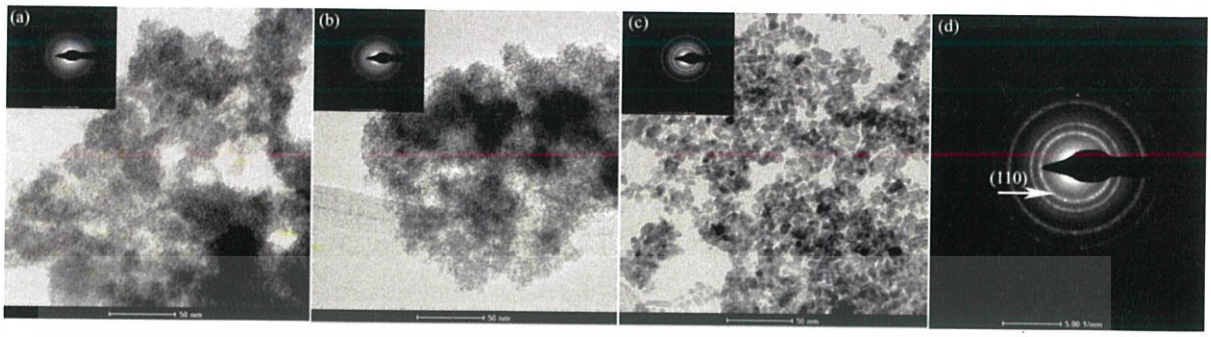

Figure 4.3 TEM images and SAED patterns of SnO_2 powders at different conditions (a) as-synthesized without (b) and (c,d) synthesized SnO_2 nanoparticles with sonication.

The TEM images and selected area electron diffraction (SAED) patterns of SnO_2 nanoparticles synthesized by precipitation method are illustrated in Figure 4.3. As seen in Figure 4.3 (a) and (b), the morphologies and particle size of as-precipitated SnO_2 nanoparticles prepared with/without sonication are unable to identify due to extremely tiny structures of the as-prepared particles reflecting their amorphosity in nature. After calcinations, the TEM image of SnO_2 nanoparticles shows excellent dispersesiveness with less agglomeration and an uniformity in particle size approximately 10-15 nm. The SAED patterns of as-precipitated nanoparticles show soft halo rings reflecting an amorphous phase. While SAED of after-calcined SnO_2 nanoparticles exhibits several strong halo rings confirming to polycrystalline and the brightest inner ring attributes to the (110) plane of SnO_2 [54].

4.2 F-doped SnO_2 nanoparticles via ultrasonic-assisted precipitation process

The XRD patterns of F-doped SnO_2 nanoparticles with different fluorine doping content of 0-20 mol.% are illustrated in Figure 4.4. All diffraction peaks of samples show the major peak of (110), (101) and (211) plane orientation corresponding to polycrystalline phase of tetragonal SnO_2 crystal structure [37]. The XRD patterns of all samples reveal only diffraction peak of pure SnO_2 without another impurity phase. It is noticeable that major peak position of F-doped SnO_2 powders shifts slightly toward the lower diffraction angles due to the prolongation of d-spacing caused by the dopant [55]. Because the ionic radius of fluorine ion (1.33 Å) is close to oxygen ion (1.32 Å). When doping, the good substitution of oxygen sites by fluorine ions can result to the alternation of d-spacing of the structure [56]. In addition, average crystallite sizes of the F-doped SnO_2

nanoparticles were calculated by well-known Scherrer's equation. The crystallite size of all samples are obtained from the FWHM of the (100) peak and summarized in Table 4.1. The crystallite size of nanoparticles slightly varies in the range of 10.2-11.2 nm by fluoride incorporation.

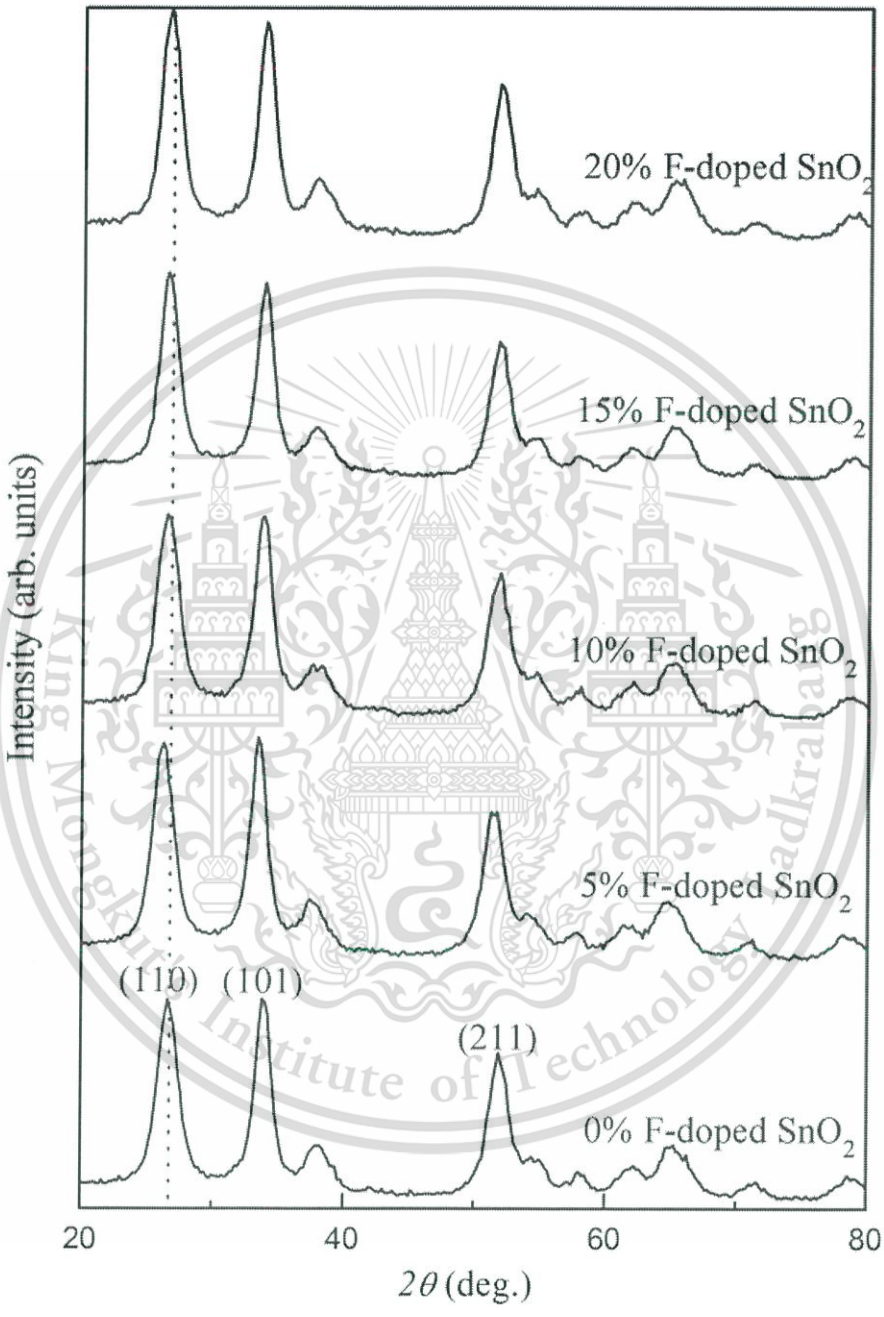

Figure 4.4 XRD patterns of F-doped SnO_2 nanoparticles with different fluorine content of 0-20 mol.%.

Table 4.1 crystallite sizes of the F-doped SnO_2 nanoparticles

F contents (mol.%)	crystallite size (nm)
0	10.2
5	10.1
10	9.8
15	11.2
20	11.0

Figure 4.5 (a) and (b) show EDX analysis of undoped and F-doped SnO_2, respectively. In Figure 4.5(a), the major elements found in EDX result are Sn and O. The existence of Cu is resulted from the Cu grid used in TEM and EDX measurement. Meanwhile the EDX result of F-doped sample as seen in Figure 4.5(b) indicates the existence of fluorine in SnO_2 nanopowder. TEM images and selected area electron diffraction (SAED) patterns of undoped and F-doped SnO_2 nanoparticles are illustrated in Figure 4.6. The TEM images of SnO_2 nanoparticles exhibit excellent dispersion with less agglomeration and uniformity of particle size in the range of 10-13 nm. It is suggested that the good dispersion of the particles is obtained by the aid of ultrasonic energy supplied during synthesis. The SAED of F-doped SnO_2 nanoparticles exhibits several strong halo rings confirming to polycrystalline structure and the brightest inner ring attributes to the (110) plane of SnO_2 structure. The halo ring has reciprocal relation with space between crystallite planes (d-spacing) [57]. The d-spacing of undoped and F-doped SnO_2 nanopowder was calculated from halo ring of (110) plane and found to be 0.33 nm and 0.39 nm, respectively. The particles size and d-spacing of samples obtained from TEM images are in harmony with XRD results. This feature is probably caused by the substitution of oxygen sites by fluorine ions.

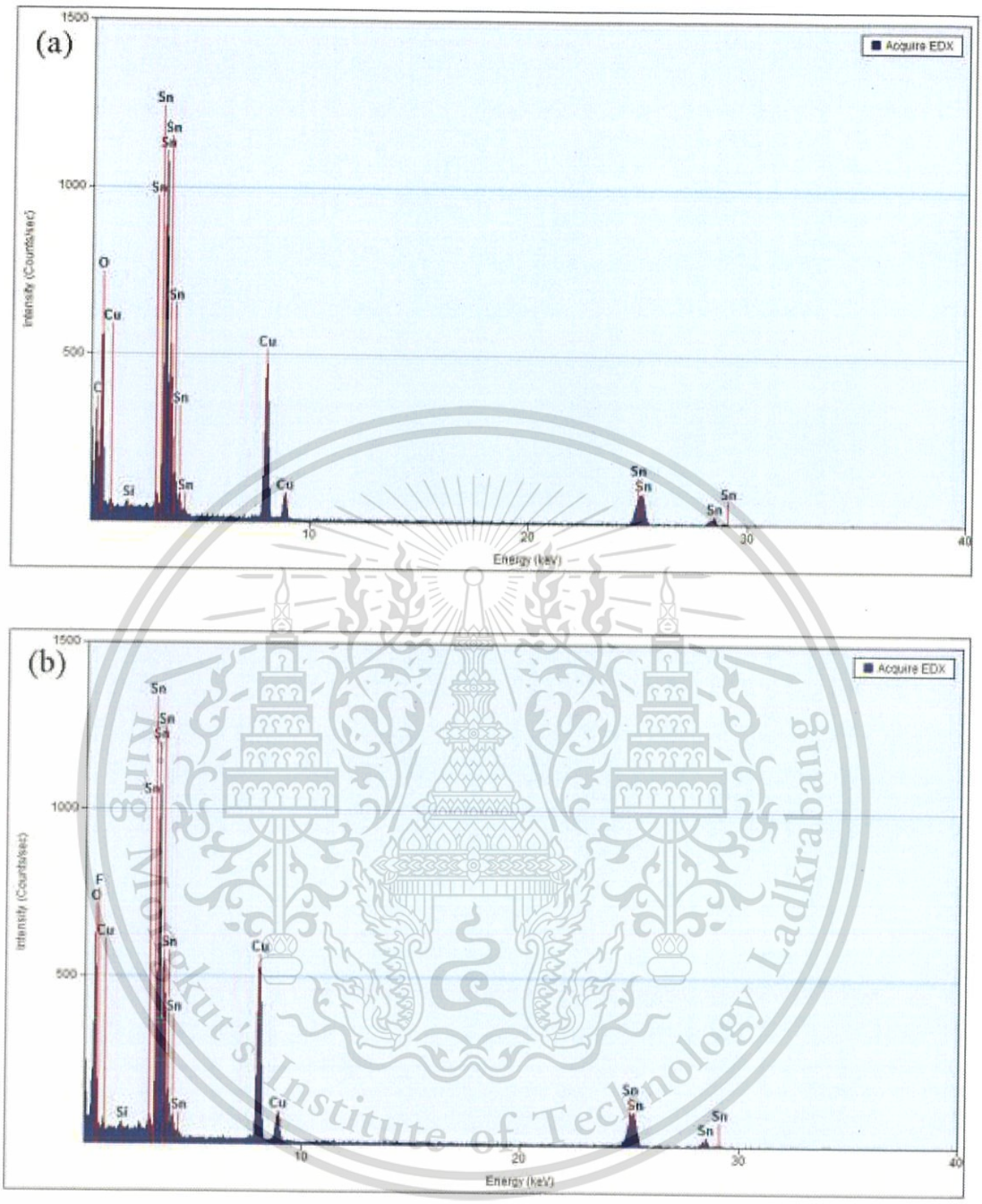

Figure 4.5 EDX analysis of (a) undoped and (b) F-doped SnO_2 nanoparticles.

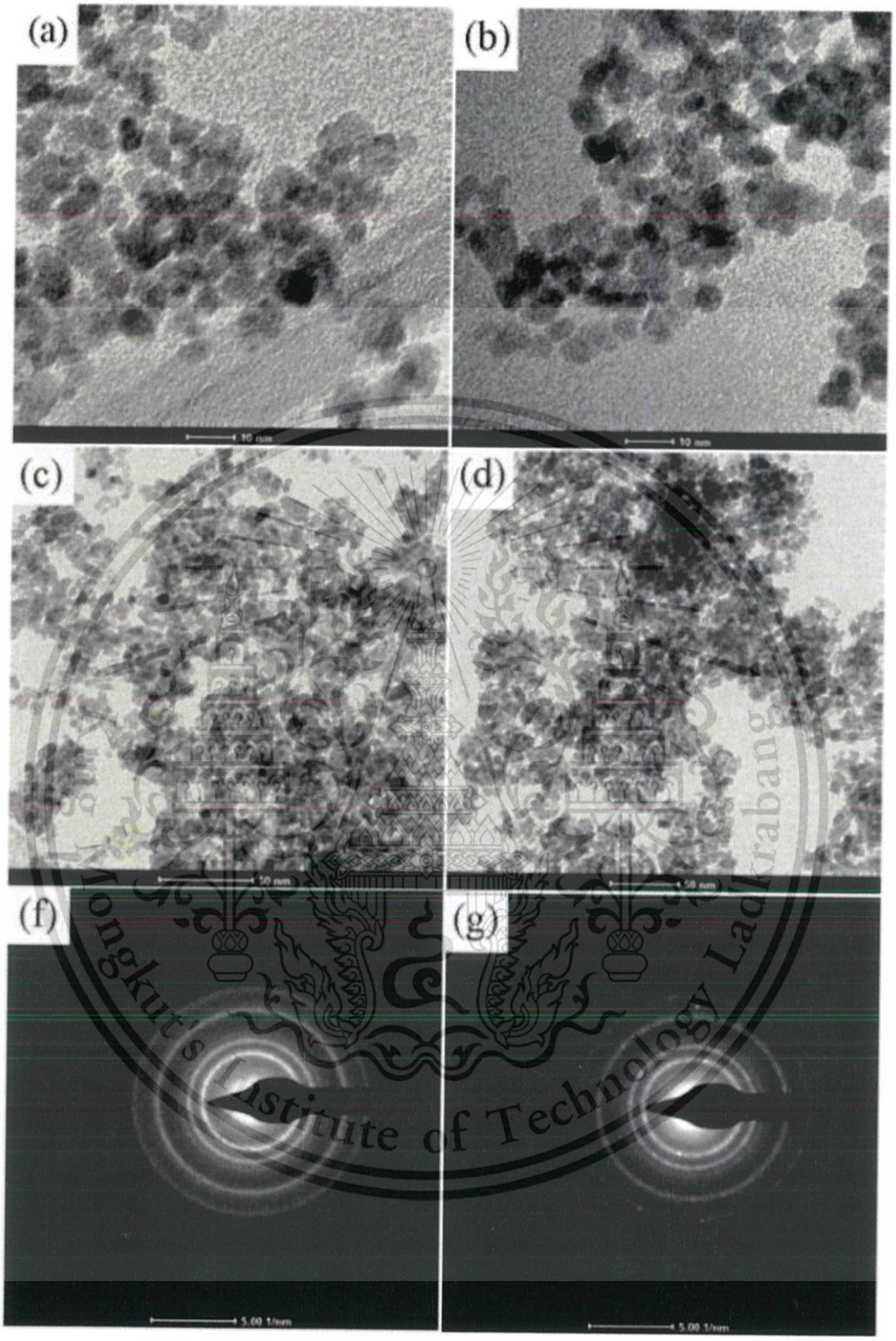

Figure 4.6 TEM images and SAED patterns of (a,c,f) undoped and (b,d,g) F-doped SnO_2 nanopowder.

4.3 Sb-doped SnO_2 nanoparticles via sonochemical assisted precipitation

Figure 4.7 shows the XRD patterns of as-synthesized ATO nanoparticles prepared via sonochemical-assisted precipitation process. The broad diffraction peaks of samples possess the major peaks of (110), (101), (211) and (301) plane orientations corresponding to tetragonal SnO_2 crystal structure [58]. It is implied that as-synthesized product obtained by this synthetic method comprises primarily polycrystalline phase of SnO_2 structure. The formation of crystalline phase of SnO_2 during sonochemical process without applying any thermal treatment could be occurred by cavitation effect during ultrasonic radiation though a precipitate solution. Under intense ultrasound irradiation, rapid collision driven by strong ultrasound energy can generate localized high temperature area, which can expedite the condensation reactions of hydroxyl groups to produce the nucleation of fine spherical nanoparticles of SnO_2 according to chemical reactions [59].

$$Sn(OH)_4 \xrightarrow{ultrasonic\ \ radiation} SnO_2 + 4H_2O. \tag{4.4}$$

This result indicates that the as-synthesized powder in SnO_2 phase can be obtained by single step sonochemical-assisted process. In addition, the sharpness and intensity of diffraction peaks drastically increase after calcinations at 400°C, reflecting that the crystallization of the oxide compounds tends towards more integrity with grater crystallite size. The average crystallite sizes of all nanoparticles were calculated from the peaks of (110) and summarized in Table 4.2. The smallest crystallite size of ~2.4 nm was obtained from as-synthesized product, while the crystallites become larger in size after calcinations due to the thermal energy promoted crystallite growth.

Table 4.2. The average crystallite sizes of all nanoparticles were calculated from the peaks of (110)

Sb concentrations (mol.%)	as-synthesized D (nm)	Calcination D (nm)
0%	2.64	11.6
1%	2.25	-
5%	2.59	9.33
10%	2.71	7.65
15%	3.71	-
20%	3.27	6.99

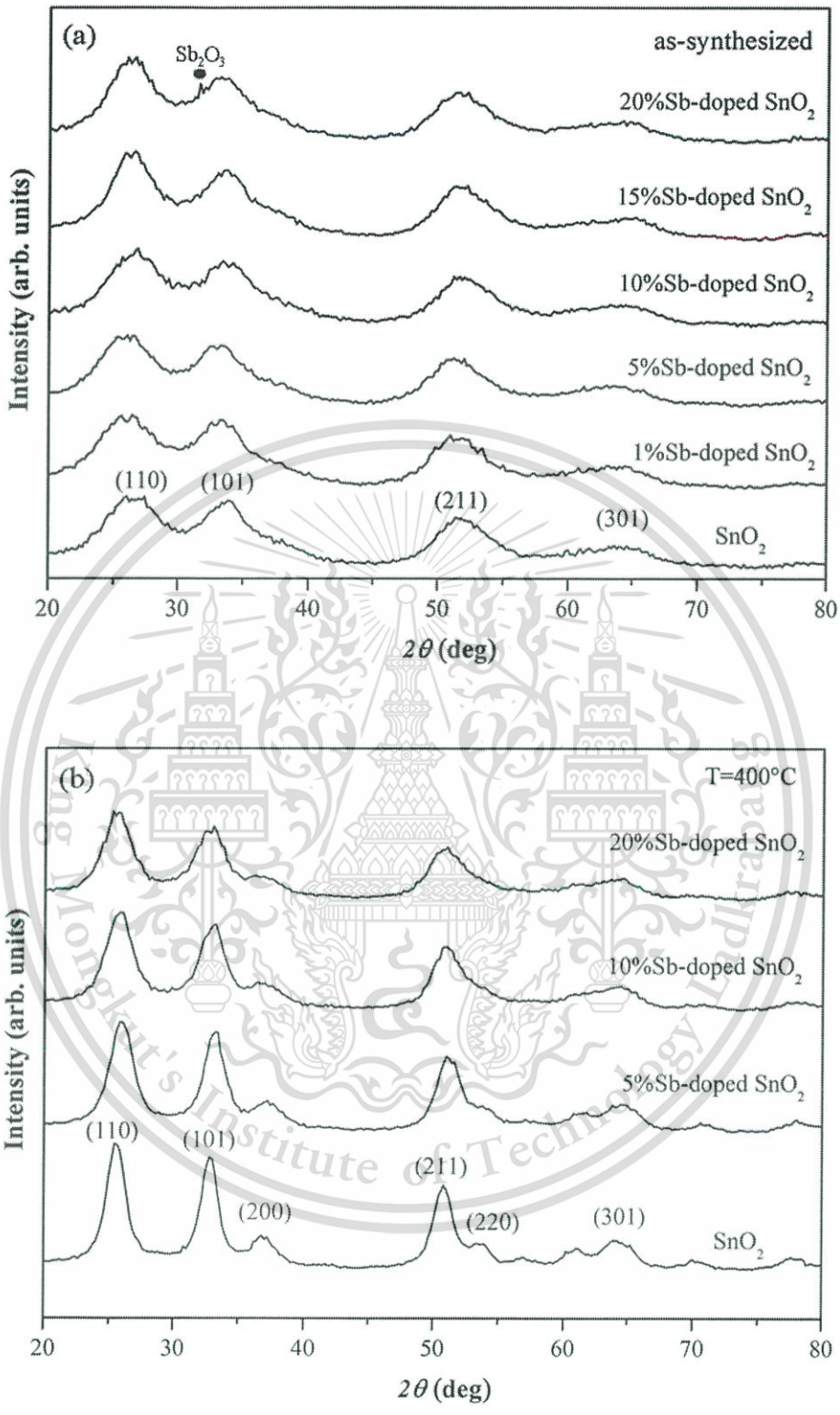

Figure 4.7 XRD patterns of Sb-doped SnO_2 nanoparticles with different Sb concentration (a) as-synthesized (b) after calcinations at 400°C.

From Figure 4.7 (a), relative intensities of all peaks reveal only diffraction peak of pure SnO_2 phase until Sb doping concentration was arised to 15 mol.%. An increase of Sb concentration up to 20 mol.%, Sb segregation was observed in phase of Sb_2O_3 [60]. The Possibility of Sb incorporated into the SnO_2 lattice was replaced by two oxidation states of Sb^{3+} which has a lager ionic radius (r = 0.76 Å) and Sb^{5+} which has a smaller ionic radius (r = 0.62 Å) than Sn^{4+}(r = 0.69 Å) [38]. A part of the Sb^{5+} is able to easily substitute into the tin oxide lattice since Sb^{5+} has a similar ionic radius to Sn^{4+} state. On the other hand, the substitution of Sb^{3+} state is more difficult to occur resulting the existence of detectable Sb_2O_3 phase. By calculation, the crystallite size of as-synthesized ATO nanoparticles decreases as Sb concentration is less than 5 mol.% and increases from 2.64 to 3.27 nm when Sb concentration is raised to 10 mol.%. This critical feature may derive from the truth that the Sb^{3+} state could occupy interstitial sites of SnO_2 lattice due to Sb^{3+} has a lager ionic radius to Sn^{4+} state causing in a large number of dislocations [61]. Therefore, the phase of Sb_2O_3 was observed since Sb^{5+} may probably be reduced to Sb^{3+} after Sb concentration up to 20 mol.%. After calcinations, this phase weakens and finally disappears due to the instability of Sb^{3+} with rather big ionic radius in the expanded crystallite size of SnO_2 structure. However, XRD patterns and crystallite size of ATO nanoparticles become weakened appearance with increasing Sb content, suggesting that Sb dopant could prevent the SnO_2 crystallite growth.

In Raman active mode, the spectra of as-synthesized Sb-doped SnO_2 nanoparticles are illustrated in Figure 4.8 (a). For as-synthesized nanoparticles, the Raman peaks located at 477 and 575 cm^{-1} are observed, which is attributed to the vibration of oxygen in the oxygen plane and small size effect of SnO_2 particle, respectively [62]. The peak position at 576 cm^{-1} is not detected obviously on Raman spectra after Sb concentration increases up to 10 mol.%. This effect may come from the segregation of Sb^{3+} state occupied interstitial sites of SnO_2 lattice, resulting in bigger crystallite size as seen in Table 4.2. In Figure 4.8 (b), it is suggested that the thermal energy provided by calcination process not only results to the disappearance of the Raman peak at 576 cm^{-1} but also influences appearance of Raman peak at 627 cm^{-1}. This peak can be attributed to the symmetric Sn-O stretching mode in nanocrystalline SnO_2, suggesting the better crystallinity of the sample can be obtained by heat treatment. However, the peak intensity of symmetric Sn-O stretching mode is absent after Sb concentration increases, implying the presence of imperfect lattice sites. The Raman results of the Sb-doped SnO_2 nanoparticles synthesized by sonochemical-assisted precipitation process coincidently affirm the crystallite growth of nanopowder, which is in good agreement to XRD results.

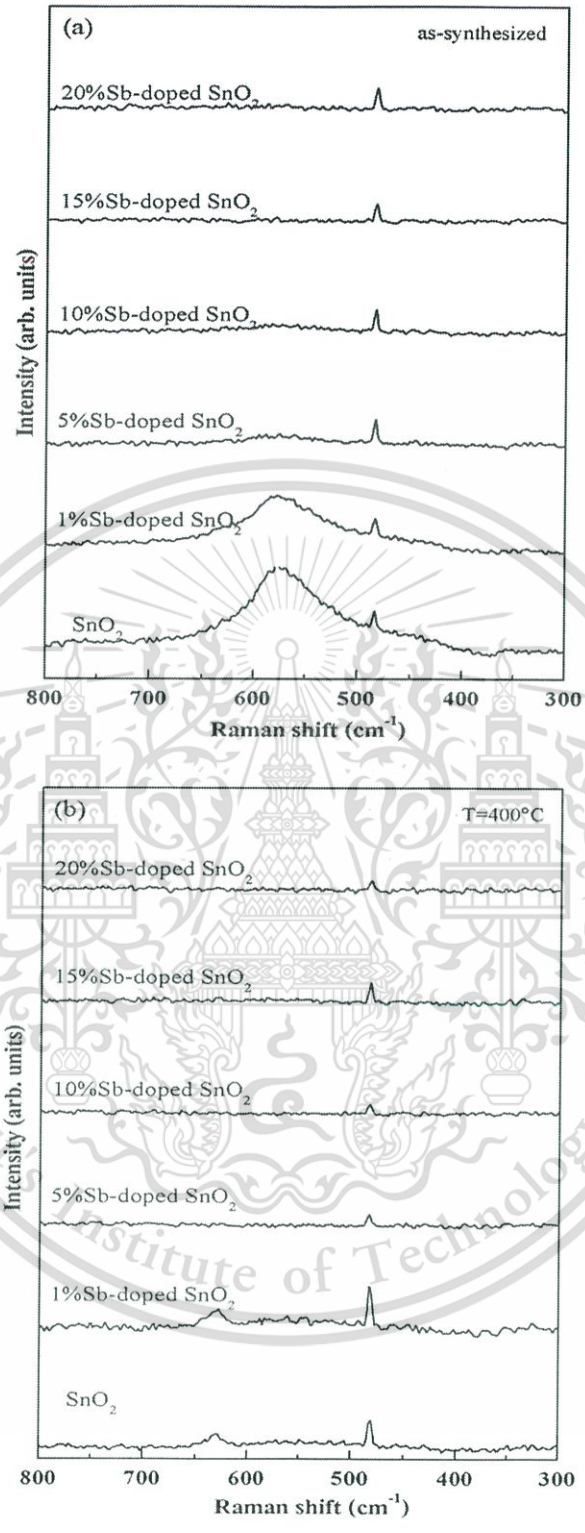

Figure 4.8 Raman spectra of Sb-doped SnO_2 nanoparticles with different Sb concentrations (a) as-synthesized (b) after calcinations at 400°C.

The TEM images and selected area electron diffraction (SAED) patterns of SnO_2 nanoparticles are illustrated in Figure 4.9 The image of as-synthesized powders as shown in Figure. 4.9 (a) is unable to identify general structure of small granular clusters. The SAED of SnO_2 nanoparticles exhibits several stronger halo rings than as-synthesized nanoparticles confirming to polycrystalline structure and the brightest inner ring attributes to the (110) plane of SnO_2 structure. It can be deduced that the crystallite growth of the nanoparticles are strongly affected by calcinations. Figure 4.9 (b) shows excellent dispersiveness with less agglomeration of the nanoparticles of the size estimated 10-13 nm. The good dispersion of the particles is obtained by the aid of ultrasonic energy supplied during synthesis. It is suggested that the sonochemical assistance not only provides energy for crystallite growth but also influences the formation process including nucleation, growth coagulation, and flocculation.

In order to gain insight of the nanoparticles, the chemical composition was analyzed by XPS. Figure 4.10 shows the XPS survey scan spectrum of ATO with 10 mol.% Sb content calcined at 400 °C, which contains the Sn3d, Sb3d, and O1s peaks. As seen in Fig. 4.10 (b), Sn3d spectra detected in two regions of 485-490 eV and 493-497 eV correspond to the spin orbital state of $3d_{5/2}$ and $3d_{3/2}$, respectively. The XPS spectrum in the binding energy range of 525-545 eV is masked by the O1s and Sb3d transition, which can be deconvoluted into O1s, $Sb3d_{5/2}$ and $Sb3d_{5/2}$ as shown in Figure 4.10 (c). The Gaussian line centered at 540.63 eV corresponds to the Sb^{4+} oxidation state resulting from the intervalence charge transfer as mixed Sb^{3+}-Sb^{5+}. The XPS spectra of Sb-doped SnO_2 also obviously confirm the existence of Sb^{3+} and Sb^{5+} incorporated into SnO_2 matrix.

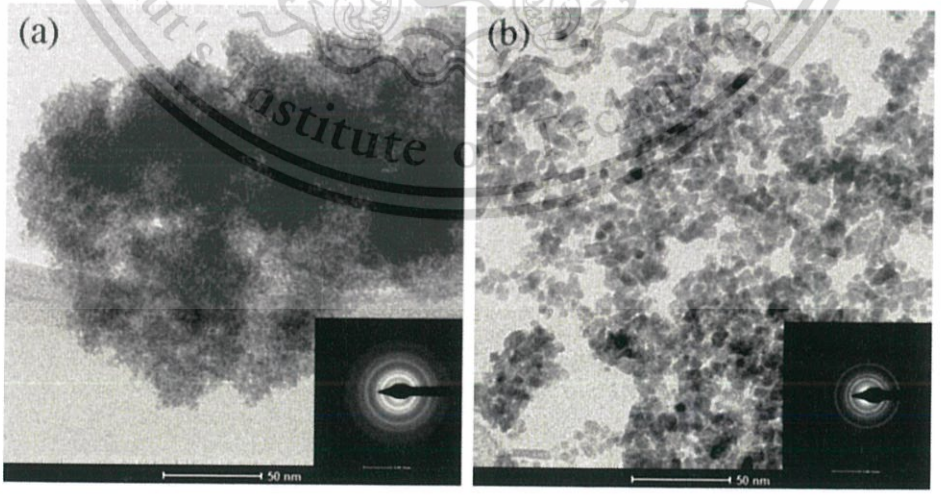

Figure 4.9 TEM images of SnO_2 nanoparticles (a) as-synthesized and (b) after calcinations at 400°C.

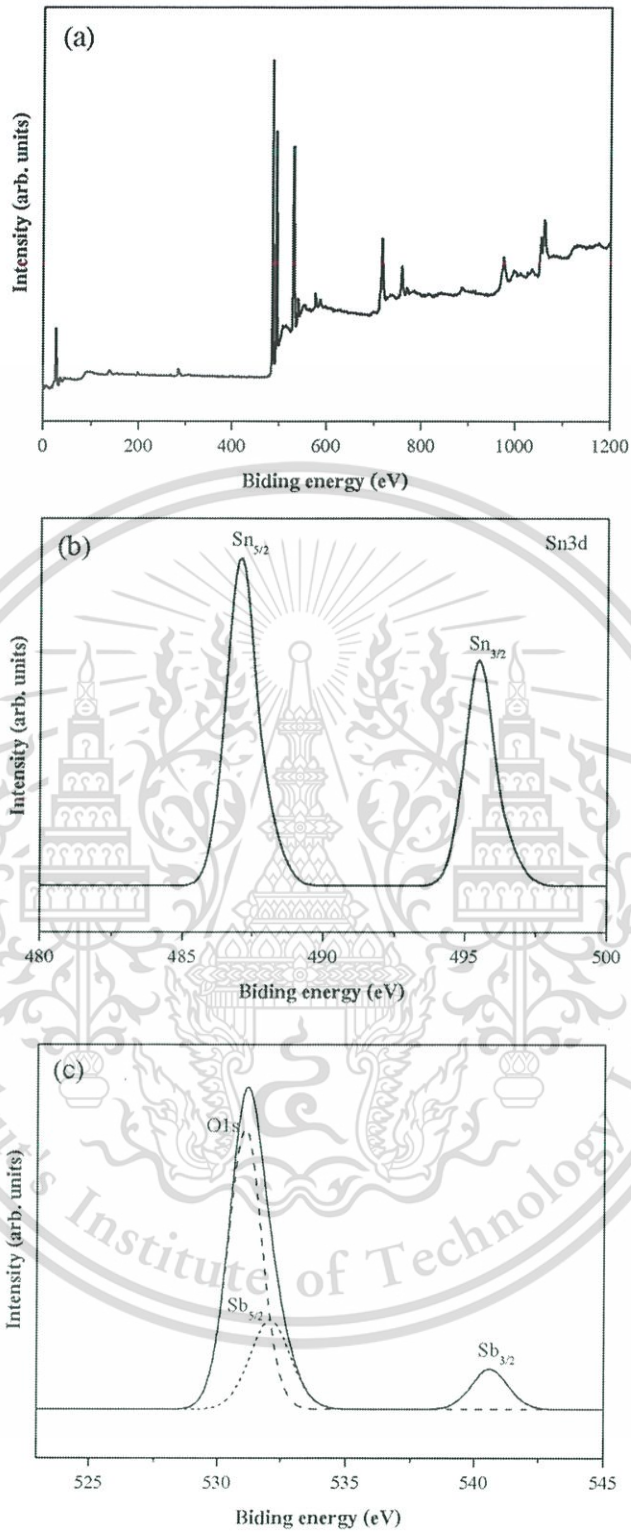

Figure 4.10 XPS spectra of Sb-doped SnO_2 nanoparticles with 10 mol.% (a) survey scan, (b) narrow scan of Sn3d, and (c) narrow scan of Sb 3d and O 1s.

Before resistance measurement, the Sb-doped SnO_2 nanoparticles were pressed in the form of pellet provided the increase in powder density and contacts between grains. The electrical resistance of nanoparticles with different Sb concentration is exhibited in Table 4.3. The high resistance of tin oxide was observed due to the oxygen vacancies of SnO_2 grains. When doping with Sb, the resistance of SnO_2 decreased dramatically, suggesting that the incorporation of Sb ions can enhance the conductivity of tin oxide. A minimum resistance value of 17.49 Ω was obtained by 5 mol.% Sb concentration and then the resistance slightly increases when Sb concentration was raised to 10 mol.%. The resistance of tin oxide can be reduced by Sb^{5+} incorporated into the SnO_2 lattice, causing the formation of donor levels appeared very close to the conduction band. These donor levels can consequently generate the extra electrons and promote the higher electron mobility into the conduction band as depicted in Fig. 4.11 (a). From XRD results, it is indicated that the phase of Sb_2O_3 can be obtained by the Sb^{5+} ions reduced to the Sb^{3+} state after excess antimony. The incorporation of Sb^{3+} ions into tin oxide can create the acceptor levels as shown in Figure 4.11 (b). Therefore, possibility of the free electrons may be trapped by the acceptor levels (Figure 4.11 (c)) leading to an increase the resistance of tin oxide. In addition, the increasing resistance can also be partially attributed to the excess antimony atoms build in the grain boundary regions which can potentially prevent the growth of SnO_2 nanocrystals [63], which is in good accordance with Raman results. These results reveal that the Sb incorporation with optimal concentration can produce lower resistance affected by the substitution of Sn^{4+} by Sb^{5+}.

Table 4.3 The electrical resistance of ATO nanoparticles.

Sb concentrations	Resistance (Ω)
0%	2190.58
1%	26.65
5%	17.49
10%	18.37
15%	57.86
20%	82.83

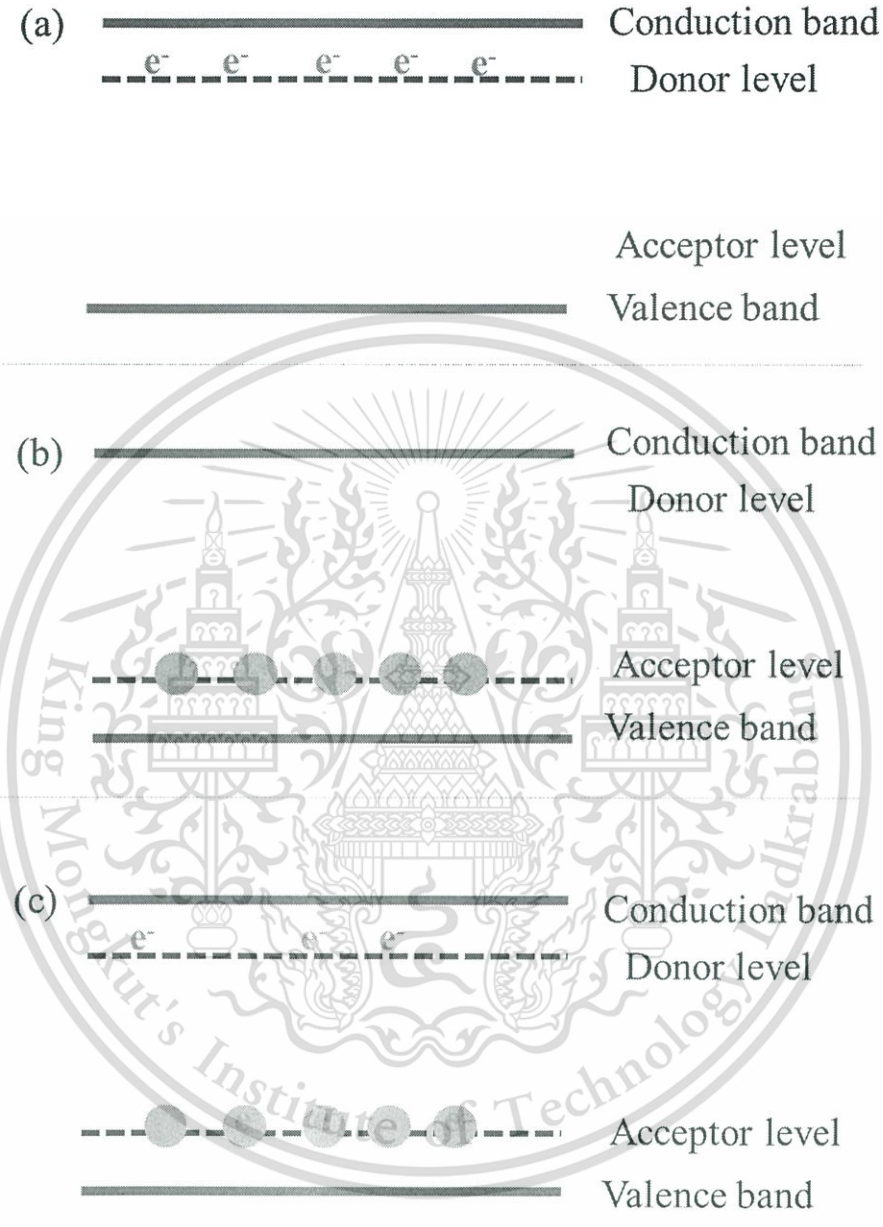

Figure 4.11 Band diagram of Sb ions incorporated into SnO_2 generating (a) donor levels by Sb^{5+}, (b) acceptor levels by Sb^{3+} and (c) the free electrons trapped by acceptor level.

4.4 F/Sb-doped SnO_2 nanoparticles via sonochemical assisted precipitation

Figure 4.12 (a) shows XRD patterns of as-synthesized samples and SnO_2 nanoparticles calcined at 400°C. For as-synthesized samples, there are noticeable diffraction peaks which are attributed to (110), (101) and (211) planes of SnO_2 with tetragonal rutile structure [64]. This result suggests that as-synthesized powder with primarily polycrystalline phase of SnO_2 ultrafine structure can be obtained by one-step sonochemical process without heat treatment process. The formation of crystalline phase of SnO_2 during sonochemical process could be initiated by cavitation effect during intense ultrasonic radiation via rapid collision forced by strong ultrasound energy. This collision is capable to rapidly elevate localized high-temperature area that can effectively quicken the condensation reactions of hydroxyl groups to produce the nucleation of fine nanoparticles of SnO_2 via according to chemical equation (1) and (4). Moreover, after calcinations at moderate temperature, it is observed that there is increasing intensity of all diffraction peaks, indicating that the better crystallinity of SnO_2 nanoparticles can be obtained by calcinations process.

XRD patterns of after-calcined FATO nanoparticles prepared via sonochemical process with various doping contents are exhibited in Figure 4.12 (b). Three prominent diffraction peaks positioned at $2\theta = 26.5°$, 34.0° and 51.9° are well-indexed to (110), (101), (211) plane orientations of tetragonal SnO_2 crystal structure, respectively. In addition, the other minor noticeable peaks situated at $2\theta = 38.0°$ and 65.3° are nicely ascribed to (200) and (301) planes of tetragonal SnO_2 structure, respectively [65]. This result suggests that the good crystallinity of tetragonal SnO_2 structure can be obtained via this synthesis method and moderate heat treatment. It is further noticed that their major peak intensities tend to decrease with increasing content of either dopant. The average crystallite size of FATO nanoparticles can be calculated from the full-width at half maximum (FWHM) of (110) most distinct peak by Scherrer's equation. It is found that the average size of the particle is ca. 10 nm indicating that tiny and uniform SnO_2-based nanoparticles can be achieved by sonochemical process. It is further interpreted from the XRD intensity that the crystallite size of FATO nanoparticles significantly changes with increasing doping content. These manners may originate from the difference in ionic radius of Sb^{3+} which has a lager ionic radius (r=0.76 Å) than that of Sn^{4+} (r=0.69 Å) and between that of fluorine ion (1.33 Å) and oxygen ion (1.33 Å) [66].

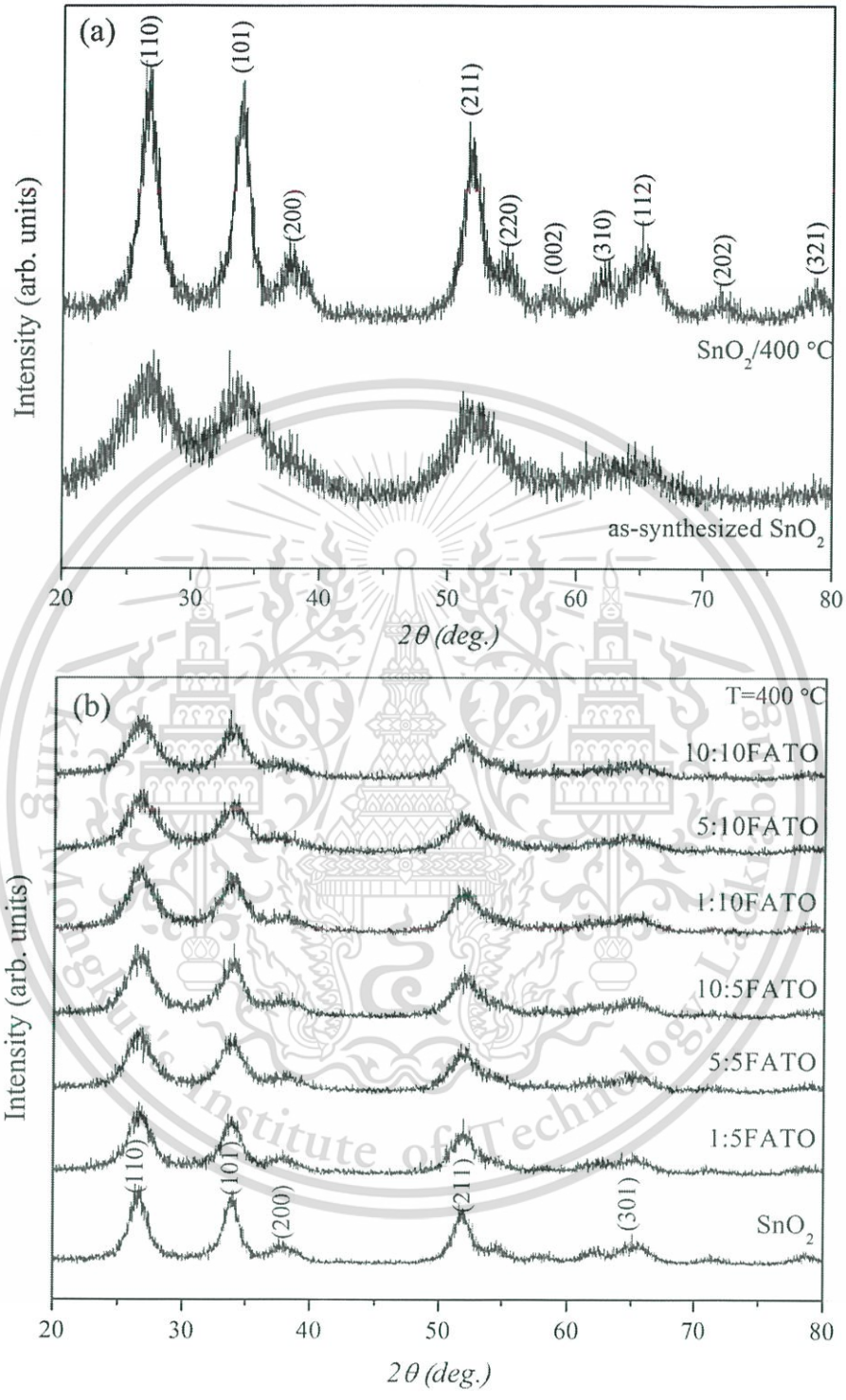

Figure 4.12 XRD patterns of (a) SnO_2 nanoparticles with different heat treatments and (b) FATO nanoparticle with different Sb and F concentrations.

The Raman spectra of SnO_2 nanoparticles with different heat-treated temperatures are illustrated in Figure 4.13 (a). For as-synthesized samples, the peaks observed at 484.89 and 576.76 cm^{-1} are attributed to the E_g vibration mode and the small size effect of nanocrystalline SnO_2 [56]. The doubly degenerated E_g mode is related to the vibration plane of oxygen in the direction of the c-axis. After calcined at 400°C, the fundamental Raman peaks of rutile SnO_2 at 633.51 and 774.25 cm^{-1} are observed, that is attributed to A_{1g} and B_{2g} vibration modes. Both peaks are corresponded to non-degenerate phonon modes vibrating in the plane perpendicular to the c-axis corresponding the expansion (A_{1g}) and contraction (B_{2g}) vibration of Sn-O bonds [67].

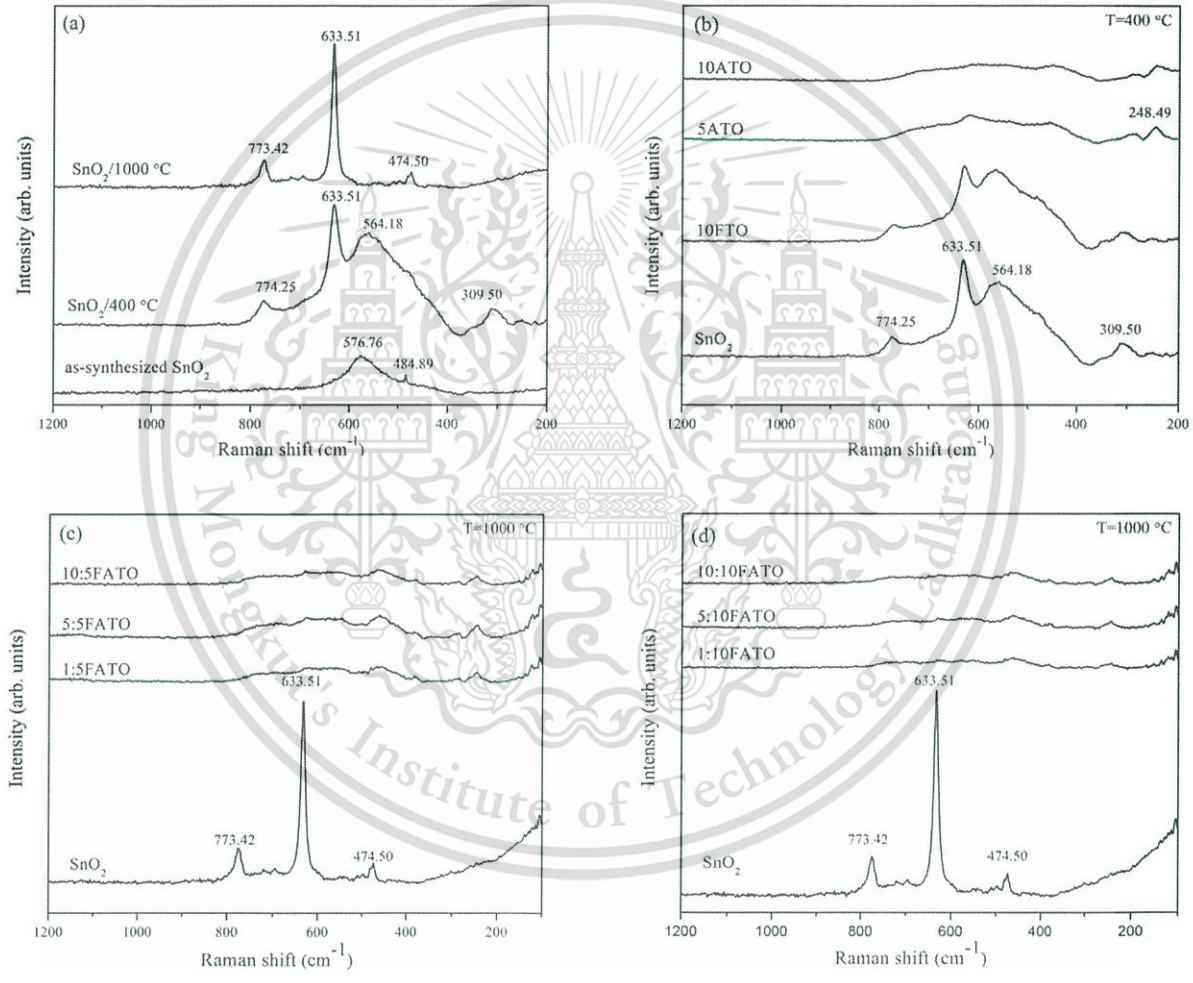

Figure 4.13 Raman spectra of SnO_2 nanoparticles with (a) different heat treatments, (b) Sb and F doping, (c) FATO at 5 mol.% Sb content and (d) FATO at 10 mol.% Sb content with different F concentrations.

Moreover, the broad peak around 400-600 cm^{-1} may originate from combination of E_g vibration mode and nanocrystalline SnO_2 system mode, whereas the peak at 309.50 cm^{-1} can be correlated to the E_u transverse optical mode. All vibration peaks are Raman active mode except in the E_u mode which is Raman-inactive caused by disorder at the interface between crystals [68]. Three fundamental Raman peaks positioned at 474.50, 633.51 and 773.42 cm^{-1} are clearly observed in the sample sintered at 1000°C. These peaks are assigned to the three characteristic spectra of rutile SnO_2 single crystal, suggesting the better crystallinity of the sample can be obtained by heat treatment. In addition, Raman spectroscopy is an important tool to confirm structural defect affected by the Sb and F substituted into SnO_2 lattice on vibrational properties. The Raman spectra of FTO and ATO nanoparticles calcined at 400°C are shown in Figure 4.13 (b). Raman result of FTO sample exhibits three fundamental Raman peaks with decreasing intensity of Sn-O bond due to the proper substitution of F ion at O site without significant alternation of SnO_2 local structure. On the other hand, three fundamental Raman peaks are evidently absent by the incorporation of Sb, implying the presence of imperfect lattice sites due to the improper substitution of Sb ion or other local defects in SnO_2 crystal [69]. This manner implies that the F and Sb dopant substitution in SnO_2 lattice results in vacant lattice site or oxygen vacancies and lattice distortion. In Fig. 2 (c) and (d), Raman spectra of codoped samples are disappeared after sintering at 1000°C, implying the presence of imperfect lattice sites and intensive reduction in lattice space symmetry.

The surface chemical characteristics of the FTO, ATO and FATO nanoparticles were analyzed by XPS. All the binding energy (BE) calibration of the spectra were referenced to the C1S peak located at 285.0±0.1 eV. Figure 4.14 (a) shows the XPS survey scan spectrum of FATO sample calcined at 400°C, indicating that the sample consists of the Sn3d, Sb3d, F1s and O1s peaks. As seen in Figure 4.14 (b), Sn3d spectra detected in two regions of 485-490 eV and 493-497 eV correspond to the spin orbital state of $3d_{5/2}$ and $3d_{3/2}$, respectively [22]. In the Sn3d spin orbital spectrum, the peak intensity of Sb-doped sample become lower and shifts to the higher binding energy than that of F-doped sample as observed in Figure 4.14 (b). The substitution of F^- anion at O^{2-} anion and Sb^{5+} or Sb^{3+}cations at Sn^{4+} site can lead to the creation of greater amount of free electrons [70]. These results indicate that Sb dopant has dominance on the decrease in peak intensity of Sn3d than F dopant and the shift in binding energy reflects to more oxidization by the dopant.

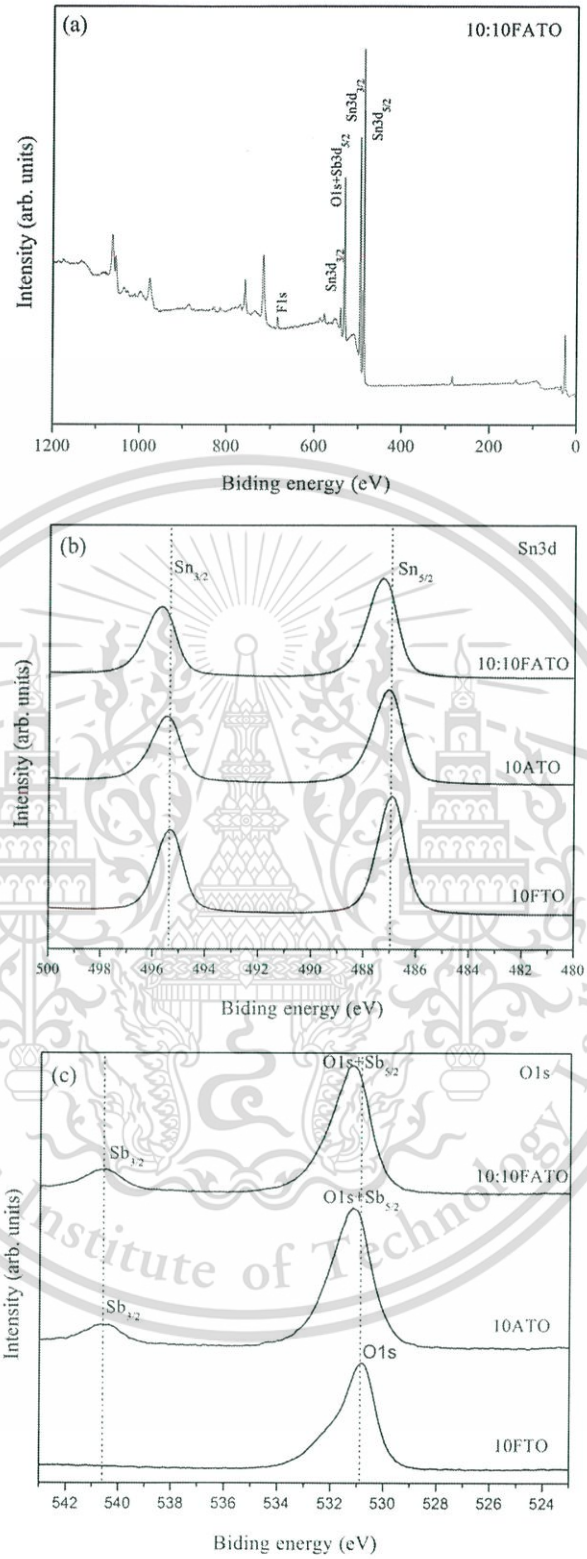

Figure 4.14 XPS spectra of FATO SnO_2 nanoparticles (a) survey scan, (b) narrow scan of Sn3d and (c) narrow scan of Sb3d+O1s.

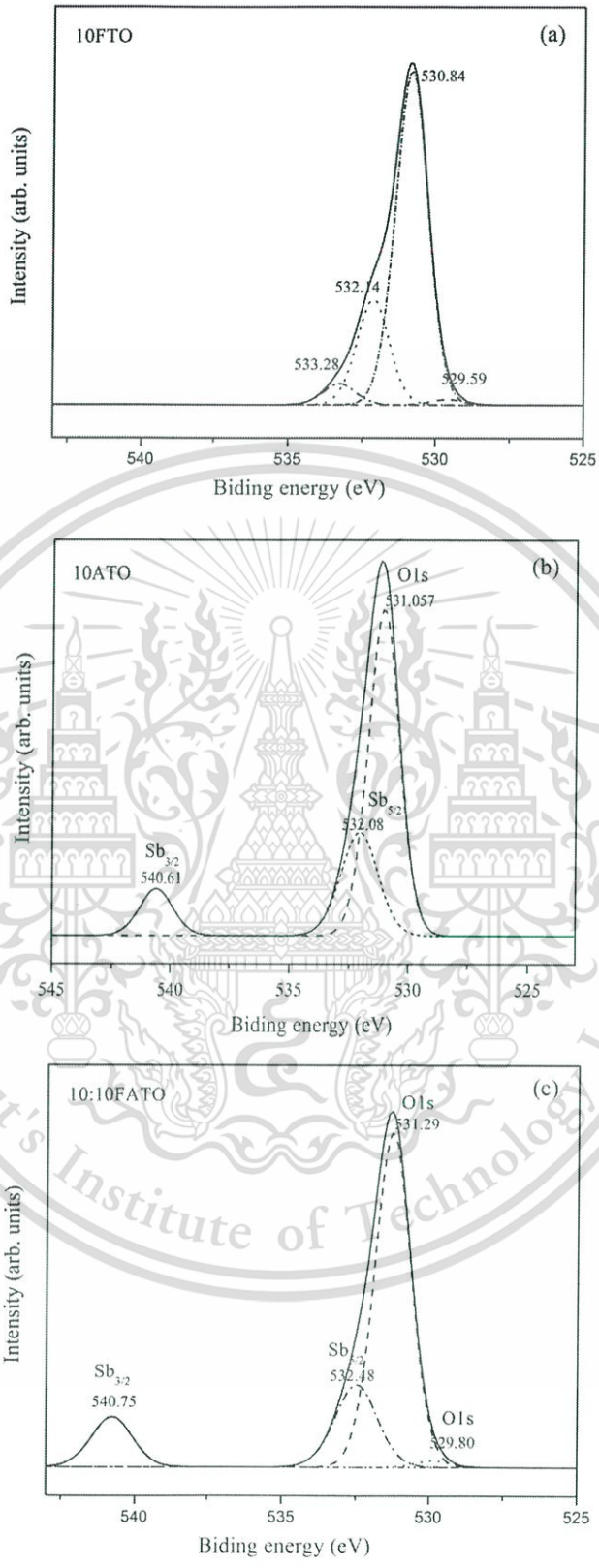

Figure 4.15 O1s deconvolution of (a) FTO, (b) ATO and FATO nanoparticles.

In narrow scan spectra, the orbital state of $Sb3d_{5/2}$ is masked by the O1s in binding energy range of 528-535 eV but $Sb3d_{5/2}$ is clearly observed at 540 eV for both samples except in FTO sample. Alternative way to study the defects in the lattice is to analyze the change at the binding energy level of O1s as noticed in Figure 4.15. The O1s core level line can be deconvoluted into four peaks components centered at 529.59 eV, 530.84 eV, 532.14 eV and 533.28 eV. The peak center at 529 eV is attributed to O^{2-} in lattice of SnO_2 structure implying a fully oxidized stoichiometric environment, while the main peak at 531 eV is associated with O ion in the oxygen deficient regions or oxygen vacancies in the lattice [71]. The binding energy at 532 eV is the combination of chemisorbed oxygen of OH^- groups on surface with orbital state of $Sb3d_{5/2}$ in Sb doped sample. The peak position of O1s is shifted to high binding energy, suggesting that the more oxygen vacancies are generated by Sb incorporated into SnO_2 structure [72]. The peak located at 533 eV is observed only in the FTO sample, which is associated with adsorbed oxygen of H_2O or CO_3 on surface of sample indicating the more hygroscopic in nature [73]. The XPS results affirm that F ions and Sb ions incorporated into the SnO_2 lattice are able to effectively provide more oxygen vacancies in the doped sample.

TEM images and selected area electron diffraction (SAED) patterns of FTO, ATO and FATO nanoparticles are illustrated in Figure 4.16. As seen in Figure 4.16 (a), the morphologies and particle size of as-synthesized SnO_2 nanoparticles are unable to identify due to general structure of small granular clusters as well as the SAED patterns show soft halo rings reflecting their amorphosity in nature. The TEM image indicates that the SnO_2 nanoparticles are excellent dispersed with less agglomeration and uniformity of particle shape which appear in spherical shape with estimated size of less than 10 nm after calcination at 400°C. The SAED of SnO_2 nanoparticle exhibits several strong halo rings confirming to polycrystalline structure and the brightest inner ring attributes to the (110) plane of SnO_2 structure, which is consistent with XRD results. It can be deduced that the crystallite growth of the nanoparticles are highly affected by heat treatment. From TEM images, it is suggested that the F dopant has slight effect on morphologies and particle sizes of SnO_2 particles while Sb dopant provide significant influence on SnO_2 structure. In addition, the morphologies of FATO particles display many spherical shaped grains formed by aggregation of nanocrystalline.

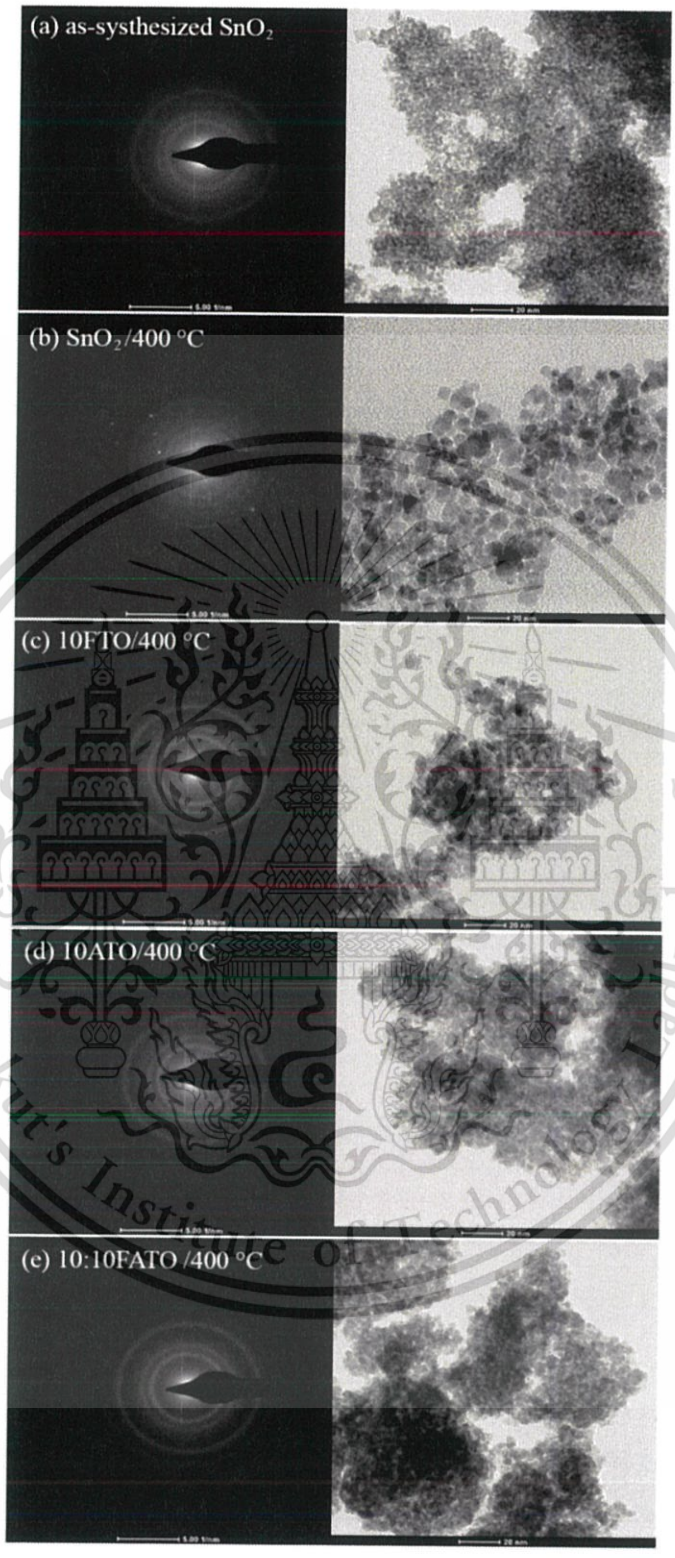

Figure 4.16 SEAD patterns and TEM images of (a) as-synthesized SnO_2 (b) SnO_2, (b) FTO, (c) ATO and (d) FATO nanoparticles.

The resistivity (ρ) and carrier concentration (n) of FATO samples are exhibited in Table 4.4. The high resistance of tin oxide is observed, while the resistivity of FTO sample decreases considerably from 10.45 Ω·cm to 13.6 Ω·cm. This feature is originated from the fact that fluoride ion incorporated in SnO_2 can contribute one exceeding free electron to SnO_2 leading to the reduction in electrical resistivity [56]. For ATO sample, its resistivity decreases dramatically down to 5.03×10^{-3} Ω·cm and 5.43×10^{-2} Ω·cm for the samples with Sb concentration of 5 mol.% and 10 mol.%, respectively. This feature is due to Sb ions incorporated into the SnO_2 lattice causing the formation of donor levels appeared very close to the conduction band [61]. These donor levels can consequently generate the extra electrons and promote the higher electron mobility into the conduction band. Both F and Sb doped SnO_2 samples can promote the higher electron mobility as shown in Table 4.4. It is observed that the lower resistivity and good carrier density are obtained as the Sb content reaches a specific content of 5 mol.%. However, the resistivity slightly increases after the Sb concentration augmented beyond 10 mol.% in the SnO_2 lattice owing to possibility of the free electrons trap by the acceptor levels. This level is created by Sb^{3+} ion incorporated in Sn^{4+} site in SnO_2 lattice when the doping exceeds the specific value [74] that can initiate the oxidation reduction of Sb^{5+} to Sb^{3+}. In addition, the resistivity greatly decreases with F/Sb codoped in SnO_2 structure due to the co-existence of oxygen vacancies and substituted Sn producing the extra electrons and the higher electron density [75]. The limitation of F:Sb codopant ratio is 1:5 mol.% providing the lowest resistivity at 3.96×10^{-3} Ω·cm. Nevertheless, the free carrier density decreases with increasing F concentration due to the Sn-F complexes formed in the grain boundaries, leading to a slight increase in the resistivity. These results reveal that the F/Sb co-incorporation in SnO_2 structure can considerably increase its carrier mobility and conductivity. Diffuse reflectance spectra of SnO_2, FTO, ATO and FATO nanoparticles in the form of pellet are shown in Figure 4.17 (a). The reflectance spectra show the sharp absorption edge in the wavelength region of 250-350 nm implying semiconductor behavior with the existence of direct optical band gap. The corresponding optical band gap could be estimated by Tauc's method. In direct transition semiconductors, the optical absorption coefficient and the optical energy band gap is expressed as [76]:

$$(\alpha h\nu) = A(h\nu - E_g)^{1/2} \tag{4.5}$$

where E_g is optical band gap, $h\nu$ is photon energy and A is constant. α is absorption coefficient which is substituted with $F(R_\infty)$. Thus the relational expression becomes:

$$(h\nu F(R_\infty))^2 = A(h\nu - E_g)^{1/2} \quad , \tag{4.6}$$

where $F(R_\infty)$ is absorption coefficient which is obtained from the acquired diffuse reflectance spectrum using Kubelka-Munk function [77]:

$$F(R_\infty) = \frac{(R_\infty - 1)^2}{2R_\infty} \quad , \tag{4.7}$$

where R_∞ is the diffuse reflectance. The optical band gap energies were interpreted from the interception of the straight section to energy axis as shown in Figure 4.17 (b) and (c). In Figure 4.17 (b) and (c), the optical band gap of SnO_2 sample increases from 3.83 eV to 3.85 eV after fluoride doping and dramatically increases to 3.90 eV and 4.04 eV for 10ATO and 1:5FATO sample, respectively. The extended optical band bap of SnO_2 samples after F, Sb incorporation may be ascribed to Bursstein-Moss effect as a result of the increase of carrier concentration. Increasing carrier concentration will cause the alternation of Fermi level moving into the conduction band leading to a broadened optical band gap [78].

Table 4.4 The resistivity and carrier density of samples by Hall measurement.

Samples	Resistivity (Ω cm)	Carrier Density ($1/cm^3$)
SnO_2	14.5	1.35×10^{16}
10FTO	13.6	3.88×10^{17}
5ATO	5.03×10^{-3}	1.04×10^{18}
10ATO	5.43×10^{-2}	4.36×10^{17}
1:5FATO	3.96×10^{-3}	1.27×10^{18}
5:5FATO	5.61×10^{-3}	1.01×10^{18}
10:5FATO	4.82×10^{-3}	3.46×10^{17}
1:10FATO	6.05×10^{-2}	2.72×10^{17}
5:10FATO	1.03×10^{-1}	3.25×10^{17}
10:10FATO	7.15×10^{-2}	9.92×10^{17}

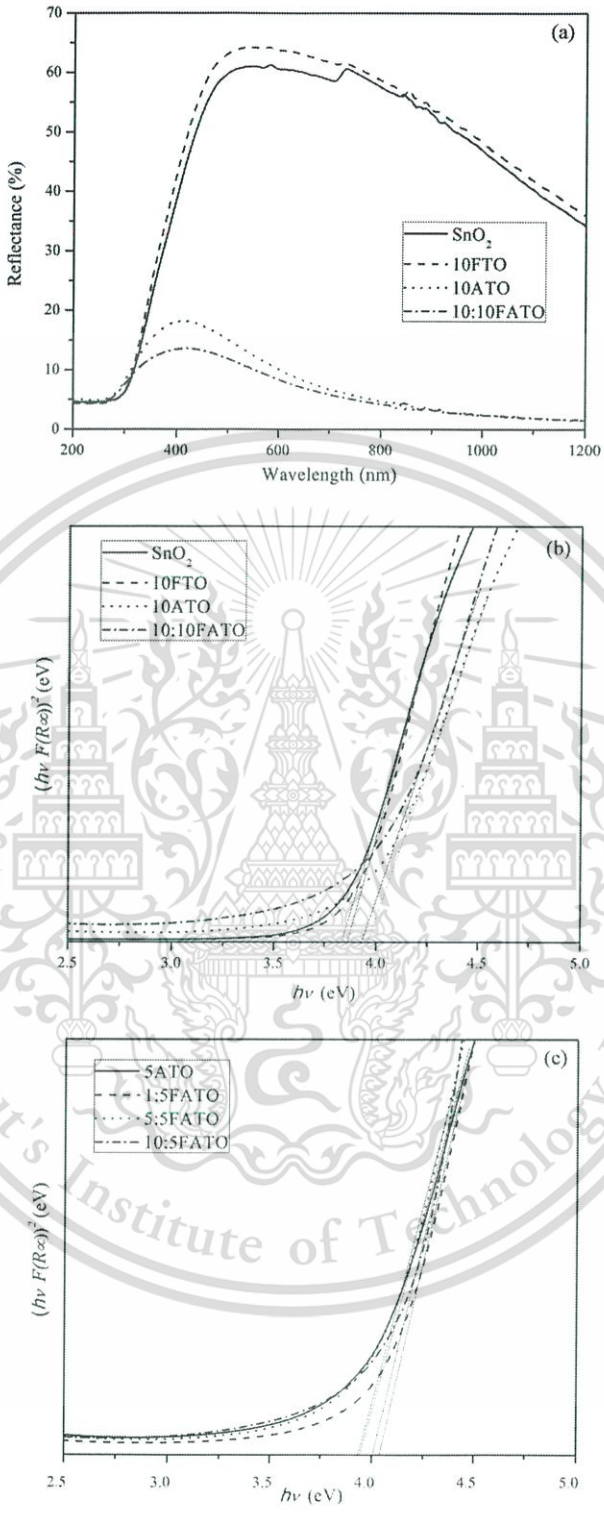

Figure 4.17 (a) Diffuse reflectance spectra and (b) The $(h\nu F(R_\infty))^2$ vs. $h\nu$ curves of SnO_2, FTO, ATO, FATO. (c) The $(h\nu F(R_\infty))^2$ vs. $h\nu$ curves of FATO at 5mol.% Sb with different F concentrations .

4.5 Composite film used as IR-shielding layer for Solar cell

Diffuse reflectance spectra of FTO, ATO nanoparticles were measured in the pellet form (Figure 4. 18) with different amounts of dopant as shown in Figure 4.19 (a) and (b), respectively. The noise spectra in the range of 750-1000 nm were occurred from instrument. The reflectance spectra of FTO nanoparticles exhibited identical characteristic of SnO_2 which is an interband transition at ~400 nm, high reflection in visible region and weak absorption in the IR region. In the other hand, the reflectance spectra of ATO nanoparticles demonstrate the low reflection in visible region and strong absorption in the IR region. Because the ATO nanoparticles appear a blue color attributed to plasma excitation of free carriers and the strong absorption in IR region. Reflectance spectra of F(x):5FATO and F(x):10FATO nanoparticles are exhibited in Figure 4.20. The results reveal that the reflectance spectra of FATO nanoparticles show similarly characteristic spectra of ATO nanoparticles. Nevertheless, the spectra exhibit the higher reflection in the visible region and deeper absorption in IR region after F incorporation in ATO nanoparticles.

Figure 4.18 Image of all nanoparticles in the pellet form.

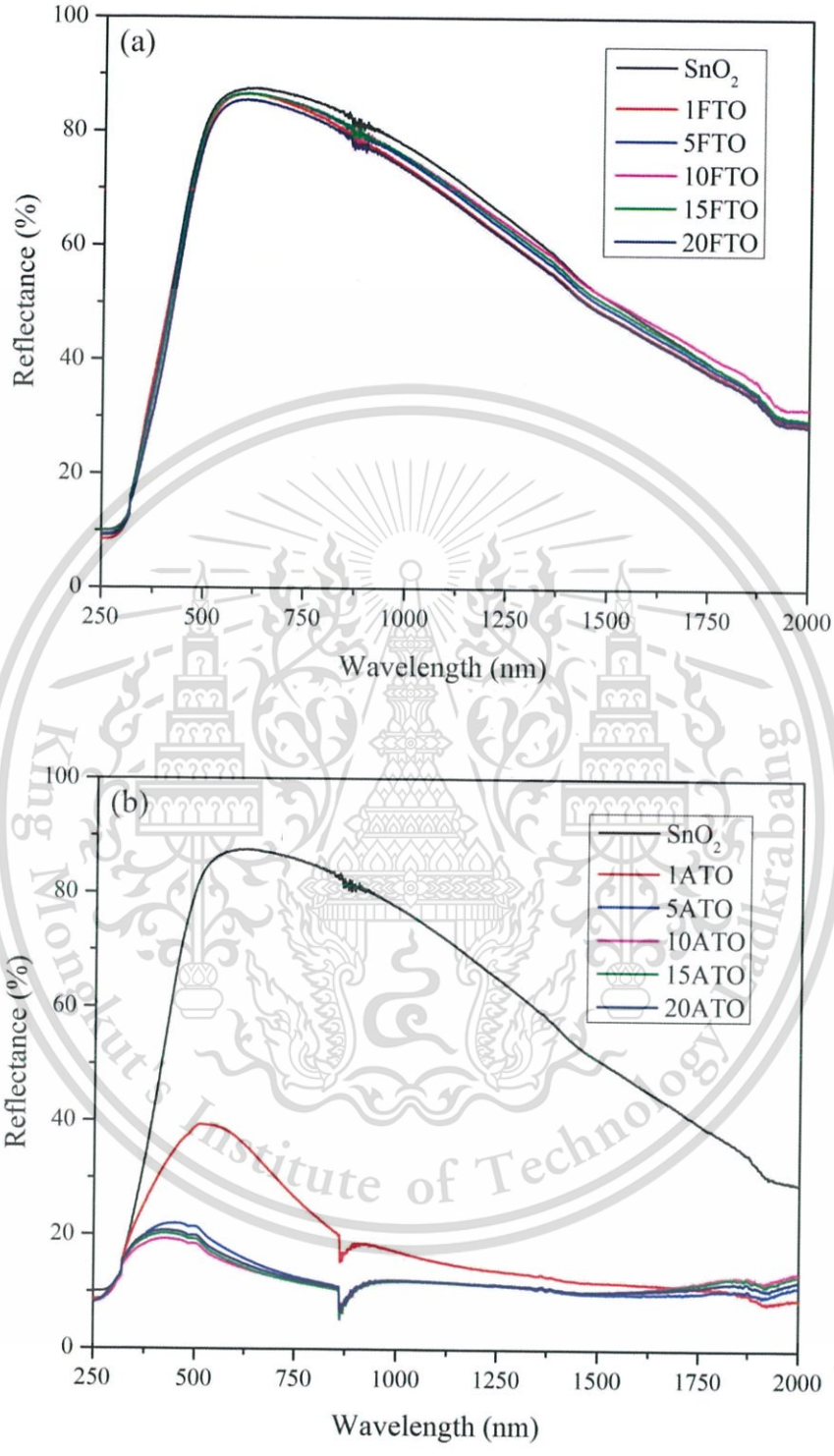

Figure 4.19 Diffuse reflectance spectra of (a) FTO and (b) ATO with different F and Sb composition, respectively.

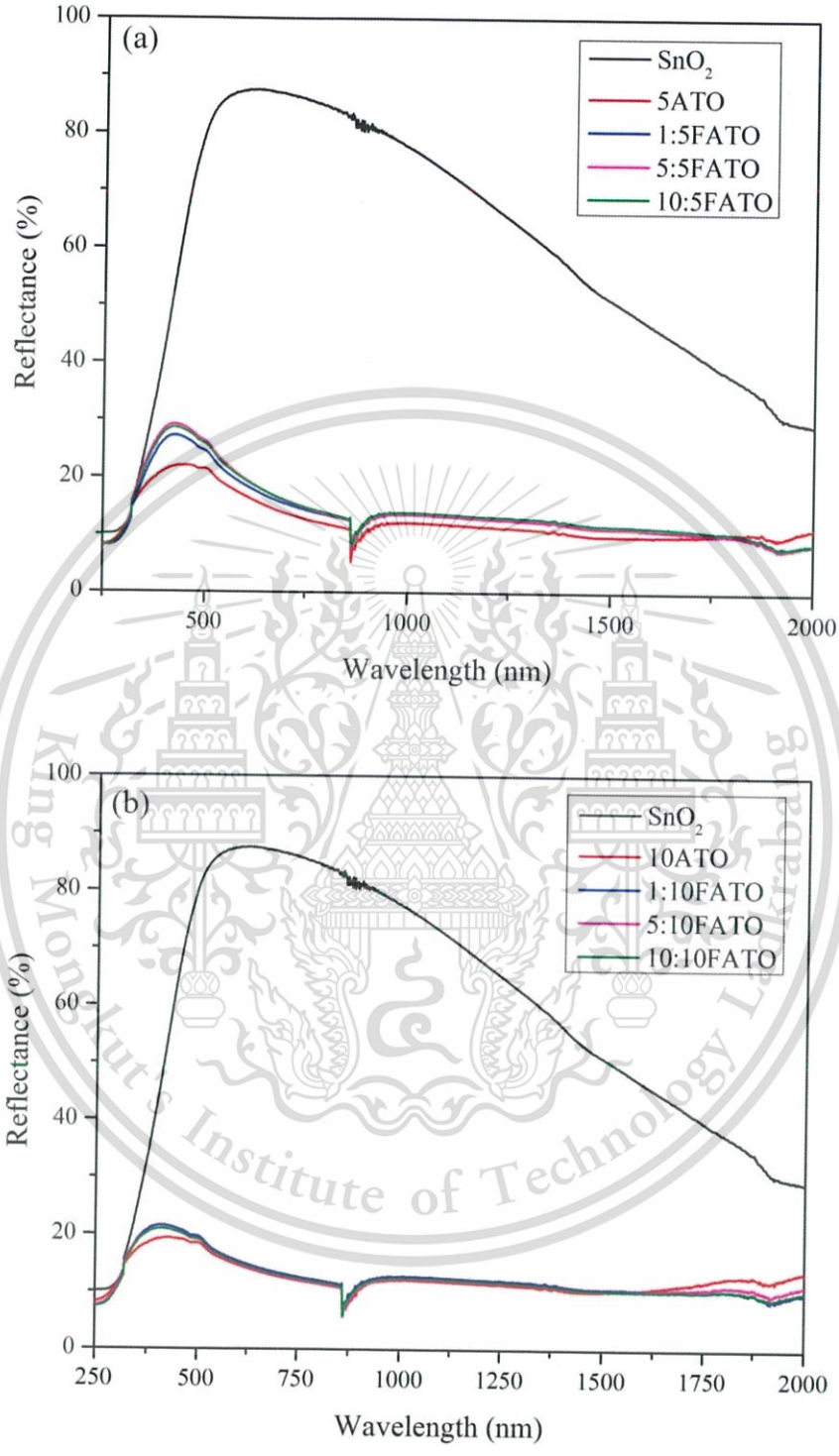

Figure 4.20 Diffuse reflectance spectra of (a) F(x):5FATO and (b) F(x):5FATO powder in the form of pellet.

The reflectance spectra of ATO nanoparticles in near infrared (NIR) region are depicted in Figure 4. 21 (a). The results indicate that the reflection in NIR increases with increasing Sb concentration as it depends on the mobility and carrier concentration, which can be explained using the classical Drude-Lorentz theory as given the follow expression [79]:

$$\omega_p = \sqrt{\frac{Ne^2}{\varepsilon_{opt}\varepsilon_0 m^*}}. \tag{4.8}$$

Where ω_p is plasma frequency, m^* is the effective optical mass of conduction electrons, N is conduction electron density, ε_0 is vacuum permittivity and ε_{opt} is the one measured in transparent spectral region which is known from the refractive index of undoped semiconductor. Absorbance spectra of ATO and FATO nanoparticles were calculated from reflection data according to the Eq. 2.1 which is A = 1-T-R. In calculation, transmission value was implied to be zero because the reflectance data was measured in pellet form resulting in no transmitted light to the detector. From Figure 2.21 (b), the ATO spectra appear the surface plasmon resonance (SPR) absorption in the IR region according to the increase in carrier concentration of nanoparticles [80]. The SPR absorption of ATO nanoparticles gradually shift to the shorter wavelength with increasing Sb concentration up to 5 mol.% due to higher densities of free electrons [49]. The free electrons were increased by Sb^{5+} incorporated into the SnO_2 lattice creating the donor levels. However, the peaks shift back to longer wavelength after Sb concentration up to 10 mol.%. These behavior associate as Sb in multivalent, significant presence of Sb^{3+} which creates acceptor states has been reported at higher doping concentration of Sb. The acceptor level created by Sb^{3+} traps the electrons and hence reduces the number of charge carriers contributed by Sb^{5+}. Furthermore the FATO absorbance spectra show stronger absorption and small shift in NIR region because replacement of O^{2-} sites with F^- atoms can promote the higher electron mobility as exhibited in Figure 2.22.

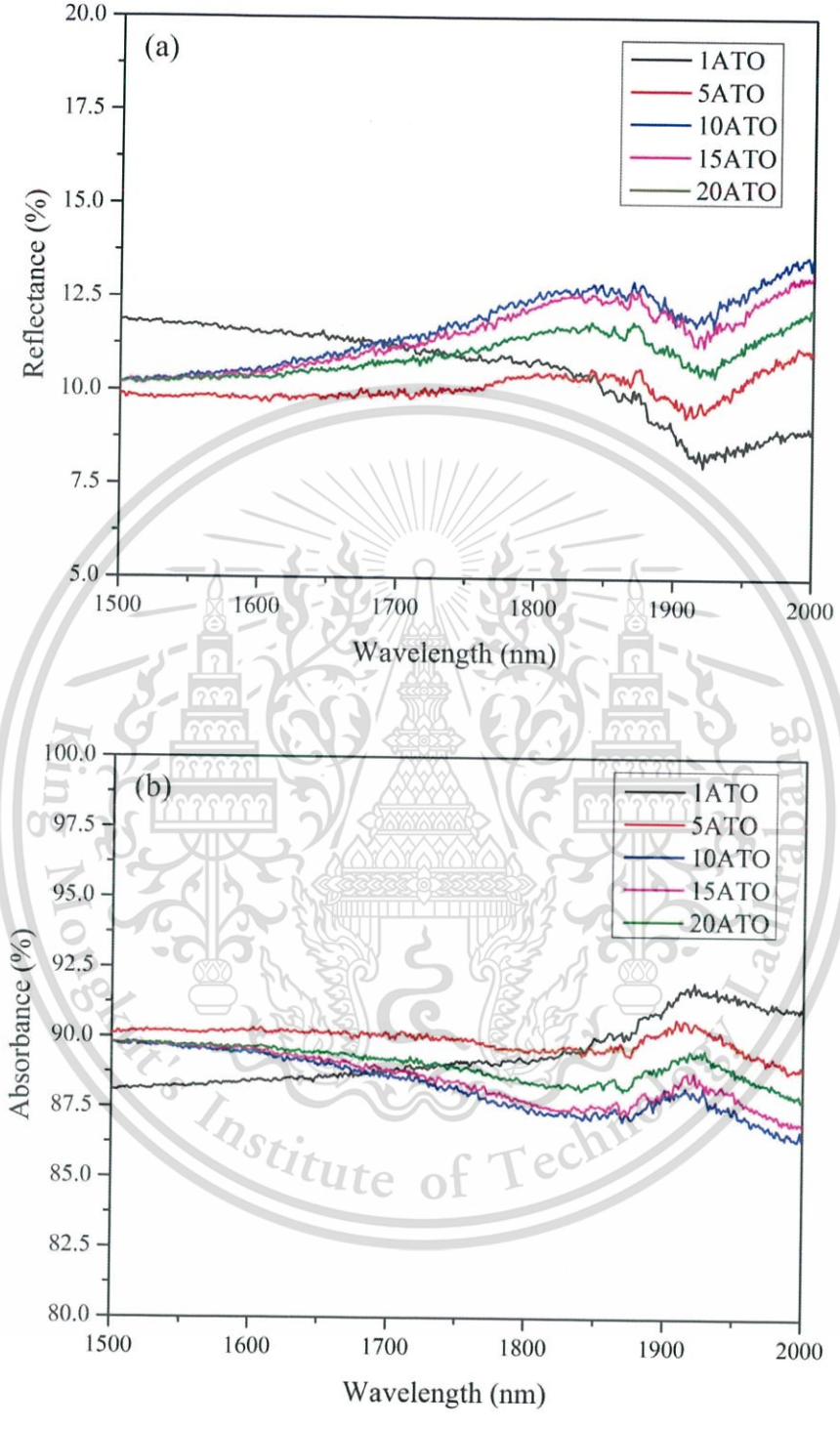

Figure 4.21 (a) diffuse reflectance spectra and (b) absorbance spectra of ATO nanoparticles with different Sb concentrations in long wavelength.

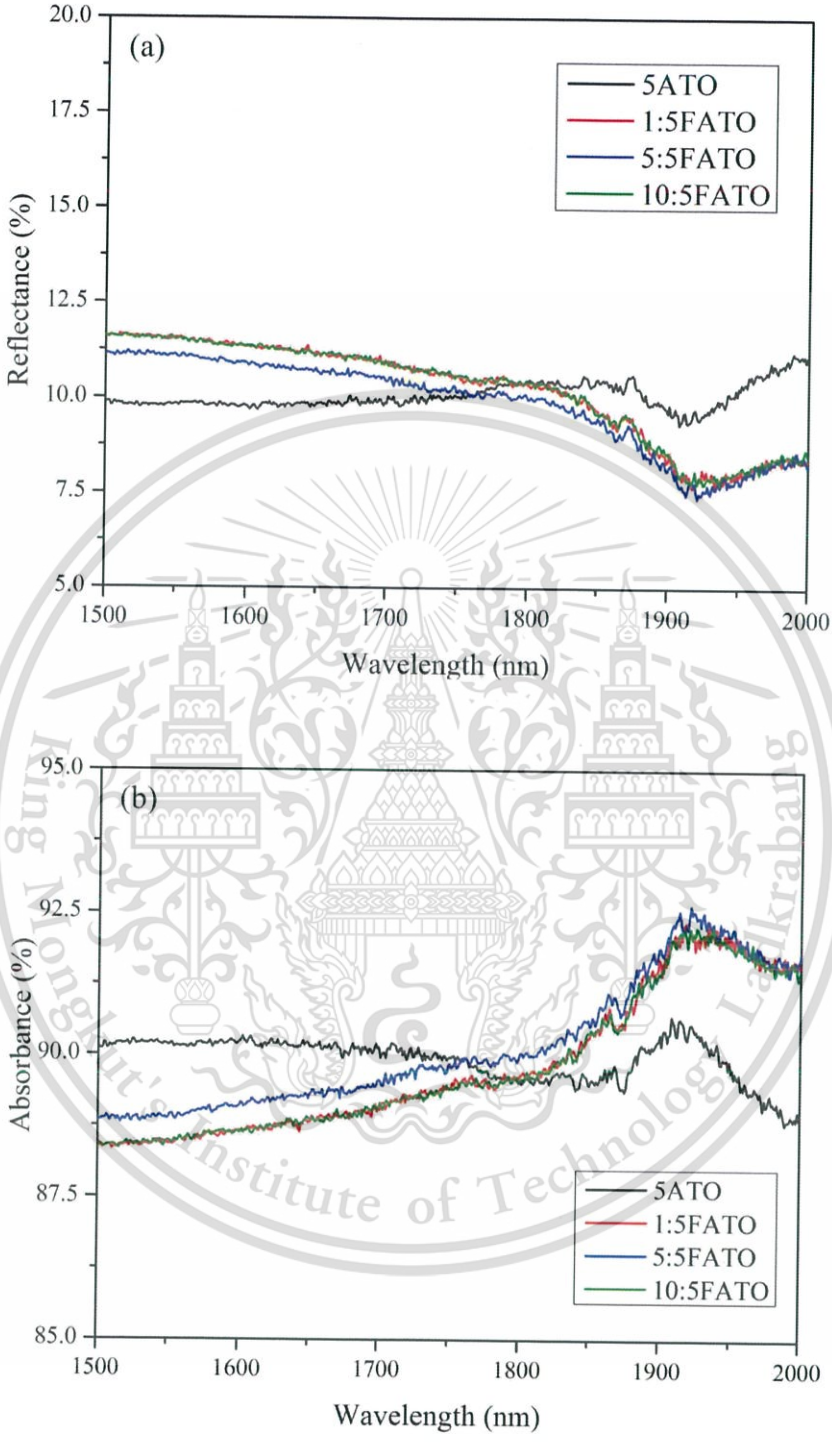

Figure 4.22 (a) diffuse reflectance spectra and (b) absorbance spectra of F(x):5FATO nanoparticles with different F concentrations in long wavelength.

Phase distribution of composite film was investigated by FE-SEM/EDX mapping. The EDX mapping confirms the presence of FATO nanoparticles dispersed in SiO_2 matrix as depicted in Figure 4.23. The image shows the O, F, Si, Sn, and Sb distribution as pink, green, white, blue and green spots, respectively. The EDX mapping confirms that Si is highly dispersed phase which is used as matrix in the sample. The Sn and Sb distribution can be inferred as the same position where elemental nanoparticles are found. Nevertheless, the presence of main small particulates illustrates incomplete dispersion in the Si matrix.

The surface morphology of the composite film of 1:5FATO nanoparticles and SiO_2 matrix was observed by the FE-SEM as shown in Figure 4.24. The morphology of SiO_2 matrix formed by thermal curing of GLYMO and TEOS precursor coated on the glass substrate exhibits an amorphous solid with smooth surface which is typical nature of SiO_2. The surface morphology of 1:5FATO nanoparticles embedded in the SiO_2 matrix to form the composite film is shown in Figure 4.24 (b). The result reveals that the synthesized FATO nanoparticles have small size in particulate form with good dispersion in the SiO_2 matrix. However, the surface morphology of 6 vol.% 1:5FATO concentration demonstrates poor uniformity with large agglomerated nanoparticles.

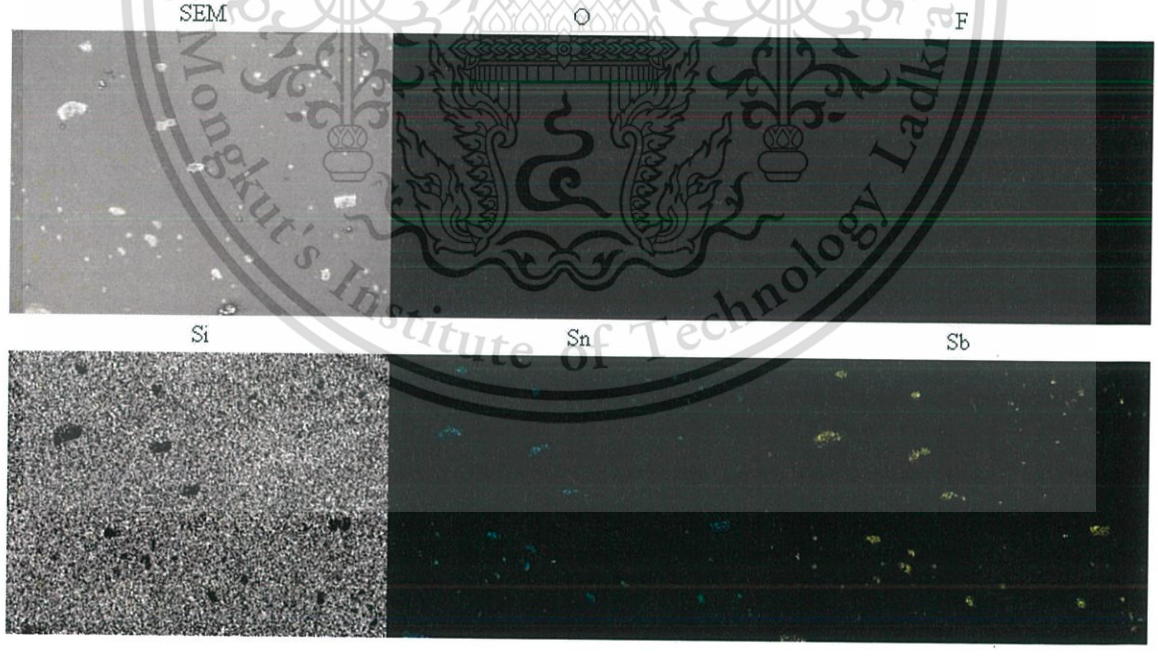

Figure 4.23 Phase distribution of 5:5 FATO nanoparticles dispersed in SiO_2 matrix.

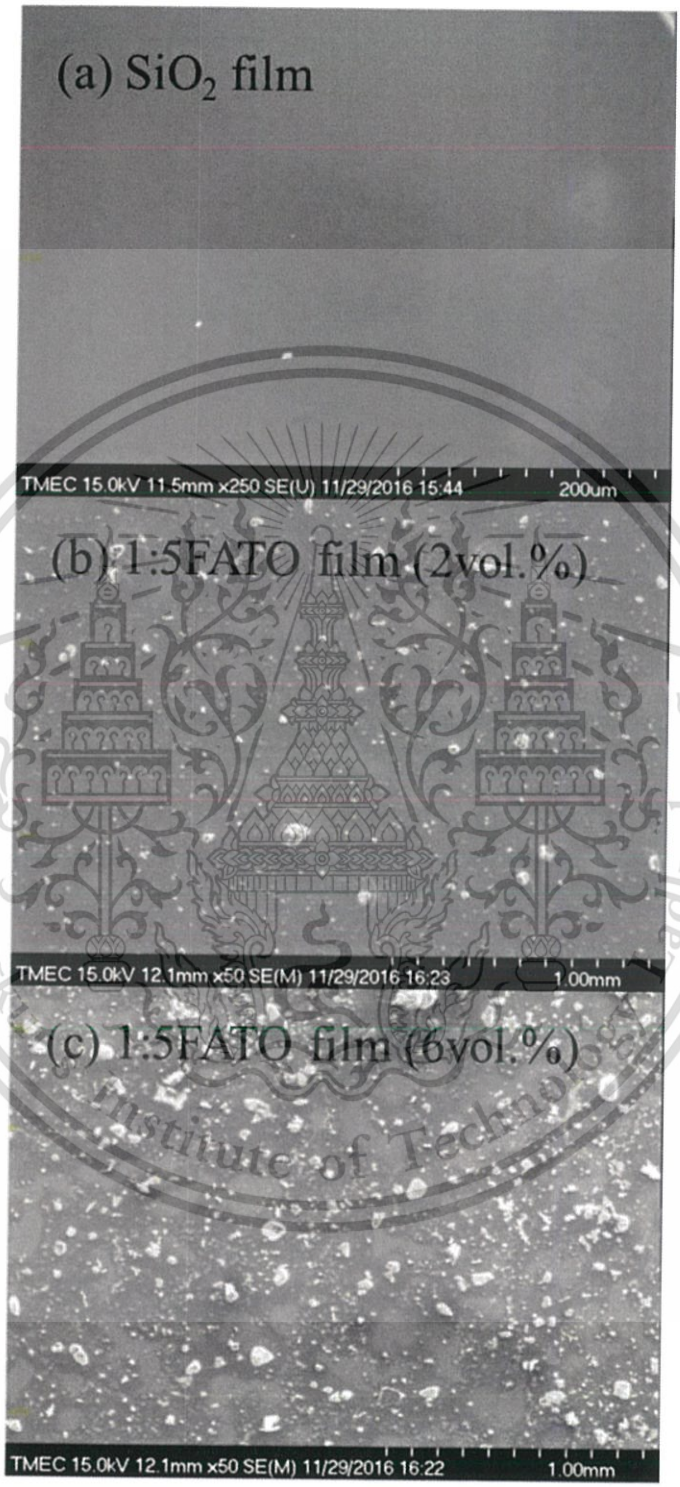

Figure 4.24 FE-SEM image of (a) SiO_2 film, (b) 1:5FATO composite film at 2 vol.% concentration and (c) 1:5FATO composite film at 6 vol.% concentration.

The thickness of the composite films determined by cross-section from FE-SEM observation is illustrated in Figure 4.25. The cross-sectional SEM images of SiO_2 and composite films illustrate the regularly uniform thickness until the concentration up to 4 vol.% of FATO nanoparticles and then the thickness is non-uniform at concentration of 6 vol.%. The thickness of SiO_2 film is ~0.83 μm and then the thickness of film increases to ~2.02 μm, ~2.9 μm and ~3.45 μm for the samples with 2 vol.%, 4 vol.% and 6 vol. % of 1:5FATO concentration, respectively. The results indicate that the thickness of composite films increase as the concentration increases. According to theory, the thickness (h) of films deposited by spin coating depends on fluid viscosity (u), the angular velocity (ω) of the turntable, and the spin total time (t), that can be evaluated with the following formula [81]:

$$h \approx \left(\frac{u}{t\omega^2}\right)^{1/2}. \tag{4.9}$$

From eq.4.9, the thickness is changed directly with viscosity which is corresponding to solid content. For this reason, the viscosity of spin-coated solution is increased by higher FATO nanoparticles adding. Therefore, the elevated thickness is definitely due to the increasing amount of FATO nanoparticles.

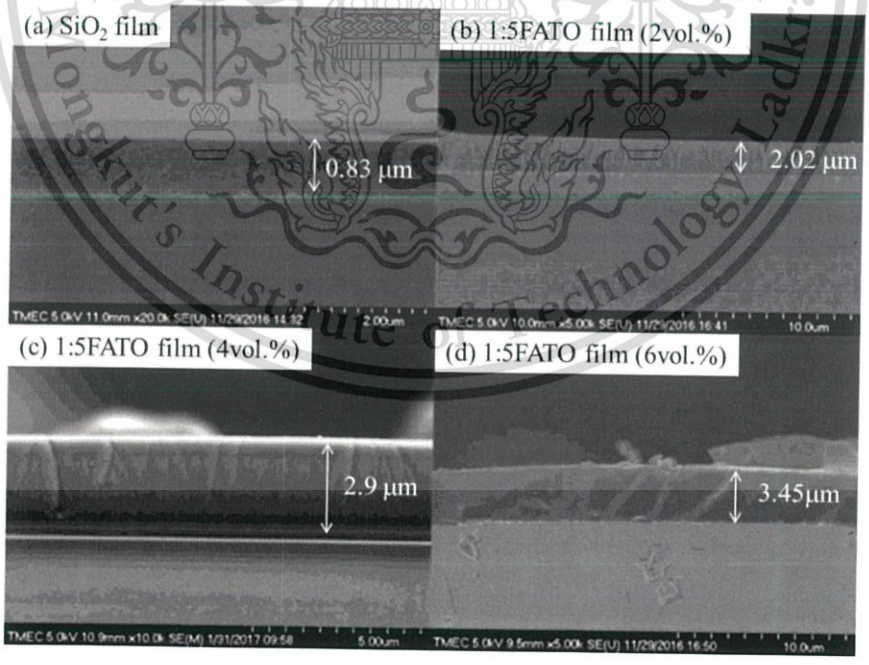

Figure 4.25 Cross-section SEM images of (a) SiO_2 film and 1:5FATO composite film at (b) 2 vol.%, (c) 4 vol.% and (d) 6 vol.% concentration.

Cross-sectional SEM images of 1:5FATO composite films at concentration of 2 vol.% with various number of spin-coated layers are shown in Figure 2.26. The FE-SEM observation exhibits significant increase in film thickness with increasing spin-coated layer from 1 to 3 times. The cross-sectional SEM images indicate that the thickness is 2.02 μm, 5.55 μm and 8.25 μm corresponding to 1 layer, 2 layers and 3 layers, respectively. However, non-uniformity of composite film was occurred in 3 spin coated layers due to improper adherent problems between deposited layers.

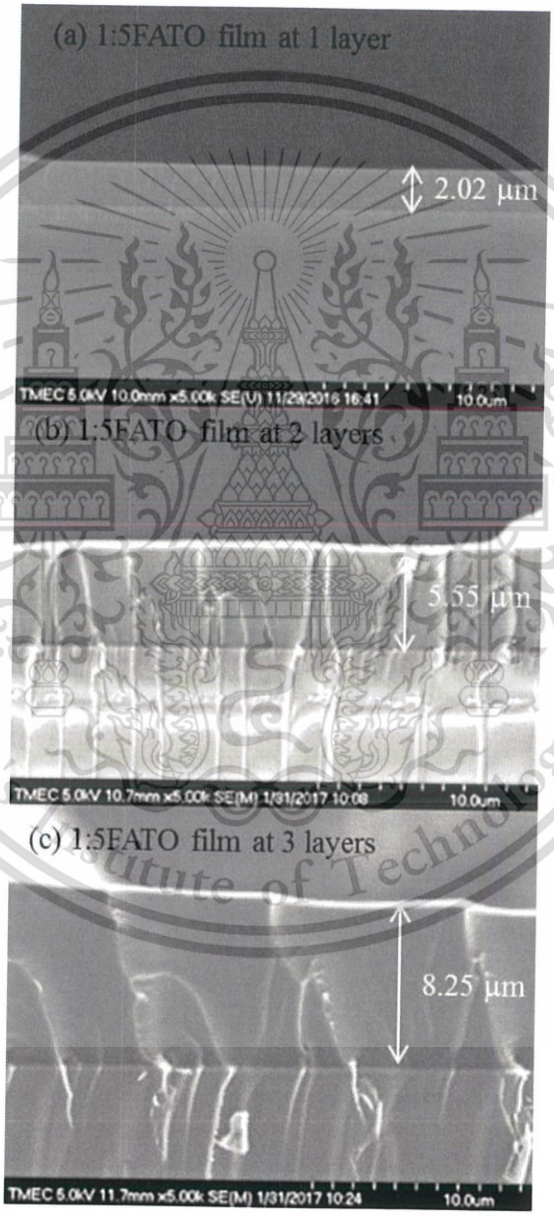

Figure 4.26 FE-SEM image of composite film at 2 vol.% concentration of 1:5FATO nanoparticles with (a) 1 layer, (b) 2 layers and 3 layers of spin coating.

In order to identify the optimal doping concentration of composite film for IR-shielding coating, its optical transmittance was investigated by UV-Vis-NIR spectrophotometer. The optical transmittance of the composite films using ATO nanoparticles deposited at 1 spin-coated layer with different Sb concentrations are illustrated in Figure 4.27. The transmittance of SiO_2 possesses high optical transparency of > 90% in visible and IR region therefore the SiO_2 film cannot reflect or absorb NIR radiation. As shown in Figure 4.27, the transmittance spectra of all composite film was slightly reduced by incorporated nanoparticle which can provide optical transparency of > 85% in visible region. The transmittance change of the SnO_2 composite film is ~4.12% in the NIR region. After Sb doping, the transmittance spectra gradually decrease at longer wavelength with increasing Sb concentration. The transmittance change of ~7.38% reaching the minimum in the NIR region was obtained from 5 mol.% and 10 mol.% Sb concentrations. Under this condition, the ATO composite film can provide IR-shielding feature depending on Sb concentration. The ATO composite films can shield IR radiation because they have higher densities of free electrons resulting to SPR absorption in long wavelength as mentioned previously [82]. From UV-Vis-NIR spectra, the appropriate IR-shielding coating is attained by the samples with 5 and 10 mol.% Sb concentrations which have similarly spectra feature in all wavelengths. Although, the samples with 15 mol.% Sb doping content possesses lower transmission in long wavelength, the transmission in visible region is lower than that of the samples with 5 and 10 mol.% Sb concentration. Therefore, the optimal Sb doping concentration is 5 and 10 mol.% which are based condition for co-doping.

UV-Vis-NIR spectra of composite films using co-doping nanoparticles which are F(x):5FATO and F(x):10FATO conditions are demonstrated in Figure 4.28 and 4.29, respectively. The results reveal that the transmittance spectra decrease in long wavelength by less F incorporation in 5ATO nanoparticle as shown in Figure 4.28. The transmittance change is 4.12 % for the 5ATO nanoparticles, while it increases to 7.38 % for the 5:5FATO sample. There is about 3.26% expansion attributed to the free carriers provided through F ion doping. In the case of heavy F-doping, the free carrier density decreases due to the Sn-F complexes formed in the grain boundaries, leading to a higher transmittance spectra in NIR region. On the other hand, the transmittance spectra of F(x):10FATO composite films exhibit higher transparency than 10ATO composite films in long wavelength. These results agree well with hall measurement result which is referring to electron density reduction by exceeded F concentration. The IR-shielding property can improve by suitable F

incorporation in 5ATO nanoparticle. The lowest transmission in longer wavelength was obtained by 5:5FATO composite films.

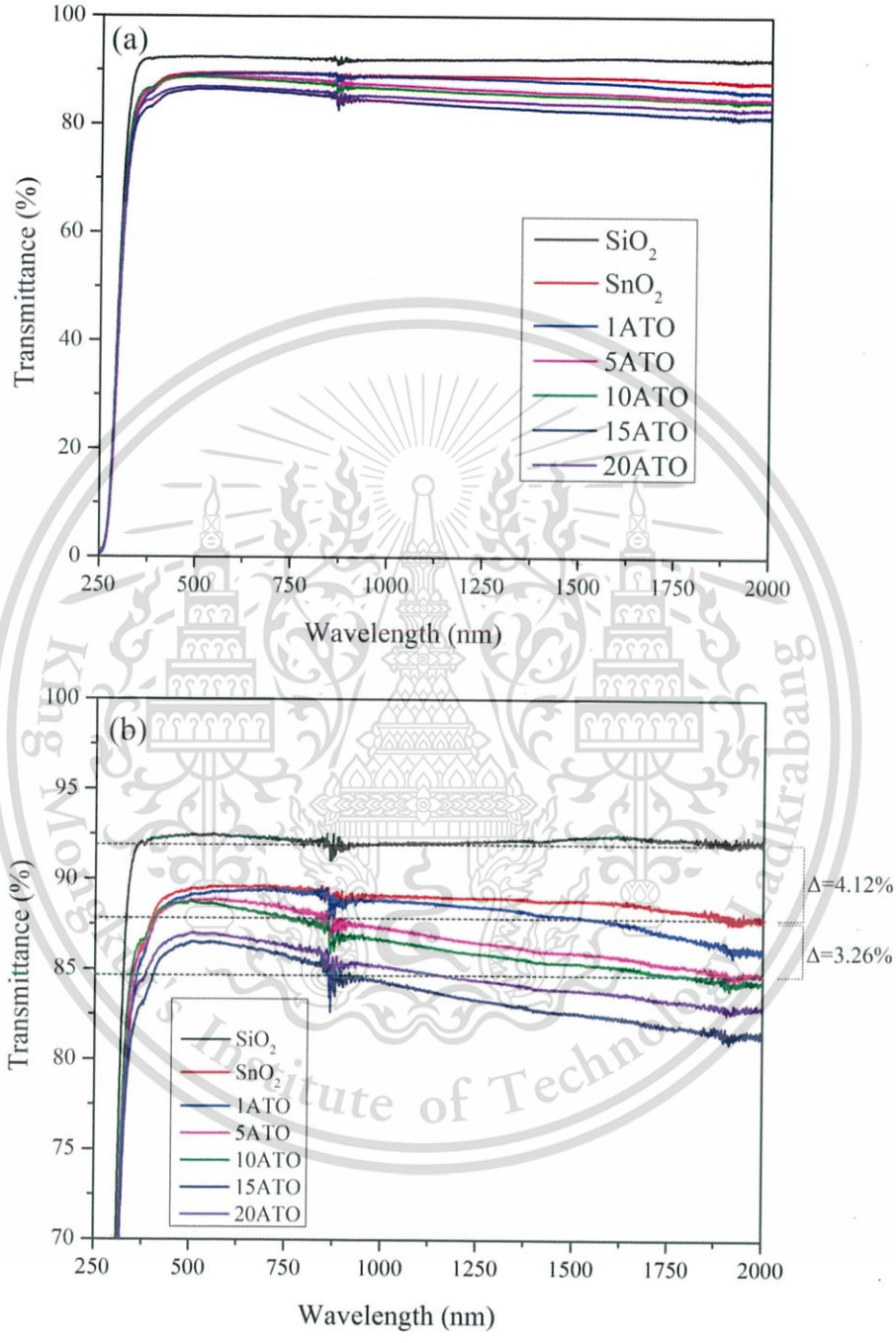

Figure 4.27 (a) UV-Vis-NIR spectra of ATO composite films with different amounts of Sb and (b) Zoom-in image with transmittance in range of 70-100%.

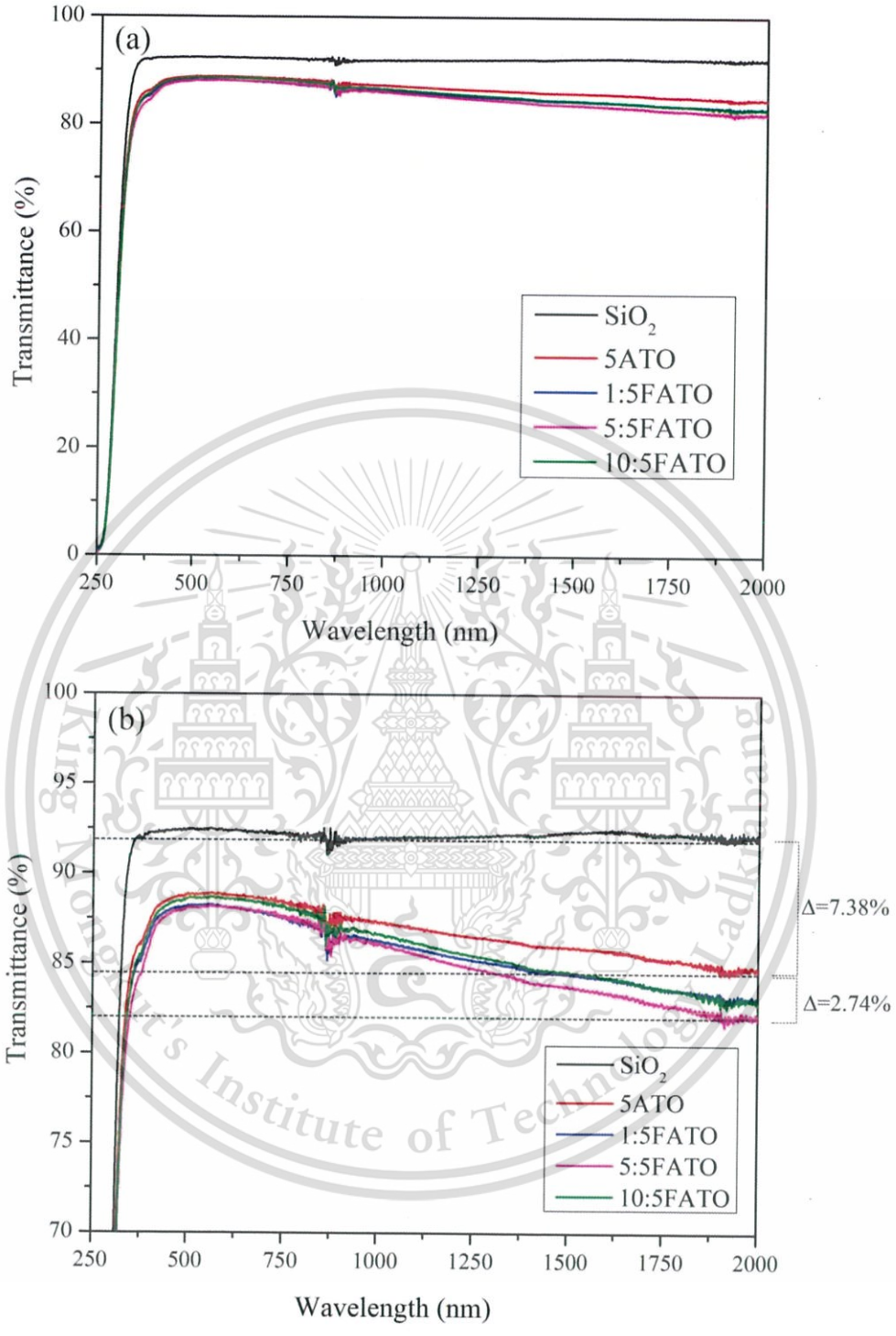

Figure 4.28 (a) UV-Vis-NIR spectra of F(x):5FATO composite films with different amounts of F and (b) Zoom-in image with transmittance in range of 70-100%.

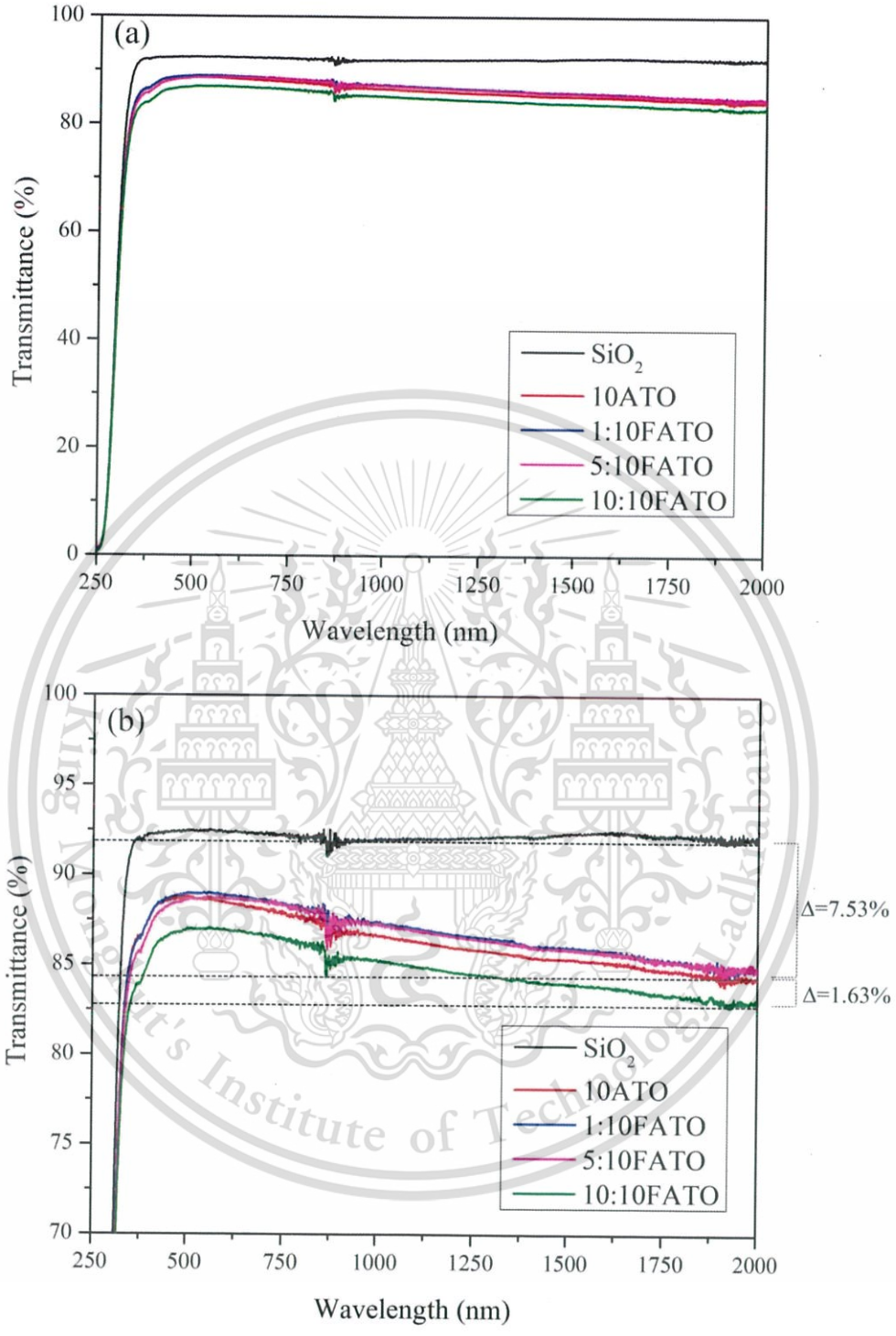

Figure 4.29 (a) UV-Vis-NIR spectra of F(x):10FATO composite films with different amounts of F and (b) Zoom-in image with transmittance in range of 60-100%.

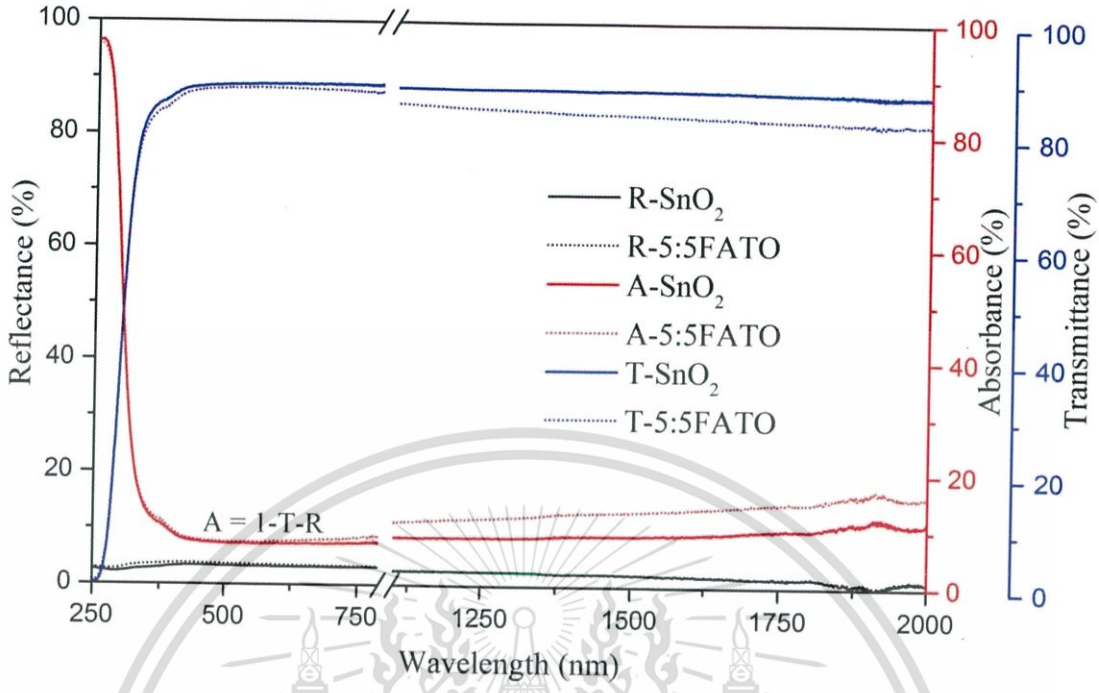

Figure 4.30 Relationship between reflectance, absorbance and transmittance spectra of composite film using SnO_2 and 5:5 FATO nanoparticles.

Relationship between reflectance, absorbance and transmittance spectra of the composite films using SnO_2 and 5:5 FATO nanoparticles is demonstrated in Figure 2.29. In the case of composite films, the absorption was calculated from the reflectance and transmittance spectra which were measured by UV-Vis-NIR spectrophotometer. The absorption peak of 5:5FATO composite film in long wavelength has the stronger absorbance than SnO_2 composite film which implies that the sample with 5:5FATO nanoparticle has the highest electron density. From Figure 2.29, the reflectance spectra of both composite films show slight reflectance, while transmittance spectra exhibit high transparency in the visible region because particles in the nanometer range practically do not scatter the visible light [48]. The composite films using 5:5FATO nanoparticles have lower transmission than SnO_2 nanoparticles due to the higher density of the electron. For IR-shielding application in solar cell, a high transmission in the visible range is exactly important and a low transmission in NIR range is also mandatory. Thus, the composite film of 5:5FATO nanoparticles dispersed in SiO_2 matrix is determined to be appropriate for IR-shielding coating.

The effect of nanoparticles concentration in composite film using 1:5FATO on the IR-shielding property were investigated. Transmittance spectra of 1:5FATO composite films with various 1:5FATO concentrations are shown in Figure 4.31. The transmittance of film in all wavelength continuously decreases in long wavelength after increased nanoparticles concentration from 2 vol.% to 6 Vol.%. As a result, the composite film with 4 vol.% concentration of 1:5FATO nanoparticles has remained high optical transparency in the visible range but it has lower transmission in long wavelength than that of 1:5FATO nanoparticles at 2 vol.% concentration. However, the transmittance spectra of 1:5FATO nanoparticles at 6 vol.% exhibits the lowest transmission in whole wavelength because the film performs hard agglomeration and opaque feature. Therefore, it is considered that the optimization of IR-shielding capability was obtained by the sample with concentration of 4 vol.%.

Next, the effect of number of spin-coated layers on the IR-shield property of the composite film coating was also studied. The 1:5 FATO nanoparticles fixed at 2 vol.% concentration were prepared by spin coating method with various number of spin-coated layers. Transmittance spectra of 1:5FATO composite films with different spin-coated layers are exhibited in Figure 4.32. The results show that the transmissions of all samples remain more than 80% transparency in visible range and then gradually decrease in NIR range. Nevertheless, the transmittance spectra in the visible region decrease slightly upon increasing the number of spin-coated layers from 1-3 layers. The IR-shielding capability of the composite films depends on the number of spin-coated layers. Therefore, the optimal number of spin-coated layers should be 2 or 3 in this system.

Moreover, the thickness of the composite films significantly affect to transmission which is related to absorption coefficient according to following equation [83]:

$$\alpha = \frac{1}{d} \ln \frac{1}{T} \cdot \tag{4.10}$$

where α in is an absorption coefficient, d is film thickness and T is its transmittance. The absorption coefficient of 1:5FATO composite films with various nanoparticle concentrations and number of spin-coated layers are shown in Figure 4.33 and 4.34, respectively. From this equation, the absorption coefficient changes inversely with the film thickness. Under both conditions, the absorption coefficient increases as the nanoparticles concentration and number of spin-coated layers increase which affects to thickness expansion of composite film

observed by FE-SEM. Actually, a material with a low absorption coefficient has a poor absorbance resulting to high transparent related with wavelength. In this case, the absorption coefficient of 1 layer has higher than 2 layers and 3 layers but the transmittance spectrum of 1 layer has transparent higher than both of the conditions. The controversial feature should be due to another related effects including scattering, the change in refractive index due to interface effect of the deposited layer that are not taken into account in this study.

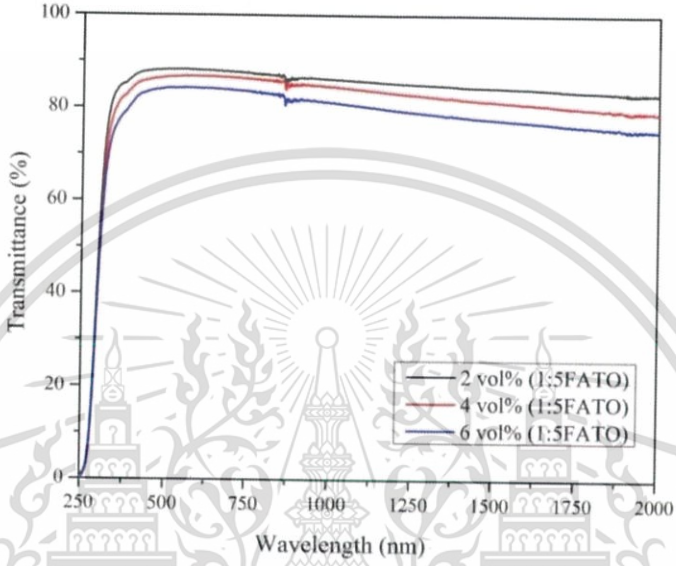

Figure 4.31 Transmittance spectra of 1:5FATO composite films at 1 spin-coated layer with different nanoparticle concentrations.

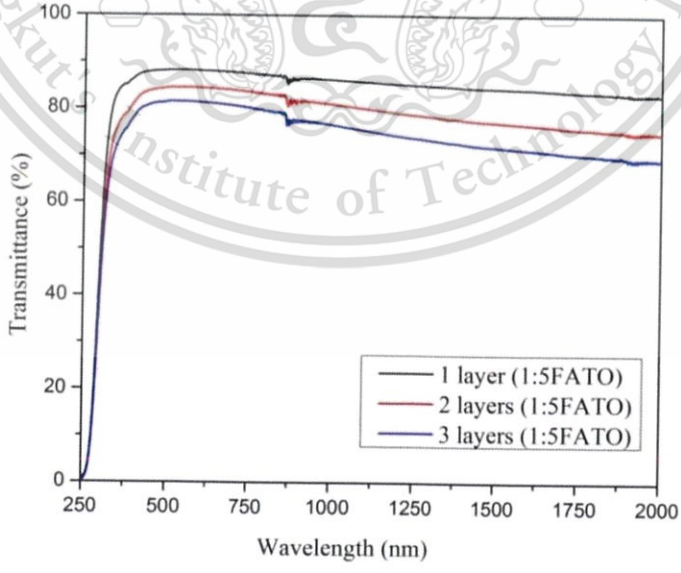

Figure 4.32 Transmittance spectra of 1:5FATO composite films with different spin-coated layers.

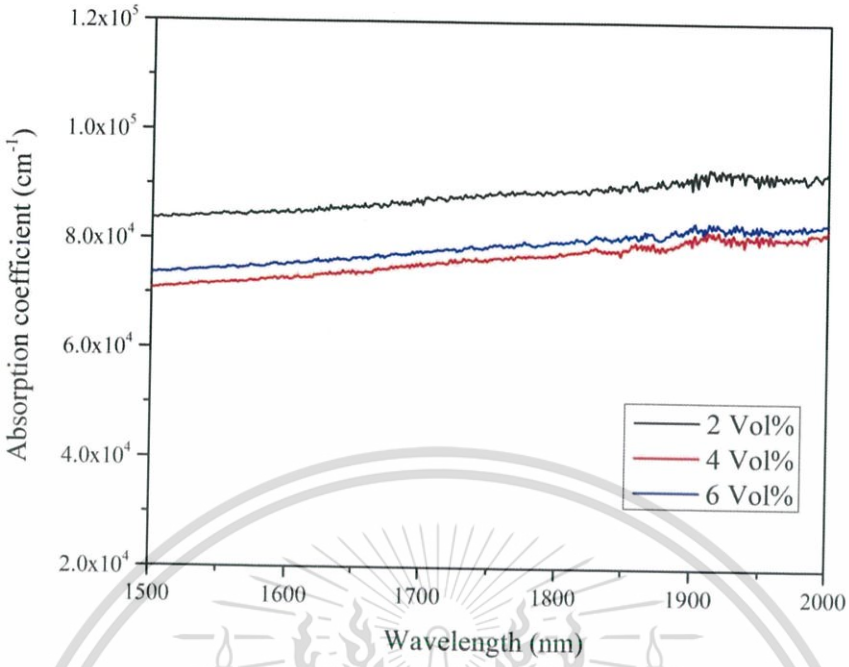

Figure 4.33 Absorption coefficients of 1:5FATO composite films at 1 spin-coated layer with different nanoparticle concentrations.

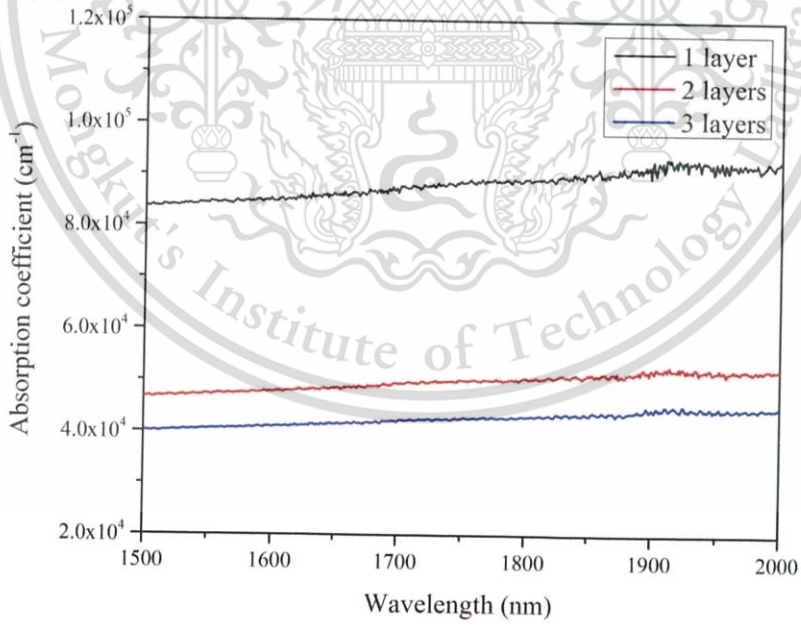

Figure 4.34 Absorption coefficient spectra of 1:5FATO composite films with different spin-coated layers.

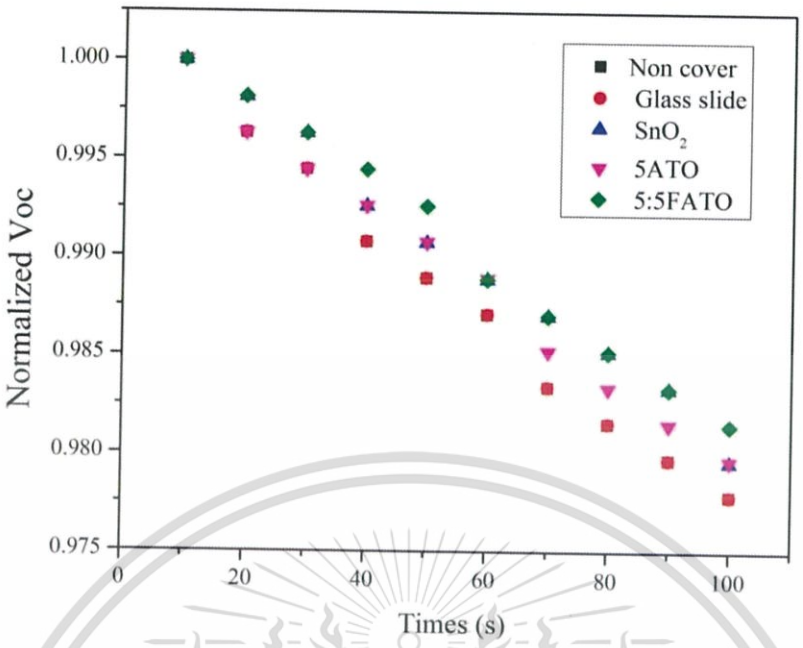

Figure 4.35 Normalized V_{oc} of solar cell with different IR-shielding coating.

In the next step, the composite films applied on the top of silicon solar cell were examined in the part of IR-shielding coating. Ordinarily, the change in temperature will affect to the efficiency (η) of the solar cell. When the solar cell temperature increase, the short-circuit current consequently increases while the open-circuit voltage should dramatically decrease as described by equation (4.11) [84]:

$$\eta \downarrow = \frac{J_{sc} \uparrow V_{oc} \Downarrow FF}{P_{in}}, \tag{4.11}$$

where *Jsc* is the short-circuit current (when V = 0), V_{oc} is the open-circuit voltage (when J = 0), *FF* is the fill factor and P_{in} is the power incident on the solar cell. The voltage is significantly dependent on the operating temperature, resulting in dramatically reduced efficiency because voltage decreases faster than the increasing current. Thus, the V_{oc} of silicon solar cell as function of exposure time was observed for IR-shielding study.

Relationship between V_{oc} and times under continuous exposure with halogen lamp using different IR-shielding film types is shown in Figure 4.35. In the case of non IR-shielding layer, the V_{oc} immediately decreases with exposure time which is similar to SiO_2 film used as matrix of nanoparticles. From this result, it indicates that the SiO_2 film unable to shield the IR irradiation. After 5ATO nanoparticles were dispersed in SiO_2

matrix, the V_{oc} of silicon solar cell was preserved, decreasing slower than the case of non IR-shielding layers or SiO_2 film. Moreover, the V_{oc} value of 5:5FATO composite film has a bit higher than that of other materials as additional exposure time, implying the feasibility of IR irradiation shielding of the composite film. The results indicate that the V_{oc} value using the composite film at 5:5 FATO is higher than those of other materials due to greater electron density as described in previous section.

The V_{oc} value of 1:5FATO composite film with various nanoparticle concentrations is illustrated in Figure 4.36. By the FE-SEM observation, the nanoparticles concentration designated at 2 vol.%, 4 vol.% and 6 vol.%, as the thickness increases gradually, provides the decreased transmittance in all wavelength with increasing concentration. From V_{oc} result, the composite film with nanoparticle concentration of 4 vol.% can preserve the slowest decrease in V_{oc} than that of the samples with 2 vol.% and 6 vol.% of nanoparticles. Because the composite film at 2 vol.% has lower nanoparticle concentration and lower thickness than other conditions. Nevertheless, the composite film at 6 vol.% has a high concentration and greater thickness, the non-uniformity of film was observed resulting in IR-shielding capability. Thus, in this case, the composite films with 4 vol.% particle content is considered to be appropriate for using as IR-shielding coating since it still has high transparency in visible range and low transmittance in IR region.

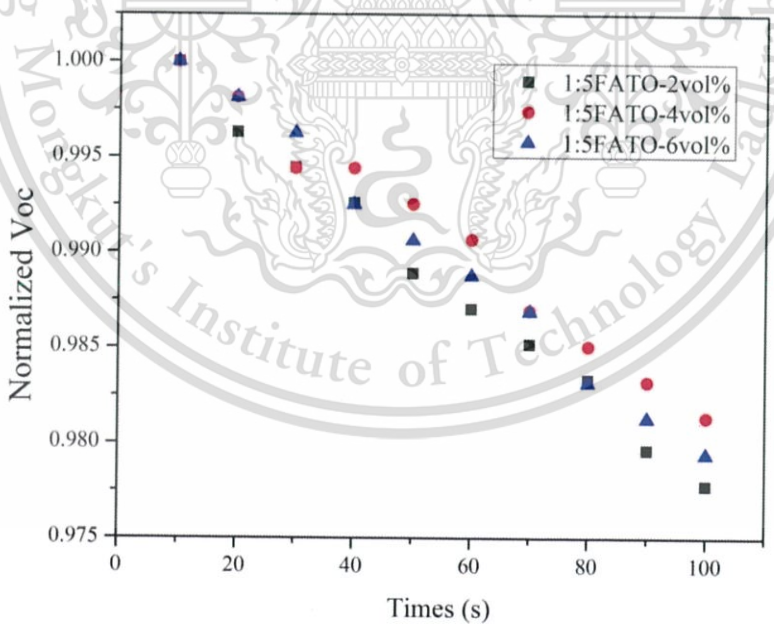

Figure 4.36 Normalized V_{oc} of solar cell using 1:5FATO composite films as IR-shielding layer at 1 spin-coated layer with different nanoparticles concentration.

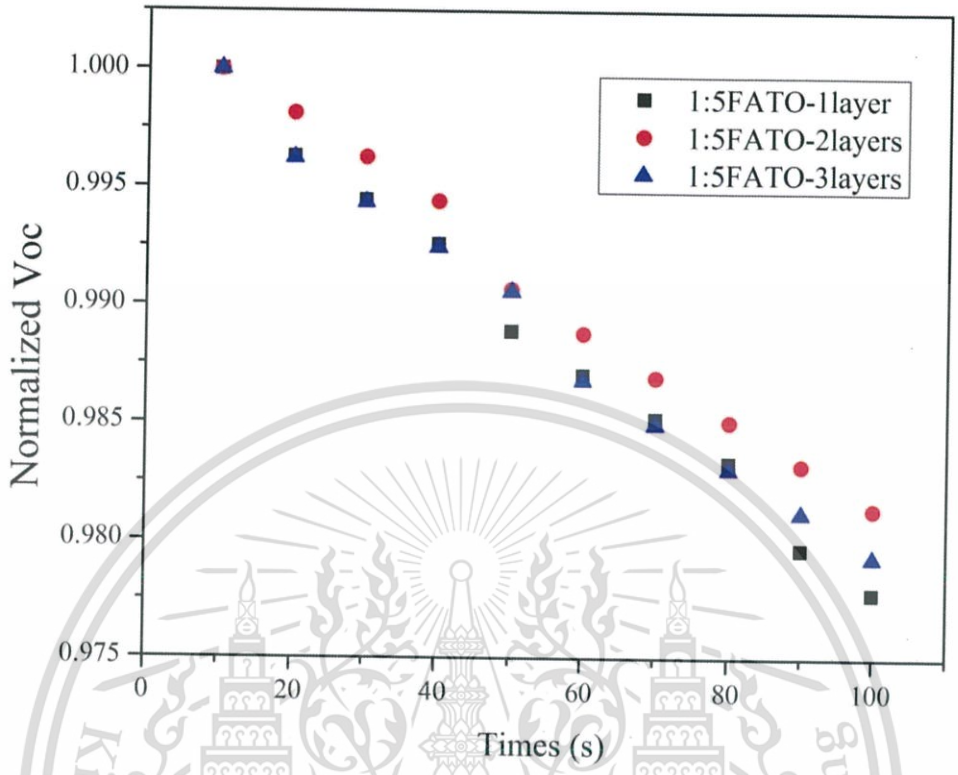

Figure 4.37 Normalized *Voc* of solar cell using 1:5FATO composite films as IR-shielding layer with different spin-coated layers.

The V_{oc} value of 1:5FATO composite film with various numbers of spin-coated layers is illustrated in Figure 4.37. By the FE-SEM observation, spin-coated layers are 1 layer, 2 layers and 3 layers, which provide the gradually increased thickness affecting to transmittance decrement in all wavelength. From V_{oc} result, the spin-coated layers at 2 layers can maintain the slower decrease in V_{oc} of silicon solar cell than others. In FE-SEM observation, the image shows less regular thickness implying that the non-uniformity was occurred. This result indicates that the suitably spin-coated layer is important to determine the thickness and uniformity of composite film used as IR-shielding module.

To confirm the IR-shielding capability, the relationship between temperature and exposure time was also studied. In this measurement, the temperature of silicon solar cell was measured using thermocouple with multimeter under solar simulator exposure. As seen in Figure 4.38 (a), the temperature of a silicon solar cell increases as exposure time increase. The result shows that the temperature of non IR-shielding layer is higher than that of solar cell shielded with the 5:5FATO composite film. Likewise, the V_{oc} of silicon solar cell of non IR-shielding layer has lower value than that of the cell accompanied with 5:5FATO composite film as exhibited in Figure 4.38 (b).

Figure 4.39 shows the *I-V* characteristic of silicon film with/without IR-shielding layer as a function of exposure time. The results indicate that the J_{sc} of both conditions increases as the exposure time increases that are resulted from the higher temperature in silicon solar cell. However, the J_{sc} value slightly decreases when the silicon solar cell is shielded with the 5:5FATO composite film due to the shielding property of the FATO particles dispersed in the matrix. .

Moreover, the relationship of efficiency, J_{sc} and V_{oc} of both conditions as a function of exposure time is depicted in Figure 4.40. Although, the J_{sc} increases as temperature increases, the efficiency of silicon solar cell gradually decreases, implying that the V_{oc} would decrease faster than J_{sc}. These overall results confirm that the V_{oc} and J_{sc} of silicon solar cell considerably changes with operating temperature, directly affecting to an efficiency of silicon solar cell. As exposure time is extended, the expectation of this result implies that the temperature of silicon solar cell is preserved by 5:5FATO composite film and the efficiency is also maintained.

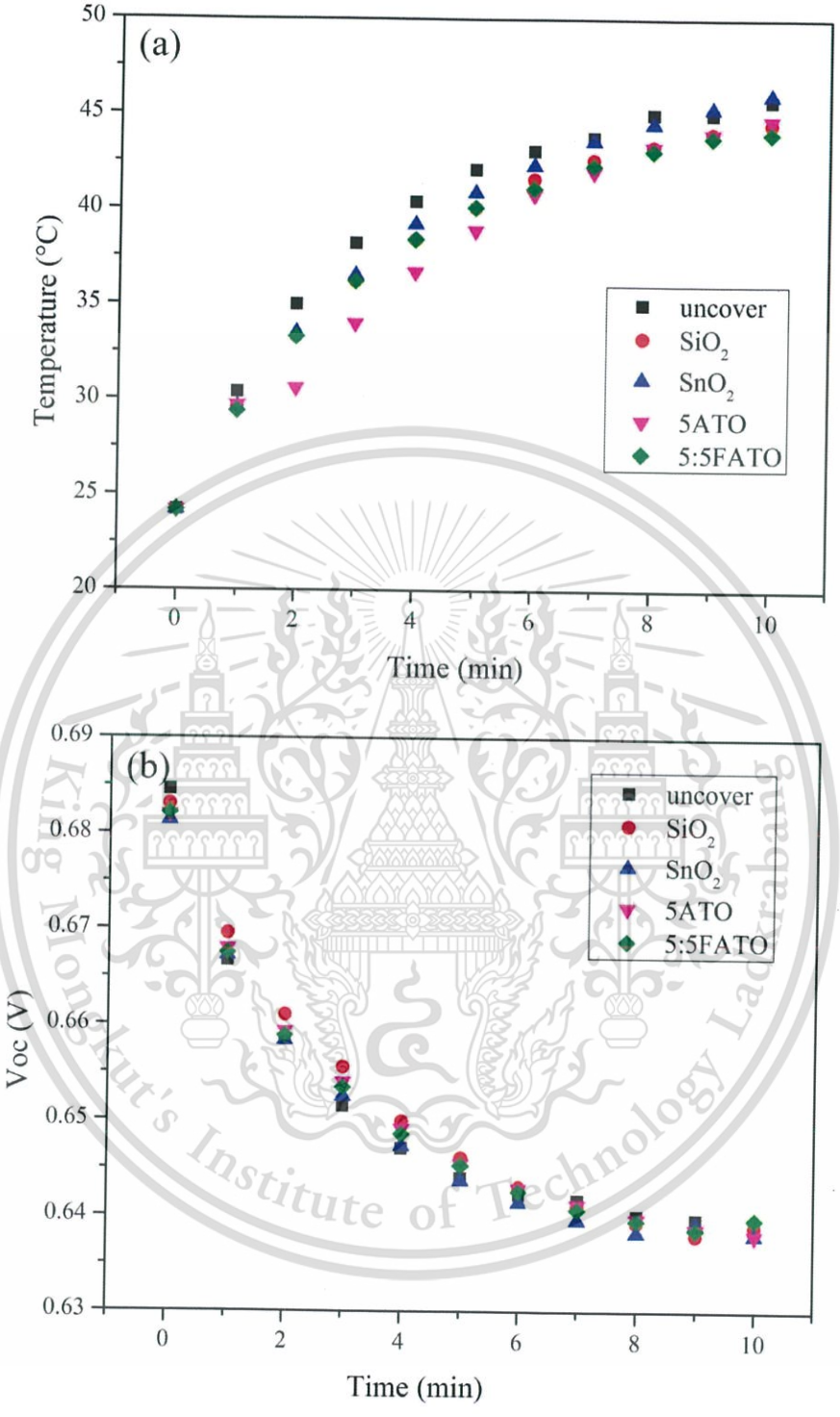

Figure 4.38 (a) The temperature of solar cell shielded with different types of shielding layer and (b) its V_{oc} as a function of exposure time.

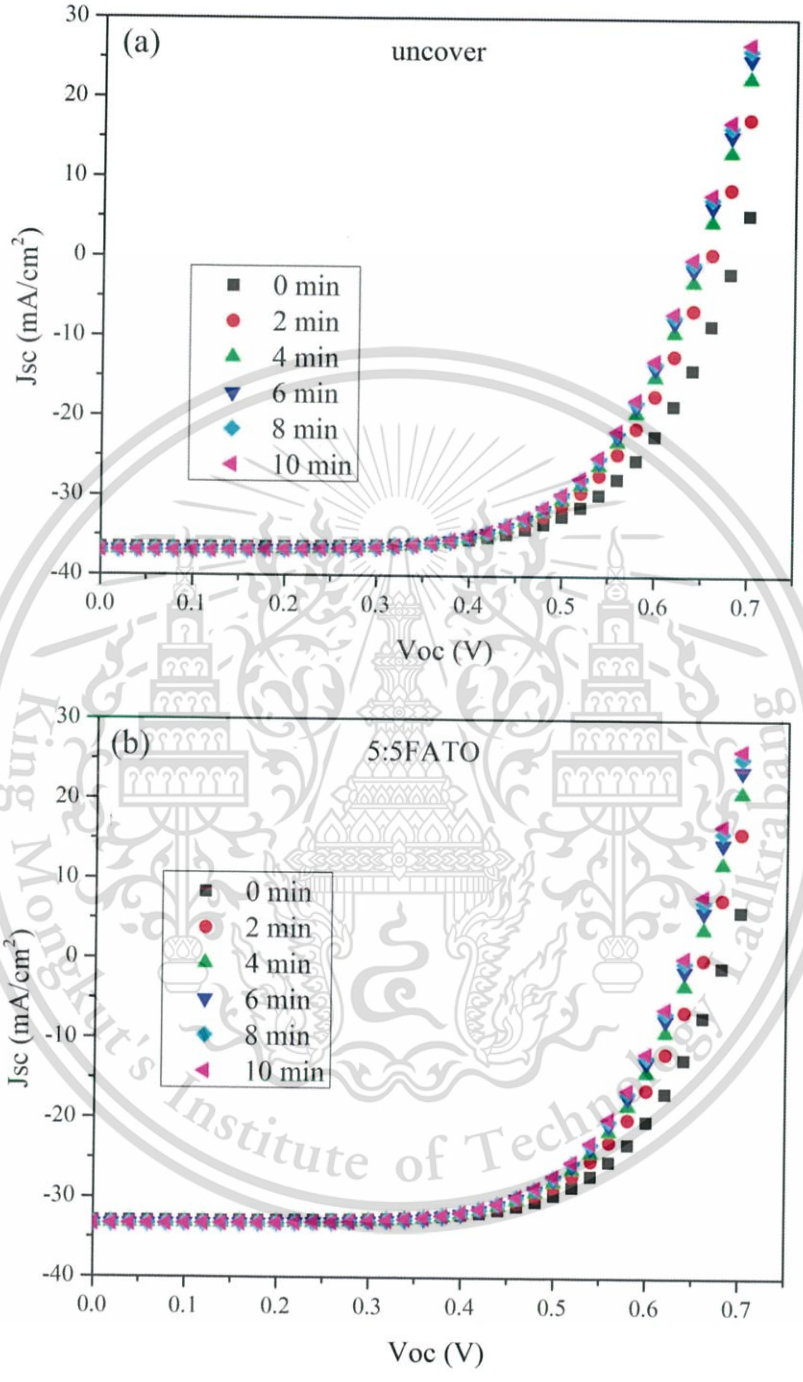

Figure 4.39 *I-V* characteristics of silicon solar cell (a) without IR-shielding layer and (b) with IR-shielding layer using 5:5FATO composite film at different exposure times.

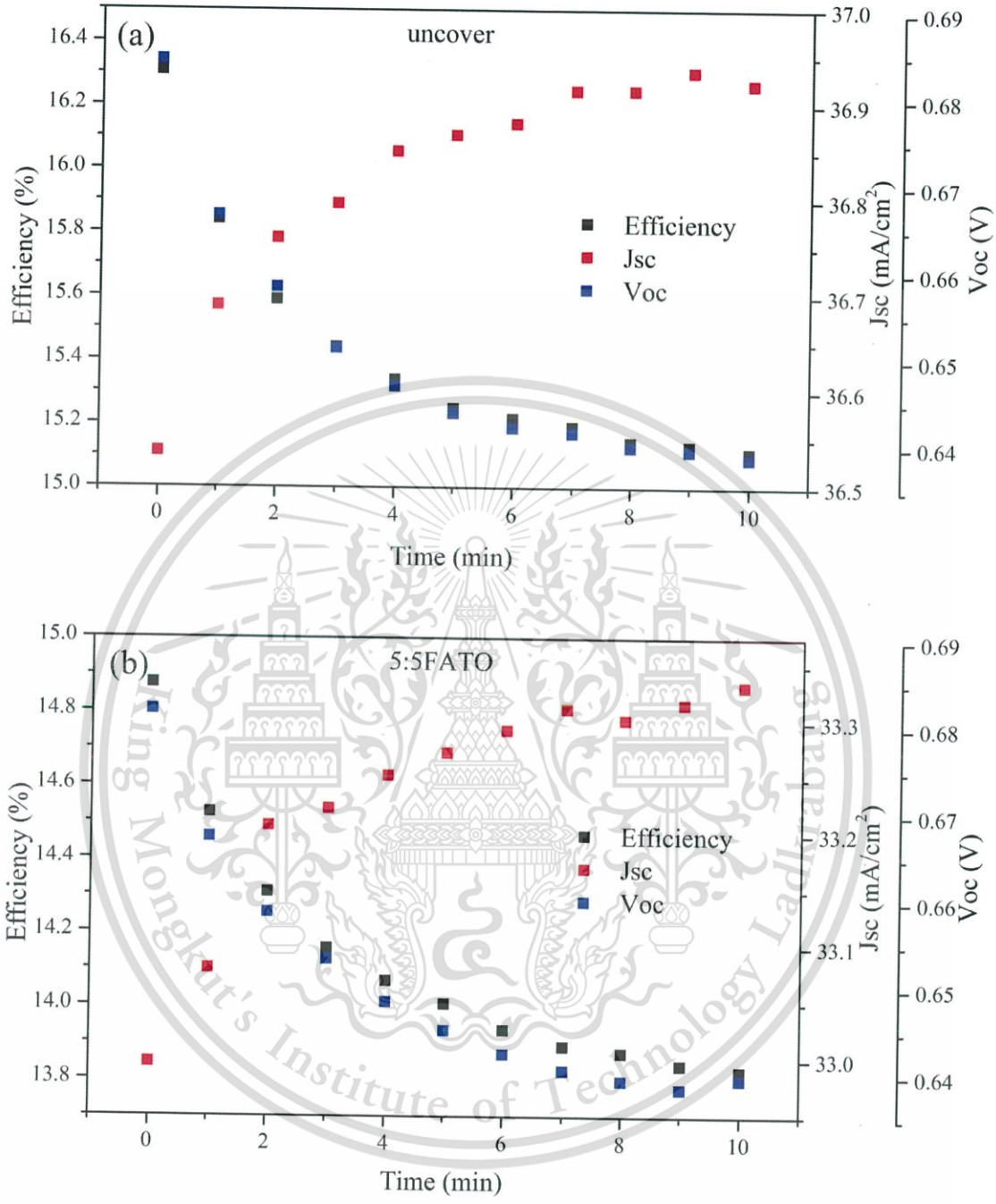

Figure 4.40 Relationship of efficiency, J_{sc} and V_{oc} of the solar cell (a) without IR-shielding layer and (b) with IR-shielding layer using 5:5FATO composite film.

CHAPTER 5

CONCLUSIONS

SnO_2 nanoparticles and F-doped SnO_2 were synthesized by ultrasonic-assisted precipitation method operated at 120 W with frequency of 40 kHz. From the TG/DTA results, ultrasonic-assisted has considerable effect on reduced temperature of phase transformation from $Sn(OH)_4$ to SnO_2 due to cavitations in solution during ultrasonic radiation. The XRD and TEM results exhibit that, by an assistance of ultrasonic energy during precipitation process in combination of calcination at rather low temperature, the well-dispersed SnO_2 and F-doped SnO_2nanoparticles with uniform size in the range of 10-15 nm can be successfully prepared. The XRD and TEM results exhibit the observable change of d-spacing and particle size caused by the substitution of oxygen sites by fluorine ions.

Sb-doped SnO_2 nanopowders were synthesized by sonochemical-assisted precipitation process operated at 750W with frequency of 20 kHz. The characterizations of the powders were conducted and the results revealed that the as-synthesized powder in SnO_2 phase with less agglomeration can be obtained by single step sonochemical process. It is suggested that the sonochemical process generates localized high temperature area guiding to crystallite growth, nucleation and flocculation of particles. When doping with Sb, the resistance of SnO_2 decreases dramatically, suggesting that the incorporation of Sb^{5+} ions can enhance the conductivity of SnO_2. However, the Sb incorporation with optimal concentration is significant since the free electrons may be trapped by the acceptor levels which are created by the substitution of Sn^{4+} by Sb^{3+} after excess antimony.

F/Sb-codoped SnO_2 nanoparticles with size less than 10 nm can be synthesized by the aid of ultrasonic energy supplied via sonochemical synthesis. It is suggested that the ultrasonic not only provides energy for crystallite growth but also prevents the agglomeration of as-synthesized nanoparticles. It is revealed that Sb dopant strongly affects the crystallinity of SnO_2 reflecting the decrease in crystallite size and the deterioration of local structure bonding of SnO_2. It was acknowledged that both dopants play significant role on the enhancement in the electrical properties. The electrical resistivity of the codoped sample with F/Sb ratio of 1:5 mol% can be lowered to $3.96 \times 10^{-3}\ \Omega\cdot cm$.

In order to identify the optimal doping concentration of composite film for IR-shielding coating was observed. The UV-Vis-NIR spectra reveal that the surface plasmon resonance (SPR) absorption in the IR region was occurred by Sb doping which creates more carrier concentration in SnO_2 nanoparticles. The UV-Vis-NIR spectra in IR range reveal that transmittance change is 4.12 % for the 5ATO composite film, while it increases to 7.38 % for the 5:5FATO sample that is attributed to the higher density of free carriers provided by F ion doping. In the case of IR-shielding study, the results show that the temperature of non IR-shielding layer is higher than that of solar cell using the 5:5FATO composite films as the IR-shielding layer. Moreover, The V_{oc} of silicon solar cell of non IR-shielding layer is lower than that of 5:5FATO composite film. These results ensure that the V_{oc} changes inversely with temperature affecting to decreased efficiency of silicon solar cell. The expectation of this result implies that the temperature of silicon solar cell is preserved by 5:5FATO composite film and the efficiency is also maintained as an extended time.

REFERENCES

[1] http://solarpowernotes.com

[2] http://greenliving.lovetoknow.com

[3] Huiyong Liu, V.Avrutin, N lzyumskaya, Ü. Özgür, H. Morkoç, "Transparent conducting oxides for electrode applications in light emitting and absorbing devices"

[4] V.Jafari Fesharaki, Majid Dehghani and J. Jafari Fesharaki, "The Effect of Temperature on Photovoltaic Cell Efficiency", Proceedings of the 1st International Conference on Emerging Trends in Energy Conservation - ETEC Tehran, Tehran, Iran, 20-21 November 2011

[5] Kiyofumi Katagiri, Ryuichi Takabatake and Kei Inumaru, "Robust infrared-shielding coating films prepared using perhydropolysilazane and hydrophobized indium tin oxide nanoparitcles with tuned surface plasmon reasonance" Applied Materials and Interface (Appl. Mater. Interfaces 2013, 5, 10240-10245)

[6] D.G. Miao, S.X. Jiang, S.M. Shang, Z.M. Chen, J. Liu, "Infrared reflective property of AZO films prepared by RF-magnetron sputtering", Advanced Performance Materials 29(6) 321-326.

[7] C.S. Long, H. Lu, D. Lii, J. Huang, "Effects of annealing on near-infrared shielding properties of Cs-doped tungsten oxide thin films deposited by electron beam evaporation", Surface and Coatings Technology 284 (2015) 75-79.

[8] C.A. Rego, P.W. May, E.C. Williamson, M.N.R. Ashfold, Q.S. Chia, K.N. Rosser, N.M. Everitt, "CVD diamond growth on germanium for IR window applications", Diamond and Related Materials 3 (1994) 939-941.

[9] Z. Ng, K. Chan, C. Low, S. Kamaruddin, K. Sahdan, "Al and Ga doped ZnO prepared by a sol-gel spin coating technique", Ceramics International 41 (2015) S254-S258

[10] X. Lu, Z. Wang, X. Yang, X. Xu, L. Zhang, N. Zhao, J. Xu, "Antifogging and antireflective silica film and its application on solar modules", Surface and coating technology 206 (2011) 1490-1494.

[11] N. Wolf, T. Stubhan, J. Manara, V. Dyakonov, C.J. Brabec, Stabilization of aluminum doped zinc oxide nanoparticle suspensions and their application in organic solar cells", Thin Solid Films 564 (2014) 213-217.

[12] Al-Habi E, Aziz AM, Oyama M, El-Naggar MA, AlZayed N, Wojciechowski A, Kityk VI, Gold nanoparticles deposited on fluorine-doped tin oxide substrates as materials for laser operated optoeletronic devices. J Mater Sci Mater Electron. 24, 2422–2425 (2013).

[13] Giraldi RT, Escote TM, Bernardi BIM, Bouquet V, Leite RE, Longo E, Verela AJ, Effect of thickness on the electrical and optical properties of Sb doped SnO2 (ATO) thin films. J Electroceram. 13, 159–165 (2004).

[14] M. Zeman, O. Isabella, K. Jager, R. Santbergen, S. Solntsev, M. Topic and J. Krc, "Advanced light management approaches for thin-film silicon solar cells", Energy Procedia 15 , 189-199 (2012)

[15] http://www.reuk.co.uk/wordpress/solar/effect-of-temperature-on-solar-panels/

[16] David S. Giney, Handbook of transparent conductors.

[17] M.Van Hest, M.S. Dabney, J.D. Perkins, D.S. Ginley, M.P. Taylor, "Titanium-doped indium oxide: A high-mobility transparent conductor", Applied Physics Letters 87 (2005) 032111.

[18] K. Fleischer, E. Arca and I.V. Shvets, "Improving solar cell efficiency with optically optimized TCO layers", Solar Energy Materials and Solar cells 101, 262-269 (2012)

[19] Yujing Liu, "Nanostructured transparent conducting oxide electrode through nanoparticle assembly" Ludwig-Maximilians-Universität Müchen (2012)

[20] http://www.advanced-energy.com/en/FAQ.html

[21] M. Ajili, M. Castangné, N.K. Turki, "Spray solution flow rate effect on growth, optoelectronic characteristics and photoluminescence of SnO_2:F thin films for photovoltaic application", Optik-International Journal for Light and electron Optic 126 (2015) 708-714.

[22] J. Mazloom, F.E. Ghodsi, M. Gholami, "Fiber-like stripe ATO (SnO_2:Sb) nanostructured thin films grown by sol-gel method: Optical, topographical and electrical properties" Journal of Alloys and Compounds 579 (2013) 384-393.

[23] K.A. John, R.R.Philip, P. Sajan, T. Manju, "In situ crystallization of highly conducting and transparent ITO thin films deposited by RF magnetron sputtering", Vacuum 132 (2016) 91-94.

[24] M. Jothibas, C. Manoharan, S. Ramlingam, S. Dhanapandian, M. Bououdina, "Spectrosopic analysis, structural, microstructural, optical and electrical properties of Zn-doped In_2O_3 thin films" Spectrochimica Acta Part A: Molecular and Biomolecular Spectroscopy 122 (2014) 171-178.

[25] Y. Sun, H. Wang, J. Chen, L. Fang, L. Wang, "Structural and optoelectronic properties of AZO thin films prepared by RF magnetron sputtering at room temperature", Transactions of Nonferrous Metals Society of China 26 (2016) 1655-1662.

[26] H. Wang, Y. Sun, L. Fang, L. Wang, B. Chang, X. Sun, L. Ye, "Growth and characterization of high transmittance GZO films prepared by sol-gel method", Thin Solid Films 615 (2016) 19-24.

[27] K.G. Godinho, A.Walh, G.W. Watson, "Energetic and electronic structure analysis of intrinsic defects in SnO_2", Journal of Physical Chemistry C 113 (2009) 439-448.

[28] B. Stjerna, E. Olsson, C.G. Granqvist, "Optical and electrical properties of radio frequency sputtered tin oxide films doped with oxygen vacancies, F, Sb, or, Mo", Journal of Applied Physics 76 (1994) 3797.

[29] R.J. Choudhary, S.B. Ogale, S.R. Shinde, V.N. Kulkani, T. Venkatessan, K.S. Harshavardhan, M. Strikovski, B. Hannoyer, "Pulsed-electron-beam deposition of transparent conducting SnO_2 films and study of their properties", Applied Physics Letters 84 (2004) 1483.

[30] Joung Youn Ellie Kim, "Nanostructured transparent conducting oxides via blockcopolymer patterning" Sidney Sussex College (2012).

[31] Kathy Lu, "Nanoparticulate materials" WILEY.

[32] Jin Chant and Eric R. Waclawik, "Colloidal semiconductor nanocrystals:controlled synthesis and surface chemistry in organic media", RSC advances 4(45), 23505-23527 (2014).

[33] N. Soltani, E. Saion, M. Erfani, K. Rezaee, G. Bahmanrokh, G.P.C. Drummen, A. Babrami and M.Z. Hussein, "Influence of polyvinyl pyrrolidone concentration on particle size and dispersion of ZnS nanoparticles synthesized by microwave irradiation", Int. J. Mol. Sci. 13(10), 12412-12427 (2012).

[34] N. Ghows, M.H. Entezari, "Fast and easy synthesis of core-shell nanocrystal (CdS/TiO_2) at low temperature by microemulsion under ultrasound", Ultrasonics Sonochemistry 18 (2011) 629-634.

[35] Y. Masuda, "Size and controlled synthesis of monodisperse metal oxide and mix oxide nanocrystal", InTech 2, 55-85 (2011)

[36] Sam Zhang, "Orgnic nanostructured thin film devices and coating for clean energy".

[37] S. Wu, S. Yuan, L. Shi, Y. Zhao, J. Fang, "Preparation, characterization and electrical properties of fluorine-doped tin dioxide nanocrystals", Journal of Colloid and Interface Science 346 (2010) 12-16.

[38] T. Krishnakumar, R .Jayaprakash, N. Pinna, R.A. Phani, M. Passacantando, S. Santucci, "Structure, optical and electrical characterization of antimony-substituted tin oxide nanoparticles", Journal of Physics and chemistry of Solids 70 (2009) 993-999.

[39] S. Li, X. Qiao, J. Chen, H. Wang, F. Jia, X. Qiu, "Effects of temperature on indium tin oxide particles synthesized by co-precipitation", Journal of Crystal Growth 289 (2006) 151-156.

[40] G.M. Silva, E.H. de Faria, E.J. Nassar, K.J. Ciuffi, P.S. Calefi, "Synthesis of indium tin oxide nanoparticles by a nonhydrolytic sol-gel method", Quimica Nova 35(3) (2012) 473-476.

[41] J. Zhang, L. Gao, "Synthesis and characterization of antimony-doped tin oxide (ATO) nanoparticles by a new hydrothermal method", Materials Chemistry and Physics 87 (2004) 10-13.

[42] D. Jung, D. Park, "Synthesis of nano-sized antimony-doped tin oxide (ATO) particles using a DC arc plasma jet", Applied Surface Science 255 (2009) 5409-5413.

[43] M. Sadegh, Y. Parast, A. Morsali, "Sonochemical-assisted synthesis of nano-structrued indium(III) hydroxide and oxide", Ultrasonics Sonochemistry 18 (2011) 375-381.

[44] A. Omidi, A. Habibi-Yangjeh, M. Pirhasemi, "Application of ultrasonic irradiation method for preparation of ZnO nanostructures doped with Sb^{3+} ions as a highly efficient photocatalyst", Applied Surface Science 276 (2013) 468-475.

[45] T.V. Tran, S. Turrell, M. Eddafi, B. Capoen, M. Bouazaoui, P. Roussel, S. Berneschi, G. Righini, M. Ferrari, S.N.B. Bhaktha, O. Cristini, C. Kinowski, "Investigations of the effects of growth of SnO_2 nanoparticles on the structural properties of glass-ceramic planar waveguides using Raman and FTIR spectroscopies", Journal of Molecular Structrure 976 (2010) 314-319.

[46] N. Li, Q. Meng, N. Zhang, "Dispersion stabilization of antimony-doped tin oxide (ATO) nanoparticles used for energy-efficient glass coating", Particuology 17 (2014) 49-53.

[47] Y. Cho, G. Yi, J. Hong, S.H. Jang, S. Yang, "Colloidal indium tin oxide nanoparticles for transparent and conductive films", Thin Solid Films 515 (2006) 1864-1871.

[48] C. Goebbert, R. Noninger, M.A. Aegerter, H. Schmidt, "Wet chemical deposition of ATO and ITO coatings using crystalline nanoparticles redispersable in solutions", Thin Solid films 351 (1999) 79-84.

[49] K. Katagiri, R. Takabatake, K. Inumaru, "Robust infrared-shielding coating films prepared using perhydropolysilazane and hydrophobized indium tin oxide nanoparticles with tuned surface plamon resonance", ACS Applied Materials and Interfaces 5 (2013) 10240-10245.

[50] S. Xiaolan, L. Dongfeng, Z. Yimeng, D. Yi, L. Mei, W. Shunkui, H. Xi and Q. Yixin, "Grain growth kinetics of SnO_2 nanocrystals synthesized by precipitation method", Journal of Wuhan University of Technology-Mater, Sci.Ed. (2010) 929-934

[51] J.F Huang, X.R. Zeng, L.Y. Cao, N.B. Xiong, "Preparation of Y_2BaCuO_5 nanoparticles by a co-precipitation process with the aid of ultrasonic irradiation", Journal of Materials Processing Technology 209 (2009) 2963-2966.

[52] S. Takenaka, R. Takahashi, S. Sato, T. Sodesawa, F. Matsumoto, S. Yoshida, "Pore size control of mesoporous SnO_2 prepared by using stearic acid", Microporous and Mesoporous Materials 59 (2003) 123-131.

[53] J.S Lee, S.C Choi, "Solvent effect on synthesis of indium tin oxide nano-powders by a solvothemal process", Jounal of European Ceamic Society 25 (2005) 3307-3314.

[54] A. Hassanzadeh, B. Moazzez, H. Haghgooie, M. Nasseri, M. Maqsood Golzan, H. Sedghi, "Synthesis of SnO_2 nanopowders by a sol-gel process using proponol-isopropanol mixture", Central European Journal of Chemistry 6(4) (2008) 651-656.

[55] Y. Kim, S.P. Kim, S.D. Kim and S.E. Kim, "Nitrogen-doped transparent tin oxide thin films deposited by sputtering", Current Applied Physic 11 (2011) S139-S142.

[56] H. Kim, R.C.Y. Auyenung, A. Piqué, "Transparent conducting F-doped SnO_2 thin films grown by pulsed laser deposition", Thin Solid Films 516 (2008) 5052-5056.

[57] A. Hassanzadeh, B. Moazzez, H. Haghgooie, M. Nasseri, M. Maqsood Golzan and H. Sedghi, "Synthesis of SnO_2 nanopowders by a sol-gel process using proponol-isopropanol mixture", Central European Journal of Chemistry 6(4) (2008) 651.

[58] M. Wang, Y. Gao, L. Dai, C. Cao, and X. Guo, "Influence of surfactants on the morphology of SnO_2 nanocrystals prepared via a hydrothermal method", Journal of Solid State Chemistry 189 (2010) 49-56.

[59] S.M. Sedghi, Y. Mortazavi A. Khodadadi, "Low temperature CO and CH_4 dual selective gas sensor using SnO_2 quantum dots prepared by sonochemical method", Sensors and Actuators B:chemical 145 (2010) 7-12.

[60] H.W. Kim, H.S. Kim, H.G. Na, J.C. Yang, M.A. Kebede, and C. Lee, Ceramics International 37 (2011) 593-598.

[61] A.B. Babar, S.S. Shinde, A.V. Moholkar, C.H. Bhosale, J.H. Kim, and K.Y. Rajpure, "Structural and optoelectronic properties of antimony incorporated tin oxide thin films", Journal of Alloys and Compounds 505 (2010) 416-422.

[62] L. Tan, L. Wang, and Y. Wang, "Hydrothermal synthesis of SnO_2 nanostructures with different morphologies and their optical properties", Journal of Nanomaterials Article ID 529874 (2011) 10 pages.

[63] L.S. Wang, H.F. Lu, R.Y. Hong, W.G. Feng, "Synthesis and electrical resistivity analysis of ATO-coated talc", Powder Technology 224 (2012) 124-128.

[64] O. Lupan, L. Chow, G. Chai, A. Schulte, S Park, H. Heinrich, "A rapid hydrothermal synthesis of rutile SnO_2 nanowires", Materials Science and Engineering: B 157 (2009) 101-104.

[65] H.J. Park, J.D. Byun, K. Lee, "Electrical and optical properties of fluorine-doped tin oxide (SnOx:FF) thin films deposited on PET by using ECR-MOCVD", Journal of Electroceramics 23 (2009) 506-511.

[66] Z.L. Liu, L.X. Wu, F. Gao, C.J. Shen, H.T. Li, K.P. Chu, "Determination of surface oxide vacancy position in SnO_2 nanocrystals by Raman spectroscopy", Solid State Communications 151 (2011) 811-814.

[67] K.R. Mishra, K.S. Pandey P.P., Sahay, "Influence of In doping on the structural, photo-luminescence and alcohol response characteristics of SnO_2 nanoparticles", Materials Research Bulletin 48 (2013) 4196-4205.

[68] V.T. Tran, S. Turrell, M. Eddafi, B. Capoen, M. Bouazaoui, P. Roussel, S. Berneschi, G. Righini, M. Ferrari, B.S. Bhaktha, O. Cristini, C. Kinowaki, "Investigations of the effects of the growth of SnO_2 nanoparticles on the structural properties of glass-ceramic planar waveguides using Raman and FTIR spectroscopies", Journal of Molecular Structure 976 (2010) 314-319.

[69] J. Kaur, J. Shah, K.R. Kotnala, C.K. Verma, "Raman spectra, photoluminescence and ferromagnetism of pure, Co and Fe doped SnO_2 nanoparticles", Ceramics International 38 (2012) 5563-5570.

[70] R.A. Babar, S.S. Shinde, V.A. Moholkar, H.C. Bhosale, H.J. Kim, Y.K. Rajpure, "Structure and optical properties of antimony incorporated tin oxide thin film", Journal of Alloy and Compounds 579 505 (2010) 416-422.

[71] S. Bang, S. Lee, Y. Ko, J. Park, S. Shin, H. Seo, H. Jeon, "Photocurrent detection of chemically tuned hierarchical ZnO nanostructures grown on seed layers formed by atomic layer deposition", Nanoscale Research Letters 7 (2012) 290.

[72] D. Chu, A. Younis, S. Li, "Direct growth of TiO_2 nanotubes on transparent substrates and their resistive switching characteristics", Journal of Physics D: Applied Physics 45 (2012) 335-306.

[73] N.J. Park, K.J. Shon, M. Jin, S.S. Kong, K. Moon, O.G. Park, H.J. Boo, M.J. Kim, "Room-temperature CO oxidation over a highly ordered mesoporous RuO_2 catalyst", Reaction Kinetics, Mechanisms and Catalysis 103 (2011) 87-99.

[74] Kh.E. Shokr, M.M. Wakkad, A.A. El-Ghanny, M.H. Ali, "Sb-doped effects on optical and electrical parameters of SnO_2 films", Journal of Physics and Chemistry of Solids 61 (2000) 75-85.

[75] B. Thangaraju, "Structural and electrical studies on highly conducting spray deposited fluorine and antimony doped SnO_2 thin films from $SnCl_2$ precursor", Thin solid Films. 402 (2002) 71-78.

[76] C.S. Tian, X.L. Chen, J. Ni, J.M. Liu, D.K. Zhang, Q. Huang, Y. Zhao, X.D. Zhang, "Transparent conductive Mg and Ga co-doped ZnO thin films for solar cells grown by magnetron sputtering: H_2 induced changes", Solar Energy Materials and Solar cells 125 (2014) 59-65.

[77] Z. López-Cabaňa, S.C. Torres, G. González, "Semiconducting properties of layered cadmium sulphide-based hybrid nanocomposites", Nanoscale Research Letters 6 (2011) 523.

[78] Z. Pan, P. Zhang, X. Tian, G. Cheng, Y. Xie, H. Zhang, X. Zeng, C. Xiao, G. Hu, Z. Wei, "Properties of fluorine and tin co-doped ZnO thin films deposited by sol-gel method", Journal of Alloy and Compounds 576 (2013) 31-37.

[79] K. Ma, N. Zhou, M. Yuan, D. Li, D. Yang, "Tunable surface plasmon resonance frequencies of monodisperse indium tin oxide nanoparticles by controlling composition, size, and morphology", Nanoscale Research Letters 9 (2014) 547.

[80] M. Kanehara, H. Koike, T. Yoshihasu, T. Teranishi, "Indium tin oxide nanoparticles with compositionally tunable surface plasmon resonance frequencies in the near-IR region", Journal of the American Chemical Society 131 (2009) 17736-17737.

[81] A. G. Emslie, F. T. Bonner, and L. G. Peck, "Flow of a Viscous Liquid on a Rotating Disk", Journal of Applied Physics 29 (1958) 858-862.

[82] H. Huang, M. Ng, Y. Wu, L. Kong, "Solvothermal synthesis of Sb:SnO_2 nanoparticles and IR shielding coating for smart window", Materials and Desing 88 (2015) 384-389.

[83] R. Noonuruk, W. Techitdheera, W. Pecharapa, "Characterization and ozone-induce coloration of $Zn_xN_{1-x}O$ thin films prepared by sol-gel method", Thin Solid Films 520 (2012) 2769-2775.

[84] J. Nelson, "The Physics of Solar Cells. London":, Imperial College 2003.

AUTHOR BIOGRAPHY

Miss Russameeruk Noonuruk

DATE OF BIRTH	19 December 1986
ADDRESS	88/6 M.3, Sam Mueang,Lat Bua Luang, Phra Nakhon Si Aytthaya, Thailand 13230
EUCATION	Bachelor degree of Science in Applied Physics and Industrial Instrument, Faculty of Science, King Mongut's Institute of Technology Ladkrabang (KMITL), Bangkok, Thailand (2009). Master of Science in Nanoscience and Nanotechnology, College of Nanotechnology, King Mongut's Institute of Technology Ladkrabang (KMITL), Bangkok, Thailand (2012).

PUBLICATION:

1. R. Noonuruk, W. Mekprasart, N. Wongpisutpaisan, N. Vittayakorn and W. Pecharapa, "SnO_2 Nanoparticle Synthesized by Ultrasonic-assisted Process", Advanced Materials Research 770 (2013) pp. 299-302.

2. Russameeruk Noonuruk, Naratip Vittayakorn, Wanichaya Mekprasart and Wisanu Pecharapa, "Sb-doped SnO_2 nanoparticles synthesized by sonochemical-assisted precipitation process", Journal of Nanoscience and Nanotechnology 15 (2015) pp.2564-2569. (IF: 1.339; 2013)

3. R. Noonuruk, W. Meakprasart, N. Vittayakorn, J. Sritharathikhun, W. Pecharapa, "Physical, electrical and optical properties of F/Sb codoped SnO_2 synthesized via sonochemical process", Ferroelectrics 490 (2016) pp. 136-148. (IF: 0.469; 2015)

CONFERENCES:

1. SnO_2 Nanoparticle Synthesized by Ultrasonic-Assisted Process "International Conference on Applied Physics and Material Applications (ICAPMA2013)" 20-22 February 2013, Cha-Am, Thailand (Oral presentation)
2. Sb-doped SnO_2 nanoparticles synthesized by sonochemical-assisted precipitation process "Nano Korea 2013 Symposium" July 2013, Seoul, Korea (Oral presentation)
3. F-doped SnO_2 Nanopowders Synthesized by Ultrasonic-Assisted Co-precipitation Method "Siam Physics Congress (SPC2013)", 22-23 March,Chaing Mai, Thailand (Poster presentation)
4. M-doped SnO_2 Nanoparticles (M=F, Sb) Prepared by Sonochemical-assisted Methods "11th Eco-Energy and Materials Science and Engineering Symposium (EMSES2013)" 18-21 December, Phuket, Thailand (Oral presentation)
5. Effect of annealing temperature on crucial optical properties of fluoride doped tin oxide films grown by sol-gel route "19th International Conference onTernary and Multinary Compounds" 1-5 September 2014, Niigata, Japan (Poster presentation)
6. Idium Tin Oxide conductive nanoparticles synthesized by sonochemical method "Southeast Asia Conference on Themoelectrics", 22-23 December 2014, Pakse, Lao
   (Poster presentation)
7. Effect of annealing temperature on the properties of ATO nanoparticles dispersed in silica films "The 41 congress on science and technology of Thailand (STT41)" 6-8 November 2015, Suranaree University of Technology , Nakhon Ratchasima, Thailand
   (Poster presentation)
8. Surface wettability of silica films modified by UV/Ozone Treatment "International Conference on Science and Technology of Emerging Materials. 27-29 July 2016, Pattaya, Thailand.
   (Poster presentation)

Advanced Materials Research Vol. 770 (2013) pp 299-302
© (2013) Trans Tech Publications, Switzerland
doi:10.4028/www.scientific.net/AMR.770.299

SnO_2 Nanoparticle Synthesized by Ultrasonic-Assisted Process

Russameeruk Noonuruk[a], Wanichaya Mekprasart[b], Narongdet Wongpisutpaisan[c], Naratip Vittayakorn[d] and Wisanu Pecharapa[e]

College of Nanotechnology, King Mongkut's Institute of Technology Ladkrabang, Bangkok, 10520, Thailand

Thailand and Center of Excellence in Physics (ThEP Center), CHE, 328 SiAyutthaya RD, Bangkok, 10400, Thailand

[a]russameeruk@gmail.com, [b]wani.mek@gmail.com, [c]mong_mooo@hotmail.com, [d]naratipcmu@yahoo.com, [e]kpewisan@gmail.com

Keywords: SnO_2 nanoparticles, Ultrasonic-assisted, Precipitation

Abstract. SnO_2 nanoparticles were synthesized by ultrasonic-assisted precipitation process using stannic chloride pentahydrate ($SnCl_4 \cdot 5H_2O$) as a precursor. The stannic chloride aqueous solution was precipitated by ammonia under sonication. The as-synthesized precipitates were dried at 80 ºC and then calcined at 400 ºC for 2 h. The physical properties of nanoparticles with/without sonication were characterized by thermogravimetic and differential thermal analysis, X-ray diffraction, and transmission electron microscope. The results reveal that ultrasonic radiation has significant influence on phase transformation mechanism from $Sn(OH)_4$ to SnO_2, grain size and uniformity of SnO_2 nanoparticles.

Introduction

Tin oxide nanoparticles (SnO_2) have received great interest from researchers owing to their wide varieties of applications in different fields such as photovotaics, photocatalysis, energy storage, sensing and optoelectronic devices [1]. The performance of these devices can be improved by controlling the structural properties of SnO_2 in form of low dimensional nanostructures. It is recognized that an improvement in physical, optical, catalytic and electric properties can be effectively achieved by reducing the size of the particles down to nanoscale regime. Due to high surface to volume ratio, the nanomaterials have fewer adjacent coordinate atoms as compared with the bulk atoms resulting to drastic increase of large specific surface areas [2]. Meanwhile, several methods have been conducted on the preparation of SnO_2 nanostructure bottom-up building form including the sol-gel methods, chemical vapor deposition, precipitation, solvothermal and hydrothermal methods. Among these techniques, the precipitation method has significant advantages over the others such as simple synthesis process, low energy consumption and simplicity of solution concentration. However, this method still has crucial problems which are the high degree of agglomeration and difficulty of controllable size distribution [3]. Recently, synthesis technology of ultra-fine nano-structured materials can be attained by utilizing ultrasonic radiation because it is able to provide high frequency clean energy to prevent the agglomeration [4]. This paper reports the synthesis of SnO_2 nanoparticles using ultrasonic-assisted precipitation process. The physical properties of nanoparticles with/without sonication were characterized by thermogravimetic and differential thermal analysis (TG/DTA), X-ray diffraction (XRD) and transmission electron microscope (TEM). Effects of sonication supplied during precipitation process on physical structures of SnO_2 nanoparticles were analysed and involved mechanisms are proposed.

Experimental

SnO_2 nanoparticles were synthesized by ultrasonic-assisted precipitation process using 0.2 M stannic chloride pentahydrate. The sonication was operated at 120 W with frequency of 40 kHz using ultrasonic bath. Firstly, 14.024 g $SnCl_4 \cdot 5H_2O$ was dissolved in 200 ml deionized water and

kept under sonication in ultrasonic bath at 60 °C for 20 min until homogeneous solution was reached. Then, the aqueous ammonia was added dropwise into solution under ultrasonic bath for 1 h. The precipitate of tin hydroxide was obtained and then aged for 24 h at room temperature. The precipitate was washed several times with deionized water and ethanol via centrifugation to remove chlorine ions and other residues. The conventional precipitation method was prepared by magnetic stirrer under similar condition. Finally, the as-synthesized precipitates were dried in oven at 80 °C and then calcined at 400 °C for 2 h.

The thermal behaviour of as-synthesized precipitates were characterized by thermogravimetic and differential thermal analysis (DTA, Perkin Elmer Pyris) operated in ambient air with heating rate of 5 °C/min in range of 40-900 °C. The physical properties of nanoparticles prepared with/without sonication were characterized by X-ray diffraction, and transmission electron microscope. XRD (Burker, D8) operated at 40 kV and 30 mA over a 2θ in the range of 20-70° using Cu-K_α radiation. The diffraction patterns were recorded with a scanning rate 2°/min. The size,shape and crystal structure of as-synthesized SnO_2 nanoparticles were observed by TEM (FEI, TECNAI $G^2$20) operated at 200 kV. Before TEM analyse, the samples was suspended in ethanol and dropped on a carbon-film coated copper grid.

Results and Discussion

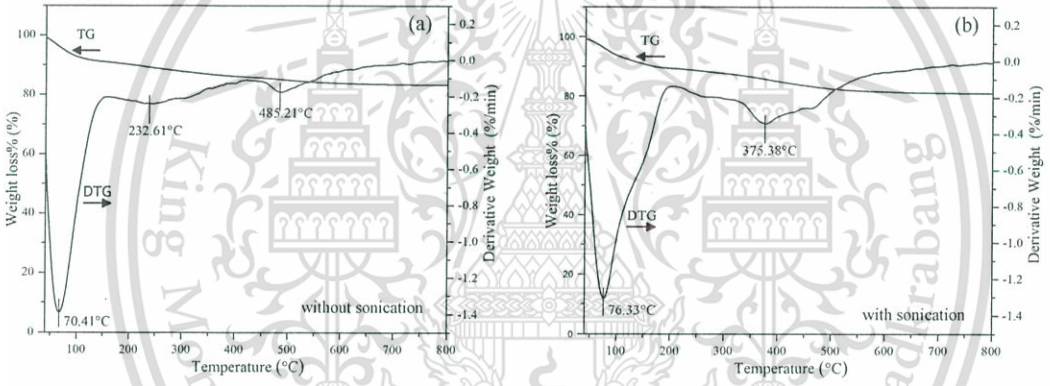

Fig. 1 TG/DTA curves of as-synthesized SnO_2 powders (a) without and (b) with sonication.

The thermal behaviors of as-synthesized precipitates SnO_2 powders prepared with and without sonication are shown in Fig.1 (a) and (b), respectively. The TG/DTA curves of as-synthesized precipitates detected at around 70 °C and 230 °C are assigned to the removal of absorbed water and alcohol and the decomposition of NH_4^+ in the powder according to the Eq.1 [5],

$$SnCl_4 + 4NH_4OH \rightarrow Sn(OH)_4 + 4NH_4Cl. \quad (1)$$

The noticeable peak position about 485 °C of sample prepared without sonication is attributed to the dehydroxylation and phase transformation of the as-precipitated product according to the Eq. 2,

$$Sn(OH)_4 \rightarrow SnO_2 + 2H_2O. \quad (2)$$

Interestingly, the phase transformation peak of sample synthesized by ultrasonic-assisted method clearly shifts to lower temperature at around 375 °C. The shift could be due to increase of the surface area possibly resulting from the size decrease of material. During ultrasonic radiation through a liquid, ultrasound can efficiently generates expansion and compression cycles leading to the cavitations in an aqueous medium. The cavitation effect in chemical process by restrains aggregation of particles can consequently decrease the particle size and reduce temperature of phase transformation [6].

Fig. 2 shows the XRD patterns of as-synthesized and SnO_2 nanoparticles synthesized with and without sonication assistance. After calcinations at 400 °C, the sharpness and intensity of diffraction peaks increases distinguishedly indicating the transformation of amorphous phase to well-defined

crystallization of SnO_2 after calcination at this temperature range. All diffraction peaks of SnO_2 nanoparticles prepared with/without sonicationevidently reveal polycrystalline phase of tetragonal SnO_2 crystal structure [7]. From Scherrer's equation [8], the broader intensity peaks of as-precipitated powders indicate that their average size is about 13-15 nm.

It is noticed that the diffraction peaks of SnO_2 powders prepared by an assistance of ultrasonic possess higher sharpness than one prepared by conventional process due to the lower temperature phase transformation of $Sn(OH)_4$ to SnO_2.

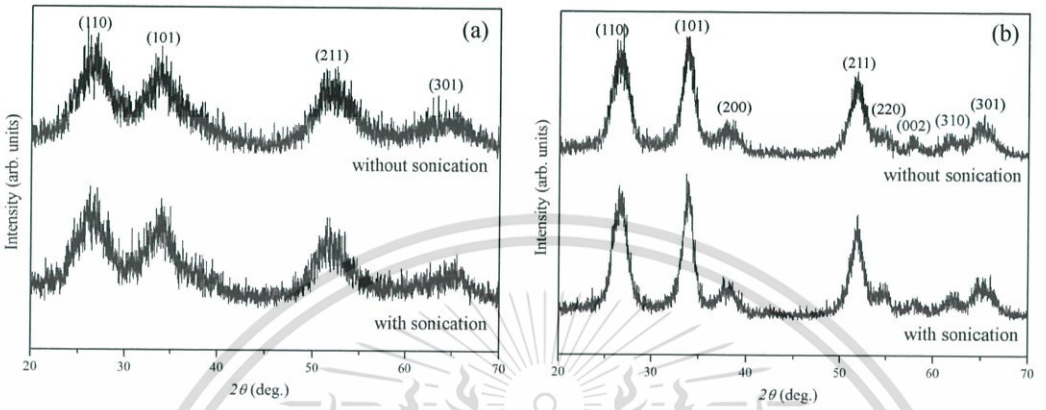

Fig. 2 XRD patterns of (a) as-precipitated powders and (b) after-calcinedSnO$_2$ nanoparticles with/without sonication.

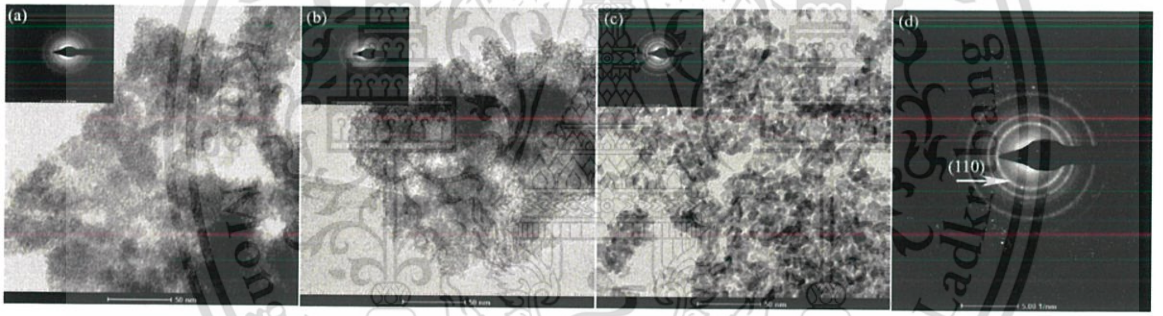

Fig. 3 TEM images and SAED patterns of SnO_2 powders at different conditions (a) as-synthesized without (b) and (c,d) synthesized SnO_2 nanoparticles with sonication.

The TEM images and selected area electron diffraction (SAED) patterns of SnO_2 nanoparticles synthesized by precipitation method are illustrated in Fig.3. As seen in Fig. 3 (a) and (b), the morphologies and particle size of as-precipitated SnO_2 nanoparticles prepared with/without sonication are unable to identify due to extremely tiny structures of the as-prepared particles reflecting their amorphosity in nature. After calcinations, the TEM image of SnO_2 nanoparticles shows excellent disperse siveness with less agglomeration and an uniformity in particle size of estimately 10-15 nm. The SAED patterns of as-precipitated nanoparticles show soft halo rings reflecting an amorphous phase. While SAED of after-calcined SnO_2 nanoparticles exhibits several strong halo rings confirming to polycrystalline and the brightest inner ring attributes to the (110) plane of SnO_2 [9].

Conclusion

SnO_2 nanoparticles were synthesized by ultrasonic-assisted precipitation method. From the TG/DTA results, ultrasonic-assisted has considerable effect on reduced temperature of phase transformation from $Sn(OH)_4$ to SnO_2 due to cavitations in solution during ultrasonic radiation. The XRD and TEM results exhibits that, by an assistance of ultrasonic energy during precipitation process in combination of calcination at rather low temperature, the well-dispersed SnO_2 nanoparticles with uniform size in the range of 10-15 nm can be successfully prepared.

Acknowledgments

This work has partially been supported by the National Nanotechnology Center (NANOTEC), NSTDA, Ministry of Science and Technology, Thailand, through its program of Center of Excellence Network. Authors would like to express deep thank to Rajamangala University of Technology Thanyaburi (RMUTT) for XRD measurement and King Mongkut's Institute of Technology Ladkrabang Research Fund (KMITL) for financially support.

References

[1] H. Mahmoudi Chenari, L. Weinhardt, N.S. Rodriguez Lastra, M.A. Ernst, F. Reinert, M.M. Golzan and A. Hassanzadeh, Structural properties and x-ray photoelectron spectroscopic study of SnO_2 nanoparticles, Mater.Lett. 85 (2012) 168-170.

[2] T. Krishnakumar, R. Jayaprakash, N. Pinna, A.R. Phani, M. Passacantando and S. Santucci, Structural, optical and electrical characterization of antimony-substituted tin oxide nanoparticles, J. Phy.Chem.Solids. 70 (2009) 993-999.

[3] K.Chang Song and Y.kang, Preparation of high surface area tin oxide powders by a homogeneous precipitation method, Mater.Lett. 42 (2000) 283-289.

[4] S.Mosadegh Sedghi, Y.Mortazavi and A. Khodadadi, Low temperature CO and CH_4 dual selective gas sensor using SnO_2 quantum dots prepared by sonochemical method, Sen.Actuat. B-chem. 145 (2010) 7-12.

[5] S.Xiaolan, L. Dongfeng, Z. Yimeng, D. Yi, L. Mei, W. Shunkui, H. Xi and Q. Yixin, Grain Growth Kinetics of SnO_2 nanocrystals Synthesized by Precipitation Method, Journal of Wuhan University of Technology-Mater, Sci.Ed. (2010) 929-934.

[6] J.F Huang, X.R. Zeng, L.Y. Cao, N.B. Xiong, Preparation of Y_2BaCuO_5 nanoparticles by a co-precipitation process with the aid of ultrasonic irradiation, J.Mmater.Process.Tech. 209 (2009) 2963-2966.

[7] S. Takenaka, R. Takahashi, S. Sato, T. Sodesawa, F. Matsumoto and S. Yoshida, Pore size control of mesoporous SnO_2 prepared by using stearic acid, Micropor.Mesopor.Mat. 59 (2003) 123-131.

[8] J.S Lee and S.C Choi, Solvent effect on synthesis of indium tin oxide nano-powders by a solvothemal process, J.Eur.Ceram.Soc. 25 (2005) 3307-3314.

[9] A. Hassanzadeh, B. Moazzez, H. Haghgooie, M. Nasseri, M. Maqsood Golzan and H. Sedghi, Synthesis of SnO_2 nanopowders by a sol-gel process using proponol-isopropanol mixture, Central European Journal of Chemistry, 6(4), (2008)651-656.

Article

Journal of
Nanoscience and Nanotechnology
Vol. 15, 2564–2569, 2015
www.aspbs.com/jnn

Sb-Doped SnO_2 Nanoparticles Synthesized by Sonochemical-Assisted Precipitation Process

Russameeruk Noonuruk[1], Naratip Vittayakorn[1], Wanichaya Mekprasart[1], Jaran Sritharathikhun[2], and Wisanu Pecharapa[1,3,*]

[1] College of Nanotechnology, King Mongkut's Institute of Technology Ladkrabang, Bangkok, 10520, Thailand
[2] National Electronics and Computer Technology Center, Pathumthani, 12120, Thailand
[3] Thailand and Center of Excellence in Physics (ThEP Center), CHE, 328 Si Ayutthaya Rd., Bangkok, 10400, Thailand

Sb-doped SnO_2 nanopowders were synthesized by sonochemical-assisted precipitation process using stannic chloride pentahydrate ($SnCl_4 \cdot 5H_2O$) and antimony chloride ($SbCl_3$) as starting precursors. Effect of sonication and Sb doping concentrations on physical structures and electrical properties of Sb-doped SnO_2 nanoparticles were investigated by X-ray diffraction, transmission electron microscope, X-ray photoelectron spectroscopy, Raman spectroscopy and two-point probe method. The results indicated that the good dispersion with less agglomeration of particles in SnO_2 phase can be obtained by single step sonochemical-assisted process. Moreover, XRD results indicated that the crystallinity of Sb-doped SnO_2 nanopowders deteriorated with increasing Sb content, suggesting that Sb dopant significantly prevent SnO_2 crystallite growth. The XPS spectra of Sb-doped SnO_2 obviously confirmed the existence of Sb ion incorporated into SnO_2 matrix. These results revealed that incorporation of Sb ions into SnO_2 lattice with specific concentration has significant influence on formation and crystallization and can dramatically enhance the conductivity of tin oxide.

Keywords: Sb-Doped SnO_2 Nanopowders, Sonochemical, Precipitation.

1. INTRODUCTION

Sb-doped SnO_2 (ATO) has recently received considerable interest due to its technological importance as a solar energy material both in energy generation and in energy saving applications such as rechargeable Li batteries,[1] transparent electrodes,[2] solar cell,[3] heat-reflection coating,[4] and photovoltaic devices.[5] In recent years, great attention has been paid on the synthesis, characterization and applications of Sb-doped SnO_2 based transparent conducting oxide owing to alternatively low-cost to rather expensive indium tin oxide and excellent electronical stability in oxidizing environment.[6] High conductivity of Sb-doped SnO_2 is typically originated from good substitution of Sn^{4+} by Sb^{5+}, leading to creation of a conducting carrier-oxygen vacancy. The oxygen vacancies can act as doubly ionized donors generating extra electrons into the conduction band.[7] Furthermore, the resistivity of Sb-doped SnO_2 particles can be reduced by controlling their sizes down to nanoscale regime, which have a high driving force of densification. The nanomaterials have fewer adjacent coordinate atoms as compared with the bulk atoms resulting to drastic increase of large specific surface areas. Up to now, several methods have been conducted on the preparation of Sb-doped SnO_2 nanostructure bottom-up building form including sol–gel method,[8] precipitation,[9] solvothermal[10] and hydrothermal method.[11] Among these techniques, the precipitation method has significant advantages over the others such as simple synthesis process, low energy consumption and simplicity of solution concentration. However, the high degree of agglomeration of ultra-fine nano powder is still the crucial problem. Recently, synthesis technology of ultra-fine nano-structured material can be attained by sonochemical method. During ultrasonic irradiation, the cavitation effect in chemical process is able to provide high frequency clean energy to prevent the agglomeration. Nevertheless, to our recent knowledge, researches devoted on sonochemical synthesis of ATO nanostructure are rarely explored. In this work, an endeavor was taken on the synthesis of Sb-doped SnO_2 nanoparticles employing

*Author to whom correspondence should be addressed.

1533-4880/2015/15/2564/006 doi:10.1166/jnn.2015.10222

sonochemical-assisted precipitation process. Effect of Sb doping concentrations on physical structures and electrical properties of Sb-doped SnO_2 nanoparticles were investigated. The characterizations of as-prepared samples were conducted using X-ray diffraction (XRD), transmission electron microscope (TEM), X-ray photoelectron spectroscopy (XPS) and Raman spectroscopy. The resistivity measurement was carried out using conventional two-point probe method.

2. EXPERIMENTAL DETAILS

Sb-doped SnO_2 nanopowders were synthesized by sonochemical-assisted precipitation process using stannic chloride pentahydrate ($SnCl_4 \cdot 5H_2O$) and antimony chloride ($SbCl_3$) as starting precursors. 0.2 M of $SnCl_4$ and $SbCl_3$ powders with Sb concentration at 0, 5, 10, 15 and 20 mol% were dissolved in absolute ethanol and then acetylacetone was added. The precursor was stirred for 20 min at room temperature until homogeneous solution was reached. The solution was sonicated for 30 min by a direct-immersion ultrasonic horn using Sonic model VCX 750 (750 W, 20 kHz). The aqueous ammonia was added drop wise to the stock solution during sonication until the pH value of the solution was reached to the range of 9–10. After sonication for 30 min, the completely precipitates product was obtained and allowed to cool down to room temperature. The precipitates were washed several times with deionized water via centrifugation at 4500 rpm for 4 min. Finally, the as-precipitated powders were dried slowly at 80 °C and calcined at temperature of 400 °C for 2 h. The structural properties of powders were characterized by XRD (LabX, XRD-6000) operated at 40 kV and 30 mA using Cu-$K\alpha$ radiation over a 2θ from 20 to 80° with steps of at 0.2°. The size, shape and crystal structure of the particles were observed by transmission electron microscope (FEI, TECNAI $G^2$20) operated at 200 kV. Chemical bonding of powders was characterized by Raman spectroscopy carried out in the range of 300–800 cm^{-1}. The surface chemical state analysis was carried out by X-ray photoelectron spectroscopy (Kratos analytical, AXIS ULTRA^{DLD}) using Al-K_α with radiation at 1.4 keV. The room-temperature resistivity measurement was carried out using typical two-point probe configuration setup with direct current. Before resistance measurement, 0.4 g Sb-doped SnO_2 powders (without added binder) were pressed by using hydraulic pelletizer with diameter of 10 mm under 4 tons for 4 min. Then the pellets were calcined at 1000 ∘C without holding times.

3. RESULTS AND DISCUSSION

Figure 1 shows the XRD patterns of as-synthesized ATO nanopowders prepared via sonochemical-assisted precipitation process. The broad diffraction peaks of samples possess the major peaks of (110), (101), (211) and (301)

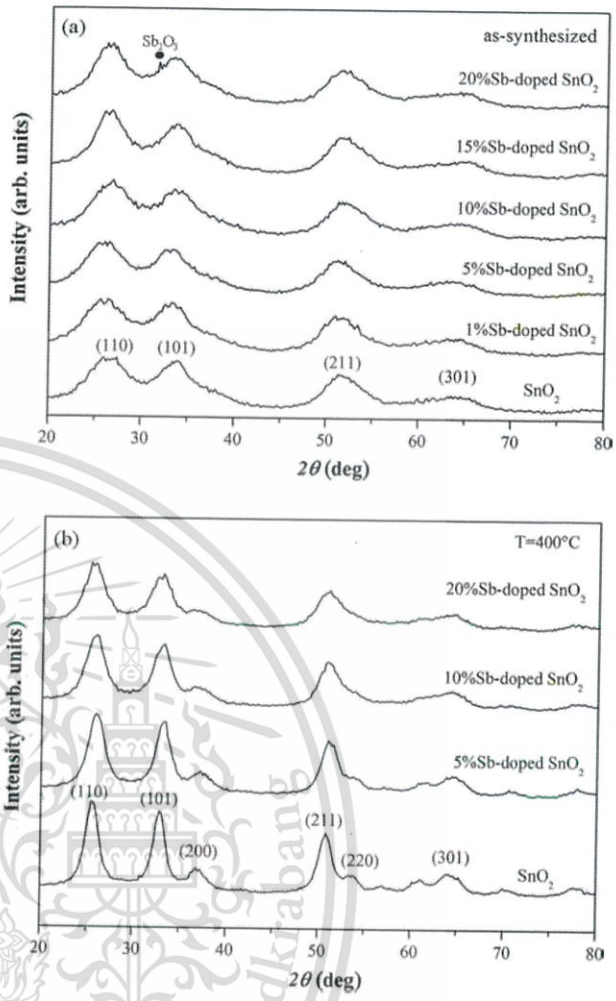

Figure 1. XRD patterns of Sb-doped SnO_2 nanopowders (a) as-synthesized (b) after calcinations at 400 °C.

plane orientations corresponding to tetragonal SnO_2 crystal structure.[12] It is implied that as-synthesized product obtained by this synthetic method comprises primarily polycrystalline phase of SnO_2 structure. The formation of crystalline phase of SnO_2 during sonochemical process without applying any thermal treatment could be occurred by cavitation effect during ultrasonic radiation though a precipitate solution. Under intense ultrasound irradiation, rapid collision driven by strong ultrasound energy can generate localized high temperature area, which can expedite the condensation reactions of hydroxyl groups to produce the nucleation of fine spherical nanoparticles of SnO_2 according to chemical ractions:[13]

$$SnCl_4 + 4NH_4OH_4 \longrightarrow SnOH_4 + 4NH_4Cl \quad (1)$$

$$Sn(OH)_4 \xrightarrow{\text{ultrasonic radiation}} SnO_2 + 4H_2O \quad (2)$$

This result indicates that the as-synthesized powder in SnO_2 phase can be obtained by single step sonochemical-assisted process. In addition, the sharpness and intensity of diffraction peaks drastically increase after calcinations at

Table I. The average crystallite sizes of all nanopowders were calculated from the peaks of (110).

% Sb concentrations (%)	As-synthesized D (nm)	Calcination D (nm)
0	2.64	11.6
1	2.25	–
5	2.59	9.33
10	2.71	7.65
15	3.71	–
20	3.27	6.99

400 °C, reflecting that the crystallization of the oxide compounds tends towards more integrity with grater crystallite size. The average crystallite size of nanopowders can be calculated from the full-width at half maximum (FWHM) by well-known Scherrer's equation as follows:

$$D = \frac{0.9\lambda}{\beta \cos\theta} \quad (3)$$

where D is the crystallite size, K is the shape factor, λ is the X-ray wavelength of Cu K_α(0.154 nm), β is the full-width at half maximum (FWHM) and θ is the Bragg angle. The average crystallite sizes of all nanopowders were calculated from the peaks of (110) and summarized in Table I. The smallest crystallite size of ~2.4 nm was obtained from as-synthesized product, while the crystallites become larger in size after calcinations due to the thermal energy promoted crystallite growth.

From Figure 1(a), relative intensities of all peaks reveal only diffraction peak of pure SnO_2 phase until Sb doping concentration was arised to 15 mol%. An increase of Sb concentration up to 20 mol%, Sb segregation was observed in phase of Sb_2O_3[14]. The Possibility of Sb incorporated into the SnO_2 lattice was replaced by two oxidation states of Sb^{3+} which has a lager ionic radius ($r = 0.76$ Å) and Sb^{5+} which has a smaller ionic radius ($r = 0.62$ Å) than Sn^{4+}($r = 0.69$ Å).[15] A part of the Sb^{5+} is able to easily substitute into the tin oxide lattice since Sb^{5+} has a similar ionic radius to Sn^{4+} state. On the other hand, the substitution of Sb^{3+} state is more difficult to occur resulting the existence of detectable Sb_2O_3 phase. By calculation, the crystallite size of as-synthesized ATO nanopowders decreases as Sb concentration is less than 5 mol% and increases from 2.64 to 3.27 nm when Sb concentration is raised to 10 mol%. This critical feature may derive from the truth that the Sb^{3+} state could occupy interstitial sites of SnO_2 lattice due to Sb^{3+} has a lager ionic radius to Sn^{4+} state causing in a large number of dislocations.[16] Therefore, the phase of Sb_2O_3 was observed since Sb^{5+} may probably be reduced to Sb^{3+} after Sb concentration up to 20 mol%. After calcinations, this phase weakens and finally disappears due to the instability of Sb^{3+} with rather big ionic radius in the expanded crystallite size of SnO_2 structure. However, XRD patterns and crystallite size of ATO nanopowders become weakened appearance with increasing Sb content, suggesting that Sb dopant could prevent the SnO_2 crystallite growth.

In Raman active mode, the spectra of as-synthesized Sb-doped SnO_2 nanopowders are illustrated in Figure 2(a). For as-synthesized nanopowders, the Raman peaks located at 477 and 575 cm^{-1} are observed, which is attributed to the vibration of oxygen in the oxygen plane and small size effect of SnO_2 particle, respectively.[17] The peak position at 576 cm^{-1} is not detected obviously on Raman spectra after Sb concentration increases up to 10 mol%. This effect may come from the segregation of Sb^{3+} state occupied interstitial sites of SnO_2 lattice, resulting in bigger crystallite size as seen in Table I. In Figure 2(b), it is suggested

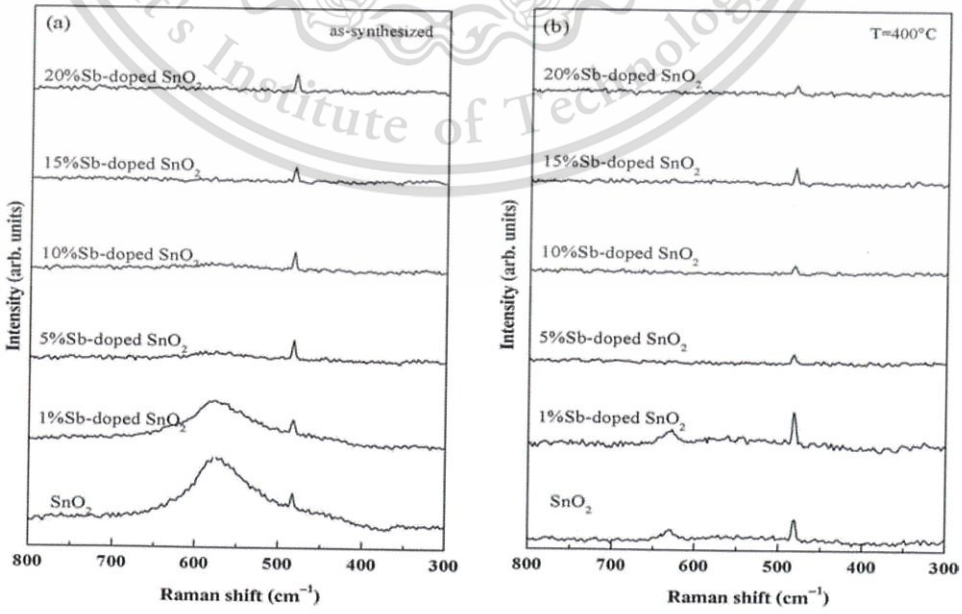

Figure 2. Raman spectra of Sb-doped SnO_2 nanopowders (a) as-synthesized (b) after calcinations at 400 °C.

that the thermal energy provided by calcination process not only results to the disappearance of the Raman peak at 576 cm^{-1} but also influences appearance of Raman peak at 627 cm^{-1}. This peak can be attributed to the symmetric Sn—O stretching mode in nanocrystalline SnO_2, suggesting the better crystallinity of the sample can be obtained by heat treatment. However, the peak intensity of symmetric Sn—O stretching mode is absent after Sb concentration increases, implying the presence of imperfect lattice sites. The Raman results of the Sb-doped SnO_2 nanopowders synthesized by sonochemical-assisted precipitation process coincidently affirm the crystallite growth of nanopowder, which is in good agreement to XRD results.

In order to gain insight of the nanoparticles, the chemical composition was analyzed by XPS. Figure 3 shows the XPS survey scan spectrum of ATO with 10 mol% Sb content calcined at 400 °C, which contains the Sn3d, Sb3d, and O1s peaks. As seen in Figure 3(b), Sn3d spectra detected in two regions of 485–490 eV and 493–497 eV correspond to the spin orbital state of $3d_{5/2}$ and $3d_{3/2}$, respectively. The XPS spectrum in the binding energy range of 525–545 eV is masked by the O1s and Sb3d transition, which can be deconvoluted into O1s, $Sb3d_{5/2}$ and $Sb3d_{5/2}$ as shown in Figure 3(c). The Gaussian line centered at 540.63 eV corresponds to the Sb^{4+} oxidation state resulting from the intervalence charge transfer as mixed Sb^{3+}–Sb^{5+}. The XPS spectra of Sb-doped SnO_2 also obviously confirm the existence of Sb^{3+} and Sb^{5+} incorporated into SnO_2 matrix.

The TEM images and selected area electron diffraction (SAED) patterns of SnO_2 nanopowders are illustrated in Figure 4. The image of as-synthesized powders as shown in Figure 4(a) is unable to identify general structure of small granular clusters. The SAED of SnO_2 nanoparticles exhibits several stronger halo rings than as-synthesized nanopowders confirming to polycrystalline structure and the brightest inner ring attributes to the (110) plane of SnO_2 structure. It can be deduced that the crystallite growth of the nanopowders are strongly affected by calcinations. Figure 4(b) shows excellent dispersiveness with less agglomeration of the nanoparticles of the size estimated 10–13 nm. The good dispersion of the particles is obtained by the aid of ultrasonic energy supplied during synthesis. It is suggested that the sonochemical assistance not only provides energy for crystallite growth but also influences the formation process including nucleation, growth coagulation, and flocculation.

Before resistance measurement, the Sb-doped SnO_2 nanopowders were pressed in the form of pellet provided the increase in powder density and contacts between grains. The electrical resistance of nanopowders with different Sb concentration is exhibited in Table II. The high resistance of tin oxide was observed due to the oxygen vacancies of SnO_2 grains. When doping with Sb, the resistance of SnO_2 decreased dramatically, suggesting that the

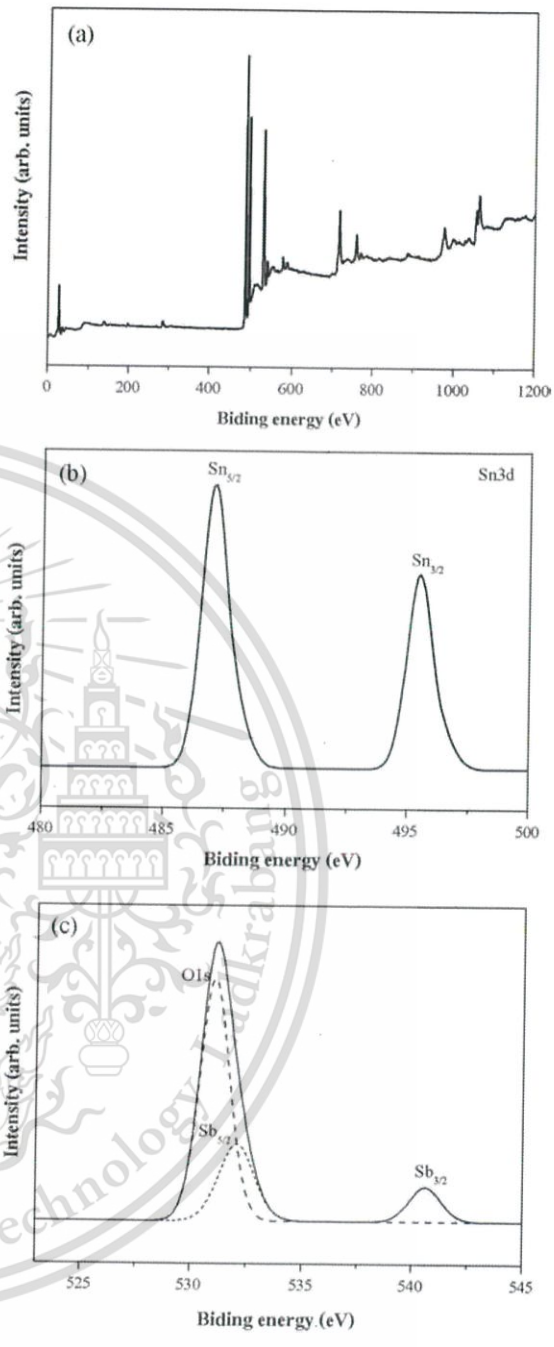

Figure 3. XPS spectra of Sb-doped SnO_2 nanopowders with 10 mol% (a) survey scan, (b) narrow scan of Sn3d, and (c) narrow scan of Sn3d and O1s.

incorporation of Sb ions can enhance the conductivity of tin oxide. A minimum resistance value of 17.49 Ω was obtained by 5 mol% Sb concentration and then the resistance slightly increases when Sb concentration was raised to 10 mol%. The resistance of tin oxide can be reduced by Sb^{5+} incorporated into the SnO_2 lattice, causing the formation of donor levels appeared very close to the conduction band. These donor levels can consequently generate the extra electrons and promote the higher electron mobility into the conduction band as depicted in Figure 5(a).

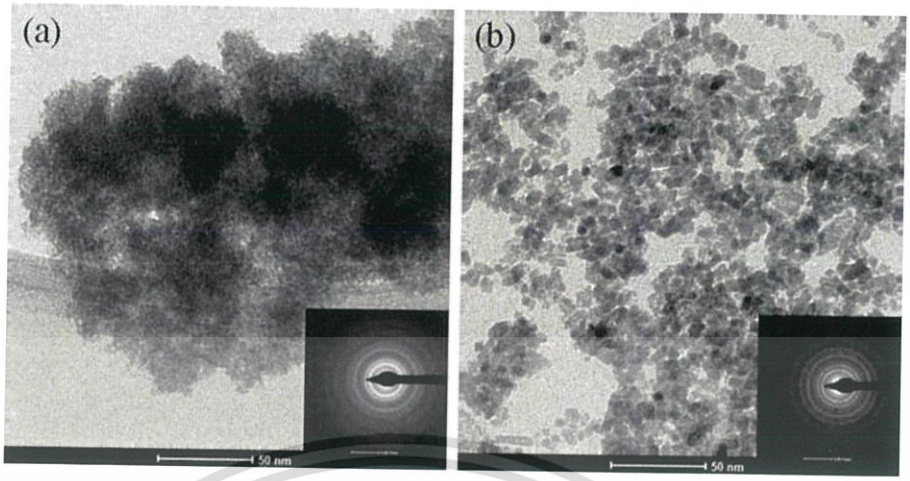

Figure 4. TEM images of SnO_2 nanopowders (a) as-synthesized (b) after calcinations at 400 °C.

Table II. The electrical resistance of ATO nanopowders.

% Sb concentrations (%)	Resistance (Ω)
0	2190.58
1	26.65
5	17.49
10	18.37
15	57.86
20	82.83

From XRD results, it is indicated that the phase of Sb_2O_3 can be obtained by the Sb^{5+} ions reduced to the Sb^{3+} state after excess antimony. The incorporation of Sb^{3+} ions into tin oxide can create the acceptor levels as shown in Figure 5(b). Therefore, possibility of the free electrons may be trapped by the acceptor levels (Fig. 5(c)) leading to an increase the resistance of tin oxide. In addition, the increasing resistance can also be partially attributed to the excess antimony atoms build in the grain boundary regions which can potentially prevent the growth of SnO_2 nanocrystals,[18] which is in good accordance with Raman results. These results reveal that the Sb incorporation with optimal concentration can produce lower resistance affected by the substitution of Sn^{4+} by Sb^{5+}.

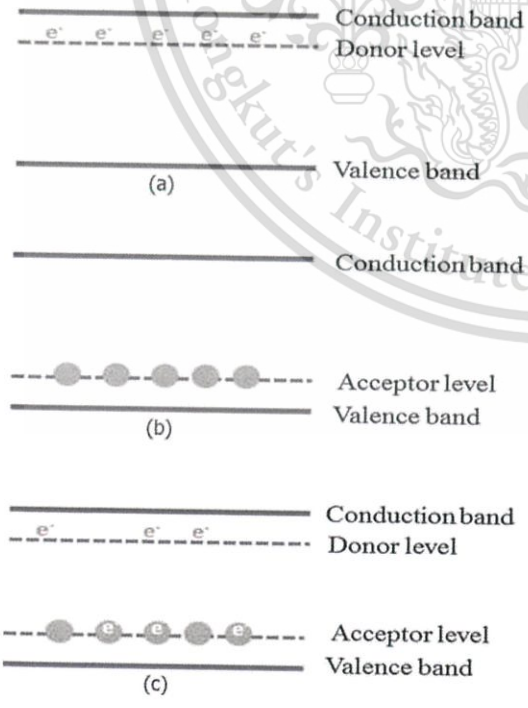

Figure 5. Band diagram of Sb ions incorporated into SnO_2 generating (a) donor levels by Sb^{5+}, (b) acceptor levels by Sb^{3+} and (c) the free electrons trapped by acceptor level.

4. CONCLUSION

Sb-doped SnO_2 nanopowders were synthesized by sonochemical-assisted precipitation process. The characterizations of the powders were conducted and the results revealed that the as-synthesized powder in SnO_2 phase with less agglomeration can be obtained by single step sonochemical process. It is suggested that the sonochemical process generates localized high temperature area guiding to crystallite growth, nucleation and flocculation of particles. When doping with Sb, the resistance of SnO_2 decreases dramatically, suggesting that the incorporation of Sb^{5+} ions can enhance the conductivity of SnO_2. However, the Sb incorporation with optimal concentration is significant since the free electrons may be trapped by the acceptor levels which are created by the substitution of Sn^{4+} by Sb^{3+} after excess antimony.

Acknowledgments: This work has partially been supported by the National Nanotechnology Center (NANOTEC), NSTDA, Ministry of Science and Technology, Thailand, through its program of Center of Excellence Network. Authors gratefully acknowledge the support College of Nanotechnology, King Mongkut's Institute of Technology Ladkrabang (KMITL) and Thailand Graduate Institute of Science and Technology (TGIST). This work was financially supported by KMITL research fund.

References and Notes

1. Y. Wang and T. Chen, *Electrochim. Acta* 54, 3510 (**2009**).
2. X. C. Chen, *Mater. Lett.* 59, 1239 (**2005**).
3. F. Chen, N. Li, Q. Shen, C. Wang, and L. Zhang, *Sol. Energ. Mat. Sol. C* 105, 153 (**20012**).
4. W. Shuo, Z, Qingnan, M. Dengkui, and D. Yuhong, *J. Rare Earth* 28, 189 (**2010**).
5. J. W. Leem and J. S. Yu, *Mat. Sci. Eng. B-Adv.* 176, 1207 (**2011**).
6. I. S. Song, S. W. Heo, J. H. Lee, J. R. Haw, and D. K. Moon, *J. Ind. Eng. Chem.* 18, 312 (**2012**).
7. J. Montero, C. Guillén, and J. Herrero,s, Philadelphia, *Sol. Energ. Mat. Sol. C* 95, 2113 (**2011**)
8. X. Zhong, B. Yang, X. Zhang, J. Jia, and G. Yi, *Particuology* 10, 365 (**2012**).
9. A. R. Babar, S. S. Shinde, A. V. Moholkar, and K. Y. Rajpure, *J. Alloy. Comp.* 505, 743 (**2010**).
10. H. J. Jeon, M. K. Jeon, M. Kang, S. G. Lee, Y. L. Lee, Y. K. Hong, and B. H. Choi, *Mater. Lett.* 59, 1801 (**2005**).
11. H. Mio, C. Ding, and H. Luo, *Microelectron. Eng.* 66, 142 (**2003**).
12. M. Wang, Y. Gao, L. Dai, C. Cao, and X. Guo, *J. Solid State Chem.* 189, 49 (**2010**).
13. S. M. Sedghi, Y. Mortazavi, and A. Khodadadi, *Sensor. Actuat. B-Chem.* 145, 7 (**2010**).
14. H. W. Kim, H. S. Kim, H. G. Na, J. C. Yang, M. A. Kebede, and C. Lee, *Ceram. Int.* 37, 593 (**2011**).
15. T. Krishnakumar, R. Jayaprakash, N. Pinna, A. R. Phani, M. Passacantando, and S. Santucci, *J. Phys. Chem. Solids* 70, 993 (**2009**).
16. A. B. Babar, S. S. Shinde, A. V. Moholkar, C. H. Bhosale, J. H. Kim, and K. Y. Rajpure, *J. Alloy. Comp.* 505, 416 (**2010**).
17. L. Tan, L. Wang, and Y. Wang, *J. Nanomater.* Article ID 529874, 10 (**2011**).
18. L. S. Wang, H. F. Lu, R. Y. Hong, and W. G. Feng, *Powder Technol.* 224, 124 (**2012**).

Received: 10 April 2013. Accepted: 24 February 2014.

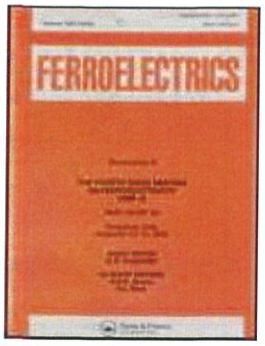

Ferroelectrics

ISSN: 0015-0193 (Print) 1563-5112 (Online) Journal homepage: http://www.tandfonline.com/loi/gfer20

Physical, Electrical and Optical Properties of F/Sb Codoped SnO_2 Synthesized Via Sonochemical Process

R. Noonuruk, W. Mekprasart, N. Vittayakorn, J. Sritharathikhun & W. Pecharapa

To cite this article: R. Noonuruk, W. Mekprasart, N. Vittayakorn, J. Sritharathikhun & W. Pecharapa (2016) Physical, Electrical and Optical Properties of F/Sb Codoped SnO_2 Synthesized Via Sonochemical Process, Ferroelectrics, 490:1, 136-148, DOI: 10.1080/00150193.2015.1072694

To link to this article: http://dx.doi.org/10.1080/00150193.2015.1072694

Published online: 29 Jan 2016.

Ferroelectrics, 490: 136–148, 2016

ISSN: 0015-0193 print / 1563-5112 online
DOI: 10.1080/00150193.2015.1072694

Taylor & Francis
Taylor & Francis Group

Physical, Electrical and Optical Properties of F/Sb Codoped SnO_2 Synthesized Via Sonochemical Process

R. NOONURUK,[1] W. MEKPRASART,[1] N. VITTAYAKORN,[1,2] J. SRITHARATHIKHUN,[3] AND W. PECHARAPA[1,4,*]

[1]College of Nanotechnology, King Mongkut's Institute of Technology Ladkrabang, Bangkok 10520, Thailand
[2]Department of Chemistry, Faculty of Science, King Mongkut's Institute of Technology Ladkrabang, Bangkok 10520, Thailand
[3]National Electronics and Computer Technology Center, National Science and Technology Development Agency, Pathumthani, 12120, Thailand
[4]Thailand and Center of Excellence in Physics (ThEP Center), CHE, 328 SiAyutthaya Rd, Bangkok, 10400, Thailand

F/Sb-codoped SnO_2 nanoparticles were synthesized via sonochemical process using stannic chloride pentahydrate ($SnCl_4{\cdot}5H_2O$) as host precursor while antimony(III) chloride ($SbCl_3$) and ammonium fluoride (NH_4F) were chosen as Sb and F dopant precursors, respectively. Their physical properties and morphologies were investigated using X-ray diffraction, Raman spectroscopy, X-ray photoelectron spectroscopy and transmission electron microscope while their electrical and optical properties were investigated by Hall measurement and diffuse reflectance spectroscopy. As-synthesized powder of polycrystalline phase SnO_2 nanoparticles can be obtained by one-step sonochemical process and its crystallinity can be improved by calcination process. The formation of crystalline phase of SnO_2 is assisted by cavitation effect provided by intense ultrasonic radiation via rapid collision. The characterization results disclose that Sb dopant has strong influence on both physical and electrical properties while F dopant provide considerable effect on electrical property of the samples. It is noticed that the codoping of both elements with certain contents can significantly heighten its electrical conductivity.

Keywords Tin oxide; fluorine-antimony codoping; sonochemical; characterization

1. Introduction

Due to its exceptional properties including wide band gap n-type semiconductor (3.67 eV), excellent thermal properties and good chemical stability [1], tin oxide has been recently recognized as a versatile metal oxide material for various practical applications such as gas sensor [2] transparent conducting electrode [3], catalyst [4] and optical electronic devices [5]. However, low optical and electrical performance due to its

Received October 26, 2014; in final form January 26, 2015.
*Corresponding author. E-mail: kpewisan@gmail.com

stoichiometry, low intrinsic carrier density and mobility are still its major drawbacks. The charge carrier concentration in SnO_2 and electrical conductivity can be effectively heightened by the incorporation of extrinsic dopants [6]. The appropriate dopants typically utilized for increasing the conductivity and optical properties of SnO_2 are In, Sb, F and Mo [7] that can provide oxygen vacancies generating free electrons to promote higher conductivity of the SnO_2 host [8].

Recently, many processes such as precipitation process [9] sol-gel method [10] and hydrothermal method [11] have been employed to synthesize tin-oxide-based materials in form of low dimensional nanostructure with the improvement in physical, optical, catalytic and electric properties. Among these techniques, the precipitation method has significant advantages over the others such as simplicity of solution concentration, simply synthesized process, ease of doping and low time and energy consumption. Nevertheless, agglomeration of ultra-fine nanoparticles is still critical for this synthesis process. This difficulty can be overcome by the assistance of sonochemical technique which is one of effective method to synthesize ultra-fine nano-structured materials with less agglomeration and rapid crystal growth due to cavitation effect in chemical process during high ultrasonic irradiation. Based on recent reports, particular researches dedicated to sonochemical synthesis of F and Sb-doped SnO_2 nanoparticles are rather limited. Therefore, this study reports the synthesis and characterization of F/Sb-codoped SnO_2 nanoparticles via sonochemical process and effects of both dopants on the variation of crucial properties of SnO_2 were investigated.

2. Experimental Procedure

2.1 Sample Preparation

F-doped SnO_2 (FTO), Sb-doped SnO_2 (ATO) and F/Sb-codoped SnO_2 (FATO) nanopowders were synthesized by sonochemical process using stannic chloride pentahydrate ($SnCl_4{\cdot}5H_2O$) as a host precursor while antimony(III) chloride ($SbCl_3$) and ammonia fluoride (NH_4F) were chosen as Sb and F dopant precursor, respectively. The composition of antimony was fixed at 5 mol% and 10 mol% while the fluoride composition was varied from 1–10 mol%. The F/Sb-codoped SnO_2 nanopowders were named F:Sb mol% FATO following the mol% ratio such as 1:5FATO. The starting precursors were dissolved in absolute ethanol and acetylacetone was slowly added. The precursor was vigorously stirred for 20 min at room temperature until homogeneous solution was reached. Ammonia solution was added drop wise to the stock solution during sonication until the pH value of the solution was reached to the range of 9–10. The solution was sonicated for 30 min by a direct-immersion ultrasonic horn using Sonic model VCX 750 (750 W, 20 kHz). The gelatinous precipitated products were obtained and allowed to cool down to room temperature then the product was washed several times with deionized water via centrifugation to remove both ammonia and chlorine ions and dried slowly at 80°C overnight in an oven. Finally, the samples were calcined at 400°C for 2 h to ensure the complete decomposition of the organic polymer and improve crystallinity of the particles.

2.2 Characterizations

The structural properties of powders were characterized by XRD (PANalytical X'Pert Pro) operated at 40 kV and 30 mA using Cu-K_α radiation over a 2θ from 20° to 80° with step of 0.02°/sec. The size, shape and crystal structure of the particles were observed by

TEM (FEI, TECNAI G^{2}20) operated at 200 kV. Chemical bonding of powders was characterized by Raman spectroscopy carried out in the range of 300–800 cm^{-1}. The chemical state analyses of the samples were carried out by X-ray photoelectron spectroscopy (Kratos analytical, AXIS ULTRA^{DLD}) using Al-K_α with radiation at 1.4 keV. The resistivity (ρ) and carrier concentration (n) of the films were measured at room temperature using Hall measurement system in Van der Pauw configuration. Before Hall measurement, the 0.6 g of nanopowder was pressed into circular pellet of 1.5 mm diameter under 2.5 ton pressures for 2 min by hydraulic pelletizer. Then the pellets were sintered at 1000°C for 30 min giving the pellet with thickness of 1 mm. Reflectance spectra were recorded in a wavelength of 200–1500 nm using UV-Vis spectrophotometer on model Shimadzu UV-3600.

3. Results and Discussion

Figure 1 (a) shows XRD patterns of as-synthesized samples and SnO_2 nanoparticles calcined at 400°C. For as-synthesized samples, there are noticeable diffraction peaks which are attributed to (110), (101) and (211) planes of SnO_2 with tetragonal rutile structure. This result suggests that as-synthesized powder with primarily polycrystalline phase of SnO_2 ultrafine structure can be obtained by one-step sonochemical process without heat treatment process. The formation of crystalline phase of SnO_2 during sonochemical process could be initiated by cavitation effect during intense ultrasonic radiation via rapid collision forced by strong ultrasound energy. This collision is capable to rapidly elevate localized high-temperature area that can effectively quicken the condensation reactions of hydroxyl groups to produce the nucleation of fine nanoparticles of SnO_2 via following chemical reactions:

$$SnCl_4 + 4NH_4OH \rightarrow Sn(OH)_4 + 4NH_4Cl \quad (1)$$

$$Sn(OH)_4 \xrightarrow{ultrasonic\ \ radiation} SnO_2 + 2H_2O. \quad (2)$$

Moreover, after calcinations at moderate temperature, it is observed that there is increasing intensity of all diffraction peaks, indicating that the better crystallinity of SnO_2 nanoparticles can be obtained by calcinations process.

XRD patterns of after-calcined FATO nanoparticles prepared via sonochemical process with various doping contents are exhibited in Fig. 1 (b). Three prominent diffraction peaks positioned at $2\theta = 26.5°$, 34.0° and 51.9° are well-indexed to (110), (101), (211) plane orientations of tetragonal SnO_2 crystal structure, respectively [11]. In addition, the other minor noticeable peaks situated at $2\theta = 38.0°$ and 65.3° are nicely ascribed to (200) and (301) planes of tetragonal SnO_2 structure, respectively [3]. This result suggests that the good crystallinity of tetragonal SnO_2 structure can be obtained via this synthesis method and moderate heat treatment. It is further noticed that their major peak intensities tend to decrease with increasing content of either dopant. The average crystallite size of FATO nanoparticles can be calculated from the full-width at half maximum (FWHM) of

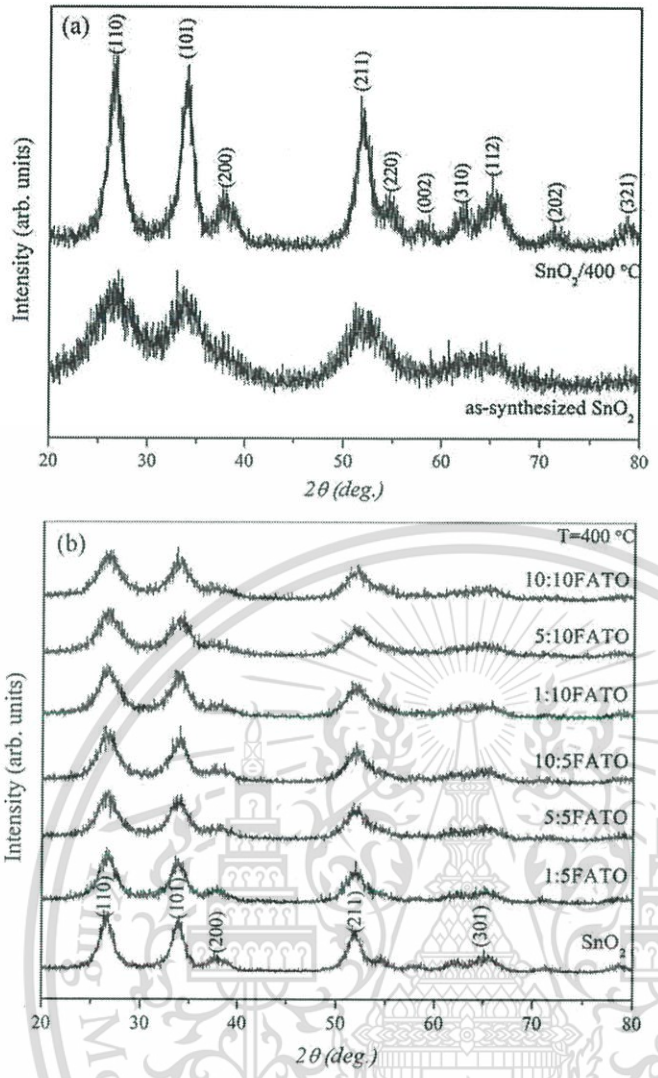

Figure 1. XRD patterns of (a) SnO_2 nanoparticles with different heat treatments and (b) FATO nanoparticle with different Sb and F concentrations.

(110) most distinct peak by Scherrer's equation expressed as follows:

$$D = \frac{0.9\lambda}{\beta \cos\theta}. \tag{3}$$

Note that D is the crystallite size, K is the shape factor, λ is the X-ray wavelength of Cu K_α (0.154 nm), β is the full-width at half maximum (FWHM) and θ is the diffraction angle. It is found that the average size of the particle is ca. 10 nm indicating that tiny and uniform SnO_2-based nanoparticles can be achieved by sonochemical process. It is further interpreted from the XRD intensity that the crystallite size of FATO nanoparticles significantly changes with increasing doping content. These manners may originate from the difference in ionic radius of Sb^{3+} which has a lager ionic radius (r = 0.76 Å) than that of

Sn^{4+} (r = 0.69 Å) [12] and between that of fluorine ion (1.33 Å) and oxygen ion (1.33 Å) [13].

The Raman spectra of SnO_2 nanoparticles with different heat-treated temperatures are illustrated in Fig. 2 (a). For as-synthesized samples, the peaks observed at 484.89 and 576.76 cm^{-1} are attributed to the E_g vibration mode and the small size effect of nanocrystalline SnO_2 [14]. The doubly degenerated E_g mode is related to the vibration plane of oxygen in the direction of the c-axis. After calcined at 400°C, the fundamental Raman peaks of rutile SnO_2 at 633.51 and 774.25 cm^{-1} are observed, that is attributed to A_{1g} and B_{2g} vibration modes. Both peaks are corresponded to non-degenerate phonon modes vibrating in the plane perpendicular to the c-axis corresponding the expansion (A_{1g}) and contraction (B_{2g}) vibration of Sn-O bonds [15]. Moreover, the broad peak around 400–600 cm^{-1} may originate from combination of E_g vibration mode and nanocrystalline SnO_2 system mode, whereas the peak at 309.50 cm^{-1} can be correlated to the E_u transverse optical mode. All vibration peaks are Raman active mode except in the E_u mode which is Raman-inactive caused by disorder at the interface between crystals [16]. Three fundamental Raman peaks positioned at 474.50, 633.51 and 773.42 cm^{-1} are clearly observed in the sample sintered at 1000°C. These peaks are assigned to the three characteristic spectra of rutile SnO_2 single crystal, suggesting the better crystallinity of the sample can be obtained by heat treatment. In addition, Raman spectroscopy is an important tool to confirm structural defect affected by the Sb and F substituted into SnO_2 lattice on

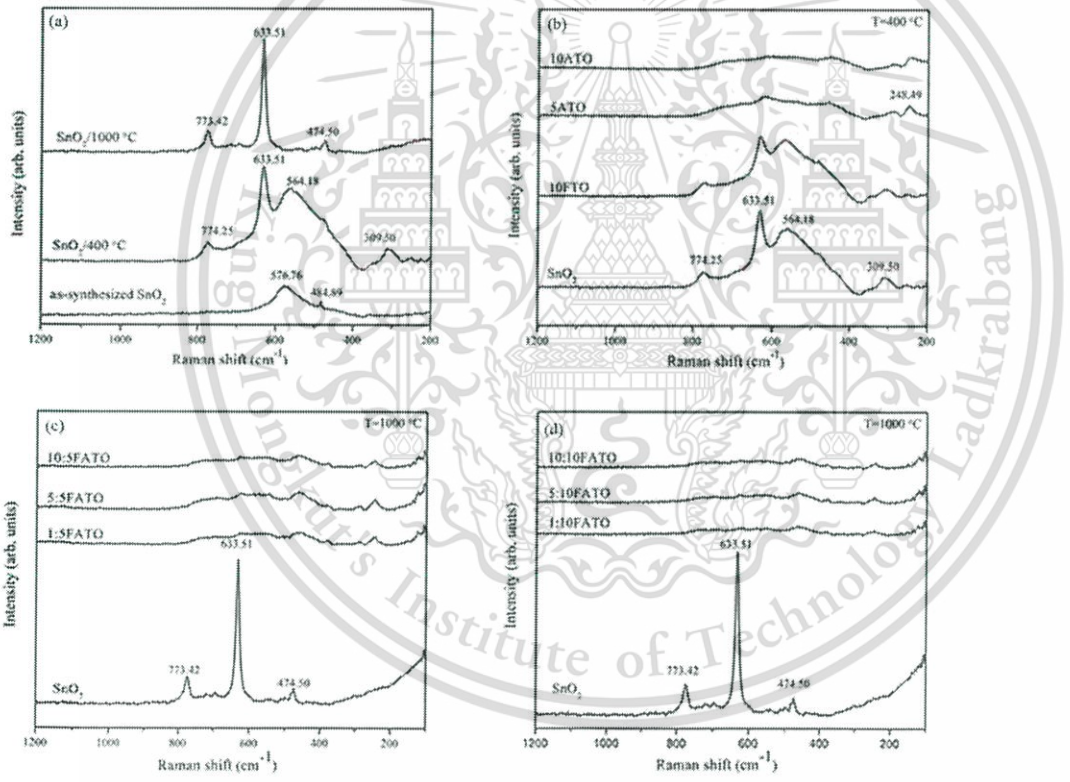

Figure 2. Raman spectra of SnO_2 nanoparticles with (a) different heat treatments, (b) Sb and F doping, (c) FATO at 5 mol% Sb content and (d) FATO at 10 mol% Sb content with different F concentrations.

vibrational properties. The Raman spectra of FTO and ATO nanoparticles calcined at 400°C are shown in Fig. 2 (b). Raman result of FTO sample exhibits three fundamental Raman peaks with decreasing intensity of Sn-O bond due to the proper substitution of F ion at O site without significant alternation of SnO_2 local structure. On the other hand, three fundamental Raman peaks are evidently absent by the incorporation of Sb, implying the presence of imperfect lattice sites due to the improper substitution of Sb ion or other local defects in SnO_2 crystal [17]. This manner implies that the F and Sb dopant substitution in SnO_2 lattice results in vacant lattice site or oxygen vacancies and lattice distortion. In Fig. 2 (c) and (d), Raman spectra of codoped samples are disappeared after sintering at 1000°C, implying the presence of imperfect lattice sites and intensive reduction in lattice space symmetry.

The surface chemical characteristics of the FTO, ATO and FATO nanoparticles were analyzed by XPS. All the binding energy (BE) calibration of the spectra were referenced to the C1S peak located at 285.0±0.1 eV. Fig. 3 (a) shows the XPS survey scan spectrum of FATO sample calcined at 400 °C, indicating that the sample consists of the Sn3d, Sb3d, F1s and O1s peaks. As seen in Fig. 3 (b), Sn3d spectra detected in two regions of 485–490 eV and 493–497 eV correspond to the spin orbital state of $3d_{5/2}$ and $3d_{3/2}$, respectively [18]. In the Sn3d spin orbital spectrum, the peak intensity of Sb-doped sample become lower and shifts to the higher binding energy than that of F-doped sample as observed in Fig. 3 (b). The substitution of F^- anion at O^{2-} anion and Sb^{5+} or Sb^{3+} cations at Sn^{4+} site can lead to the creation of greater amount of free electrons [19,20]. These results indicate that Sb dopant has dominance on the decrease in peak intensity of Sn3d than F dopant and the shift in binding energy reflects to more oxidization by the dopant. In narrow scan spectra, the orbital state of $Sb3d_{5/2}$ is masked by the O1s in binding energy range of 528–535 eV but $Sb3d_{5/2}$ is clearly observed at 540 eV for both samples except in FTO sample. Alternative way to study the defects in the lattice is to analyze the change at the binding energy level of O1s as noticed in Fig. 4. The O1s core level line can be deconvoluted into four peaks components centered at 529.59 eV, 530.84 eV, 532.14 eV and 533.28 eV. The peak center at 529 eV is attributed to O^{2-} in lattice of SnO_2 structure implying a fully oxidized stoichiometric environment, while the main peak at 531 eV is associated with O ion in the oxygen deficient regions or oxygen vacancies in the lattice [21]. The binding energy at 532 eV is the combination of chemisorbed oxygen of OH^- groups on surface with orbital state of $Sb3d_{5/2}$ in Sb doped sample. The peak position of O1s is shifted to high binding energy, suggesting that the more oxygen vacancies are generated by Sb incorporated into SnO_2 structure [22]. The peak located at 533 eV is observed only in the FTO sample, which is associated with adsorbed oxygen of H_2O or CO_3 on surface of sample indicating the more hygroscopic in nature [23]. The XPS results affirm that F ions and Sb ions incorporated into the SnO_2 lattice are able to effectively provide more oxygen vacancies in the doped sample.

TEM images and selected area electron diffraction (SAED) patterns of FTO, ATO and FATO nanoparticles are illustrated in Fig. 5. As seen in Fig. 5 (a), the morphologies and particle size of as-synthesized SnO_2 nanoparticles are unable to identify due to general structure of small granular clusters as well as the SAED patterns show soft halo rings reflecting their amorphosity in nature. The TEM image indicates that the SnO_2 nanoparticles are excellent disperse with less agglomeration and uniformity of particle shape which appear in spherical shape with estimated size of less than 10 nm after calcination at 400°C. The SAED of SnO_2 nanoparticle exhibits several strong halo rings confirming to polycrystalline structure and the brightest inner ring attributes to the (110) plane of SnO_2 structure, which is consistent with XRD results. It can be deduced that the

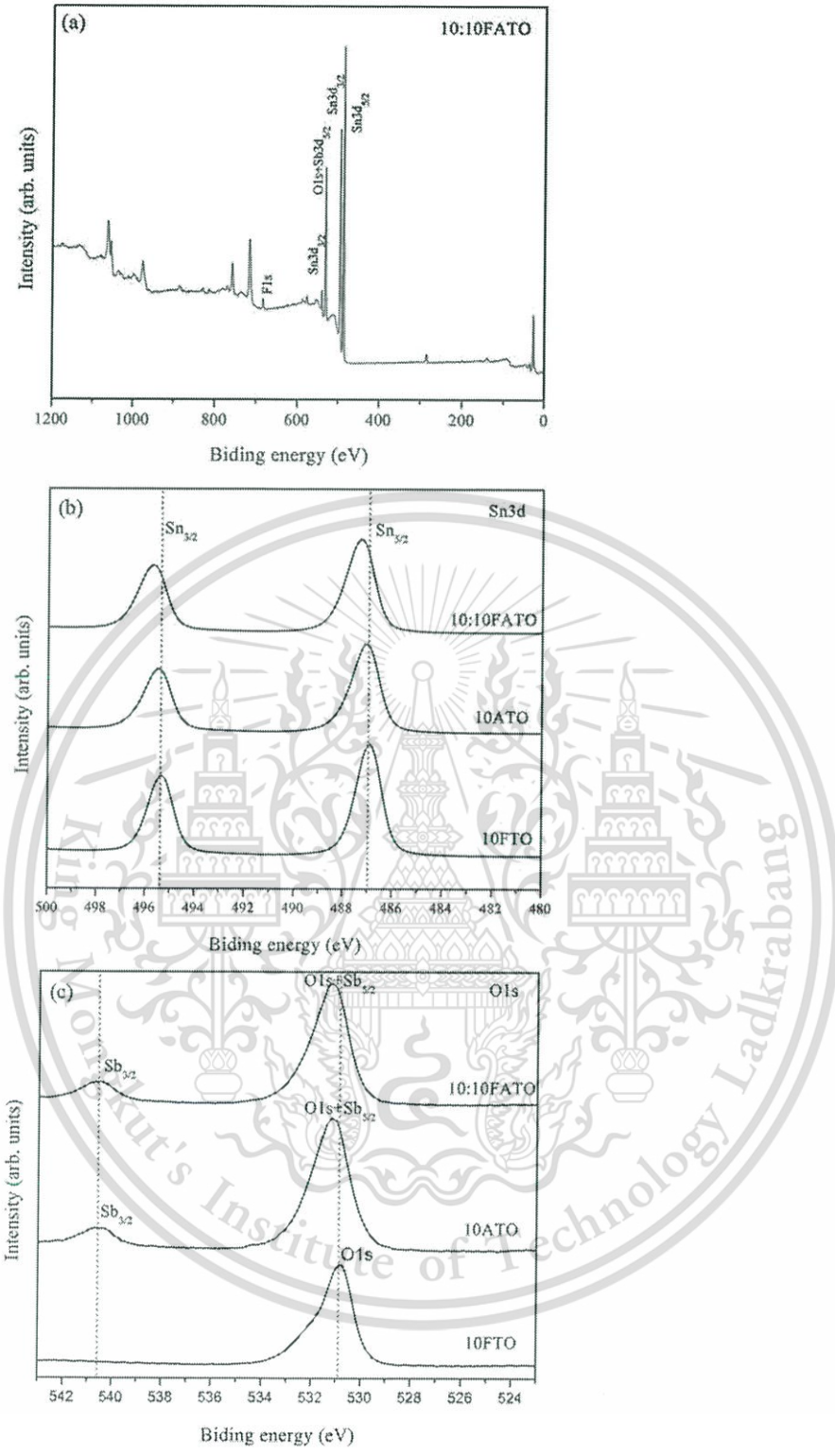

Figure 3. XPS spectra of FATO SnO_2 nanoparticles (a) survey scan, (b) narrow scan of Sn3d and (c) narrow scan of Sb3d+O1s.

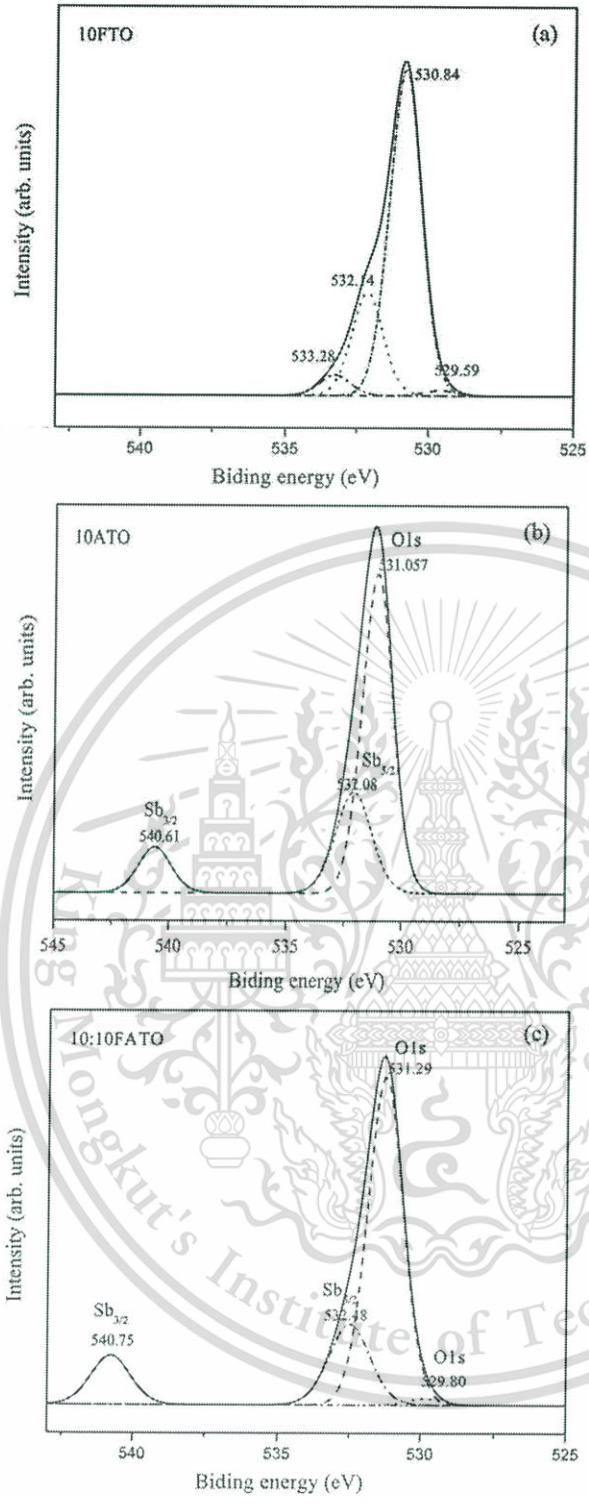

Figure 4. O1s deconvolution of (a) FTO, (b) ATO and (c) FATO nanoparticles.

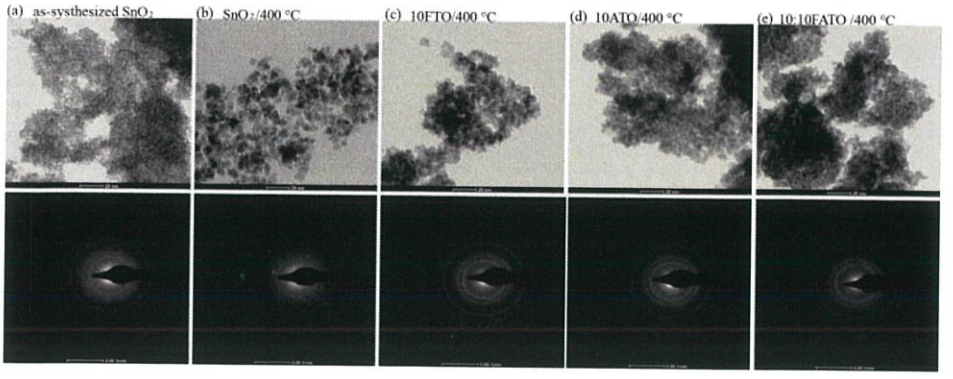

Figure 5. TEM images of (a) as-synthesized SnO_2 (b) SnO_2, (c) FTO, (d) ATO and (e) FATO nanoparticles.

crystallite growth of the nanopowders are highly affected by heat treatment. From TEM images, it is suggested that the F dopant has slight effect on morphologies and particle sizes of SnO_2 particles while Sb dopant provide significant influence on SnO_2 structure. In addition, the morphologies of FATO particles display many spherical shaped grains formed by aggregation of nanocrystalline.

The resistivity (ρ) and carrier concentration (n) of FATO samples are exhibited in Table 1. The high resistance of tin oxide is observed, while the resistivity of FTO sample decreases considerably from 10.45 Ω·cm to 13.6 Ω·cm. This feature is originated from the fact that fluoride ion incorporated in SnO_2 can contribute one exceeding free electron to SnO_2 leading to the reduction in electrical resistivity [13]. For ATO sample, its resistivity decreases dramatically down to 5.03×10^{-3} Ω·cm and 5.43×10^{-2} Ω·cm for the samples with Sb concentration of 5 mol% and 10 mol%, respectively. This feature is due to Sb ions incorporated into the SnO_2 lattice causing the formation of donor levels appeared very close to the conduction band [12]. These donor levels can consequently generate the extra electrons and promote the higher electron mobility into the conduction band. Both F and Sb doped SnO_2 samples can promote the higher electron mobility as shown in Table 1. It is observed that the lower resistivity and good carrier density are obtained as the Sb content reaches a specific content of 5 mol%. However, the resistivity slightly

Table 1
The resistivity and carrier density of samples by Hall measurement

Samples	Resistivity (Ω cm)	Carrier Density ($1/cm^3$)
SnO_2	14.5	1.35×10^{16}
10FTO	13.6	3.88×10^{17}
5ATO	5.03×10^{-3}	1.04×10^{18}
10ATO	5.43×10^{-2}	4.36×10^{17}
1:5FATO	3.96×10^{-3}	1.27×10^{18}
5:5FATO	5.61×10^{-3}	1.01×10^{18}
10:5FATO	4.82×10^{-3}	3.46×10^{17}
1:10FATO	6.05×10^{-2}	2.72×10^{17}
5:10FATO	1.03×10^{-1}	3.25×10^{17}
10:10FATO	7.15×10^{-2}	9.92×10^{17}

increases after the Sb concentration augmented beyond 10 mol% in the SnO_2 lattice owing to possibility of the free electrons trap by the acceptor levels. This level is created by Sb^{3+} ion incorporated in Sn^{4+} site in SnO_2 lattice when the doping exceeds the specific value [24] that can initiate the oxidation reduction of Sb^{5+} to Sb^{3+}. In addition, the resistivity greatly decreases with F/Sb codoped in SnO_2 structure due to the co-existence of oxygen vacancies and substituted Sn producing the extra electrons and the higher electron density [25]. The limitation of F:Sb codopant ratio is 1:5 mol% providing the lowest resistivity at 3.96×10^{-3} Ω·cm. Nevertheless, the free carrier density decreases with increasing F concentration due to the Sn-F complexes formed in the grain boundaries, leading to a slight increase in the resistivity. These results reveal that the F/Sb co-incorporation in SnO_2 structure can considerably increase its carrier mobility and conductivity.

Diffuse reflectance spectra of SnO_2, FTO, ATO and FATO nanoparticles in the form of pellet are shown in Fig. 6 (a). The reflectance spectra show the sharp absorption edge in the wavelength region of 250–350 nm implying semiconductor behavior with the existence of direct optical band gap. The corresponding optical band gap could be estimated by Tauc method. In direct transition semiconductors, the optical absorption coefficient and the optical energy band gap is expressed as [26]:

$$(\alpha h\nu) = A(h\nu - E_g)^{1/2} \tag{4}$$

where E_g is optical band gap, $h\nu$ is photon energy and A is constant. α is absorption coefficient which is substituted with $F(R_\infty)$. Thus the relational expression becomes:

$$(h\nu F(R_\infty))^2 = A(h\nu - E_g)^{1/2} \tag{5}$$

where $F(R_\infty)$ is absorption coefficient which is obtained from the acquired diffuse reflectance spectrum using Kubelka-Munk function [27]:

$$F(R_\infty) = \frac{(R_\infty - 1)^2}{2R_\infty} \tag{6}$$

where R_∞ is the diffuse reflectance. The optical band gap energies were interpreted from the interception of the straight section to energy axis as shown in Fig. 6 (b) and (c). In Fig. 6 (b) and (c), the optical band gap of SnO_2 sample increases from 3.83 eV to 3.85 eV after fluoride doping and dramatically increases to 3.90 eV and 4.04 eV for 10ATO and 1:5FATO sample, respectively. The extended optical band bap of SnO_2 samples after F, Sb incorporation may be ascribed to Bursstein-Moss effect as a result of the increase of carrier concentration. Increasing carrier concentration will cause the alternation of Fermi level moving into the conduction band leading to a broadened optical band gap [28].

4. Conclusion

In summary, spherical F/Sb-codoped SnO_2 nanoparticles with size less than 10 nm can be synthesized by the aid of ultrasonic energy supplied via sonochemical synthesis. It is suggested that the ultrasonic not only provides energy for crystallite growth but also prevents the agglomeration of as-synthesized nanoparticles. It is revealed that Sb dopant strongly affects the crystallinity of SnO_2 reflecting the decrease in crystallite size and the deterioration of

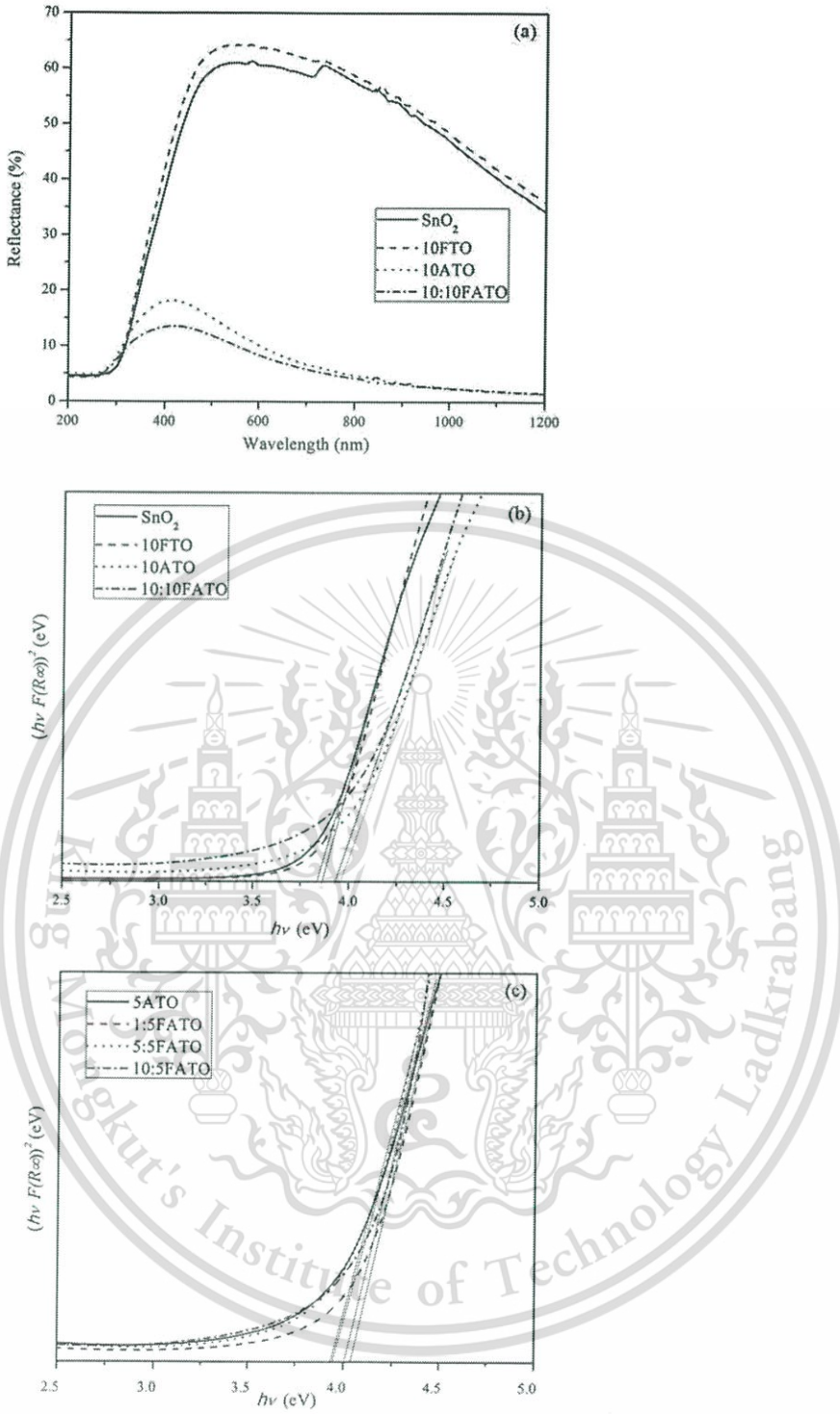

Figure 6. (a) Diffuse reflectance spectra and (b) the $(h\nu F(R_\infty))^2$ vs. $h\nu$ curves of SnO_2, FTO, ATO, FATO. (c) The $(h\nu F(R_\infty))^2$ vs. $h\nu$ curves of FATO at 5mol% Sb with different F concentrations.

local structure bonding of SnO_2. It was acknowledged that both dopants play significant role on the enhancement in the electrical properties. The electrical resistivity of the codoped sample with F/Sb ratio of 1:5 mol% can be lowered to 3.96×10^{-3} Ω·cm.

Acknowledgments

The authors gratefully acknowledge the support of the College of Nanotechnology, King Mongkut's Institute of Technology Ladkrabang (KMITL), Faculty of Engineering, Rajamangala University of Technology Thanyaburi (RMUTT) for XRD measurement, Center of Excellence in Glass Technology and Material Science (CEGM), Nakhon Pathom Rajabhat University for diffuse reflectance measurement and Thailand Graduate Institute of Science and Technology (TGIST, contract No. 0156009).

Funding

This work was financially supported by KMITL research fund. This work has partially been supported by the National Nanotechnology Center (NANOTEC), NSTDA, Ministry of Science and Technology, Thailand, through its program of Center of Excellence Network.

References

1. Babar RA, Shinde SS, Moholkar VA, Rajpure YK, Electrical and dielectric properties of co-precipitated nanocrystalline tin oxide. *J Alloy Compd.* **505**, 743–749 (2010).
2. Lee CY, Tan KO, Huang H, Tse S M, Deposition and gas sensing properties of tin oxide thin films by inductively coupled plasma chemical vapor deposition. *J Electroceram.* **16**, 507–509 (2006).
3. Park HJ, Byun JD, Lee K, Electrical and optical properties of fluorine-doped tin oxide (SnOx: FF) thin films deposited on PET by using ECR-MOCVD. *J Electroceram.* **23**, 506–511 (2009).
4. Chhina H, Campbell S, Kesler O, An oxidation-resistant indium tin oxide catalyst support for proton exchange membrane fuel cells. *J Power Sources.* **161**, 893–900 (2006).
5. Al-Habi E, Aziz AM, Oyama M, El-Naggar MA, AlZayed N, Wojciechowski A, Kityk VI, Gold nanoparticles deposited on fluorine-doped tin oxide substrates as materials for laser operated optoeletronic devices. *J Mater Sci Mater Electron.* **24**, 2422–2425 (2013).
6. Giraldi RT, Escote TM, Bernardi BIM, Bouquet V, Leite RE, Longo E, Verela AJ, Effect of thickness on the electrical and optical properties of Sb doped SnO_2 (ATO) thin films. *J Electroceram.* **13**, 159–165 (2004).
7. Wang SL, Lu FH, Hong YR, Feng WG, Synthesis and electrical resistivity analysis of ATO-Coated Talc. *Powder Technol.* **224**, 124–128 (2012).
8. Montero J, Guillén C, Herrero J, Discharge power dependence of structural, optical and electrical properties of DC sputtered antimony doped tin oxide (ATO) films. *Sol Energ Mat Sol C.* **95**, 2113–2119 (2011).
9. Song CK, Kang Y, Preparation of high surface area tin oxide powders by a homogeneous precipitation method. *Mater Lett.* **42**, 283–289 (2000).
10. Gnanam S, Rajendran V, Synthesis of tin oxide nanoparticles by sol-gel process: effect of solvents on the optical properties. *J Sol-Gel Sci Technol.* **53**, 555–559 (2010).
11. Lupan O, Chow L, Chai G, Schulte A, Park S, Heinrich H, A rapid hydrothermal synthesis of rutile SnO_2 nanowires. *Mater Sci Eng B.* **157**, 101–104 (2009).
12. Krishnakumar T, Jayaprakash R, Pinna N, Phani RA, Passacantando M, Santucci S, Structure, optical and electrical characterization of antimony-substituted tin oxide nanoparticles. *J Phys Chem Solids.* **70**, 993–999 (2009).

13. Kim H, Auyenung YCR, Piqué A, Transparent conducting F-doped SnO_2 thin films grown by pulsed laser deposition. *Thin Solid Films*. **516**, 5052–5056 (2008).
14. Liu ZL, Wu LX, Gao F, Shen CJ, Li HT, Chu KP, Determination of surface oxide vacancy position in SnO_2 nanocrystals by Raman spectroscopy. *Solid State Commun*. **151**, 811–814 (2011).
15. Mishra KR, Pandey KS, Sahay PP, Influence of In doping on the structural, photo-luminescence and alcohol response characteristics of SnO_2 nanoparticles. *Mater Res Bull*. **48**, 4196–4205 (2013).
16. Tran VT, Turrell S, Eddafi M, Capoen B, Bouazaoui M, Roussel P, Berneschi S, Righini G, Ferrari M, Bhaktha BNS, Cristini O, Kinowaki C, Investigations of the effects of the growth of SnO_2 nanoparticles on the structural properties of glass-ceramic planar waveguides using Raman and FTIR spectroscopies. *J Mol Struct* **976**, 314–319 (2010).
17. Kaur J, Shah J, Kotnala KR, Verma CK, Raman spectra, photoluminescence and ferromagnetism of pure, Co and Fe doped SnO_2 nanoparticles. *Ceram Inter*. **38**, 5563–5570 (2012).
18. Mazloom J, Ghodsi EF, Gholami M, Fiber-like stripe ATO (SnO_2:Sb) nanostructured thin films grown bysol-gel method: Optical topographical and electrical properties. *J Alloy Compd*. **579**, 384–393 (2013).
20. Babar RA, Shinde SS, Moholkar VA, Bhosale HC, Kim HJ, Rajpure YK, Structure and optical properties of antimony incorporated tin oxide thin film. *J Alloy Compd* **505**, 416–422 (2010).
21. Bang S, Lee S, Ko Y, Park J, Shin S, Seo H, Jeon H, Photocurrent detection of chemically tuned hierarchical ZnO nanostructures grown on seed layers formed by atomic layer deposition. *Nanoscale Res Lett*. **7**, 290 (2012).
22. Chu D, Younis A, Li S, Direct growth of TiO_2 nanotubes on transparent substrates and their resistive switching characteristics. *J Phys D: Appl Phys*. **45**, 335–306 (2012).
23. Park NJ, Shon KJ, Jin M, Kong SS, Moon K, Park OG, Boo HJ, Kim MJ, Room-temperature CO oxidation over a highly ordered mesoporous RuO_2 catalyst. *Reac Kinet Mech.Cat*. **103**, 87–99 (2011).
24. Shokr KhE, Wakkad MM, El-Ghanny Abd HA, Ali MH, Sb-doped effects on optical and electrical parameters of SnO_2 films. *J Phy Chem Solids*. **61**, 75–85 (2000).
25. Thangaraju B, Structural and electrical studies on highly conducting spray deposited fluorine and antimony doped SnO_2 thin films from $SnCl_2$ precursor. *Thin solid Films*. **402**, 71–78 (2002).
26. Tian CS, Chen XL, Ni J, Liu JM, Zhang DK, Huang Q, Zhao Y, Zhang XD, Transparent conductive Mg and Ga co-doped ZnO thin films for solar cells grown by magnetron sputtering: H_2 induced changes. *Sol Energ Mat Sol C*. **125**, 59–65 (2014).
27. López-Cabaña Z, Torres SMC, González G, Semiconducting properties of layered cadmium sulphide-based hybrid nanocomposites. *Nanoscale Res Lett*. **6**, 523 (2011).
28. Pan Z, Zhang P, Tian X, Cheng G, Xie Y, Zhang H, Zeng X, Xiao C, Hu G, Wei Z, Properties of fluorine and tin co-doped ZnO thin films deposited by sol-gel method. *J Alloy Compd*. **576**, 31–37 (2013).